



Dipl.-Ing. Christoph Staudinger, BSc

# **Optical High Performance Sensor Materials for Oceanography**

## **DISSERTATION**

zur Erlangung des akademischen Grades  
Doktor der technischen Wissenschaften

eingereicht an der

**Technischen Universität Graz**

Betreuer

Prof. Ingo Klimant

Institut für Analytische Chemie und Lebensmittelchemie

Assoc. Prof. Sergey Borisov

Graz, August, 2018



## **EIDESSTATTLICHE ERKLÄRUNG**

Ich erkläre an Eides statt, dass ich die vorliegende Arbeit selbstständig verfasst, andere als die angegebenen Quellen/Hilfsmittel nicht benutzt, und die den benutzten Quellen wörtlich und inhaltlich entnommenen Stellen als solche kenntlich gemacht habe. Das in TUGRAZonline hochgeladene Textdokument ist mit der vorliegenden Dissertation identisch.

---

Datum

---

Unterschrift

---

## Abstract

In this work innovative optical pH sensor materials optimized for oceanographic pH measurements are presented. The sensor concept is based on luminescence quenching of a fluorescent indicator molecule depending on the pH value of the sample. aza-BODIPY dyes were chosen as pH indicator due to their good brightness, excellent photostability, suitable excitation and emission wavelengths and straightforward chemical modification. The stability of the sensor materials was enhanced by covalent coupling of the indicators to a cross-linked polymeric matrix material. To facilitate fast response times even at low water temperatures, a novel purely hydrophilic matrix polymer based on cross-linked acryloylmorpholine was prepared. This resulted in fast and stable sensor materials, but significantly increased the effort of sensor material production. For this reason, two subsequent generations of pH sensor materials were developed, which optimized the dynamic range as well as the production procedure to enable preparation of large amounts of sensor material.

The sensor materials were developed as part of the EU-project SenseOcean, which aimed to develop a set of oceanographic sensors for a common platform. During this project the sensors were successfully tested in multiple field trips. They were deployed for depth profiling and continuous surface pH measurements on a ship on the Baltic Sea and for stationary measurements in the harbors of Kiel (Germany) and Southampton (England).

Additionally, a set of novel, purely photoinduced electron transfer (PET) based aza-BODIPYs was developed to reduce undesired effects, such as Förster Resonance Energy Transfer (FRET) and inner-filter-effect. An application of these dyes was demonstrated in a ratiometric light-harvesting concept for imaging. Furthermore, they are currently investigated as indicators for pH imaging on concrete surfaces.

---

## Kurzfassung

Die fortschreitende Versauerung der Meere durch den ansteigenden CO<sub>2</sub>-Gehalt in der Atmosphäre stellt eine immer gravierendere Bedrohung für das marine Ökosystem dar. Die Messung dieser langsamen Abnahme des pH-Wertes im Meerwasser kann bislang nicht gleichzeitig präzise und kostengünstig durchgeführt werden, so dass eine globale Überwachung dieser Veränderung nicht ausreichend möglich ist. Diese Arbeit beschäftigt sich daher mit der Entwicklung von neuen optischen pH-Sensormaterialien für den Einsatz in der Meeresforschung. Aufgrund ihrer exzellenten Eigenschaften wurden aza-BODIPYs als Indikatorfarbstoffe für die Sensormaterialien ausgewählt. aza-BODIPYs besitzen eine hohe Helligkeit, ausgezeichnete Fotostabilität, geeignete Absorptions- und Emissions-Wellenlängen und sie können einfach chemisch modifiziert werden um ihren pK<sub>s</sub> zu optimieren oder Ankergruppen einzuführen. Um möglichst stabile Sensormaterialien zu erhalten wurden die Farbstoffe kovalent an das quervernetzte Matrix-Polymer gebunden. Schnelle Ansprechzeiten bei tiefen Temperaturen wurden durch die Verwendung eines neuen, rein hydrophilen Matrix-Polymers auf Basis von Acryloylmorpholin erreicht. Dadurch wurden zwar stabile und schnelle pH-Sensormaterialien erhalten, aber der Aufwand zu ihrer Herstellung war signifikant größer. Deshalb wurde als nächster Schritt die Produktion der Materialien optimiert, indem ein separater Kopplungsschritt eingeführt wurde, der eine Abtrennung der Nebenprodukte ermöglicht. Durch diesen separaten Schritt ist es auch möglich größere Mengen des gefärbten Polymers mit konstanten Farbstoffkonzentrationen zu erhalten.

Diese Sensormaterialien wurden im Rahmen des EU-Projekts SenseOcean entwickelt, welches darauf abzielte eine breite Palette an verschiedenen Sensoren auf einer gemeinsamen Plattform zu vereinen. Während dieses Projektes wurden die entwickelten Sensoren mehrmals an verschiedenen Orten getestet. Tests wurden auf einem Schiff in der Ostsee, im Hafen von Kiel (Deutschland), in einem Seegrass-Feld am Limfjord (Dänemark) und im Hafen von Southampton (England) durchgeführt. Dabei wurden Tiefenprofile und Oberflächenprofile von Forschungsschiffen aus gemessen und auch stationäre Anwendungen getestet.

---

In einem weiteren Teilbereich dieser Arbeit wurde ein neues Set von aza-BODIPY Indikatoren entwickelt, welches rein auf Photoinduced Electron Transfer (PET) basiert. Im Gegensatz zu den meisten bisher publizierten Farbstoffen zeigen diese ein pH-unabhängiges Absorptionsspektrum. Das wurde erreicht, indem die pH sensitive OH-Gruppe von der para- auf die meta-Position der Phenylgruppen verschoben wurde. Dadurch wird diese elektronisch entkoppelt und kann die spektralen Eigenschaften des Farbstoffes nicht mehr stark beeinflussen. Eine Anwendung dieser neuen pH-Indikatoren wurde demonstriert, indem ein ratiometrisches light-harvesting Konzept für pH-Imaging verwendet wurde. Des Weiteren werden diese neuen Farbstoffe derzeit zur pH-Messungen von Beton-Proben verwendet, wobei sie signifikante Vorteile gegenüber bestehenden Systemen bieten.

---

## Dedication

Es ist wirklich schwierig mich auf einer Seite bei allen Leuten zu bedanken, denen ich einen großen Danke aussprechen möchte.

Zuerst möchte ich Ingo Klimant und Sergey Borisov nennen. Vielen Dank für eure Unterstützung während dieser Dissertation! Diese Arbeit wäre ohne euch nicht möglich gewesen. Sergey, dir möchte ich besonders dafür danken, dass du immer für Hilfe zur Verfügung gestanden bist, auch wenn du eigentlich gerade keine Zeit hattest.

Als nächstes muss ich die gesamte Arbeitsgruppe erwähnen. Ihr schafft es, ein so angenehmes Arbeitsklima aufzubauen, dass man (fast) jeden Tag gerne in die Arbeit geht. Ich werde die Mittags- und Kaffeepausen sehr vermissen und auch die zahlreichen wissenschaftlichen, als auch weniger wissenschaftlichen Diskussionen. Hier möchte ich mich besonders bei Berni, Silvia, David, Tanja und Monika bedanken.

Des Weiteren möchte ich mich bei meinen Bachelor- und Masterstudenten bedanken. Vielen Dank an Johanna, Yvonne und Fabian für eure tolle Arbeit! Ohne euch wäre ich nicht so weit gekommen. In diesem Zusammenhang muss ich mich auch bei Eveline und Anna bedanken. Ihr wart immer für mich da wenn ich irgendetwas gebraucht habe.

Bei meiner Familie möchte ich mich für den Rückhalt während des gesamten Studiums bedanken und natürlich auch für die finanzielle Unterstützung während dieser Zeit.

Birgit, zu guter Letzt möchte ich mich bei dir bedanken. Gemeinsam haben wir eine sehr schöne Studienzeit erlebt. Wir haben gemeinsam sehr viel gesehen und erlebt. Vielen Dank für deine ganze Unterstützung und vielen Dank dafür, dass du mich immer wieder mit Gedanken aus der Arbeit gerissen hast!

Dipl.-Ing. Christoph Staudinger, BSc

Graz, August, 2018



---

# Contents

|          |   |          |
|----------|---|----------|
| <b>1</b> | <b>Scope and Outline of the Thesis</b>              | <b>1</b> |
| <b>2</b> | <b>Introduction</b>                                 | <b>3</b> |
| 2.1      | pH  | 3        |
| 2.1.1    | Significance  | 4        |
| 2.1.2    | Ionic Strength and Activity: Debye-Hückel Law       | 4        |
| 2.2      | pH in Oceanography                                  | 6        |
| 2.2.1    | Ocean Acidification                                 | 7        |
| 2.2.2    | Challenges of Oceanographic pH Measurements         | 8        |
| 2.2.3    | pH Scales   | 10       |
| 2.2.4    | Requirements on Measurement Systems                 | 12       |
| 2.3      | pH Measurement Methods                              | 14       |
| 2.3.1    | pH Indicators and Indicator Paper                   | 14       |
| 2.3.2    | Harned Cell   | 14       |
| 2.3.3    | pH Electrode  | 16       |
| 2.3.4    | Ion Selective Field Effect Transistor (ISFET)       | 21       |
| 2.3.5    | Spectrophotometric pH Measurements                  | 23       |
| 2.3.6    | Optodes   | 28       |
| 2.4      | Optical pH Sensor Materials for Marine Applications | 30       |
| 2.4.1    | Advantages of Optodes in Seawater                   | 30       |
| 2.4.2    | Challenges for Optodes in Seawater                  | 31       |
| 2.4.3    | Principle   | 32       |
| 2.4.4    | Temperature Sensitivity                             | 34       |
| 2.4.5    | Ionic Strength Sensitivity                          | 35       |
| 2.4.6    | Indicators  | 39       |
| 2.4.7    | Matrices  | 42       |

---

|          |  |           |
|----------|--|-----------|
| 2.4.8    | Referencing . . . . .  | 43        |
| 2.4.9    | Dual Lifetime Referencing . . . . .  | 43        |
| 2.4.10   | Mathematical Description . . . . .   | 48        |
| <b>3</b> | <b>An Optode for O<sub>2</sub>, CO<sub>2</sub> and pH with Integrated Battery and Logger</b> | <b>52</b> |
| 3.1      | Preface to the Manuscript . . . . .  | 52        |
| 3.2      | Abstract . . . . .   | 54        |
| 3.3      | Introduction . . . . .   | 55        |
| 3.4      | Materials and Procedures . . . . .   | 57        |
| 3.4.1    | Optode Sensor System . . . . .   | 57        |
| 3.4.2    | Read-out Device . . . . .  | 57        |
| 3.4.3    | Sensor Caps . . . . .  | 60        |
| 3.4.4    | Temperature and Salinity Compensation . . . . .  | 64        |
| 3.4.5    | Characterization and Calibration of the Optodes . . . . .                                    | 64        |
| 3.4.6    | Reference Values . . . . .   | 65        |
| 3.5      | Assessment . . . . .   | 65        |
| 3.5.1    | Temperature and Salinity Cross-talk of the pH Optodes . . . . .                              | 65        |
| 3.5.2    | Stability Test of the pH and Oxygen Sensor Materials . . . . .                               | 67        |
| 3.5.3    | Application of the Optode System for Profiling in the Baltic Sea . . . . .                   | 70        |
| 3.5.4    | Continuous Surface Water pH Measurements . . . . .   | 71        |
| 3.5.5    | Simultaneous Monitoring of Oxygen and pH in Kiel Harbor . . . . .                            | 71        |
| 3.6      | Conclusions . . . . .  | 78        |
| 3.7      | Supporting Information . . . . .   | 80        |
| 3.7.1    | Preparation of the pH Sensing Films . . . . .  | 80        |
| 3.7.2    | Preparation of the pCO <sub>2</sub> Sensing Films . . . . .                                  | 81        |
| 3.7.3    | Buffers for pH Sensor Characterization . . . . .   | 81        |
| 3.7.4    | Buffers for pH Sensor Calibration . . . . .  | 82        |
| 3.7.5    | Experimental Details of the Stability Experiment . . . . .                                   | 82        |
| <b>4</b> | <b>Optical pH Sensors for Oceanographic Applications</b>                                     | <b>86</b> |
| 4.1      | Preface to the Manuscript . . . . .  | 86        |
| 4.2      | Abstract . . . . .   | 88        |
| 4.3      | Introduction . . . . .   | 89        |

---

|          |  |            |
|----------|--|------------|
| 4.4      | Materials and Methods . . . . .  | 90         |
| 4.4.1    | Materials . . . . .  | 90         |
| 4.4.2    | Methods . . . . .  | 91         |
| 4.4.3    | Synthesis . . . . .  | 92         |
| 4.4.4    | Polymer Synthesis . . . . .  | 93         |
| 4.4.5    | Preparation of Sensor Materials . . . . .  | 94         |
| 4.4.6    | Characterization of the Sensor Materials . . . . .                                   | 96         |
| 4.5      | Results and Discussion . . . . .   | 98         |
| 4.5.1    | pH Optodes: General Considerations . . . . .   | 98         |
| 4.5.2    | Choice of Materials . . . . .  | 99         |
| 4.5.3    | Overview of the New pH Sensing Materials . . . . .                                   | 100        |
| 4.5.4    | In-situ pH Monitoring with the New Sensor Materials . . . . .                        | 114        |
| 4.5.5    | Comparison Between the Sensor Materials . . . . .                                    | 114        |
| 4.5.6    | Comparison with State-of-the-art pH Optodes for Oceanographic Applications . . . . . | 116        |
| 4.6      | Conclusions . . . . .  | 120        |
| 4.7      | Supporting Information . . . . .   | 121        |
| 4.7.1    | Synthesis of the Dyes . . . . .  | 121        |
| 4.7.2    | Synthesis of the Polymers . . . . .  | 126        |
| 4.7.3    | Experimental Details on Deployments and Calibration . . . . .                        | 127        |
| 4.7.4    | Additional Information on Sensor Calibration and Cross-talk . . . . .                | 129        |
| 4.7.5    | NMR and MS spectra of the indicator dyes . . . . .                                   | 131        |
| <b>5</b> | <b>Near-infrared aza-BODIPY PET Dyes</b>   | <b>134</b> |
| 5.1      | Preface to the Manuscript . . . . .  | 134        |
| 5.2      | Abstract . . . . .   | 136        |
| 5.3      | Introduction . . . . .   | 136        |
| 5.4      | Experimental . . . . .   | 138        |
| 5.4.1    | Materials . . . . .  | 138        |
| 5.4.2    | Methods . . . . .  | 139        |
| 5.4.3    | Synthesis . . . . .  | 141        |

---

|           |   |            |
|-----------|---|------------|
| 5.5       | Results and Discussion . . . . .                              | 143        |
| 5.5.1     | Synthesis . . . . .   | 143        |
| 5.5.2     | Photophysical Properties . . . . .                            | 143        |
| 5.5.3     | pH Sensing Properties . . . . .                               | 144        |
| 5.5.4     | Application of the Dyes in Light Harvesting Systems . . . . . | 146        |
| 5.5.5     | Ratiometric Imaging of pH Distribution . . . . .              | 148        |
| 5.6       | Conclusions . . . . .   | 151        |
| 5.7       | Supporting Information . . . . .                              | 152        |
| 5.7.1     | Synthesis . . . . .   | 152        |
| <b>6</b>  | <b>Summary and Conclusion</b>                                 | <b>167</b> |
| <b>7</b>  | <b>References</b>   | <b>169</b> |
| <b>8</b>  | <b>Curriculum Vitae</b>                                       | <b>185</b> |
| <b>9</b>  | <b>List of Figures</b>  | <b>188</b> |
| <b>10</b> | <b>List of Tables</b>   | <b>192</b> |

---

# 1 Scope and Outline of the Thesis

pH is one of the most important parameters of any aqueous solution. In oceanography it is a parameter of special interest due to the ongoing ocean acidification caused by uptake of emitted anthropogenic carbon dioxide into the surface waters of the ocean. This slow but continuous process is expected to have severe influences on marine life in the future and must be investigated.

So far, no accurate and inexpensive pH sensors, suitable for widespread oceanographic pH monitoring, are available. Optodes could be an important tool to improve this situation. They are based on an optical read-out device and a pH sensitive material. Until now only a few optodes were developed specifically for oceanography and all suffer from different drawbacks. For this reason, we developed novel optical pH sensor materials optimized for seawater measurements and assessed their potential during multiple deployments using read-out devices provided by the company Pyroscience GmbH.

This thesis is written in a cumulative manner. The manuscripts presented are already accepted, under revision or prepared for submission in peer reviewed journals.

Chapter 2 introduces the necessary theoretical background, gives an overview of available sensor technology and discusses their advantages and drawbacks. It highlights the challenges for obtaining accurate pH measurements in seawater and explains the correct evaluation of measured data.

Chapter 3 describes the results obtained from multiple field excursions to test a set of pH, CO<sub>2</sub> and O<sub>2</sub> sensor materials, with a combined read-out device. The sensors were deployed at the Baltic Sea, Kiel (Germany), Limfjord (Denmark) and Southampton (England). Deployments were demonstrated for depth profiling as well as for stationary measurements.

Chapter 4 describes the development of four pH sensor materials optimized for oceanographic measurements. While the first material suffers from long response times at low temperatures, the other materials utilize a novel hydrophilic matrix material, which eliminates these long

response times. Importantly, the sensor materials based on this new matrix material utilize both covalent coupling of the dye and cross-linking of the matrix to enhance the long-term stability of the sensor. The materials were thoroughly characterized in regard to their temperature and ionic strength sensitivity and deployed during multiple field excursions as described in chapter 3.

Chapter 5 describes the development of novel aza-BODIPY indicator dyes with optimized optical properties. The new indicators show quenching by photoinduced electron transfer (PET) without a shift in the absorption spectrum. This was conducted to reduce non-ideal sensor behavior, induced by pH dependent changes in inner-filter-effect, and Förster resonance energy transfer (FRET)-efficiency. The utility of the novel dyes was demonstrated with a ratiometric light-harvesting concept for pH imaging. Besides the optical properties, the new indicators offer high  $pK_a$  values and are therefore suitable for pH imaging on concrete surfaces. The first publication based on this topic is currently under revision in a peer reviewed journal and the second manuscript is currently in preparation.

---

## 2 Introduction

### 2.1 pH

In general, pH is a measure for the acidity or alkalinity of a solution. The term pH was defined in 1909 by Sørensen in terms of concentration of  $\text{H}^+$  ions and on a scale of 0 to 14 based on the ionic product of water[1]. In the same year the pH glass electrode was developed [2]. In 1923, the concept of activity was introduced [3] and Sørensen et al. [4] proposed a new definition of pH based on the activity of hydrogen ions (eq. 2.1)[5].

$$pH = -\log_{10} a_{\text{H}^+} = -\log_{10}(m_{\text{H}} \cdot \gamma_{\text{H}}/m^0) \quad (2.1)$$

Where  $a_{\text{H}^+}$  is the molality based activity,  $\gamma_{\text{H}}$  is molal activity coefficient at molality  $m_{\text{H}}$  and  $m^0$  is  $1 \text{ mol kg}^{-1}$ .

Thereby, a pH of 7 is in general regarded as neutral as the concentration of hydrogen ions is equal to the concentration of hydroxide ions due to the self-ionization constant of water:  $K_w = c_{\text{H}^+} \cdot c_{\text{OH}^-} \approx 10^{-14} \Rightarrow pH + pOH = 14$ . However, this is only true at standard conditions (25°C). At lower temperatures the equilibrium of self-ionization shifts to the side of water and neutrality is obtained at higher pH values. Obviously at higher temperatures the opposite trend is observed and lower pH values have to be regarded as neutral.

The dissociation of water to  $\text{H}^+$  and  $\text{OH}^-$  is a frequently used simplification but not strictly true. In fact, no free hydrogen ions are present in water. The hydrogen ions associate with water and form hydronium ions ( $\text{H}_3\text{O}^+$ ), which in turn react with 3 more water molecules and form ( $\text{H}_9\text{O}_4^+$ ). This equilibrium is always completely on the side of  $\text{H}_9\text{O}_4^+$  and therefore  $\text{H}^+$  is a valid shorthand.

### 2.1.1 Significance

pH is one of the most important parameters of all aqueous samples. The pH value describes the protonation equilibria of all acidic or alkaline species in water, which effects their properties and their reactivity. Therefore, nearly all reactions in aqueous media depend on the pH value and consequently pH monitoring is essential for nearly all chemical processes conducted in water and is routinely measured in chemical industry. Moreover, the growth and metabolism of microorganisms is highly affected by pH [6]. Therefore, pH control is desired to steer the metabolism of microorganisms in biotechnological applications or simply to prevent undesired growth of microorganisms. Besides industrial applications, pH is also important as environmental parameter. It is, for example, essential for aquatic organisms like algae [7–9], all calcifying organisms [10–12], fish and their larvae [12–14] and many other marine organisms [12]. It is also an important parameter in agriculture, as the availability of nutrients in soil depends on its pH [15, 16]. Furthermore, pH is an interesting parameter in medical applications. The pH of blood and urine is routinely measured and also other applications frequently utilize pH measurement [17, 18]. Besides all these applications, pH is also a routine parameter in water analysis. It is measured for drinking water, river water, process water, etc. to detect potential problems or pollutants.

Due to the great importance of pH and the widespread and diverse application of pH measurements innovative, versatile or less expensive measurement methods are desirable.

### 2.1.2 Ionic Strength and Activity: Debye-Hückel Law

Electrostatic interactions between ions in solution cause attraction between ions of different charge and cause a short-range order. These attracted ions cause a "shielding" of the central ion and therefore reduce its reactivity [19, 20]. Hence, the solution acts as if the ion concentration was lower. This phenomenon is described by the activity ( $a$ ) of an ion species, which is the amount of "active" component in solution. The relation between concentration and activity is given by equation 2.2.

$$a = \gamma \cdot c \tag{2.2}$$

Where  $a$  is the activity,  $\gamma$  is the activity coefficient and  $c$  is the concentration. The activity coefficient depends on the total ionic strength of a solution. This was described by Debye

and Hückel in 1923, who formulated the Debye-Hückel limiting law to describe this relation (equation 2.3) [20, 21].

$$\ln \gamma_i = -\frac{z_i^2 q^2 \kappa}{8\pi \epsilon k_B T} = -\frac{z_i^2 q^3 \sqrt{N_A}}{4\pi (\epsilon k_B T)^{1.5}} \cdot \sqrt{\frac{I}{2}} = -A z_i^2 \sqrt{I} \quad (2.3)$$

$$\kappa = \sqrt{\frac{2Iq^2}{\epsilon k_B T}}$$

Where  $z_i$  is the charge of the ion,  $q$  is the elementary charge,  $N_A$  is Avogadro's number,  $\epsilon$  is the permittivity of the medium,  $k_B$  is Boltzmann's constant,  $T$  is the temperature and  $I$  is the ionic strength expressed as molality. In case of aqueous solutions the equation can be simplified. Thereby,  $A$  is a constant which depends only on temperature, and has a value of  $1.172 \text{ mol}^{-0.5} \text{ kg}^{0.5}$  at  $25^\circ\text{C}$ . The ionic strength is calculated by equation 2.4 with all ions in a solution.

$$I = \frac{1}{2} \sum_i c_i \cdot z_i^2 \quad (2.4)$$

In this equation  $I$  is the ionic strength,  $c$  is the concentration and  $z$  the charge of the respective ion.

However, equation 2.3 is only valid for dilute solutions ( $\leq 0.001 \text{ mol L}^{-1}$ ) and many practical applications are conducted at much higher ionic strengths, therefore multiple extensions of the Debye-Hückel-law exist. For example, the extended Debye-Hückel law (equation 2.5) considers the hydrated radius of the ion [19].

$$\ln \gamma_i = -\frac{z_i^2 q^2 \kappa}{8\pi \cdot \epsilon \cdot k_B \cdot T} \cdot \sqrt{\frac{\kappa}{1 + \kappa \cdot r_i}} \quad (2.5)$$

This equation introduces  $r_i$  as the radius of the ion. However, even the extended Debye-Hückel law is only valid for concentrations lower than  $0.1 \text{ mol L}^{-1}$  [21]. For even higher concentrations (e.g. seawater  $0.72 \text{ mol L}^{-1}$ ) empirical equations exist. The Davies equation 2.6 is useful till  $0.5 \text{ mol L}^{-1}$  and is an extension of the Debye-Hückel equation by an additional linear term ( $-0.3 \cdot I$ ), which approaches zero at low ionic strengths [22, 23]. For even higher ionic strengths the Specific Ion Interaction theory [24] or the Pitzer equations [25] can be used, which require experimental determination of the activity coefficients.

$$-\lg(\gamma) = A \cdot z_1 \cdot z_2 \left( \frac{\sqrt{I}}{1 + \sqrt{I}} - 0.3 \cdot I \right) \quad (2.6)$$

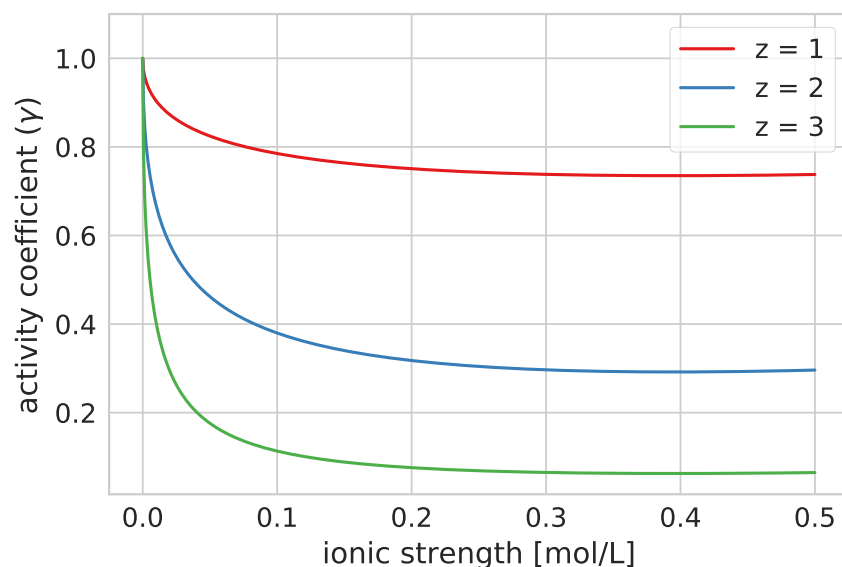


**Figure 2.1:** Theoretical development of the activity coefficient with increasing ionic strength for differently charged ions. Calculated with the Davies equation for the ionic charges 1, 2 and 3.

In Figure 2.1 the activity coefficient is plotted in dependence of the ionic strength for different charges of the ions. As can be seen, ions with multiple charges are much more affected by increasing ionic strength, which can be explained by the quadratic influence of the charge in equation 2.3.

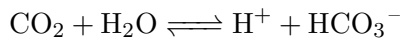
## 2.2 pH in Oceanography

Oceanography is the study of all the different aspects of the oceans and pH is an important parameter for the biological processes in it [26–29]. pH is one of the basic parameters of oceanographic water samples besides temperature, salinity, dissolved inorganic carbon, dissolved oxygen, alkalinity and dissolved carbon dioxide and is therefore routinely measured [30–32]. It is an important measure for the biological activity of a water mass. Decomposition of organic material leads to production of carbon dioxide and hence reduced pH and photosynthetic activity consumes carbon dioxide and leads to an increase in pH. Therefore, biological processes can be assessed by measurement of pH or even better by a combined measurement of pH, dissolved oxygen and dissolved carbon dioxide [33]. In turn, pH also affects biological processes and the

growth and metabolism of marine organisms [12]. For all these reasons pH measurements are essential for oceanography. Moreover, due to the continuous anthropogenic carbon dioxide emissions and the subsequent acidification of the ocean, measurement of pH is becoming even more important.

### 2.2.1 Ocean Acidification

The continuously rising carbon dioxide levels in our atmosphere do not only cause global warming but also affect our oceans [32, 34, 35]. An estimated amount of nearly 50% of the global carbon dioxide emissions is absorbed by the surface waters of the oceans [36]. While this reduces the extend of global warming by scavenging a substantial part of the carbon dioxide emissions it has an undesired side effect. The carbon dioxide dissociates in bicarbonate and *protons*.



Hence, the absorbed carbon dioxide causes a decrease of the pH value. As long as the atmospheric carbon dioxide concentrations are rising, the surface waters of the oceans will continue to absorb more and more carbon dioxide and the pH will continue to decrease. So far the average surface pH of the oceans has decreased by approximately 0.1 pH units from pre-industrial  $\approx 8.25$  to 8.15 [37]. While this doesn't appear dramatic at first, it indicates an increase by  $\approx 20\%$  in hydrogen-ion concentration [29, 37]. Furthermore, this process is ongoing and a pH of 7.85 is predicted for the year 2100 under the SRES A1B emission scenario [37]. This would mean a 2.5 fold increase of the hydrogen-ion concentration. This problem has been titled "the other CO<sub>2</sub> Problem" and might heavily affect the whole marine ecosystem [38–40]. As mentioned above, this shift in pH causes a shift in all protonation equilibria. Most importantly the carbonate equilibrium is shifted from CO<sub>3</sub><sup>2-</sup> to HCO<sub>3</sub><sup>-</sup> and the concentration of available carbonate is reduced.



Therefore, increasing areas of the oceans are no longer saturated with CaCO<sub>3</sub> (aragonite) [29, 35], which reduces the viability of calcifying organisms, as it affects their ability to form their skeletons [35]. Hence, this might affect the whole marine food chain. Furthermore, larvae of fish or other marine organisms are especially sensitive to pH during their growth, which

might pose another threat to the ecosystem [13, 14]. While the oceans have been even more acidic in prehistoric times [41], the decrease has never been this fast. Therefore, the marine ecosystem faces severe challenges to adapt in time. For all these reasons pH monitoring is of great importance in marine science to track and characterize the changes in the marine pH and to determine the consequences [42].

## 2.2.2 Challenges of Oceanographic pH Measurements

### Salinity

Often, pH measurements are conducted in media with low ionic strength (e.g. drinking water, river water) or medium ionic strength (e.g. physiological conditions ( $\approx 150$  mM)[43]). Measurements in media with higher ionic strengths are much less frequently conducted. The ionic strength of seawater in the open ocean is typically at  $\approx 720$  mM with a composition of  $28.175 \text{ mol kg}^{-1} \text{ Cl}^-$ ,  $24.206 \text{ mol kg}^{-1} \text{ Na}^+$ ,  $1.457 \text{ mol kg}^{-1} \text{ SO}_4^{2-}$ ,  $2.726 \text{ mol kg}^{-1} \text{ Mg}^{2+}$ ,  $0.531 \text{ mol kg}^{-1} \text{ Ca}^{2+}$ ,  $0.527 \text{ mol kg}^{-1} \text{ K}^+$ ,  $0.0886 \text{ mol kg}^{-1} \text{ HCO}_3^-$  and other minor components [44–46]. This composition has a salt content of approximately 35 g salt per 1 kg seawater (or 35 ‰) and was defined based on conductivity measurements as 35 PSU (practical salinity unit) [47]. However, it should be noted that the use of this definition is by now discouraged and a new definition considering the composition should be used (TEOS-10) [47, 48]. This definition uses gram salt per kilogram seawater as unit. Most areas of the ocean are quite close to these conditions and only small fluctuations occur between areas due to evaporation of water or dilution by rain and rivers. However, a few regions with significantly different composition exist, for example Areas behind narrow straits can have different average salinities. Thereby, areas which are dominated by water evaporation (e.g. Mediterranean Sea (38 PSU[49]), Red Sea (36-41 PSU[50]), show higher than average salinities and areas, which are dominated by dilution with river water (e.g. Baltic Sea 3-10 PSU on the surface[51]), Black Sea (18-22 PSU[52]) show lower salinities. Especially in low salinity regions, stratification between different salinities is common and high variations can occur between different depths.

These comparably very high and variable salinities in seawater affect all measurement methods. Most importantly, the liquid-junction of the pH reference electrode is influenced at high ionic strengths, due to diffusion potentials [30, 53]. This leads to unstable and unreproducible measurements. Therefore, adaptations to existing methods or new measurement methods are

required. Another issue is the absence of suitable reference buffers. For most non-oceanographic measurements the pH is traced back to "standard" buffers supplied for example by the National Institute of Standards and Technology. However, these buffers are only available for low ionic strengths and calibrations conducted at these conditions can not be transferred to high salinity seawater measurements without significant error [30, 54].

Another challenge resulting from the high salinity in seawater is its influence on the various activity coefficients. As mentioned above, pH is defined classically as *activity* of  $H^+$ . The activity of ionic species decreases with rising ionic strength, therefore the pH increases at constant  $H^+$  concentration with rising ionic strength. This issue is addressed by special pH scales developed for oceanographic use (see section 2.2.3). Besides the activity coefficients of  $H^+$  also the activities of other ionic species (e.g. charged dyes for spectrophotometric measurements or in optodes) are affected. This behavior can be described at low ionic strengths ( $< 0.1$  mM) by the law from Debye and Hückel. To extend the model also to higher ionic strengths, multiple extensions with empiric coefficients were developed, as described in section 2.1.2.

## Accuracy

One of the biggest challenges for marine measurements is the required accuracy. In biotechnological applications an accuracy of few hundreds of a pH unit is sufficient for most processes. However, especially the pH changes due to carbon dioxide absorption are very small and they occur over long periods. In addition, while the absolute pH changes are small, the affected amount of water is enormous and therefore even small changes indicate huge quantities of absorbed carbon dioxide. Moreover, the data of many measurements distributed over multiple years and on multiple widely distributed locations are required for modeling of ocean acidification. Therefore, high accuracy is required to be able to compare the results.

The variable measurement conditions are especially a challenge for sensors deployed for in situ measurements. In contrast to lab measurements, where temperature control is common, neither the temperature nor the salinity can be controlled. Because of the high requirements on the measurement data, cross-sensitivities to both parameters must be well characterized for any sensor and they have to be compensated by additional temperature and conductivity measurements.

## Size

Maybe the greatest challenge for oceanographic measurements in general is size. 71 % of the surface of the earth are covered with water and only very limited resources are available to conduct measurements. Therefore, the oceans are dramatically undersampled [39] and conclusions have to be drawn with very limited data. This adds additional requirements to sensors. They should be inexpensive, easy to use, small and suitable for different forms of deployment and ideally they should be deployable independently for longer periods of time without any maintenance. Such a sensor would greatly improve the availability of pH data and would improve the models on ocean acidification.

## Benefits for Optical Systems

Despite all these challenges the marine environment has also some advantage for optical measurement systems. The ionic strength is high and in most cases rather constant. Therefore, the cross-sensitivity to fluctuations of salinity are low. Even more importantly, the typical pH values for seawater are in the range of 7.5 to 8.4 [55], with an average surface pH of 8.1 [26]. Only in a few exceptions (e.g. anoxic zones) pH values down to 7 are reached. This is beneficial for indicator-based measurements (e.g. spectrophotometric or optodes), as these methods offer high sensitivity, but only in a limited range of approximately 2 pH units.

### 2.2.3 pH Scales

The traceability of oceanographic pH measurements to commercially available standard buffers (which are in turn traceable to the Harned cell ( $\text{H}_2/\text{Pt} \mid \text{H}^+$ ) measurements) is nearly impossible due to the big differences in ionic strength and the strong effect of ionic strength on all measurement methods. However, for marine measurements not the absolute pH value, but its influence on protonation equilibria is of importance. As long as consistent measurements are possible no direct traceability to "standard" buffers is required. Therefore, practical pH scales were introduced which are based on buffer solutions with ionic strength similar to seawater [56]. These buffers are based on tris(hydroxymethyl)aminomethane (TRIS) and are prepared in artificial seawater. TRIS was chosen because it is well characterized [57] and its  $\text{pK}_a$  value is suitable for buffers in the range of 7 to 9 [56]. The differences between the NBS scale and the

other scales can be up to 0.12 pH units, therefore they should not be mixed. The following 4 different pH scales can be found in oceanographic publications.

### NIST or NBS Scale

The standard pH scale used for most non-oceanographic measurements is called NIST (for National Institute of Standards and Technology) or historically NBS (National Bureau of Standards) scale to distinguish it from the pH scales developed for oceanographic measurements. It is traceable to commercially available buffer solutions from the National Institute of Standards and Technology, which in turn are traceable to H<sub>2</sub>/Pt measurements. However, the buffer issued on this scale are not suitable for oceanographic measurements, due to the big differences in ionic strength between the buffers and seawater.

$$pH_{NBS} = -\log_{10}(a(\text{H}^+)) \quad (2.7)$$

### Total Scale

The total scale was developed based on buffers in artificial seawater. In contrast to the NBS-scale, pH is not defined by the activity of hydrogen ions but by its concentration. Furthermore, hydrogen sulfate ions are included in the definition to account for protonated sulfate species in seawater [30].

$$pH_T = -\log_{10}(c(\text{H}^+) + c(\text{HSO}_4^-)) \quad (2.8)$$

This scale is the most frequently used scale in oceanographic pH measurements and most characterizations of material constants are given in this scale.

### Free Scale

The free pH scale is based on the concentration of hydrogen ions without consideration of hydrogen sulfate [30]. The conversion between the total and the free scale requires the concentration and exact pK<sub>a</sub> of hydrogensulfate. This is not always straightforward, therefore the total scale is usually preferred.

$$pH_F = -\log_{10}(c(\text{H}^+)) \quad (2.9)$$

## Seawater Scale

The seawater scale is in principle an extension of the total scale. It additionally considers the protonation equilibrium of fluoride.

$$pH_T = -\log_{10}(c(\text{H}^+) + c(\text{HSO}_4^-) + c(\text{HF})) \quad (2.10)$$

However, sulfate is much more abundant in seawater than fluoride, therefore the differences between seawater scale and total scale are only minor.

### 2.2.4 Requirements on Measurement Systems

The requirements on pH measurement equipment are as diverse as the different applications. Possible application for pH sensors include:

- In laboratories for samples [39, 58]
- In laboratories for biological experiments
- Monitoring of fish or muscle farms [59]
- On ships for samples [60, 61]
- Continuous measurements in Ferrybox systems for surface profiling [62]
- Depth profiling on CTD-rosettes [63]
- Stationary measurements on moorings [39, 63]
- Landers [64]
- Argo floats [65, 66]
- Gliders [67]
- AUVs [68]

For all these applications, different requirements need to be fulfilled. In typical lab applications the devices need not be submersible, temperature control is possible, size and weight is usually not an issue and frequent recalibration is feasible. Moreover, response time of the sensors can be long. Therefore, precision and accuracy are the most important criteria. The same is true for

measurement sampling applications on research vessels. However, simple handling of the devices to avoid errors is more important and robustness and portability of the devices is necessary.

For deployments of sensors in situ the requirements are different. First of all, the devices must be water-proof and pressure resistant and as compact as possible. Furthermore, temperature control is no longer possible and hence temperature compensation is required. Easy integration in existing platforms for data transfer and power supply is desirable. For profiling measurements (either depth or surface profiling) fast response times and good temporal resolution are required. For stationary deployments on moorings, long servicing periods are essential. Usually, the sensors are deployed and collected weeks or months afterwards. In between, no recalibration or other servicing is possible. In some cases, power can be supplied to the sensors and data recorded remotely, however, an independent power supply and data logging are preferred and enable much more widespread application without high requirements on infrastructure.

Another possible field of application are deployments on small (autonomous) devices (e.g. Argo floats, gliders, autonomous underwater vehicles (AUVs), etc.). They have only very limited space, carry capacity and power supply. Therefore, the deployed devices must be small, have low weight in water and require only low amounts of power. These devices can be deployed for very different time scales. While gliders and AUVs are often only deployed for short periods of time, Argo floats are used for many years.

However, for all sensors systems some common demands exist. User friendly devices reduce the potential of errors during measurements and enhance the quality of the obtained data. Low cross-sensitivities to other parameters (most importantly temperature and salinity) are advantageous. This reduces requirements in the measurement of these values and reduces uncertainty. High sensitivity in the narrow range of marine pH is desirable as it enhances the precision of the measurement system and allows for detection of minor pH fluctuations. Cost-effective equipment is also desirable. While this is not as important for lab devices, it is critical if autonomous wide spread monitoring is desired. As mentioned above, water covers more than half of our planet and only limited resources are available to monitor it. Low cost devices could contribute to obtaining much more data and significantly enhance the knowledge about the oceans.

The requirements in accuracy, precision, response time and measurement interval on the different sensing systems depend on the aims of the users. While only data of highest accuracy is useful for climate research and to track the ongoing ocean acidification, other criteria are

more important for other applications. To investigate biological activity, day/night, low/high tide fluctuations, depth profiling or other fast processes high temporal resolution and if possible high spatial resolution with multiple inexpensive devices is more interesting.

While pH optodes are not yet suitable for all the mentioned applications, they offer multiple advantages which could make them invaluable tools in marine research. Optodes can be small, lightweight, easy to use, fast responding, have low power requirements and are inexpensive. They could enable widely distributed pH measurements to observe changes so far overlooked and enhance our knowledge of the oceans.

## **2.3 pH Measurement Methods**

Determination of pH is of great importance in many different fields. Therefore, a great variety of measurement methods was developed and new methods are still under development. In this section the most important measurement methods are described and their advantages and disadvantages are discussed.

### **2.3.1 pH Indicators and Indicator Paper**

Maybe the simplest method for determination of pH is with pH indicators or paper, which is impregnated with one or more pH indicators. The measurement principle is based on color changes upon protonation or deprotonation of the indicators. After submerging the paper in the test solution its color is compared with a chart, which enables estimation of the solution's pH. While this method is very old and imprecise it is still in use, due to its simplicity and low costs, if only a rough estimate of pH is required.

### **2.3.2 Harned Cell**

The so called Harned cell [5, 69, 70] is the most robust measurement method for pH and is recommended for pH measurements by the International Union of Pure and Applied Chemistry [71]. This method is used for pH determination of primary buffers. One of the major uncertainties of pH determination with electrodes are liquid junction potentials. The Harned cell contains no liquid junction and thereby eliminates these problems (Fig. 2.2). The cell consists of a platinum electrode submerged in the sample which is flushed with hydrogen. In the neighboring compartment a silver/silver chloride electrode is placed. Importantly, the two compartments

are directly connected and no liquid junction is used. This cell can be denoted as: Pt|H<sub>2</sub>|buffer, Cl<sup>-</sup>|AgCl|Ag and the measured potential can be described by equation 2.11.

$$E = E^0 - k \cdot \log(a_{\text{H}}/m^0) \cdot (m_{\text{Cl}}\gamma_{\text{Cl}}/m^0) \quad (2.11)$$

Where  $E^0$  is the standard potential of the Ag/AgCl electrode,  $m_{\text{Cl}}$  and  $\gamma_{\text{Cl}}$  are the molality and activity coefficients of chloride, respectively, and  $k$  is the Nernstian slope ( $k = RT \ln 10/F$ )

However, the measurement with Harned cells is a very delicate and time consuming process and a single measurement requires multiple hours. The most important measurement steps are [5, 72]:

- $E^0$  of the Ag/AgCl electrode is determined with a measurement in hydrochloric acid (usually 0.01 mol kg<sup>-1</sup>).
- The sample buffer is filled into the cell and the potential between the half cells is measured at 3 or more different concentrations of chloride between 0.005 and 0.02 mol kg<sup>-1</sup>.
- An auxiliary quantity is defined as:  $pa = (E - E^0)/k + \log(m_{\text{Cl}}/m^0)$  and extrapolated to zero chloride concentration.
- The activity coefficient of chloride ( $\gamma_{\text{Cl}}$ ) is calculated with the Bates-Guggenheim convention and equation 2.5.
- and is used to calculate the pH of the buffer:  $pH = pa_0 + \log \gamma_{\text{Cl}}$ .

Obviously this procedure is too laborious for everyday measurements and even for manufacturing of commercial calibration buffers. It is usually only conducted at national institutes for preparation of primary buffers [5].

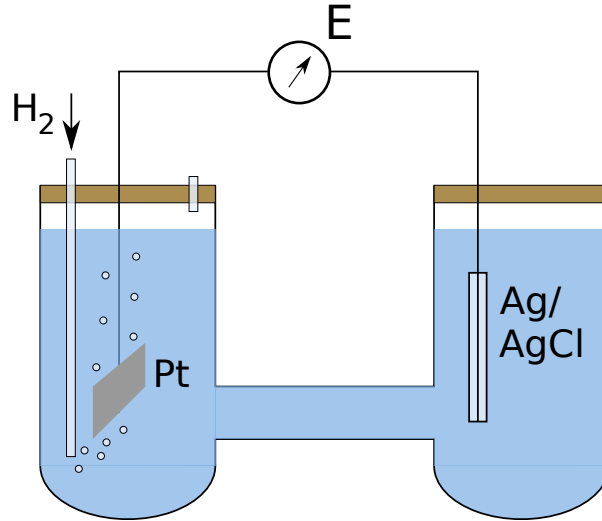


**Figure 2.2:** Pt/H<sub>2</sub> | AgCl/Ag cell (Harned cell) for pH measurements, adapted from [5]

### Secondary Buffer Solutions

Secondary buffers, which can be obtained at much reduced costs, are prepared by measurements against primary buffers in so called Baucke cells. The Baucke cell can be used to measure the pH of a buffer against a primary buffer of the same composition. The Baucke cell uses two Pt|H<sub>2</sub> half-cells which are separated by a liquid junction ((Pt|H<sub>2</sub>| buffer1 || buffer2 H<sub>2</sub>|Pt), Fig. 2.3) and its potential is given by equation 2.12 [5].

$$E_{\text{Cell}} = E_2 - E_1 + E_j \quad (2.12)$$

Where  $E_1$  and  $E_2$  are the potentials of the half cells and  $E_j$  is the liquid junction potential. However, as the two buffers are virtually identical in composition the liquid junction potential is usually neglected and the pH of the secondary buffer can be calculated with equation 2.13.

$$\text{pH}_2 = \text{pH}_1 - \frac{E_{\text{Cell}}}{k} \quad (2.13)$$

This measurement method is much less time consuming and requires only a single measurement. It is the basis for commercially available secondary calibration buffers [5].

### 2.3.3 pH Electrode

So far the most often applied and most common measurement method for pH is the pH glass electrode. It is used in many different applications, such as routine analysis of water samples,

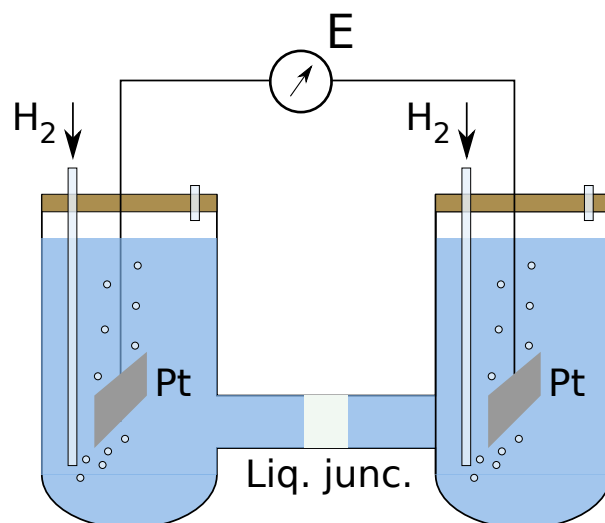


**Figure 2.3:** Pt/H<sub>2</sub> || Pt/H<sub>2</sub> (Baucke cell) for pH measurements, adapted from [5].

chemical processes, biotechnology and many more. The pH glass electrode was developed in the early 20<sup>th</sup> century. The first pH measurements with a glass electrode were conducted by Haber and Klemensiewicz [2] in 1909 [73]. It is an outstanding sensor with a dynamic range of 14 decades of H<sup>+</sup> concentration and the most widely employed ion selective electrode.

pH measurement with a glass electrode is a potentiometric measurement and is based on measuring the potential between a glass electrode and a reference electrode. Often, both electrodes are combined in a single rod and sold as combination electrodes (Fig. 2.4). The components of such a system are described below:

### Glass Membrane

The glass electrode itself consists of multiple parts, the most important part being the glass membrane. It is made from special glasses (today usually lithium-silicate glasses to minimize the alkaline error), which form a thin, water swollen layer by exchanging alkali metal ions with water and hydrating the remaining silica structure to form hydroxy-groups. This layer can have a thickness of up to 500 nm and exchanges hydrogen ions with the surrounding medium [74]. The inside of the reference electrode is filled with a buffer solution (pH 7) which contains potassium chloride. In this solution an internal secondary electrode is placed, which is usually of the same type as the external reference electrode. While the hydrogen ion concentration on the internal side of the glass electrode is constant, the hydrogen ion content on the outside of the membrane depends on the pH of the surrounding medium. This causes a potential, which

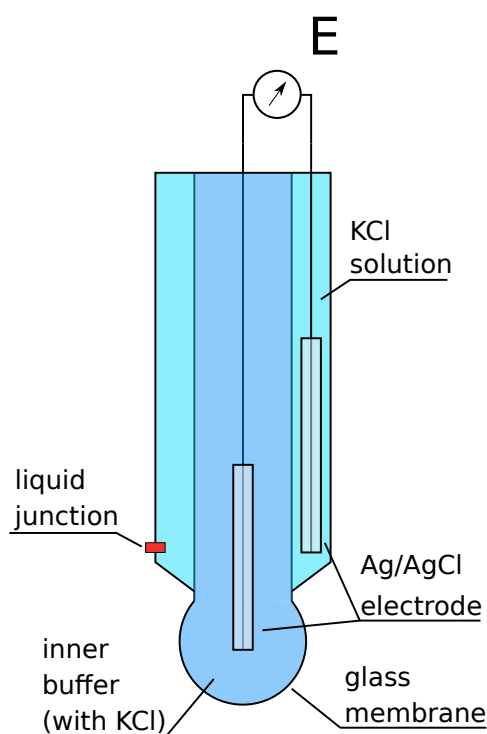


**Figure 2.4:** Scheme of a glass electrode.

can be measured. The membrane materials of pH glass electrodes are optimized to be only sensitive to hydrogen ions and to minimize the influence of other ions. However, at high pH values ( $> 12$ ) the concentration of hydrogen ions is very low and already small cross-sensitivity to alkali ions can cause errors (too low pH values). Because of the size of the ions, lithium and sodium cause usually much larger errors than potassium [74].

### Reference Electrode

Measurement of only one element of a galvanic cell is not possible. Therefore, a reference electrode with a stable potential is required. For this purpose electrodes, which do not depend on the concentration of the dissolved metal but on the concentration of the electrolyte, are preferred. Historically  $\text{Hg}/\text{Hg}_2\text{Cl}_2$  was the most often used reference electrode and it still offers the most constant reference potential [74]. However, due to its toxicity it has been mostly replaced by the  $\text{Ag}/\text{AgCl}$  reference electrode. A novel reference electrode is the  $\text{I}_2/\text{I}^-$  reference system whose main advantage is near complete temperature independence. Furthermore, it contains no silver ions which can interact with sulfur containing molecules (e.g. proteins,  $\text{H}_2\text{S}$ ) or TRIS-base [75]. However, the  $\text{Ag}/\text{AgCl}$  is still the most common reference system.

## Liquid Junction

The reference electrode must be connected to the sample with an ionic conductor to close the electric circuit and enable measurements. To avoid direct contact a liquid junction is used. The insides of the Ag/AgCl and the Hg/Hg<sub>2</sub>Cl<sub>2</sub> electrode are filled with concentrated potassium chloride solution (3M or saturated). This salt was selected as both ions have very similar diffusion coefficients. Therefore, both ions migrate at the same speed and no diffusion potential is formed in the liquid junction. The liquid junction is designed to enable a small outflow of the electrolyte to the surrounding media to constantly flush it and to reduce the junction potentials which would result from ingress of other ions. The liquid junction is one of the most critical components of a pH electrode and different types of liquid junctions were developed to adapt to different problems. The most important types of liquid junctions are the ceramic and ground joint types. The ceramic junction uses the pores in a ceramic material and has only a low outflow of approximately 0.2 mL/day. It is therefore not suited for high ionic strength media. The ground joint junction uses the gap in a ground joint as liquid junction. It has a high electrolyte outflow of approximately 3 mL/day and is suited for polluted and high ionic strength media. However, it requires frequent refilling of the electrolyte reservoir. Reference electrodes utilizing gel electrolytes require different junctions. The interface between the gel and the sample functions as liquid junction itself and a higher surface area can be exposed to the sample. For this purpose annular gap junctions can be used [74].

## Error Potentials

Two error potentials are known of the glass electrode, which affect measurements and reduce the accuracy and precision of the system:

**Asymmetry Potential** The asymmetry potential of a glass electrode is caused by differences between inner and outer hydrated layer of the glass membrane. Even when the inner and the outer pH are exactly the same the measured potential is not zero. This residual potential is called the asymmetry potential. It is not avoidable but is minimized in carefully prepared pH electrodes and it is usually low with only a few mV. This small non-ideal potential can be compensated by the calibration of the electrode [74].

**Liquid Junction Potential** The second and most important error potential of pH measurements using the glass electrode occurs at the liquid junction of the reference electrode. This error potential is caused by the different diffusion speeds of different ionic species. If an electrolyte consisting of a fast and a slow ion are in contact with a solution without the two ions they will diffuse into it with different speeds. Thereby a separation of charges is induced which causes a potential. The same effect is observed at the liquid junction of the reference electrode. Therefore,  $K^+$  and  $Cl^-$  are chosen as electrolyte for the reference electrode, as they have a very similar diffusion speed, which minimizes the liquid junction potential. However, in environments with high ionic strength (e.g. seawater) ions with different diffusion speed and charges can migrate into the liquid junction and can cause an error potential. Therefore, the selection of the liquid junction is essential and in general a high outflow of electrolyte is preferred for challenging environments, as migration into the junction is reduced. Still, liquid junction potentials can cause deviation of up to 0.1 pH units [74, 76].

### Nernst Equation

The pH measurement with the glass electrode is a potentiometric measurement and the measured potentials can be described with the Nernst equation. The Nernst equation describes the potential of a half-cell in dependence of the concentration of the reduced and oxidized forms.

$$E = E^0 + \frac{RT}{zF} \ln \left( \frac{a_{\text{ox}}}{a_{\text{red}}} \right) \quad (2.14)$$

Where  $E$  is the potential,  $E_0$  is the standard potential,  $R$  is the gas constant,  $T$  is the temperature in Kelvin,  $z$  is the amount of involved electrons,  $F$  is the Faraday constant and  $a_{\text{ox}}$  and  $a_{\text{red}}$ , are the activities of the oxidized and reduced forms respectively.

The system for glass electrode measurements can be described as a galvanic cell [5]:  $Ag|AgCl|$  internal buffer (pH7) +  $KCl||$ glass membrane $||$  sample  $||$  liquid junction  $||$   $KCl$  solution $|AgCl|Ag$ .

In this setup the potentials of the  $Ag/AgCl$  electrodes cancel each other out and only the potential on the glass membrane remains. Thereby the potential at the inside of the membrane is constant and only the potential on the outer side of the membrane is detected. This potential can be described by the Nernst equation:

$$E = \frac{R \cdot T}{1 \cdot F} \ln a_{H^+} = 2.303 \cdot \frac{R \cdot T}{1 \cdot F} \lg a_{H^+} \quad (2.15)$$

At 25 °C the first part of the equation can be simplified to 59.16 mV, which is the typical slope of a pH electrode. A direct consequence of this equation is the temperature dependence of the pH electrode. At lower temperatures the slope is also lower and at higher temperatures the electrode is more sensitive.

### Summary

pH measurement with the glass electrode is the standard method for almost all applications and the discussed issues with the liquid junction can be neglected in most cases. However, especially in seawater the electrode is not ideal, as the liquid junction potentials can be severe, in general irreproducible and the accuracy and precision are below the requirements [77]. Liquid junctions with high outflow of electrolyte could reduce this issue but would demand frequent service which is not compatible with long deployment times. Furthermore, the glass surface is not very robust and can be damaged easily.

#### 2.3.4 Ion Selective Field Effect Transistor (ISFET)

The ISFET was invented by Bergveld in 1970 [78] and was described as a tool for pH measurement of ionic fluxes around a nerve. By now, the ISFET has been used for a multitude of applications [79]. Among other applications, it is used for oceanographic pH measurements [39, 61, 63, 80–84].

A field-effect transistor (FET) is a transistor whose conductivity is controlled by an electric field. In such a transistor the flow of carrier transporters from the source to the drain of the resistor is controlled by the voltage applied to the gate. Thereby a voltage can both enhance and reduce the conductivity [85]. A special case of a FET is the metal-oxide-semiconductor field-effect transistor (MOSFET), which is obtained by oxidation of a metal or semiconductor. ISFETs are very similar to MOSFETs and the most important difference is that the gate connection is no longer in direct contact with the chip, but connected to the reference electrode submerged in an aqueous solution, which is in turn in contact with the gate oxide (Fig. 2.5 [79]). These surface oxides can be protonated and deprotonated depending on the pH of the solution [86]. The change in charge upon (de)protonation causes a change in conductivity and is responsible for the sensor signal. Multiple surface oxides were tested for this purpose ( $\text{SiO}_2$  [87],  $\text{Al}_2\text{O}_3$  [87],  $\text{Si}_3\text{N}_4$  [79],  $\text{Ta}_2\text{O}_5$  [79]).  $\text{Ta}_2\text{O}_5$  has favorable properties [79] and near Nernstian behavior, while for example  $\text{SiO}_2$  has a sensitivity of only 30 mV/pH units [79, 80].

The most important advantages of ISFETS are that they are more robust, can be easily miniaturized and they can be manufactured at much reduced cost in comparison to pH electrodes [79]. However, ISFETS also face a few challenges. They are cross-sensitive to light [79, 88] and pressure [89] and the main issue of ISFET technology is the reference electrode. Similar to pH glass electrodes a reference potential is required for the measurement. While the ISFET itself is robust, cost-effective and miniaturizable, the reference electrode is not smaller than for a conventional glass electrode and reduces the advantages of the ISFET technology. Moreover, the reference electrode and the liquid junction are the most critical parts of the glass electrode setup and responsible for most of its issues [77]. Hence, multiple approaches were developed to cope with this issue. One approach is the development of an ISFET which is insensitive to the analyte and can be used to obtain a reference potential (REFET) [79]. However, due to stability issues this approach has not yet resulted in devices suitable for long-term measurements. Therefore, electrodes with Ag/AgCl in hydrogels with a liquid junction are still the most used reference system [80].

Another approach, which is developed specifically for oceanographic pH measurements, is the use of a solid state chloride sensitive electrode as reference electrode [39, 80, 89]. This electrode consists of AgCl and Ag<sub>2</sub>S and is in direct contact with the seawater without any internal electrolyte or liquid junction [39]. Thereby, liquid-junction potentials are eliminated, but a cross-sensitivity to the chloride content of the seawater is introduced. This sensitivity can be compensated by calculating the chloride concentration from the measured salinity of the seawater [39]. However, the system requires simultaneous salinity measurements and the compensation can be challenging in environments with high-freshwater input (e.g. estuaries, Baltic Sea), as the ion composition of river water is different from seawater and the chloride content can no longer be calculated from salinity alone.

The most important ISFET for oceanographic applications is the DuraFET<sup>®</sup> from Honeywell ([www.honeywell.com](http://www.honeywell.com)), which was tested and deployed multiple times for oceanographic applications and is the basis for the SeaFET<sup>®</sup> from Sea-bird scientific ([www.seabird.com](http://www.seabird.com)). This sensor uses a Ag/AgCl reference electrode and a chloride sensitive reference electrode without liquid junction simultaneously.

In conclusion, marine ISFET sensors are already in use and commercialized (e.g. SeaFET from SeaBird Scientific). A precision of 0.0005 pH units and a stability better than 0.005 pH units over months are reported [39]. However, the reference electrode is a remaining issue of

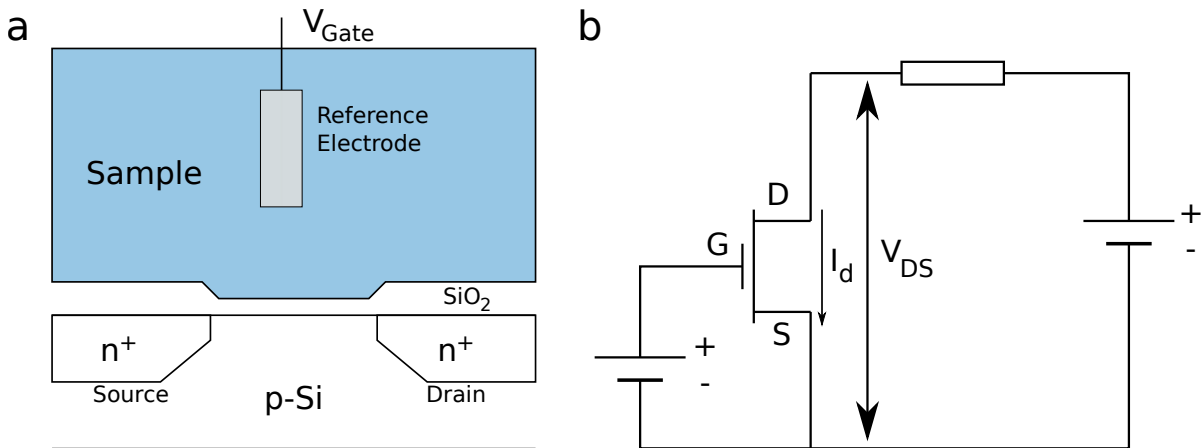


**Figure 2.5:** Schematic representation of an ISFET (a) and a measurement circuit (b), D, G and S are drain, gate and source, respectively,  $V_{DS}$  is the applied constant potential and  $I_d$  is the current. Adapted from [79].

the system. While the used combination of a chloride sensitive electrode with conductivity measurements for chloride estimation is suitable for open ocean measurements the calculation of the reference potential is not straightforward in areas with freshwater inflow due to the fluctuation in ion composition.

### 2.3.5 Spectrophotometric pH Measurements

Spectrophotometric pH measurements are currently the most accurate method for pH determination in oceanography [90, 91]. The principle is based on measurement of the pH dependent absorption spectrum of a water-soluble indicator [92]. The indicator is added to the sample and after mixing, the absorption spectrum of the indicator is recorded. Thereby, m-cresol purple (mcp) is the most commonly used indicator for oceanographic measurements. It features good solubility in water, a strong shift of absorption upon (de)protonation, both forms show good molar absorption coefficients and its  $pK_a$  (8.006 at 25°C and 35 PSU [93]) is close to the typical seawater pH. Importantly, this method is self referenced and the accuracy depends only on the purity of the indicator, the optical setup and the quality of the temperature control. As only the absorption ratio between the two indicator forms is measured, the exact concentration of the indicator is not critical. In general, the drift of this system is very low as the indicator is replaced for every individual measurement and only changes in the optical setup have to

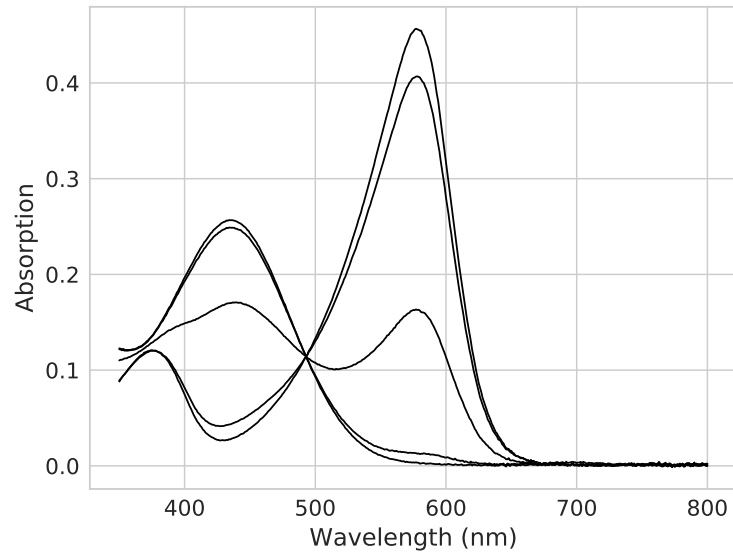


**Figure 2.6:** Spectra of m-cresol purple at different pH values. The peaks at approximately 430 nm and 580 nm are the absorptions of the mono-anionic di-anionic forms of the m-cresol purple, respectively.

be considered. However, these changes are usually small ( $< 0.004$  pH units [94]) and can be compensated by baseline measurements [63].

### Calculation and Indicator Characterization

The measurement is based on determining the concentration ratio of the anionic and the di-anionic form of the indicator by absorption measurements. The relation between pH and the concentrations is given by equation 2.16.

$$pH = pK_a^{mcp} + \lg \left( \frac{[I^{2-}]}{[HI^-]} \right) \quad (2.16)$$

Thereby  $pK_a^{mcp}$  is the  $pK_a$  of m-cresol purple at the measurement temperature and  $I_2^-$  and  $HI^-$  are the concentrations of the di-anionic and mono-anionic forms of the indicator, respectively. The ratio between  $I_2^-$  and  $HI^-$  can be determined by absorption measurements at the respective absorption maxima. The absorptions is described by the equations 2.17 and 2.18.

$$A_1 = \epsilon_1^{\text{HI}^-} \cdot [\text{HI}^-] + \epsilon_1^{\text{I}^{2-}} \cdot [\text{I}^{2-}] \quad (2.17)$$

$$A_2 = \epsilon_2^{\text{HI}^-} \cdot [\text{HI}^-] + \epsilon_2^{\text{I}^{2-}} \cdot [\text{I}^{2-}] \quad (2.18)$$

$A_1$  and  $A_2$  are the absorptions at two wavelengths and  $\epsilon_1^{\text{HI}^-}$ ,  $\epsilon_1^{\text{I}^{2-}}$ ,  $\epsilon_2^{\text{HI}^-}$  and  $\epsilon_2^{\text{I}^{2-}}$  are the absorption coefficients of both species at the two wavelengths. These equations can be combined to equation 2.19 which enables calculation of the concentration-ratio between di-anionic and mono-anionic form of the indicator.

$$\frac{[\text{I}_2^-]}{[\text{HI}^-]} = \frac{\frac{A_1}{A_2} - \frac{\epsilon_1^{\text{HI}^-}}{\epsilon_2^{\text{HI}^-}}}{\frac{\epsilon_1^{\text{I}^{2-}}}{\epsilon_2^{\text{HI}^-}} - \frac{A_1 \cdot \epsilon_2^{\text{I}^{2-}}}{A_2 \cdot \epsilon_2^{\text{HI}^-}}} \quad (2.19)$$

This equation can be shortened by substituting the constant absorption coefficients with  $e_1 = \epsilon_1^{\text{HI}^-} / \epsilon_2^{\text{HI}^-}$ ,  $e_2 = \epsilon_1^{\text{I}^{2-}} / \epsilon_2^{\text{HI}^-}$  and  $e_3 = \epsilon_2^{\text{I}^{2-}} / \epsilon_2^{\text{HI}^-}$ . Furthermore the absorption ratio can be expressed with  $R = A_1 / A_2$ . After substitution of this simplifications and insertion in equation 2.16, equation 2.20 is obtained.

$$pH = pK_a^{mcp} + \lg \left( \frac{R - e_1}{e_2 - R \cdot e_3} \right) \quad (2.20)$$

This equation (or slight variations [95]) is used to calculate the pH from the spectrophotometric measurements [93, 95, 96]. To allow exact measurements the parameters of this equation ( $e_1$ ,  $e_2$ ,  $e_3$ ,  $pK_a$ ) and their dependence on temperature and salinity must be characterized thoroughly. Especially the  $pK_a$  shows a strong dependence on temperature (-0.0126 pH units / K [95]) and salinity (0.00125 and 0.00407 pH units / PSU at 35 and 20 PSU, respectively [95]). However, also the absorption coefficients require compensation for temperature and salinity to achieve maximum accuracy [95]. Multiple characterizations for m-cresol purple were conducted for pH measurements in seawater which cover different ranges of temperature and salinity. The most important were conducted by Clayton and Byrne in 1993 [93] (20 °C to 30 °C and 30 PSU to 37 PSU), Mosley et al. [96] (25 °C, 0 PSU to 40 PSU) and Liu et al. [95] (5 °C to 35 °C, 20 PSU to 40 PSU). Liu et al. [95] used purified m-cresol purple for their characterization and reported a deviation of up to 0.01 pH units in measurements with unpurified m-cresol purple from different vendors. Therefore, dye purification is necessary to obtain optimal accuracy. However, this significantly increases the costs of operation as the dye is constantly consumed for every

measurement. Therefore, methods were developed to compensate the dye impurities by batch calibrations [97]. Interestingly, Liu et al. [95] observed temperature and salinity sensitivities of the absorption coefficients, which are compensated in their characterization.

### Temperature Sensitivity

The temperature sensitivity of this method demands high accuracy in temperature measurements. A temperature accuracy of better than 100 mK is required to enable pH measurements with an accuracy of 0.001 pH units. In laboratories the temperature is often controlled with a thermostat and set to 25.0 °C. While this simplifies the characterization of m-cresol purple as only one temperature is required this approach has also disadvantages. Bubble formation can disturb the measurement and hence degassing is necessary. Furthermore carbon dioxide can be lost during the degassing step which influences the pH of the sample. As the pH of seawater depends on temperature as well, the measured pH value must be converted to in situ conditions, which introduces another potential source of error [63].

### Salinity Sensitivity

Besides temperature, salinity is the second important cross-sensitivity of spectrophotometric measurements. As the theory of Debye and Hückel states (see eq. 2.3) the activity coefficients of ions depend on the surrounding medium. The electrostatic interactions between the ions cause a "shielding" of the individual ionic species and reduce thereby their activity. Therefore, the ions appear as if they are present at a lower concentration. This shifts chemical equilibria and hence the  $pK_a$  value of indicator dyes. Unfortunately, the extent of this effect depends on the charge of the ionic species and molecules with higher charges are more affected. This is caused by the stronger electrostatic attraction of multiply charged molecules [20, 98]. Therefore, the activity of  $I^{2-}$  in equation  $HI^- \rightleftharpoons H^+ + I^{2-}$  is reduced the most, the equilibrium shifts to the right and the  $pK_a$  is reduced. The same effect is observed for all indicator dyes, however, it is more pronounced with multiply charged indicators [98]. Importantly, open-ocean seawater has only small fluctuations of salinity, therefore the salinity effects are usually small. However, for highest accuracy these effects must still be compensated and some areas show a strong dynamic in salinity (e.g. Baltic Sea or estuaries). In these environments salinity compensation is crucial.

### **pH Perturbation by the Indicator**

Seawater is only weakly buffered and the addition of indicator solution perturbs the pH of the sample. Most often measurement cells utilize a path length of 10 cm to allow low indicator concentrations of only  $1 \mu\text{mol kg}^{-1}$  to  $10 \mu\text{mol kg}^{-1}$ , which minimizes the pH deviation [63, 91, 93, 99]. Nevertheless, corrections need to be applied and are conducted by adding different amounts of indicator and extrapolation of the pH to zero indicator concentration [91].

### **Challenges of Spectrophotometric Sensors**

Despite all the advantages of spectrophotometric measurements, sensor development is challenging with this method and most spectrophotometric devices are used for lab measurements from seawater samples. However, sampling is too expensive and laborious to establish a dense network of seawater pH data. While sensors based on pH electrodes or ISFETs require in principle only a water-proof pressure housing for the electronics, the development of spectrophotometric devices is much more challenging.

In contrast to other methods, pumps and valves are required to transfer the sample in the measurement cell and to mix it with the indicator dye. This dramatically increases power consumption in comparison with other systems and limits the measurement interval. In practical applications, the flow speed of the sample is limited to reduce the power consumption [63]. Furthermore, the devices consume indicator which needs to be supplied in reservoirs and limits the number of possible measurements and increases the operation costs. Due to the necessary optical path length, the fluidic parts and reservoirs, the devices are usually bulky and hard to miniaturize. Therefore, the hardware costs are high. Besides the costs, the large size and high power consumption limit the applicability in floats.

To overcome these issues, microfluidic spectrophotometric measurement devices are being developed [100–102]. However, while size, weight and power consumption are reduced, they are still large in contrast to other devices.

### **Summary**

In conclusion, spectrophotometric measurements are accurate and precise and suitable for ocean acidification observation [63]. However, while this method is well suited for lab or on-ship measurements, sensor development is challenging, due to the required moving parts and fluidics.

### **2.3.6 Optodes**

pH optodes are an alternative method for oceanographic pH measurement. This technique is very similar to spectrophotometric measurements, but in contrast to a soluble indicator dissolved in the sample, spectrophotometric measurements utilize sensor membranes with an immobilized indicator dye. Optodes can in principle detect any change in optical properties (e.g. absorption, refractive index) but luminescence intensity is most prominent, as the readout is straightforward and very sensitive. Usually a single optical fiber (or optical window) is used to transmit the excitation light and collect the pH sensitive emission of the indicator. However, unreferenced measurement of emitted fluorescence is highly unreliable as any change in the optical path will affect the measurement. Hence, a scheme for ratiometric measurement is required for practical applications. In principle two possibilities exist for this purpose: two-wavelength ratiometric measurements or Dual Lifetime Referencing (DLR)[103]. The DLR scheme is often preferred (see section 2.4.9), due to its advantages such as no additional filters, photodiodes or LEDs in contrast to dual wavelength referencing. However, maybe the most important advantage is that optodes developed for lifetime based oxygen measurements can be used for pH measurement without any changes in hardware, provided that the spectral properties of the pH indicator and reference phosphor are compatible. Therefore, existing hardware for marine oxygen measurements can be used with no or only minimal adaptations. This might significantly speed up the spread of optode technology.

#### **Advantages and Disadvantages**

Optodes offer numerous advantages over other state-of-the-art sensor systems. The problematic reference electrode as in electrochemical sensors (glass electrode and ISFETs) is not required. Furthermore, in contrast to spectrophotometric devices, no indicator is consumed during the measurement. Therefore, the deployment time and number of samples is not limited by the amount or shelf life of the indicator solution. Most importantly, no handling and pumping of liquids is required. This significantly simplifies the construction of a sensor. No pumps, valves, ports or static mixers are necessary and the readout of a sensor film can be conducted with a simple optical feed-through from a pressure housing. This drastically reduces the power consumption of the devices as the fluidics require the most energy in spectrophotometric devices.

Therefore, optodes are energy efficient, cost effective and easy to miniaturize in contrast to spectrophotometric devices and have found widespread applications for oxygen sensing.

Besides all these advantages pH Optodes still face many obstacles. First of all, read-out devices developed specifically for marine measurements are required. These devices must be water-proof, pressure resistant and an independent power-supply and logging capability would be useful. The second challenge is the development of sensor materials suitable for this application. The sensor materials must be stable for long-term applications, their sensitive range must be optimized, their response time must be sufficiently fast in cold seawater and most importantly their behavior must be characterized excellently for influences of temperature and salinity. For comparison, the characterization for m-cresol purple for oceanography started in 1993 [93], multiple improved characterizations were published [95, 96] and efforts are still ongoing to obtain characterizations suitable for the whole temperature and salinity range. However, optical pH sensor materials can be constructed from indicators carrying fewer charges than m-cresol purple and promises therefore a reduced cross-sensitivity to ionic strength and easier characterization (see section 2.1.2). In contrast to spectrophotometric devices stability is a bigger challenge in pH optodes. While spectrophotometric measurements use a new portion of indicator for every measurement, multiple thousand to million measurements should be conducted with the same indicator in the case of optodes. This demands excellent leaching-resistance, photostability and chemical stability from the sensor material.

## **Conclusion**

Optodes are already established for O<sub>2</sub> measurements due to their advantages. The same could happen for pH optodes if the challenges for seawater measurements can be overcome. The two main issues are missing dedicated read-out devices and optimized sensor materials. The SenseOcean project within the EU Seventh Framework Programme was a central part of this thesis. During this project the company Pyroscience GmbH focused on the development of optical read-out devices suitable for oceanographic applications and the sensors group at Graz University of Technology focused on the development of O<sub>2</sub>, pH and CO<sub>2</sub> sensor materials compatible to the device. In this thesis, the focus was on the development of novel pH sensor materials and testing of the combined system. Information on the CO<sub>2</sub> sensor materials developed within this project can be found in the publication of Fritzsche et al. [104] and

information on compatible O<sub>2</sub> sensor materials can be found in publications from Larsen et al.[105], Müller et al.[106] and Zach et al.[107].

## 2.4 Optical pH Sensor Materials for Marine Applications

The development of optical pH sensor materials optimized for marine applications is the core topic of this thesis. Therefore, their properties, strengths and weaknesses are discussed in detail in this chapter. However, this chapter is focused on the topics of most importance for the development of a planar sensor material suitable for seawater measurements, therefore some aspects of optical pH sensors are only covered superficially. More general information can be found in reviews on this topic (e.g. Wencel et al. [108]).

In many applications of optical pH sensors, the versatility of formats is their main advantage. pH sensor materials can be used for imaging applications to visualize the pH distribution of samples [109, 110], as nanoparticles with real time response [111] for in situ measurements in cells [112, 113], or on the tips of optical fibers for minimal invasive measurements [114, 115]. Furthermore, they can be easily miniaturized and integrated in microfluidic chips to allow for pH control in experiments. pH sensor materials are inexpensive and can be utilized as disposables, which reduces maintenance, cleaning costs and reduces contamination between experiments. Another important advantage is the possibility of remote read-out. Sensor materials can for example be mounted in the inside of a glass reactor or small vial and the read-out can be conducted from the outside with an optical fiber, without an additional port for a sensor.

### 2.4.1 Advantages of Optodes in Seawater

For oceanographic measurements another advantage is of greatest importance: in contrast to sensors based on glass electrodes or ISFETs, optical pH sensors do not require a reference electrode. The reference electrode, or more specific the liquid junction of the reference electrode, is the main weakness for applications in media with high ionic strength. Diffusion of media ions into the liquid junction causes irreproducible potentials which influence the measurements and often result in low accuracy and precision. The sensor materials themselves are inexpensive and the only part of the sensor which is exposed to the sample. Hence they can be constructed as disposables and replaced after every deployment if they are affected by bio-fouling or suffered mechanical damage (e.g. by scratches). Therefore, pH optodes can be very cost-effective and

require low maintenance. Furthermore, optodes offer high sensitivity at pH values close to their  $pK_a$ .

Seawater is a well suited sample for optical pH sensors. Some of the typical shortcomings of pH optodes are no issue in seawater. For example, the low dynamic range of optical pH sensors of only  $\pm 1.5$  pH units is a challenge in many applications. However, this is no issue in seawater as the expected pH range is between 7.5 and 8.4 [55]. Furthermore, the cross-sensitivity to ionic strength is less pronounced at high ionic strengths (see section 2.1.2).

### 2.4.2 Challenges for Optodes in Seawater

However, oceanographic measurements introduce new requirements on the sensor materials. The pH changes induced by ocean acidification are slow (0.0003 pH units / year [37]), therefore excellent accuracy and precision are required to obtain useful data. While for most industrial or biochemical applications precision of a few hundreds of a pH unit are sufficient, oceanographers desire a precision in the range of few thousands of a pH unit. Furthermore, the sensor materials should be suitable for autonomous long-term deployments without servicing or recalibration. Hence, the materials should show outstanding drift stability to maintain the requirements on precision throughout the deployment.

Optodes are already well established in marine science for oxygen measurements. However, optodes for other analytes, most notably pH and  $CO_2$ , are gaining increasing attention. To utilize the high level of development of  $pO_2$  optodes it is sensible to adapt these novel sensor materials to the optics of the already available read-out devices. Thereby, the new pH sensor systems would be available much faster to scientist, who already employ  $O_2$  optodes, and the costs for developing new hardware are avoided. Therefore, the optical pH sensor materials presented in this work were developed to be compatible to  $O_2$  optodes utilizing benzoporphyrin indicator dyes. The novel sensor materials can be read-out with the devices from the company Pyroscience GmbH, which was a partner in the EU project SenseOcean. While the work at Graz University of Technology was focused on the development of new sensor materials, Pyroscience GmbH adapted their devices to developed multiple water-proof and pressure resistant optodes with integrated battery and logger.

### 2.4.3 Principle

The functional principle of optical pH sensor materials is based on changes of optical properties in dependence on pH due to protonation or deprotonation of an indicator. In contrast to spectrophotometric measurement methods, where the indicator is dissolved in the sample, the indicator is immobilized in a sensor matrix. This matrix is insoluble in water but enables direct contact between the indicator and the sample by swelling due to water uptake. While the changes in many different properties are feasible for optode measurements (e.g. fluorescence, luminescence lifetime, absorption, refractive index)[116, 117], a change in fluorescence intensity is clearly the preferred mode of operation, due to the straightforward read-out. In principle, luminescence lifetime would be an even better parameter, as it would offer self-referenced measurements similar to oxygen optodes. A few pH indicators with suitable changes in luminescence lifetime were developed so far [118–120], but they are usually cross-sensitive to dissolved oxygen. All other pH indicators exhibit no changes in lifetime or changes in lifetime in the ns-range, which is only measurable with bulky and expensive equipment [121–123], and clearly not suitable for oceanography. The measurement of changes in the absorption spectrum is a more promising approach, but still inferior to changes in fluorescence as more complicated inner filter schemes are necessary for sensor readout. In addition, fluorescence based sensors offer better sensitivity [117].

A drawback of fluorescence based sensors is the concentration dependence of their apparent  $pK_a$  ( $pK_a'$ ), due to Förster Resonance Energy Transfer between the emissive and non-emissive indicator (homo-FRET). If the emission spectrum of the indicator in "on" state overlaps with the absorption spectrum of the indicator in "off" state, FRET is possible between the two molecules. Thereby energy is transferred from the emissive to the non-emissive indicator species which results in a reduction of fluorescence intensity. This effect is concentration dependent, as FRET is highly sensitive to indicator distance and the average distance between molecules decreases at larger concentration of indicator. Due to this effect the observed emission at the true  $pK_a$  of the indicator is less than 50 %, which results in an apparent reduction of the  $pK_a$ . Therefore,  $pK_a$  values obtained from fluorescence measurements should be called apparent  $pK_a$  values and it should be kept in mind that this value is concentration dependent. However, to a small extent this effect can be used for fine-tuning of the sensor dynamics.

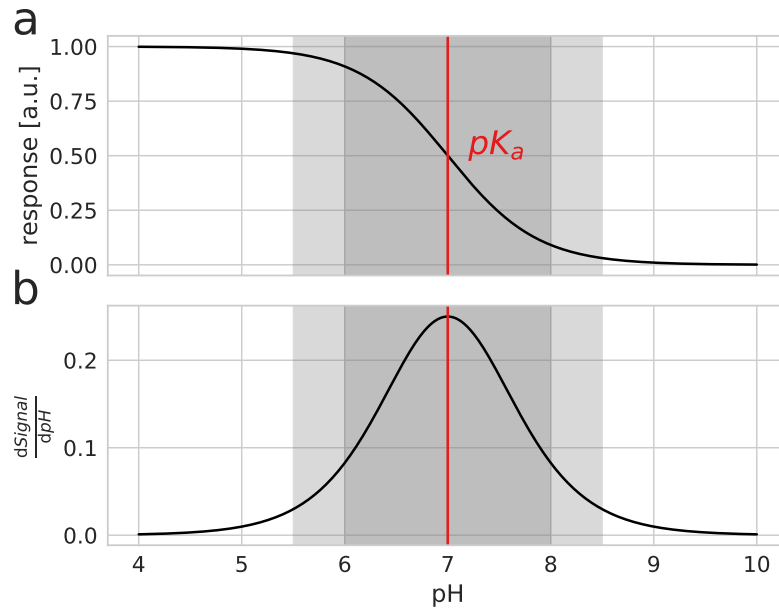


**Figure 2.7:** Dynamic range of a pH sensor material with  $pK_a$  7. In (a) the response of a pH sensor material over pH is plotted and in (b) the derivate  $dSignal/dpH$ , which describes the sensitivity of the sensor is plotted. The red line marks the  $pK_a$  of the sensor material, the dark gray area marks the range of highest sensitivity and the light gray are the range of sufficient sensitivity.

### Dynamic Range

Optical pH sensor materials have a limited range of operation of usually 2 to 3 pH units. This can be explained with the Henderson-Hasselbalch equation (eq. 2.37). This equation describes the ratio between the protonated and deprotonated species of the indicator in dependence on the pH of the medium. As the fluorescence intensity of the sensor foil is directly proportional to the concentration of the fluorescent species, this equation can be used to describe the sensor response. If the medium pH is at the  $pK_a$  of the indicator, the concentrations of protonated and deprotonated form are equal and the system is very sensitive to changes of pH. If the pH is one unit above or below the  $pK_a$  the ratio is approximately 91:9 and much smaller changes are induced in this ratio by changes in pH. Two pH units above or below the  $pK_a$  the ratio is close to 99:1 and hardly any sensitivity is left. Therefore, the useful dynamic range of an optical pH sensor is often defined as  $\pm 1.5$  pH units. This relation is visualized in Figure 2.7.

Figure 2.7 depicts the response of a simple pH sensor material with only one indicator. If a higher dynamic range is desired it is possible to combine multiple indicators in a single sensor layer [124–127]. However, this approach would complicate sensor development and is not necessary for marine applications due to the narrow pH range of seawater, provided that a suitable indicator can be obtained. An ideal indicator for marine applications should exhibit a  $pK_a$  close to 8 between 4 °C and 20 °C.

#### 2.4.4 Temperature Sensitivity

Similar to all other measurement methods of pH (and the pH of a sample itself), optical pH sensor materials are sensitive to temperature. Thereby, the most important influence is on the  $pK_a$  value of the pH indicator. The equilibrium of protonation of a pH indicator can in general be described with the reaction  $HA \rightleftharpoons H^+ + A^-$ . The position of this equilibrium, as described by the equilibrium constant  $K_a$  (eq. 2.21), is temperature dependent.

$$K_a = \frac{[H^+] \cdot [A^-]}{[HA]} \quad (2.21)$$

This dependence on temperature is a function of the free energy ( $\Delta G$ ) of the deprotonation reaction (eq. 2.22).

$$\Delta G = -R \cdot T \ln K_a \quad (2.22)$$

Where  $R$  is the ideal gas constant and  $T$  is the temperature in Kelvin.  $\Delta G$  can be replaced in this equation with  $\Delta G = \Delta H - T\Delta S$ , which results in equation 2.23.

$$\ln K_a = \frac{\Delta H}{R \cdot T} - \frac{\Delta S}{R} \quad (2.23)$$

Where  $\Delta H$  is the change in free enthalpy and  $\Delta S$  is the change in entropy. From this equation the Van't Hoff equation (2.24) is obtained by derivation after  $T$ .

$$\frac{d \ln K_a}{dT} = \frac{\Delta H}{R \cdot T^2} \quad (2.24)$$

This equation describes the changes of  $K_a$  over temperature as a function of the reaction enthalpy. Hence, reactions with a low change in free enthalpy show a low dependence on temperature and vice versa. Strong acids and carboxylic acids usually show deprotonation enthalpies close to 0 and are hence only weakly affected by temperature, while phenols and

amines show increasingly positive enthalpies (in correlation with their  $\text{pK}_a$  values) and are therefore more affected. In practice strong acids and carbonic acid show  $\text{dpK}_a/\text{dT}$  values close to 0, phenols show  $\text{dpK}_a/\text{dT}$  values between -0.007 to -0.012 and amines show  $\text{dpK}_a/\text{dT}$  values of up to 0.031 [128–131]. Hence pH indicators based on the deprotonation of a carboxylic acid group would result in nearly temperature independent sensor materials. However, chromophores do not react strongly to deprotonation of a carboxylic acid moiety. Moreover, the obtained  $\text{pK}_a$  values are too low for sensor materials for physiological conditions or seawater. Hence phenols and amines are often the sensitive groups of choice [98, 132, 133] and their cross-sensitivity has to be compensated by additional temperature measurements. The most common indicator for spectrophotometric pH measurements, m-cresol purple, utilizes a phenol group as sensitive moiety and shows the expected temperature sensitivity of -0.0126 pH units / K [95]. Interestingly, the pH dependence of seawater is similar to that of phenols (0.0114 pH units / K [134]), reducing the requirements on the accuracy of temperature measurements, as the errors compensate each other.

Besides the influence on the  $\text{pK}_a$  of the indicator, changes of temperature influence the quantum yield, the spectra of the pH indicator [95] or the spectral properties of a potential reference. If the DLR-scheme is employed for referencing, an influence on the luminescence lifetime and quantum yield of the reference phosphor is to be expected [135, 136]. However, the magnitudes of these influences are highly specific to every material and have to be compensated individually.

In conclusion, all optical pH sensor materials exhibit a cross-sensitivity to temperature. This sensitivity is usually not negligible and has to be compensated by additional temperature measurement. Therefore, a temperature sensor on an optode is very useful to enable measurements independent on externally supplied data. Moreover, the temperature should be measured as close to the sensor material as possible to reduce errors from temperature gradients.

#### 2.4.5 Ionic Strength Sensitivity

Ionic strength is the second most important cross-sensitivity of optical pH sensor materials. The activity of charged species is reduced at higher ionic strengths (see section 2.1.2). This shifts all equilibria, which includes charged species, and hence influences the protonation degree of indicator dyes. Moreover, pH itself is defined by the activity of  $\text{H}^+$  by the NBS scale. Therefore, pH shifts by itself upon an increase of ionic strength, even if the concentration of  $\text{H}^+$  would

remain constant. This is only the case for the NBS pH scale and not for the total scale, as it is defined by the concentration of  $H^+$ . It should be kept in mind that in optical sensing the signal is proportional to the concentrations of the indicator species and not their activity. However, the protonation equilibrium of the indicator still depends on the activity of  $H^+$ . Therefore, it is of interest to observe apparent  $pK_a$  values, which are defined via the concentrations instead of activities and their dependence on ionic strength (eq. 2.25)[30]. This dependence can be described for the NBS scale and the total scale with different results and was conducted for a few selected reactions of interest. The activity coefficients can be estimated with the Davies equation (eq. 2.6), which is useful for ionic strengths of up to 0.5 mM.

$$pK'_a = pH - \log \left( \frac{[A^-]}{[HA]} \right) \quad (2.25)$$

**Simple acid:**  $HA \rightleftharpoons H^+ + A^-$

This reaction describes the (first) deprotonation of an acid (e.g. carbonic acid, phenol, etc). In this reaction the activities of  $H^+$  and  $A^-$  are simultaneously reduced upon an increase in ionic strength. Hence the reaction equilibria shifts to the right, the apparent  $pK_a$  ( $pK'_a$ ) decreases and protons are released. On the normal (NBS) pH scale the effect on pH is reduced because the activity of protons is reduced as well, but this cannot compensate the effect and  $pK'_a$  on the NBS scale can be calculated with equation 2.26. On the total scale this dampening does not occur as only the concentration of  $H^+$  is observed and  $pK'_a$  on total scale can be calculated with equation 2.27.

$$\text{NBSscale : } pK'_a = pK_a + \log \gamma_1(I) \quad (2.26)$$

$$\text{Totalscale : } pK'_a = pK_a + \log (\gamma_1(I)^2) \quad (2.27)$$

$pK_a$  is the ideal  $pK_a$  in dilute solution,  $\gamma_1(I)$  is the activity coefficient for an ion with charge one, in dependence on the ionic strength.

**Simple base:**  $HB^+ \rightleftharpoons H^+ + B$

This reaction describes the behavior of many organic bases (e.g. amines). In this reaction both sides are affected by an increase in ionic strength. Therefore, the equilibrium does not shift in theory. However, on the NBS scale the pH increases upon an increase of ionic strength,

as the activity of  $H^+$  decreases (eq. 2.28). The total pH scale remains unaffected in theory as only the concentration of  $H^+$  is observed (eq. 2.29). However, the ionic strength dependence of the activity coefficient depends on the size of the ion. Hence, some shift of equilibrium is to be expected. This reaction is interesting in oceanography as it promises a nearly ionic strength independent system and is used with the TRIS buffer system ( $TRISH^+ \rightleftharpoons H^+ + TRIS$ ).

$$\text{NBS - scale : } pK'_a = pK_a - \log \gamma_1(I) \quad (2.28)$$

$$\text{Total - scale : } pK'_a = pK_a \quad (2.29)$$

**Second deprotonation of an acid:**  $HI^- \rightleftharpoons H^+ + I^{2-}$

This reaction describes the second deprotonation of an acid and is similar to the first reaction. This reaction shifts to the right side and a decrease in apparent  $pK_a$  is observed. However, this behavior is much more pronounced in this case, as the ionic strength dependence of the activity depends on the square of the ions charge. Again this is partly compensated by the decrease of  $H^+$  activity (for NBS scale). This behavior is of interest for oceanographic pH measurements, as m-cresol purple follows this reaction. m-cresol purple carries one charge from a deprotonated sulfonic acid group and the detected reaction is the deprotonation of the phenol moiety. Due to this double charge, m-cresol purple is very sensitive to changes in ionic strength and salinity compensation is required for all measurements. The second important example of this reaction is phosphate buffer (in the physiological pH region). The second deprotonation of phosphoric acid occurs around pH 7 and follows this reaction scheme. Hence phosphate buffers are highly ionic strength sensitive and not suited for oceanographic applications.

$$\text{NBS - scale : } pK'_a = pK_a - \log \frac{\gamma_1(I)}{\gamma_2(I)} \quad (2.30)$$

$$\text{Total - scale : } pK'_a = pK_a + \log \gamma_2(I) \quad (2.31)$$

Where  $\gamma_2(I)$  is the activity coefficient for an ion with a charge of 2 in dependence on the ionic strength.

These relations between  $pK'_a$  and ionic strength are plotted in Figure 2.8. As can be seen, the effect of ionic strength is much more pronounced for reactions with doubly charged species

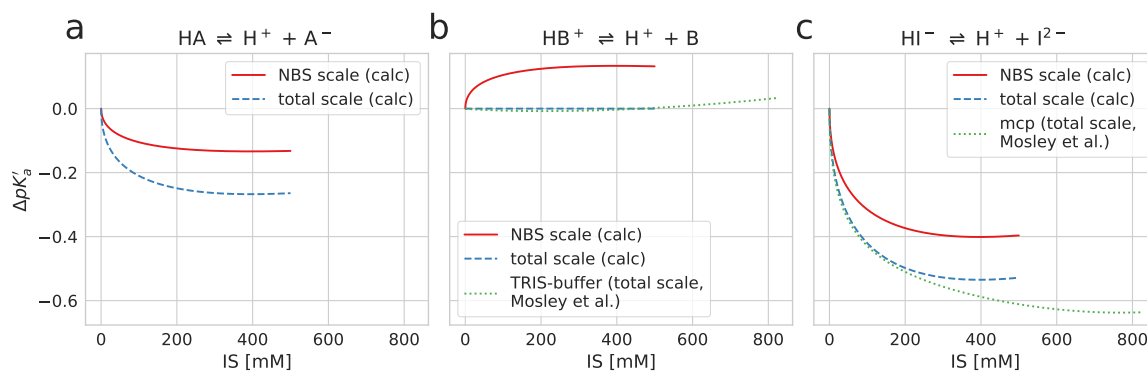


**Figure 2.8:** Ionic strength dependence of different acid/base reactions. The solid red lines and the dashed blue lines indicate calculated data on the NBS and the "total" pH scale, respectively. These calculations were conducted on basis of the Davies equation 2.6. The dotted green lines for TRIS and m-cresol purple (mcp) were plotted based on the measurements and fits of Mosley et al. [96]. Different cases are plotted: (a) first deprotonation of an uncharged acid, (b) deprotonation of a protonated base and (c) second deprotonation of an acid.

and at ionic strengths below 150 mM ( $\approx$  7PSU). Furthermore, it is visible that the calculated dependencies fit well to the observed data at lower ionic strengths for TRIS and m-cresol purple, indicating that the calculations for Figure 2.8a are accurate. However, at higher ionic strengths the influence on the  $pK_a$  is underestimated in the case of m-cresol purple. Several conclusions can be drawn from this Figure: i) TRIS is well suited as buffer substance for oceanography as it is nearly ionic strength independent (on total scale), ii) the ionic strength dependence of m-cresol purple is not ideal, iii) an indicator with a charge of 0 or +1 in the protonated state offers a significant reduction in ionic strength sensitivity.

Amine groups offer a +1 to 0 charge transition, however, they have the drawback of relative high temperature cross-sensitivities (see section 2.4.4) and typically temperature fluctuations are more pronounced than salinity fluctuations in oceanography. Moreover, this advantage is only true for measurements on the total scale. For non-marine measurements the NBS scale is of higher relevance and in these applications indicators with a 0 to -1 transition are equally suited. Therefore, phenol moieties, as used in m-cresol purple, are an excellent choice as pH sensitive groups in an indicator.

In conclusion, the ionic strength sensitivity of an indicator can be minimized by reducing its charge. The standard indicator for spectrophotometric measurements, m-cresol purple, carries 2 charges when deprotonated and is therefore quite sensitive to ionic strength influences. Spectrophotometric measurements require water-soluble indicators and charges greatly increase the solubility and are therefore difficult to remove. However, optode indicators must not be water soluble. Therefore, they can be selected or designed with fewer charges, reducing their sensitivity to ionic strength [98].

#### 2.4.6 Indicators

Many different classes of indicators have been used for the development of pH sensor materials. The most important classes are, 8-hydroxy-1,3,6-pyrenetrisulfonic acid (HPTS) [137–142] fluoresceins [98, 133, 143, 144], rhodamines [145, 146], perylenes [147–149], BODIPYs [150–154] and aza-BODIPYs [124, 132, 154–158]. Among these indicators HPTS, fluoresceins and rhodamines absorb best in the blue to green part of the electromagnetic spectrum and emit visible light. Therefore, they are susceptible to interference from background fluorescence. Additionally fluorescein-based indicators exhibit bad photostability [108, 159]. HPTS offers better photostability and a  $pK_a$  ( $\approx 7.5$  [140]) which is suitable for oceanographic measurements. However, it is highly charged (transition between -3 and -4) and hence shows a pronounced cross-sensitivity to ionic strength [140]. aza-BODIPYs are an especially promising class of indicator dyes due to several favorable properties. aza-BODIPYs feature high molar absorption coefficients ( $\approx 80\,000\text{ L mol}^{-1}\text{ cm}^{-1}$ ), good quantum yields ( $\approx 20\text{--}25\%$ ), excellent photostability and they absorb the red light and emit in the near infrared region of the electromagnetic spectrum [124, 132, 156]. Moreover, their  $pK_a$  is highly tunable [124, 132], they are water insoluble (prevents leaching) and anchor groups for improved physical entrapment or even covalent coupling can be attached. Moreover, they transition only between the charges 0 and -1, which reduces their sensitivity to ionic strength and further reduces their solubility.

The high brightness ( $\epsilon \cdot QY$ ) allows thin sensor films with good response times and good signal to noise ratio, to achieve high resolution. However, their most important properties are their excellent photostability, which enables the development of long-term stable sensor materials without limitations on the measurement frequency, and their spectral properties, which are compatible to optodes developed for benzoporphyrin based oxygen sensor materials. This class of indicators was used for all sensor materials developed during this thesis (see chapter 4), both

physically entrapped and covalently coupled to the sensor matrix. Thereby, covalent coupling of the indicator was preferred as it offers higher stability and reduces effects as migration and aggregation of indicator.

### **pH Sensitivity**

pH sensitivity in aza-BODIPY dyes is mainly introduced by two mechanisms: Intramolecular Charge Transfer (ICT) and Photoinduced Electron Transfer (PET) [160]. ICT is characterized by a change in the internal charge distribution of a molecule. Indicator dyes utilizing this approach often use an amine or phenol moiety conjugated to the dye core which can be protonated and deprotonated, respectively. Upon protonation of the amino group it can no longer donate its free electron pair to the electronic system of the dye, which results in a shift of absorption and emission spectrum and potentially a turn "on" or "off" of fluorescence. This is similar for the phenol groups. Deprotonated phenols are strong electron donors while protonated phenols donate only weakly into the system. Importantly, the ICT effect does not necessarily lead to a quenching of the indicator. Often only a spectral shift is observed which can be utilized for ratiometric measurements [161]. A requirement for this effect is conjugation of the electron pairs to the core of the dye system to enable either a +M or -M effect. Non-conjugated phenols and amines can cause only very weak effects. This was utilized during this thesis for the development of novel aza-BODIPY indicators which show pure PET quenching (see chapter 5).

The second feasible approach for introducing pH sensitivity into pH indicators is PET [145, 147, 149, 150, 160, 162]. PET is characterized by the transfer of an electron between the quencher moiety and the dye core in the excited state. This transfer results in a fluorescence quenching. Importantly, the shape of the absorption and emission spectrum of the indicator is not influenced [160]. This quenching mechanism is depicted in Figure 2.9. As can be seen, the fluorescence is quenched by electron transfer from the quencher to the excited fluorophore. After this initial energy transfer, the excited electron from the dye is transferred non-radiatively to the quencher. Phenols [124, 132, 147, 163] and amines [145, 149, 150] are thereby popular choices as PET-donors [145, 149]. However, this energy transfer is only possible as long as the quencher's HOMO is above the dye's HOMO. This can be used to obtain pH sensitivity in a dye/quencher pair. The HOMO from phenols and amines is lowered upon protonation, which inhibits PET quenching and leads to a turn "on" effect of indicator fluorescence. PET is also

possible with electron transfer from the dye to the quencher, but this concept is less frequently employed [160].

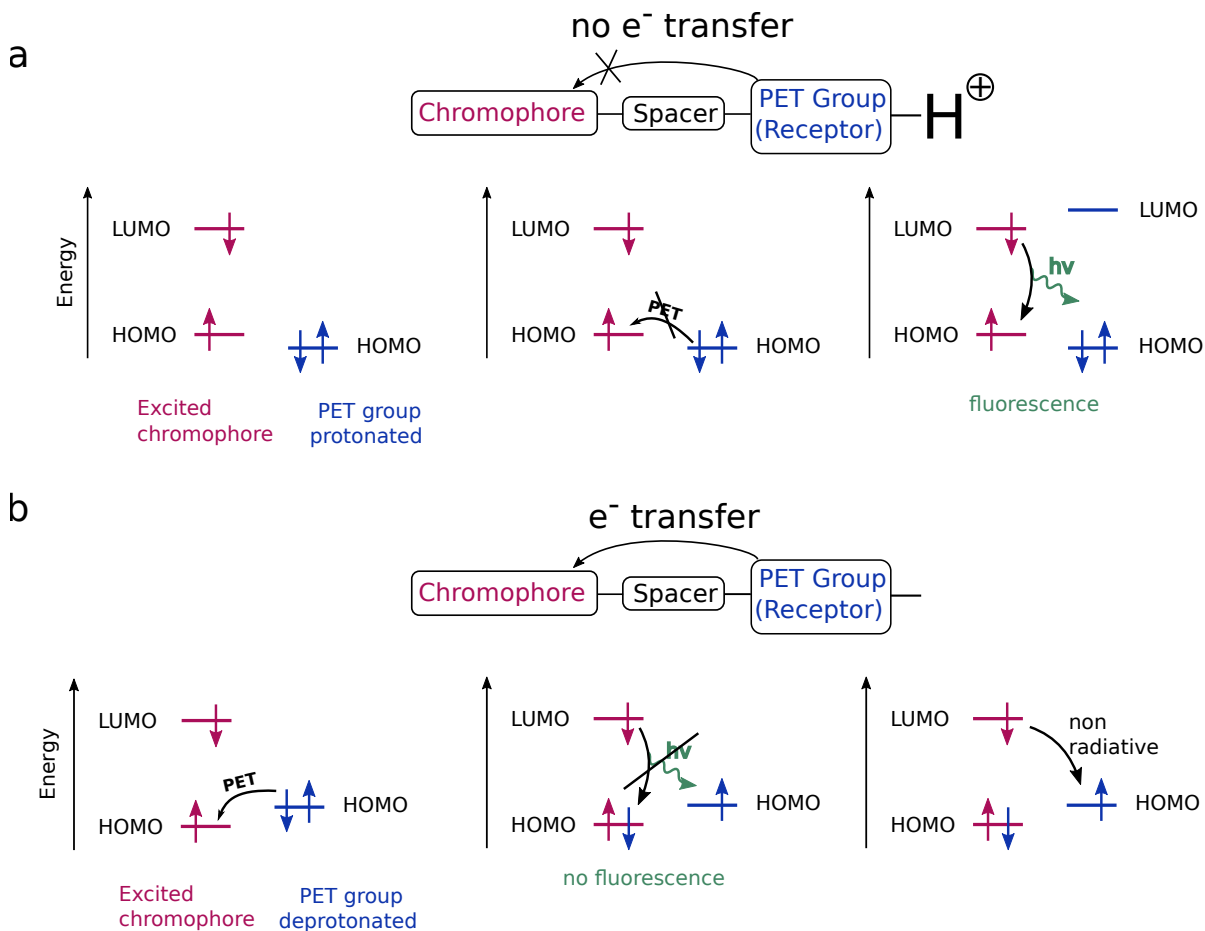


**Figure 2.9:** Mechanism of PET quenching for pH sensing. (a) The receptor group (e.g. amine or phenol) is protonated and PET quenching is inhibited. Hence the indicator is fluorescent. (b) The receptor is deprotonated and the indicator is quenched by PET.

While ICT based pH sensor materials offer straightforward implementation of ratiometric measurements, PET based systems have different advantages. Due to the decoupling of dye and receptor, both can be tuned independently. For example, the dye can be modified with electron withdrawing groups to enhance the photostability without influence on the pK<sub>a</sub> of the receptor moiety. The same is true for pK<sub>a</sub> tuning of the receptor. Electron donating or withdrawing groups can be introduced without severe influence on the spectral properties of

the dye. Furthermore, the absorption spectrum of a PET indicator is pH independent, which results in simpler sensor behavior (see chapter 5).

### **2.4.7 Matrices**

To obtain pH sensitive sensor materials the pH indicators must be immobilized in a hydrophilic matrix material. This matrix material must on one hand stabilize the hydrophobic and water-insoluble indicator dyes, and on the other hand must be water swellable to enable direct contact between the indicator and the sample. Multiple different matrix materials were used for this purpose. The most important materials include polyurethane hydrogels [98, 124, 132, 150], crosslinked acryloylmorpholines [149], silica particles [145, 164, 165], poly(vinylchloride) with plasticizer [147], ethyl cellulose [166] and sol-gels [167, 168]. The indicators can be immobilized in the sensor matrix by simple physical entrapment or by more complex covalent coupling. The approach of physical entrapment is very straightforward and indicators can be immobilized without any chemical modifications, and sensor layers can be prepared by simple knife-coating of a solution of indicator and matrix material. While the process of covalent coupling is often much more laborious, it offers many advantages. First of all, covalent coupling offers an improved stability of the sensor materials, as processes like migration (and consequent aggregation) and leaching are suppressed. Moreover, the compatibility of an indicator to a non-ideal matrix can be enhanced as the steric hindrance by coupling to the matrix and the reduced mobility prevent aggregation. Therefore, covalent coupling is preferable for sensors with long deployment types, which is an important feature in marine applications.

The first matrix material of choice during this thesis was hydrogel D4 from hydromed™, which was used for physical entrapment. This polymer is a heterogeneous polymer which forms hydrophilic and hydrophobic domains in the water swollen state. While the water-insoluble indicator is mainly located in the hydrophobic domains the hydrophilic domains enable contact with the water phase [98]. However, it was discovered that this heterogeneous composition results in a slow second kinetic in the response behavior of sensor materials at temperatures below 25 °C (see chapter 4, Figure 4.4). This behavior was explained by migration effects induced by the polarity change of the indicator upon protonation or deprotonation. It is expected that the more hydrophilic deprotonated indicator migrates to the surface of the hydrophobic domains and the protonated indicator migrates into the core of the hydrophobic domains to achieve equilibrium. Apparently this process is sufficiently fast above room temperature, but becomes

extremely slow at low temperatures. This results in  $t_{95}$  values of  $\approx 3$  h at  $4^\circ\text{C}$  which is unfeasible for oceanographic applications. Therefore, the consequent development of sensor materials was focused on matrix materials with a homogeneous and hydrophilic structure. However, these polymers show bad compatibility to hydrophobic aza-BODIPY indicators. Hence the acryloylmorpholine was chosen as the bulk material of the matrix polymer and covalent coupling was implemented to further reduce tendencies of aggregation in the matrix polymer [149].

### 2.4.8 Referencing

While luminescence lifetime is self referenced and an excellent choice for oxygen sensing, lifetime measurements are no option for pH optodes, as no indicators with sufficiently long luminescence lifetimes are available. However, unreferenced read-out is not feasible in practical measurements, as any change in the optics (e.g. temperature change of LED, bending of the fiber, movement of the sensor spot, changes in reflectance of the sample, etc.) would immediately result in a change in the measured intensity. Therefore, ratiometric readout methods are required. While ratiometric two-wavelength measurements are possible and often utilized [126, 166, 167, 169], this technique was never applied for seawater pH measurements to the best of my knowledge. Drawbacks of this method include the wavelength dependence of refractive effects and scattering, and the requirement for an additional emission filter and photodiode (or excitation filter and LED). A popular alternative to this method is the Dual Lifetime Referencing (DLR) scheme [103, 124, 141, 170–172]. For example, the commercially available pH sensor materials from Presens GmbH are based on DLR read-out. This method enables ratiometric measurements with only one LED, one photodiode and one set of excitation and emission filters. Moreover, devices developed for lifetime readout of oxygen sensor materials can be used for DLR based pH measurements, which reduces the costs of developing new devices.

### 2.4.9 Dual Lifetime Referencing

DLR is used to measure the intensity ratio between a prompt (fluorescence) and a delayed emission (often phosphorescence). For this method indicator and reference must be excitable at the same wavelength, their emission wavelengths must be similar to be collected with a single photodetector, and the luminescence lifetime must be significantly different [103, 170]. An important advantages of this method is, that the emission of both indicator and reference can be at the same wavelength as the separation is conducted based on the difference in

luminescence lifetime. This reduces disturbances by refraction, scattering or absorption by sample components [103, 170, 172]. Furthermore, hardware costs are reduced as only one emission filter and photodiode is necessary. DLR can either be conducted in the time domain (t-DLR) or in the frequency domain (f-DLR).

### **t-DLR**

One possible implementation of the DLR method is measurement in the time domain (t-DLR). In the first step of this method, the mixed emission of fluorophore and reference is measured under illumination ( $I_{on}$ ). Then the excitation source is turned off and after a short delay only the emission of reference remains. This emission is recorded as the second value ( $I_{off}$ ) (Figure 2.10). These two measurement windows are usually in the range of the luminescence lifetime of the reference material (multiple microseconds) [173] and the experiment is usually repeated multiple times and the results are averaged. With equation 2.32 a value ( $R$ ) is obtained which is proportional to the ratio of indicator to reference intensity and is used as the measurement signal.

$$R = \frac{I_{on}}{I_{off}} = \frac{I_{ind}^{on} + I_{ref}^{on}}{I_{ref}^{off}} \quad (2.32)$$

Where  $I_{ind}$  and  $I_{ref}$  are the intensities of the indicator and the reference, respectively, and the superscripts indicate if the excitation source was turned on or off during the measurement.

This method was used for multiple different applications [174] and is especially popular for imaging applications as large areas can be recorded simultaneously with special cameras [109, 173, 175] and was also applied for oceanographic measurements [141].

### **f-DLR**

An alternative to t-DLR is measurement in the frequency domain [103, 170, 174, 176]. Thereby the sensor material is excited with modulated excitation light in the shape of a sine wave. The fluorescent indicator responds without any delay and hence shows a phase shift of zero. Due to the longer lifetime of the reference material, its emission is phase shifted compared to the excitation source. These two signals are superimposed and detected by the optode, which contains a lock-in amplifier measuring the overall phase shift ( $\Phi$ ) and amplitude. This relation is visualized in Figure 2.11. As can be seen a low fluorescence intensity results in a high phase

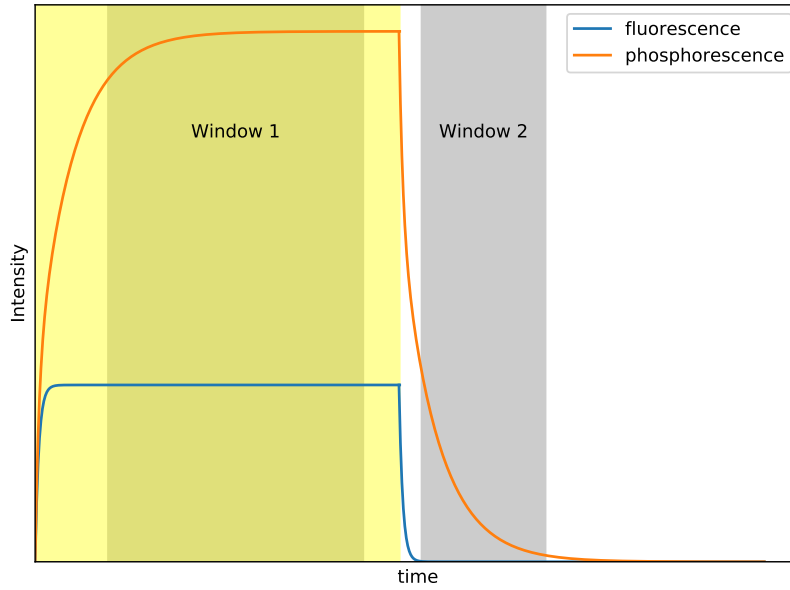


**Figure 2.10:** Schematics of the t-DLR concept. The yellow area indicates the time when the excitation light is on. The two gray areas are the measurement windows, where the mixed emission of indicator and reference and the pure reference are measured.

shift close the the phase shift of the pure reference, while a high fluorescence intensity results in low phase shifts. This relation can be expressed with equation 2.33, which offers  $\cot \Phi$  as a value proportional to the ratio between fluorescence and phosphorescence intensity. Therefore,  $\cot \Phi$  is used a measurement result of f-DLR measurements instead of  $\Phi$ .

$$\cot \Phi = \cot \Phi_{ref} + \frac{1}{\sin \Phi_{ref}} \cdot \frac{A_{ind}}{A_{ref}} \quad (2.33)$$

Where  $\Phi_{ref}$  is the phase shift of the pure reference and  $A_{ind}$  and  $A_{ref}$  are the amplitudes of the indicator and reference, respectively. The modulation frequency has to be chosen based on the luminescence lifetime of the reference material. The relation between the lifetime ( $\tau$ ), modulation frequency ( $f$ ) and phase angle is given by equation 2.34

$$\Phi = \arctan(2 \cdot \pi \cdot f \cdot \tau) \quad (2.34)$$

However, while a high phase shift is good to increase the dynamic range of the phase angle, the modulation frequency is limited by the demodulation of the reference. At too high frequencies

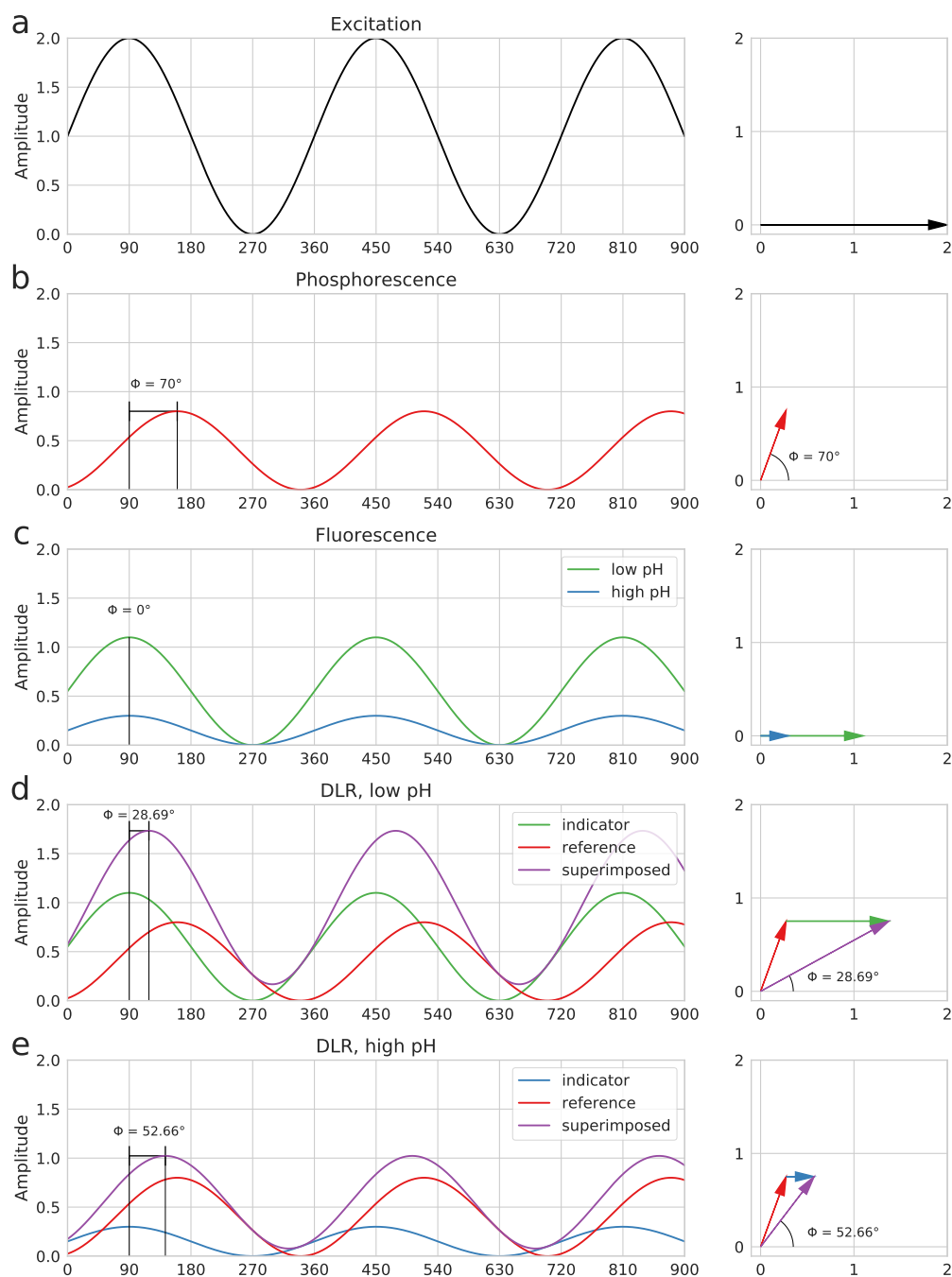


**Figure 2.11:** Schematics of the f-DLR concept for an indicator. In the left column the signals are depicted against time and in the right column the values are shown in polar plots. In line (a) the phase of the excitation light is shown and in the lines (b) and (c) the responses of the phosphorescent reference and the fluorescent indicators are depicted. In the polar plots the amplitude of the signals is visualized as the length of the arrows. In lines (d) and (e) the superimposed signals at low pH and high pH are shown (valid for indicators which are in the "on" state when protonated (e.g. aza-BODIPYs)).

the reference material has not sufficient time to relax to the ground state, which results in a decrease of amplitude as described by equations 2.35 and 2.36.

$$\kappa = \frac{1}{1 + \sqrt{(2 \cdot \pi \cdot f)^2 \cdot \tau^2}} \quad (2.35)$$

$$A = I \cdot \kappa \quad (2.36)$$

Where  $\kappa$  is the demodulation,  $f$  is the modulation frequency,  $\tau$  is the luminescence lifetime,  $A$  is the observed amplitude and  $I$  is the total intensity of emission. Based on these considerations, an optimal modulation frequency is selected. A luminescence lifetime of  $\approx 100 \mu\text{s}$  (e.g. Egyptian blue [135]) with a modulation frequency of 10 kHz would result in a phase angle of  $\approx 81^\circ$  but the modulation factor would be only  $\approx 0.16$ . A modulation frequency of 1 kHz would result in modulation factor of  $\approx 0.85$  but a phase shift of only  $\approx 32.1^\circ$ , while 4 kHz as a compromise result in a phase angle of  $\approx 68.3^\circ$  and a demodulation factor of  $\approx 0.37$ .

An important advantage for f-DLR is the fact, that many oxygen optodes are phase fluorometers which utilize equation 2.34 to calculate the phosphorescence lifetime of the oxygen indicator from the phase shift. Hence, these devices are more easily available and can be utilized for DLR measurements if the spectral properties are suitable.

### DLR Reference Materials

The selection of a suitable reference material is a challenge in DLR. The requirements on the reference material include a suitable luminescence lifetime, spectral compatibility to the optode and the indicator, high chemical stability and high photostability, no interaction with the indicator and an as low as possible sensitivity to environmental influences (especially pH, T and  $\text{O}_2$ ). Often utilized reference materials for DLR are tris(4,7-diphenyl-1,10-phenanthroline)ruthenium(II) complexes incorporated in matrices with low oxygen permeability [170, 173, 176–178]. This encapsulation significantly reduces the cross-sensitivity to oxygen, but cannot eliminate it completely [177]. Therefore, DLR sensors utilizing this reference are always cross-sensitive to oxygen, which is problematic for oceanographic pH measurements if strong fluctuations of oxygen are observed, or even anoxic conditions are present. An alternative to these reference materials based on an oxygen indicator in an impermeable matrix are small particles of inorganic phosphors. These reference materials are completely insensitive to oxygen and extremely

photostable [135, 179]. The pigment Egyptian blue has been used multiple times as DLR sensor material [104, 180, 181] and was selected as reference material for the pH sensors developed in this work.

A common challenge of all phosphorescent DLR sensor materials is their lifetime and intensity dependence on temperature. This introduces additional cross-sensitivity to temperature which must be compensated.

#### 2.4.10 Mathematical Description

To calculate pH values from measurement results, a mathematical description of the response of the sensor materials is necessary. This model must describe the relation between  $\cot \Phi$  and pH, and must contain parameters to compensate the temperature and ionic strength sensitivity of the sensor material. The starting point for this model is the Henderson-Haselbalch equation, which connects the pH with the concentration of protonated indicator. We utilized aza-BODIPY indicators which are fluorescent when protonated, hence  $[\text{HA}]$  is proportional to the fluorescence intensity ( $[\text{HA}] \propto I_F$ ) (equation 2.38).

$$pH = pK_a + \lg \frac{[\text{A}^-]}{[\text{HA}]} \quad (2.37)$$

This equation was solved for  $[\text{HA}]$ :

$$I_F \propto [\text{HA}] = \frac{[\text{HA}]_0}{1 + 10^{pH-pK_a}} \quad (2.38)$$

and inserted into the DLR-equation (eq. 2.33).

$$\cot \Phi = \frac{1}{\cot \Phi_{ref}} + \frac{\frac{[\text{HA}]_0}{\sin \Phi_{ref} \cdot A_{ref}}}{1 + 10^{pH-pK_a}} \quad (2.39)$$

For a given sensor composition the terms  $\frac{1}{\cot \Phi_{ref}}$  and  $\frac{[\text{HA}]_0}{\sin \Phi_{ref} \cdot A_{ref}}$  are constant and the lowest value  $\cot \Phi$  can reach (*Bottom*) and the range in which it can vary (*Top - Bottom*), respectively. Therefore, the equation can be simplified to equation 2.40.

$$\cot \Phi = \textit{Bottom} + \frac{\textit{Top} - \textit{Bottom}}{1 + 10^{pH-pK_a}} \quad (2.40)$$

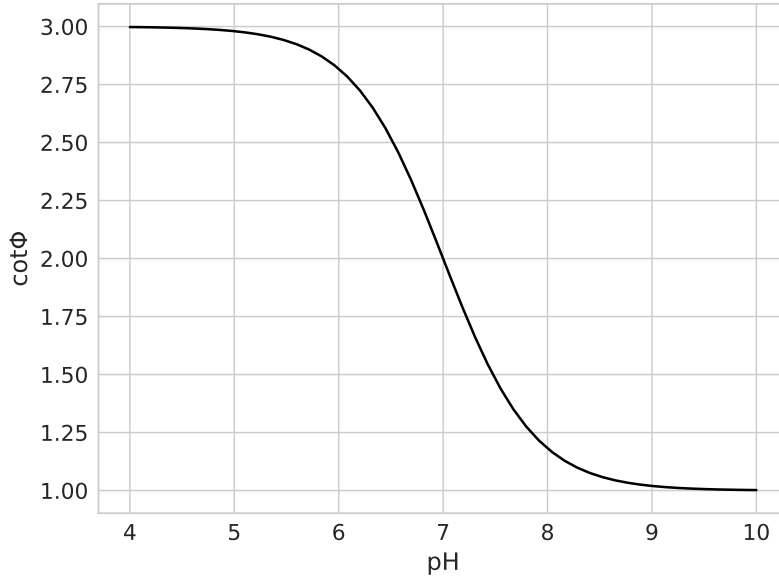


**Figure 2.12:** Example of a Boltzmann sigmoid

This equation is very similar to the Boltzmann sigmoid (eq. 2.41) which is frequently used for fitting of pH sensor data.

$$Y = Bottom + \frac{Top - Bottom}{1 + e^{\frac{V_{50} - X}{slope}}} \quad (2.41)$$

In fact the only differences are the additional parameter *slope* which describes the steepness of the curve and the exponent, which is to the basis of *e* instead of 10. Therefore, the Boltzmann sigmoid was used for fitting the sensor data, but the exponent was exchanged to basis 10, which is better suited for the pH scale and results in a *slope* close to 1 if the sensor behaves ideally (eq. 2.42). This fit is visualized in Figure 2.12.

$$\cot \Phi = Bottom + \frac{Top - Bottom}{1 + e^{\frac{pH - pK_a}{slope}}} \quad (2.42)$$

### Temperature Compensation

To allow for temperature compensation, linear temperature coefficients were added to the Boltzmann sigmoid. Unfortunately, many of the parameters can be influenced by temperature. As was mentioned in sections 2.4.4 and 2.4.9, the  $pK_a$  of indicators is always temperature dependent ( $\approx 0.01$  pH units / K), which can be compensated directly with a linear coefficient.

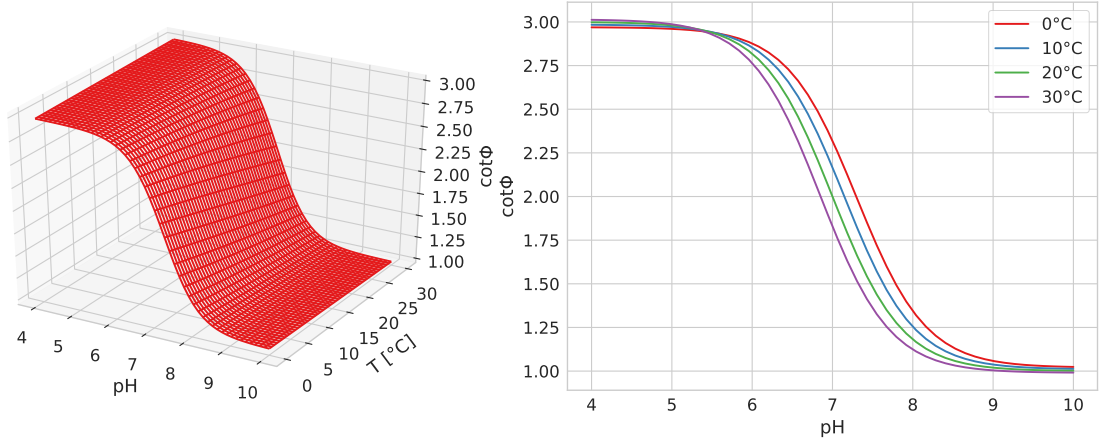


**Figure 2.13:** Example of a temperature compensated Boltzmann sigmoid with linear coefficients for *Top*, *Bottom* and  $pK_a$ : (left) 3 dimensional plot depicting the response surface; (right) Temperature projected curves for better visualization.

Besides the  $pK_a$ , the luminescence lifetime and quantum yield of most reference materials depends on temperature. This influences both the *Bottom* and *Top* coefficients and results in two additional temperature coefficients. These effects are not expected to be exactly linear with temperature, however, if the observed changes are small, they can be approximated linearly. These considerations lead to equation 2.43.

$$\cot \Phi = (Bottom + Bottom_T \cdot (T - 20)) + \frac{Top + Top_T \cdot (T - 20) - (Bottom + Bottom_T \cdot (T - 20))}{1 + 10^{\frac{pH - (pK_a + pK_{aT} \cdot (T - 20))}{slope}}} \quad (2.43)$$

Where  $Bottom_T$ ,  $Top_T$  and  $pK_{aT}$  are the linear temperature coefficients for *Bottom*, *Top* and  $pK_a$ , respectively, and  $T$  is the Temperature. This equation is visualized in Figure 2.13.

### Ionic Strength Compensation

Besides temperature, the ionic strength is an important cross-sensitivity of optical pH sensor materials. The extend of the cross-sensitivity can be minimized (see section 2.4.5) and due to the high salinity of seawater the effects are often small. However, compensation can still be necessary. Therefore, the temperature compensated Boltzmann sigmoid (eq. 2.43) was further

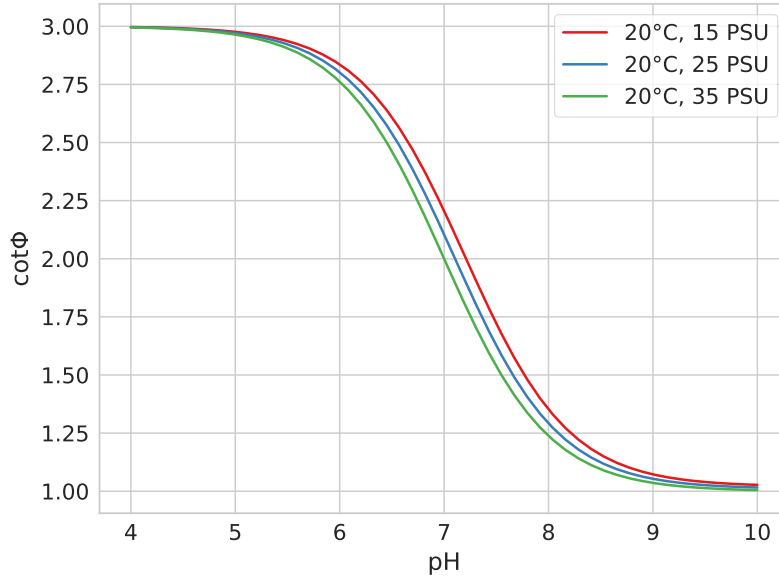


**Figure 2.14:** Temperature and salinity projections of the 4 dimensional surface with fixed temperature and varied salinity.

extended with linear coefficients for  $pK_a$  and the *Bottom* value (eq. 2.44). While the coefficient for  $pK_a$  is theoretically founded, the coefficient for *Bottom* cannot be explained in theory, but improved the quality of the fits. While the coefficients are not expected to be linear, all cross-sensitivities observed in this work were small and could be approximated linearly.

$$\cot \Phi = (Bottom + Bottom_T \cdot (T - 20) + Bottom_S \cdot (S - 35)) + \frac{Top + Top_T \cdot (T - 20) - (Bottom + Bottom_T \cdot (T - 20) + Bottom_S \cdot (S - 35))}{1 + 10^{\frac{pH - (pK_a + pK_{aT} \cdot (T - 20) + pK_{aS} \cdot (S - 35))}{slope}}} \quad (2.44)$$

Where  $Bottom_S$  and  $pK_{aS}$  are linear salinity coefficients. This equation has 3 independent variables and can no longer be plotted. However, projections to certain temperatures and salinities are possible (Figure 2.14).

However, due to the conducted optimizations of the ionic strength sensitivity the sensor materials developed during this work showed only small sensitivities to ionic strength, which can be neglected for the salinity range 15 PSU to 40 PSU. Hence most sensor data was fitted with equation 2.43.

---

# 3 A Versatile Optode System for Oxygen, Carbon Dioxide, and pH Measurements in Seawater with Integrated Battery and Logger

## 3.1 Preface to the Manuscript

This publication was published at *Limnology and Oceanography: Methods*.

This publication describes the development and evaluation of sensing materials for oxygen, carbon dioxide and pH with combined read-out devices. These devices feature an integrated battery sufficient for deployments of 1 year with a measurement interval of 30 s and a logger unit with a storage capacity of 20 million measurement points. The devices are small and cost effective and can be deployed without any requirements on existing infrastructure.

The devices were developed by Pyroscience GmbH as part of the EU-project "SenseOcean" and tested in combination with sensor materials developed at Graz University of Technology. The deployed CO<sub>2</sub> sensor materials were developed by Susanne Schutting, Pia Gruber and Eva Fritzsche [104]. The development of the pH sensor material were started in a joint project between many members of the working group to participate in the "Wendy Schmidt Ocean Health Xprize", a worldwide competition between research groups and companies for developing cost-effective and accurate sensor systems for oceanography. The results from this project were used to continue the development of pH sensors during this thesis in cooperation with Martin Strobl.

This publication contains data from multiple generations of sensor materials and field-trips to the Baltic Sea, Kiel (Germany), Limfjord (Denmark) and Southampton (England). Deployments in profiling applications on CTD rosettes as well as on stationary moorings were conducted.

The utility of the individual sensors is demonstrated by multiple measurements. However, the most important aspect is the information, which can be obtained by the combined sensor set. At multiple locations, excellent correlation between the different sensors was observed with high temporal resolution, allowing for example observation of biological activity or tidal water exchange.

# A Versatile Optode System for Oxygen, Carbon Dioxide, and pH Measurements in Seawater with Integrated Battery and Logger

Authors: Christoph Staudinger,<sup>1</sup> Martin Strobl,<sup>1</sup> Jan P. Fischer,<sup>2</sup> Roland Thar,<sup>2</sup> Torsten Mayr,<sup>1</sup> Daniel Aigner,<sup>1</sup> Bernhard J. Müller,<sup>1</sup> Bernhard Müller,<sup>1</sup> Philipp Lehner,<sup>1</sup> Günter Mistlberger,<sup>1</sup> Eva Fritzsche,<sup>1</sup> Josef Ehgartner,<sup>1</sup> Peter W. Zach,<sup>1</sup> Jennifer S. Clarke,<sup>4</sup> Felix Geißler,<sup>4</sup> André Mutzberg,<sup>4</sup> Jens D. Müller,<sup>3</sup> Eric P. Achterberg,<sup>4</sup> Sergey M. Borisov,<sup>1\*</sup> Ingo Klimant<sup>1</sup>

1. Institute of Analytical Chemistry and Food Chemistry, Graz University of Technology, Stremayergasse 9, 8010 Graz, Austria
2. Pyro Science GmbH, Hubertusstraße 35, 52064 Aachen, Germany
3. Department of Marine Chemistry, Leibniz Institute for Baltic Sea Research Warnemünde, Seestraße 15, 18119 Rostock, Germany
4. GEOMAR Helmholtz Centre for Ocean Research, 24148, Kiel, Germany

\*email: sergey.borisov@tugraz.at

Keywords: optode, phase fluorometry, sensor, oxygen, pH, carbon dioxide, seawater

## 3.2 Abstract

Herein, we present a small and versatile optode system with integrated battery and logger for monitoring of O<sub>2</sub>, pH, and pCO<sub>2</sub> in seawater. Three sensing materials designed for seawater measurements are optimized with respect to dynamic measurement range and long-term stability. The spectral properties of the sensing materials were tailored to be compatible with a commercially available laboratory oxygen logger that was fitted into a pressure housing. Interchangeable sensor caps with appropriate “sensing chemistry” are conveniently attached to the end of the optical fiber. This approach allows using the same instrument for multiple analytes, which offers great flexibility and minimizes hardware costs. Applications of the new optode system were demonstrated by recording depth profiles for the three parameters during a research cruise in the Baltic Sea and by measuring surface water transects of pH. The optode

was furthermore used to monitor the concentration of dissolved oxygen in a seagrass meadow in the Limfjord, Denmark, and sensor packages consisting of  $pO_2$ , pH, and  $pCO_2$  were deployed in the harbors of Kiel, Germany, and Southampton, England, for 6 days. The measurements revealed that the system can resolve typical patterns in seawater chemistry related to spatial heterogeneities as well as temporal changes caused by biological and tidal activity.

### 3.3 Introduction

Oxygen, pH, and  $pCO_2$  are important parameters in marine science [30, 32, 33, 105]. All three parameters are useful to characterize water masses and are excellent indicators for many biological processes [29]. Furthermore, simultaneous measurement of pH and  $pCO_2$  is sufficient, although not ideal, for a complete characterization of the carbonate system [182]. Since the increasing atmospheric carbon dioxide ( $CO_2$ ) concentrations result in ocean acidification [32, 34], pH and  $pCO_2$  measurements are of increasing interest to study the influence of this ongoing process on marine life.

Despite the fact that many methods are available for the measurement of these parameters, only some of them are suitable for in-situ monitoring. Oxygen sensors are widely used for oceanographic applications and are either electrochemical (Clark electrode) or optical (luminescent sensors). However, in-situ pH measurements are more challenging. For instance, the classical pH glass electrode is not suitable for long-term measurements in high salinity water due to ionic strength induced liquid junction potentials, which result in unstable and inaccurate results [30, 53]. In recent years, Ion Selective Field Effect Transistors (ISFET) based systems have received increasing attention as an alternative to glass electrodes [39, 80, 83, 89]. However, they still face obstacles such as stability of the reference electrode, pressure cross-talk and light cross-talk [39, 83, 89, 183, 184]. Another popular method is spectrophotometric measurements. Here, the pH dependent absorption spectrum of an indicator dye (most commonly m-cresol purple) is measured [92, 93]. These systems offer very high accuracy and precision as well as low drift, and they are used routinely for reference measurements in the laboratory. However, they require reservoirs for the indicator and the waste, as well as appropriate fluidic components such as pumps and valves. Therefore, spectrophotometric systems are comparably bulky and expensive, have dramatically increased power consumption (e.g. 6.5 W [185]) and operate usually with low

sampling rate. Despite these challenges, major advances in recent years made it possible to build autonomous miniaturized spectrophotometric pH sensing systems [63, 100, 101].

A promising alternative to these methods are pH optodes, which have received increasing attention in the last few years [141]. Similarly to spectrophotometric systems, pH optodes require no potentially unstable reference electrode, they are much easier to miniaturize and are more cost-effective compared to ISFET and spectrophotometric devices. Advantageously, they do not require moving parts or reagents.

Several different sensor schemes have been developed to measure carbon dioxide in seawater. A large number of carbon dioxide sensors for oceanography are based on IR-spectroscopy [186–191]. These sensors are based on the diffusion of carbon dioxide through a semi-permeable membrane into an internal gas phase and quantification of the analyte via IR absorption. Such sensor systems deliver precise and high resolution data. However, carbon dioxide sensors based on IR-spectroscopy require high power input (e.g. 0.5-7 W) [188, 192], regular drift corrections and they are typically bulky.

In a wet-chemical approach, the pH change of a solution induced by carbon dioxide, is recorded spectrophotometrically [193–195]. Since carbon dioxide has to diffuse through a membrane and dissolve in the aqueous solution of the indicator, the response times are long ( $t_{63} \geq 2$  min [192]). Other limitations of the spectrophotometric carbon dioxide sensors include membrane deterioration, light source instabilities and battery lifetime [192, 195, 196]. Electrochemical carbon dioxide sensors (which rely on the pH electrode as a transducer) have also been evaluated for oceanographic measurements [68, 197, 198]. However, they suffer the same drawbacks as pH glass electrodes. As for pH measurements, optodes represent a promising alternative for carbon dioxide measurements [104, 192, 199–202].

Optodes usually consist of two main components: a read-out device and a luminescent or colorimetric sensing material. The optodes utilize the analyte-dependent change in the optical properties of this sensing material, most commonly luminescence lifetime (in case of oxygen optodes), fluorescence intensity or absorption/reflectance for other analytes. This change in optical properties is quantified by the read-out device. Optodes enable remote read-out, are easy to miniaturize, have low power consumption (0.5 mW, optode with logger, 30 s measurement interval, presented in this work), and are not influenced by electromagnetic interferences. Due to these advantages, optodes are highly promising for application in numerous fields of science and technology. While O<sub>2</sub> optodes are already widely used in oceanography (e.g. Aanderaa

Data instruments AS, Sea & Sun Technology GmbH, Sea-Bird Scientific), pH and CO<sub>2</sub> optodes are at a lower Technology Readiness level (TRL) level, with a lack of specialized readout devices and dedicated sensing materials limiting more widespread application. Further development will enable reliable and cost-effective measurement of both pH and pCO<sub>2</sub>. Herein, we address this challenge and present a new versatile optode system, which enables autonomous measurements of oxygen, pH, or carbon dioxide in seawater.

## 3.4 Materials and Procedures

### 3.4.1 Optode Sensor System

The optode sensor system (Fig. 3.1) includes two essential components: the read-out device and the sensing material covering the top of the screw-on sensor cap. The read-out device is designed to enable autonomous long-term measurement and includes an internal Li-polymer battery and a logger in addition to the optoelectronic part. A cost-effective polyoxymethylene (POM) pressure housing is used to enable deployments down to 500 m water depth.

### 3.4.2 Read-out Device

The optoelectronic unit of the optode is based on a modified version of the commercially available laboratory and field oxygen meter FireSting GO2 (PyroScience GmbH). The device utilizes a 625 nm LED for excitation, a shortpass excitation filter and a longpass emission filter to eliminate the influence of the excitation light on the photodetector. The optoelectronic unit is essentially a compact phase fluorimeter allowing for modulation of light over a broad range. The luminescence phase shift delivers analytical information for all parameters and is either used directly to calculate the luminescence decay time of the oxygen indicator, or to access the luminescence intensity ratio (indicator/reference) in the case of pH and pCO<sub>2</sub> sensors, according to the so called Dual Lifetime Referencing (DLR [103]) scheme. Modulation frequencies between 2 and 4 kHz are optimal for all the sensing materials used in this work.

The optode is contained in a POM housing with a wall thickness of 15 mm, which enables an operation depth down to 500 m. An optical feedthrough with a fiber thickness of 2 mm and a theoretical pressure resistance to 3000 m is used to connect optical sensing materials. The outer end of the feedthrough is equipped with an M6x0.75 outer thread. This is used to mount the

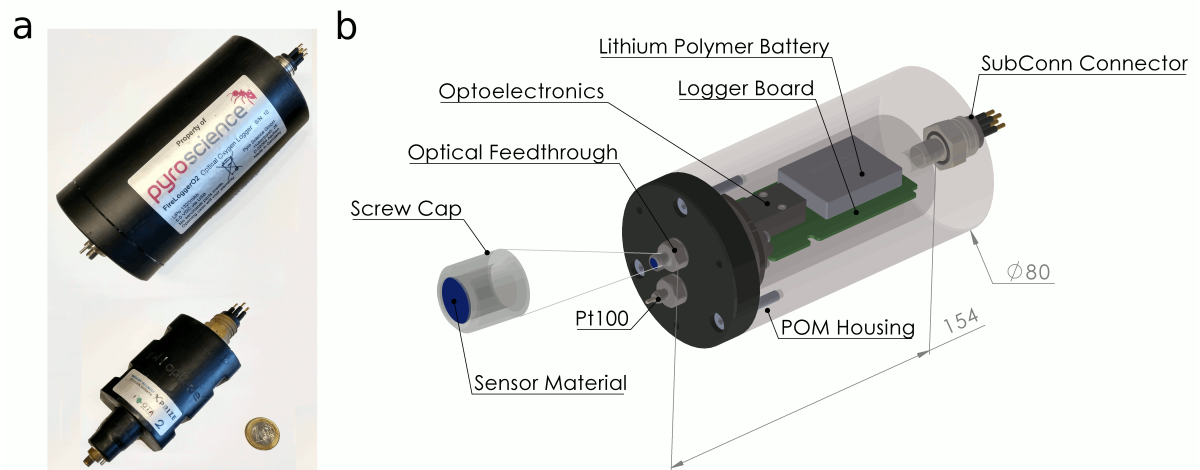


**Figure 3.1:** a: Photographic images of the optodes with a 1 Euro coin for size comparison. Optode in a polyoximethylene (POM) housing for measurements at up to 500 m water depth (upper image) and the optode molded in polyurethane for shallow water measurements (lower image). b: Sketch of the optode in a pressure housing with logic boards, Li-Polymer battery, optical feedthrough, temperature feedthrough, Subconn® connector and screw-able sensor cap.

sensing materials, which are glued onto transparent poly(methyl methacrylate) (PMMA) caps with the respective internal thread.

Another feedthrough is implemented for a Pt-100 resistance thermometer. The temperature data is especially useful for internal temperature compensation of the sensing materials. A 6-pin Subconn® connector is used for power supply and communication. The choice of POM instead of titanium as housing material results in a very cost-effective and lightweight device for shallow water operations. The optode is 154 mm long, has a diameter of 80 mm and weights 970 g in air and 200 g in water. The small size and low weight in water significantly simplifies integration into floats, as only little additional buoyancy is required. The main drawback of the POM housing is the limited operation depth of 500 m. However, this is sufficient for many coastal applications and for example the entire Baltic Sea. In these areas, the low pressure deployment limit is not an issue and the cost-effective build enables more widespread monitoring at constant costs. The estimated hardware costs in the range of 1000 Euro per device. For other applications, e.g. profiling in the open ocean, a conventional titanium housing could be readily designed but with increased manufacturing costs.

Autonomous measurements and long-term deployments are possible due to an internal Li-Polymer battery (1320 mAh) and logger. Due to a highly optimized power consumption of the optode and the logger, this battery capacity is sufficient for approximately 1.4 million single measurement points, which is equivalent to a deployment time of more than one year with a measurement interval of 30 s. The internal logger is able to trigger periodic measurements between 1 s and 1 h and features an internal flash memory with a storage capacity sufficient for approximately 20 million data points. Hence, both battery and storage capacity are more than sufficient for typical servicing periods of buoys and other measurement stations. Device configuration and data readout is performed via USB port using the standard Windows-based software of the device.

A second version of the device was developed for shallow water measurements up to 100 m water depth (Fig. 3.1A (bottom)). In this device, the components of the optode are molded directly in polyurethane. This construction is in principle even more cost-effective as no machined housing is required. A casting mold was prepared from silicone rubber with a stereolithographically 3D printed positive of the device. This resulted in a very compact design and enabled the inclusion of structural features such as grooves for simple and fast mounting.

In this version, a 5-pin SubConn® connector was used, instead of the 6-pin connector used for the device with a pressure housing.

### 3.4.3 Sensor Caps

The sensing materials are mounted with a screw-cap system (Fig. 3.1) on an optical feedthrough. Thereby, the “sensing chemistry” (and hence the analyte of the optode) is easily exchangeable. All three sensing materials are coated onto a transparent and mechanically stable polyester support. The individual spots (5 mm diameter) are stamped out and glued onto the sensing cap. The three sensing materials are selected to enable shared optoelectronics of the read-out device such that no exchange of excitation source or optical filters is necessary. The dyes are excitable with red light and emit in the near infrared part of the spectrum (Fig. 3.2). Since measurement of luminescence intensity is unreliable and is affected by numerous parameters, a referenced readout is used for all the sensing materials. Luminescence phase shift measured by the optoelectronic unit provides the analytical information.

The  $pO_2$  sensing material utilize a platinum(II) benzoporphyrin as an indicator dye immobilized in a polystyrene matrix [203, 204]. The utilized oxygen-sensing material was obtained from PyroScience GmbH. Importantly, this sensing material can be substituted by a trace oxygen sensor also available from PyroScience GmbH or by trace and ultra-trace sensing materials published previously, which rely on benzoporphyrins immobilized in highly gas-permeable, amorphous perfluorinated polymers [105, 204]. Since all these oxygen indicators show long-lived phosphorescence, the emission phase shift  $\phi$  can be directly measured by a phase fluorimeter and converted into the luminescence decay time  $\tau$  according to eq. 3.1:

$$\tau = \frac{\tan(\phi)}{2 \cdot \pi \cdot f} \quad (3.1)$$

where  $f$  is the modulation frequency.

The response of oxygen indicators in solutions of organic solvents is described by the Stern-Volmer equation (eq. 3.2), where  $\tau$  is the luminescence lifetime,  $\tau_0$  is the luminescence lifetime in absence of oxygen,  $K_{SV}$  is the Stern-Volmer constant and  $pO_2$  is the oxygen partial pressure.

$$\frac{\tau_0}{\tau} = 1 + K_{SV} \cdot pO_2 \quad (3.2)$$

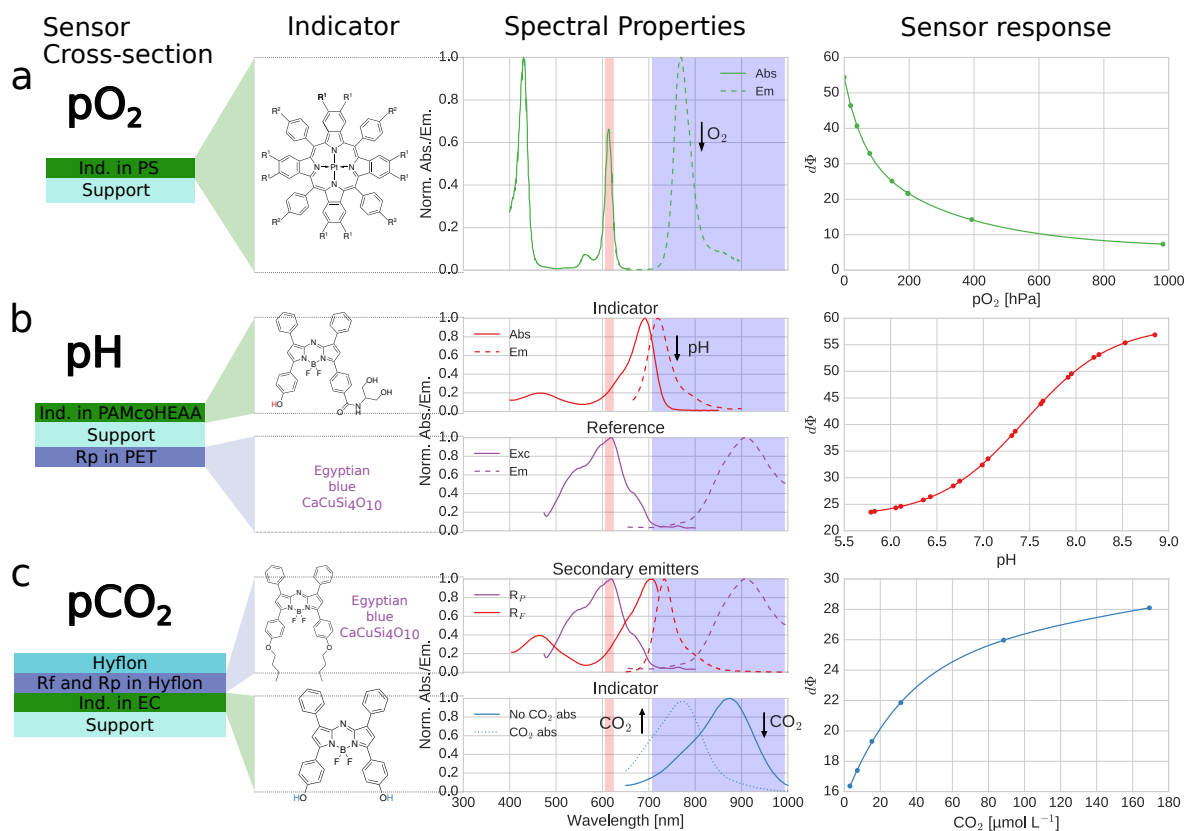


**Figure 3.2:** From left to right: cross-section of the sensing materials; chemical structures of the indicators and the reference materials; absorption/excitation and emission spectra of the utilized dyes and phosphors; examples of calibration curves. The red and blue areas in the spectra indicate the excitation and signal collection wavelengths, respectively. Calibration curves were recorded at 10 °C and at salinity 10. Ind=indicator, PS=polystyrene, PAM-coHEAA=copolymer of acryloylmorpholine and hydroxy ethyl acrylamide, Rf=fluorescent reference (dibutoxy aza-BODIPY), Rp=phosphorescent reference (Egyptian blue), EC=ethyl cellulose

However, the response of polymer-immobilized dyes is not linear in most cases. The so called “two-site-model” postulates the existence of two domains in the polymer characterized by different oxygen permeabilities and thus different Stern-Volmer constants (eq. 3.3) [203]. This equation excellently describes the behavior of the porphyrin indicators immobilized in polystyrene and other matrices.

$$\frac{\tau_0}{\tau} = \frac{1}{\frac{\alpha}{1+K_{SV1} \cdot pO_2} + \frac{1-\alpha}{1+K_{SV2} \cdot pO_2}} \quad (3.3)$$

Where  $K_{SV1}$  and  $K_{SV2}$  are the Stern-Volmer constants for the two different domains and  $\alpha$  is the distribution coefficient.

The pH sensing materials rely on a fluorescent indicator belonging to the aza-BODIPY group. These dyes feature large molar absorption coefficients, good quantum yields and excellent photostability [124, 132]. Most importantly, they are excitable in the red part of the spectrum and emit in the near infrared region, thus being fully compatible with the optoelectronic unit (Fig. 3.2b). The indicator shows strong fluorescence when protonated which is completely quenched upon deprotonation. Although the dynamic range of optical pH sensors is typically limited to  $\pm 1.5$  pH units around the  $pK_a$  value of the indicator dye, this is not critical providing that an indicator adequate for the envisaged application is found. Therefore, the mono-hydroxyphenyl-substituted aza-BODIPY dye was chosen to cover the pH range between 7 and 8.5 required for marine applications.

The sensing materials employed in this work utilize a cross-linked copolymer of 99 % acryloylmorpholine and 1 % hydroxyethyl acrylamide as a proton-permeable hydrogel matrix. The indicator dye was covalently coupled to the matrix polymer, which is cross-linked with the commercially available polyisocyanate crosslinker Desmodur®N75 MPA/X from Covestro AG. The covalent coupling of the dye and crosslinking of the matrix improves the long-term stability of the sensing material by preventing the dye from leaching or migrating into the polymeric support (poly(ethylene terephthalate)). Whereas the material “pH 1” is covalently coupled to the matrix during the cross-linking process, in the second material (“pH 2”) the pH indicator is first coupled to the polymer which is then cross-linked in the following step. The detailed procedures for the preparation of the sensing materials is provided in the Supporting Information.

Since fluorescence is an ambiguous parameter, which is influenced by the intensity of the excitation light, sensitivity of the photodetector, concentration of the indicator, and thickness of the sensing film, a dual lifetime referencing scheme (DLR [103]) is utilized to enable reliable

read-out. For this purpose, an additional layer containing calcium copper silicate (Egyptian blue) is added onto the opposite site of the transparent support. Egyptian blue is an inorganic phosphor which shows excitation and emission spectra matching the optical set-up (Fig. 3.2b) and is inert to  $p\text{O}_2$ , pH and  $p\text{CO}_2$ . It features a long luminescence decay time (107  $\mu\text{s}$  [205]) so that the overall phase shift measured by the phase fluorometer is proportional to the fluorescence amplitude of the indicator ( $A_{ind}$ ) and thus the concentration of its protonated form:

$$\cot(\phi_m) = \cot(\phi_{ref}) + \frac{1}{\sin(\phi_{ref})} \cdot \frac{A_{ind}}{A_{ref}} \quad (3.4)$$

where  $\phi_m$  is the measured overall phase shift, and  $\phi_{ref}$  and  $A_{ref}$  are the phase shift and the amplitude of the reference, respectively (both are constant for a given composition of the sensing material).

The  $p\text{CO}_2$  sensing material has been presented elsewhere [104]. The detailed procedure for the preparation of the  $p\text{CO}_2$  planar sensors is provided in the Supporting Information. It relies on a colorimetric aza-BODIPY indicator showing  $p\text{CO}_2$ -dependent absorption in the NIR part of the spectrum (Fig. 3.2c). The sensing material is of the so called “plastic type“ [206, 207]. The indicator dye is immobilized in ethyl cellulose together with tetraoctylammonium hydroxide as a lipophilic base. This indicator layer is covered by a water and proton impermeable, but highly carbon dioxide-permeable Hyflon AD 60 layer. Hence the indicator dye is in its deprotonated form (dianionic form) at low  $p\text{CO}_2$  and becomes protonated (monoanionic form) at high carbon dioxide partial pressures. An indicator with a high  $pK_a$  value (10.3 for the second deprotonation equilibrium of the dihydroxy aza-BODIPY dye [202]) was chosen to ensure sufficient sensitivity for measurements of atmospheric  $p\text{CO}_2$  levels. Importantly, neither the monoanionic nor the dianionic forms of the dye are fluorescent, but the absorption maximum shifts from 745 nm to 805 nm upon the second deprotonation (Fig. 3.2c) [202]). In order to convert this analytical information into luminescence phase shift, two types of luminescent materials are added into the reference layer to make use of the inner-filter effect. The fluorescence emission of the first phosphor (dibutoxy aza-BODIPY,  $\lambda_{\text{max}}$  733 nm) overlaps with the absorption of the mono-anionic form of the indicator, whereas the emission of the inorganic phosphor (Egyptian blue,  $\lambda_{\text{max}}$  908 nm [202]) shows excellent overlap with the absorption of the dianionic form. Overall phase shift depends on the ratio of both emissions and therefore is the highest at high  $p\text{CO}_2$  (low intensity of fluorescence and high intensity of phosphorescence) and is the lowest

at low pCO<sub>2</sub>. Thus, this scheme enables quantification of pCO<sub>2</sub> via referenced phase shift measurement similar to DLR.

#### 3.4.4 Temperature and Salinity Compensation

As expected, all three sensing materials show cross-sensitivity to temperature. Due to this fact, and because temperature itself is an important parameter in oceanographic measurements, a temperature sensor was incorporated into the device. The response of the pH optodes is also influenced by ionic strength and therefore salinity, albeit to a much lesser extent. This cross-talk is marginal in ocean water but in other environments (brackish water) has to be compensated with help of external salinity data. Salinity data can be obtained via conventional conductivity measurement or using a recently reported sodium optode [180].

#### 3.4.5 Characterization and Calibration of the Optodes

Characterization of the pH sensing materials was conducted by recording temperature and salinity calibrations in artificial seawater [208] with a mixture of buffer substances (all obtained from Carl Roth GmbH & Co KG (carlroth.com)). Details about the buffer composition and measurement procedure can be found in the Supporting information. The set pH values were measured with a glass pH electrode calibrated against spectrophotometric measurements [209] and pH values were calculated according to Liu et al.[95]. The long-term stability test was performed in artificial seawater buffered with 50 mM TRIS. The pH changes were induced via addition of NaOH or HCl. The composition of the solution and the detailed procedures are provided in the Supporting information.

The oxygen optodes were calibrated prior to deployments with air-saturated and oxygen-free water. Air-saturated water was obtained by repeated vigorous shaking of a water bottle. 5% aqueous solution of sodium sulfite with a catalytic amount of cobalt(II) chloride was used to ensure anoxic conditions.

Prior to deployments pH optodes were re-calibrated with two calibration buffers based on TRIS and BIS-TRIS. This re-calibration was conducted to determine the Top and Bottom coefficients of the calibration equation (see below), which are influenced by the indicator-to-reference ratio, and optical setup and may be different between individual sensor spots. The buffers were prepared for the in-field calibration of the pH-optodes based on a recipe for artificial seawater [208]. The recipes can be found in the supporting information.

The pCO<sub>2</sub> optodes were calibrated prior to deployments at three different carbon dioxide levels. A 0.1 M phosphate buffer with a pH of 7.7 (NBS scale, 23°C) and a salinity of 9.4 was prepared and flushed with nitrogen for 2 h to remove dissolved carbon dioxide. Dissolved inorganic carbon (DIC) levels of 751 and 3415 μM were set by addition of an 890 mM sodium bicarbonate solution into this buffer. The corresponding carbon dioxide concentrations were calculated according to the constants determined by Roy et al. [210]. Thereby, the temperature dependence of the phosphate buffer was considered. The response of the optode was measured until a stable signal was reached (> 1.5 h). Additionally, a third calibration point (complete saturation of the optode with carbon dioxide) was recorded using soda water (30 min). After the calibration, the sensor material was kept wet prior to deployment [104].

### 3.4.6 Reference Values

Discrete water samples were taken manually from Niskin bottles at different depths to validate the obtained data for oxygen, pH and carbon dioxide. Two samples (250 mL) were taken at each depth and poisoned with saturated mercury chloride (100 μL) right after sampling. Total alkalinity (TA), DIC and pH were measured for each sample. DIC was measured using a SOMMA system (Single Operator Multi-Parameter Metabolic Analyzer) at 15 °C [208]. TA was obtained by using an open-cell titration at 20 °C [208]. The indicator dye m-cresol-purple was used to measure the pH spectrophotometrically at 25 °C [96]. The CO2SYS program by Lewis and Wallace 1998 [211] was used to calculate the carbon dioxide concentrations (from DIC and pH values) with the constants from [210] and the pH at in-situ conditions in total scale.

## 3.5 Assessment

### 3.5.1 Temperature and Salinity Cross-talk of the pH Optodes

The response of the pH sensing material is influenced by temperature and salinity. Therefore, prior to measurements, the salinity and temperature cross-talk of the sensor was investigated. For the tests in the Baltic Sea, the calibration curves for temperatures between 4 and 15 °C and salinities of 3, 6.5 and 10 PSU were recorded for the material “pH-1”. The sensor material

“pH-2“ was characterized between 0 and 25 °C at salinity 35. The calibration curves (Fig. 3.3a) were fitted with a Boltzmann sigmoid function:

$$\cot \Phi = Bottom + \frac{Top - Bottom}{1 + 10^{\frac{pH - V50}{slope}}} \quad (3.5)$$

where  $\Phi$  is the phase angle, *Bottom* is the lower limit of the calibration curve, *Top* is the upper limit of the calibration curve, *pH* is the pH value and *V50* is the point of inflection, and *slope* describes the *slope* at the point of inflection. The same data points were fitted with additional temperature coefficients for the *V50*, *Top* and *Bottom* coefficients:

$$\cot \Phi = Bottom + B_t \cdot (T - 20) + \frac{Top + T_t \cdot (T - 20) - (Bottom + B_t \cdot (T - 20))}{1 + 10^{\frac{pH - (V50 + V50_t \cdot (T - 20))}{slope}}} \quad (3.6)$$

where  $B_t$ ,  $T_t$  and  $V50_t$  are the additional linear temperature coefficients for the *Bottom*, *Top* and *V50* coefficients, respectively, and  $T$  is the temperature in °C. Equation 3.6 was used for all measurements without salinity compensation. The recorded calibration points were fitted with this equation to obtain *V50*, *slope* and the temperature coefficients. Individual calibrations of the sensor spots were conducted by fitting the *Top* and *Bottom* coefficients after measuring buffers in artificial seawater.

Due to an expected salinity sensitivity at the low salinities of the Baltic Sea the ionic strength dependency of the sensing material pH-1 was characterized between 3 and 10 PSU (Figure 3.3b). For every tested salinity, temperature calibrations at 4, 6, 8, 10, 12 and 15 °C were recorded (18 calibration curves total, Figure 3.3). A small cross-talk is evident for a ca. 3-fold salinity increase. To compensate for this cross-talk, additional coefficients for *V50* and *B* were introduced (eq. 3.7) and simultaneous fitting of all recorded data points (4-15 °C; 3, 6.5, 10 PSU) was performed.

$$\cot \Phi = Bottom + B_t \cdot (T - 20) + B_S \cdot (S - 35) + \frac{Top + T_t \cdot (T - 20) - (Bottom + B_t \cdot (T - 20) + B_S \cdot (S - 35))}{1 + 10^{\frac{pH - (V50 + V50_t \cdot (T - 20) + V50_S \cdot (S - 35))}{slope}}} \quad (3.7)$$

where  $B_S$  and  $V50_S$  are linear salinity coefficients for the *Bottom* and *V50* parameters and  $S$  is the salinity in PSU. This calibration curve has 3 independent parameters and can therefore not be plotted. In contrast to the conditions in the Baltic Sea, the salinity of ocean water is

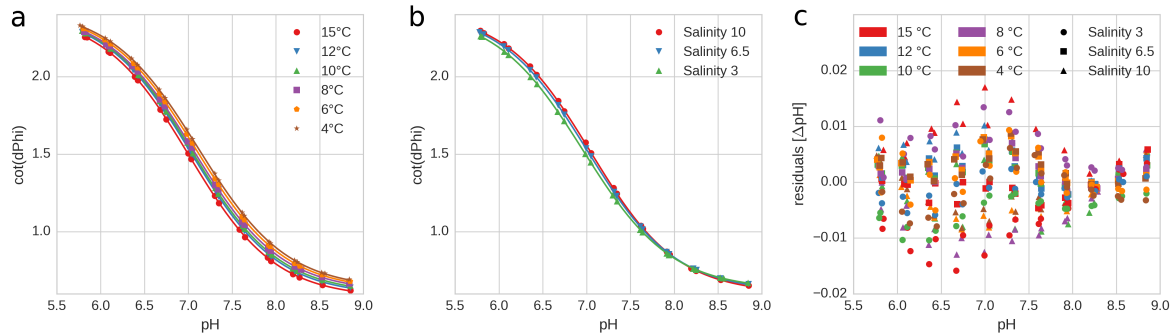


**Figure 3.3:** Temperature and salinity calibration of the pH sensing material pH-1. a: Calibration curves at salinity 10 for temperatures between 4 and 15 °C, fitted with a Boltzmann sigmoid; b: Calibration at salinities 3, 6.5 and 10 at constant temperature of 10 °C, c: Residuals of the fit-function with coefficients for temperature and salinity; the same calibration curves fitted with temperature coefficients for V50, Top and Bottom.

nearly constant ( $\approx 35$  PSU) and the minor variations do not affect the response of the sensor, and therefore, no compensation for these fluctuations is required. The residuals of the calibration of sensing material "pH-2" were equal to that of "pH-1" presented in Figure 3.3.

### 3.5.2 Stability Test of the pH and Oxygen Sensor Materials

Figure 3.4 depicts a simulated long term deployment ( $> 40$  days) in artificial seawater conducted for the pH and oxygen sensing materials. The experimental details can be found in the supporting information. The long term stability of the carbon dioxide sensor was already assessed elsewhere [104] in a similar experiment over 35 days. Thereby, no indication of sensor poisoning or drift was found. The oxygen sensors were tested over 48 days and the pH sensors over 42 days at approximately 24 °C. The sensors recorded one measurement point every 30 seconds, which corresponds to approximately 120 000 and 140 000 measurement points for the pH and oxygen sensor materials, respectively. The pH value was changed by addition of 250 mL 0.72 M hydrochloric acid on day 8, 21, 22, 23 and the addition of 40 mL NaOH on day 10 and 10 mL on the days 41, 42, 43. The spectrophotometric pH measurements were always conducted at 23 °C and converted to in situ conditions with a TRIS temperature coefficient of  $-0.0313/\text{K}$  at salinity 35 [212]. The measured  $\text{pO}_2$  values were converted with the oxygen solubility constants determined by Garcia et al. [213].

During most deployments lower temperatures and longer sampling intervals and hence lower stress on the materials can be expected. At these rather high temperatures, we observed a drift of the sensor signal (approximately 0.003 pH units / day) indicating that a drift correction was necessary for long-term measurements. The drift of the sensor materials is predictable and characterized by a decrease in maximum fluorescence intensity, which results in a decrease of the Top coefficient and hence a reduction in sensor dynamics (Top – Bottom). Therefore, it was possible to determine the drift constant and correct the sensor readings (Supporting information). However, the drift constant is temperature dependent and much lower at lower temperatures. At 10 °C the drift constant was determined as 0 and therefore no drift correction was applied to the measurements during the field trips. It is evident that after the performed correction, the pH sensors show stable performance over 1.5 months of continuous operation, and the calculated pH values correlate well to the values obtained in the reference spectrophotometric measurement (Figure 3.4). The readings provided by the 5 pH sensors match very well (correlation coefficients > 0.9987). The precision of the pH sensor was excellent with average standard deviations of 0.0023 and 0.0019 pH units for pH  $\approx$ 8.02, and  $\approx$ 8.55, respectively. The standard deviations were determined over periods with nearly constant pH and temperature (day 11 to 13 for pH  $\approx$ 8.55 and day 25 to 32 for pH  $\approx$ 8.02). The pH drift of the buffer due to uptake of carbon dioxide was compensated linearly for these calculations and the minor fluctuations of pH of the TRIS-buffer due to temperature changes were compensated according to literature [212]. The accuracy of the sensors can be estimated by their average absolute deviation from the reference values which was 0.020 pH units. The oxygen sensor materials required no drift compensation and fit well to the recorded reference points throughout the experiment with an average absolute deviation of 0.25 mg/L. Furthermore, they showed good correlation between each other with correlation coefficients above 0.974.

This stability test demonstrates that the sensing materials can be used for deployments of at least 1.5 months and more than 100 000 single measurement points can be recorded. However, in real world applications long deployments may require protection against biofouling. This issue was not the aim of the current work since only short term deployments were envisaged, but it has to be addressed in future to broaden the application range of the sensors.

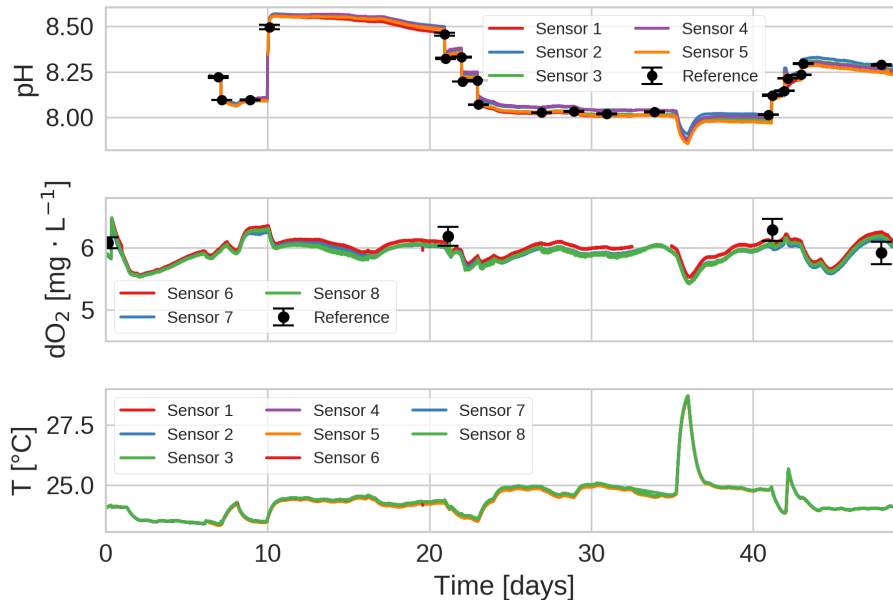


**Figure 3.4:** Stability measurement of the pH and  $pO_2$  sensor materials. Sensors 1 to 5 are pH sensors based on the material pH-2; sensors 6-8 are oxygen sensors. Changes in pH were induced by addition of either a 0.72 M hydrochloric acid or a 40,% sodium hydroxide solution. The sharp increase of dissolved oxygen on day 1 is due to bubbling of pressurized air through the buffer for 1 hour. Reference values were obtained by sampling and spectrophotometric pH measurements and Winkler titration for pH and oxygen, respectively. The temperature spike on day 35 was induced by the waste heat of a nearby device. The missing data of sensor 6 was caused by an unexpected restart of a computer used for data logging.

### 3.5.3 Application of the Optode System for Profiling in the Baltic Sea

An application of the optode system was demonstrated during a research cruise in the Baltic Sea in October 2015. Overall 12 devices were deployed. The number of deployed oxygen, pH, and carbon dioxide optodes was varied throughout the field trip.

During the cruise overall 12 profiles with multiple optodes and analytes to a maximum depth of 230 m were recorded. Examples of the measured depths profiles are displayed in Figure 3.5. Oxygen, pH and carbon dioxide optodes were deployed simultaneously for this measurement. Since the carbon dioxide dynamics is large and the response of the carbon dioxide sensors is slow ( $t_{90} > 1$  h) at temperatures below 15 °C, stops were made during the downcast to allow for complete equilibration of the carbon dioxide sensors. During these stops, samples for reference measurements were taken. Unfortunately, no reference values for dissolved oxygen (DO) could be obtained due to a failure of the oxygen sensor of the CTD-probe. As can be seen, concentration of dissolved oxygen (DO) strongly decreases below 50 m. Although the concentration approaches 0 below the halocline, at around 70 m water depth, a significant increase to about 50  $\mu$ M is visible between 150 and 220 m. This effect can be explained by a strong inflow of oxygen rich saltwater from the North Sea in December 2014 [214, 215].

The pH profile mirrors that of oxygen demonstrating a strong pH decrease (1 pH unit) at the depth below 70 m. This is expected because microbial respiration consumes oxygen and produces carbon dioxide which results in a decrease of pH. Again, a slight increase of pH of around 0.05 pH units is clearly visible between 150 and 220 m. The profiles obtained by the pH optode are in good agreement with the reference values with an average absolute difference between the optode and the spectrophotometric reference measurements of 0.033 pH units over all 10 recorded profiles. On average the optode recorded 0.013 pH units higher values than the spectrophotometric reference. This deviation is probably due to calibration errors in the low salinity environment of the Baltic Sea. The obtained profile for carbon dioxide shows a trend consistent to the other two optodes. However, between 70 and 100 m the profile is distorted due to the long response time of the carbon dioxide optode ( $t_{90}$  approximately 1 h) and very large changes in the carbon dioxide concentration (15 to 200  $\mu$ M). Nevertheless, after equilibration of the sensor at the depth of 100 m (1 h stop), the reading obtained by the optode matches very well with the reference data. Again, the concentration of carbon dioxide was nearly constant below 70 m. A ca. 10-fold increase of the carbon dioxide concentration between the surface

water and the depth of 100 m correlates very well with the pH decrease of about 1 pH unit. It should be noted that this profile was presented by [104] without the corresponding pH and O<sub>2</sub> data. Compared to the previous presentation of the carbon dioxide data, additional corrections have been made: (i) temperature influence on the calibration buffers was accounted for and (ii) the pH of the buffers was converted to total scale to be compatible with the coefficients reported by Roy et al. [210].

Overall similar trends are visible from all three sensing materials. The average pH deviation between the optode and the reference measurements for the cast depicted in Figure 3.5 was 0.051 pH units and the average deviation in carbon dioxide concentration was 12 µM. These measurements demonstrate that this novel optode system is capable of a simultaneous measurement of all parameters required to fully characterize the carbonate system.

#### **3.5.4 Continuous Surface Water pH Measurements**

Throughout the same field survey in the Baltic Sea, a FerryBox system (equipped with a seawater pump and a pH optode) was used for continuous pH measurements of the surface water for 7 days. Spectrophotometric reference points for these measurements were obtained from samples taken from the mixed water column during the profiles. The breaks in the measurement on 21<sup>st</sup>, 23<sup>rd</sup> / 24<sup>th</sup> and 26<sup>th</sup> of October are due to shutdowns of the system during stops in harbors. During the stop on October 24<sup>th</sup> the pH sensor was recalibrated. As can be seen in Figure 3.6, the data for the surface pH obtained with the optode are in good agreement with the reference points. The average absolute deviation from the reference measurements was 0.019 pH units.

#### **3.5.5 Simultaneous Monitoring of Oxygen and pH in Kiel Harbor**

During a field-survey in Kiel, Germany, oxygen and pH optodes were deployed in combination over the course of 5 days. Throughout the deployment, pH reference values were obtained by spectrophotometric measurements of discrete water samples.

The system dynamics measured by the oxygen and pH optodes shows good correlation (Figure 3.7). High oxygen concentration corresponds to high pH values and a Pearson correlation coefficient of 0.54 is obtained between the two variables. This is likely due to photosynthetic activity of algae in the water masses. High photosynthetic activity results in an increase in oxygen concentration and, due to the consumption of carbon dioxide, in high pH values. This

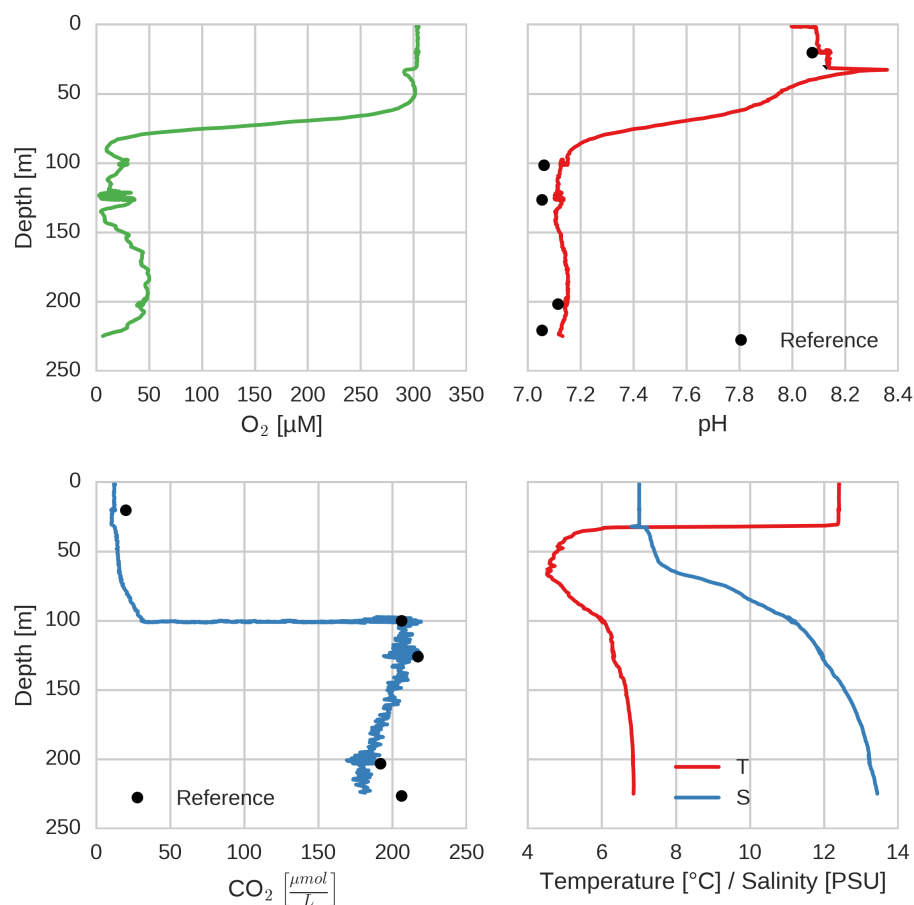


**Figure 3.5:** Profiles recorded at the Gotland deep monitoring station BY15 (station 5 in Figure 5a, GPS: 57.32041, 20.05197), 5 stops at 20 m (1 h 30 min), 100 m (1 h), 12 m (1 h), 200 m (1 h 50 min) and 230 m (45 min) water depth to allow equilibration of the carbon dioxide sensor. The CTD was lowered with a speed of 0.15 m/s. Reference values were obtained by DIC and spectrophotometric pH measurements from samples. The pH spike at  $\approx 30$  m is an artifact caused by the different response times of the pH sensor material and the temperature sensor used for correction of the temperature cross-talk.

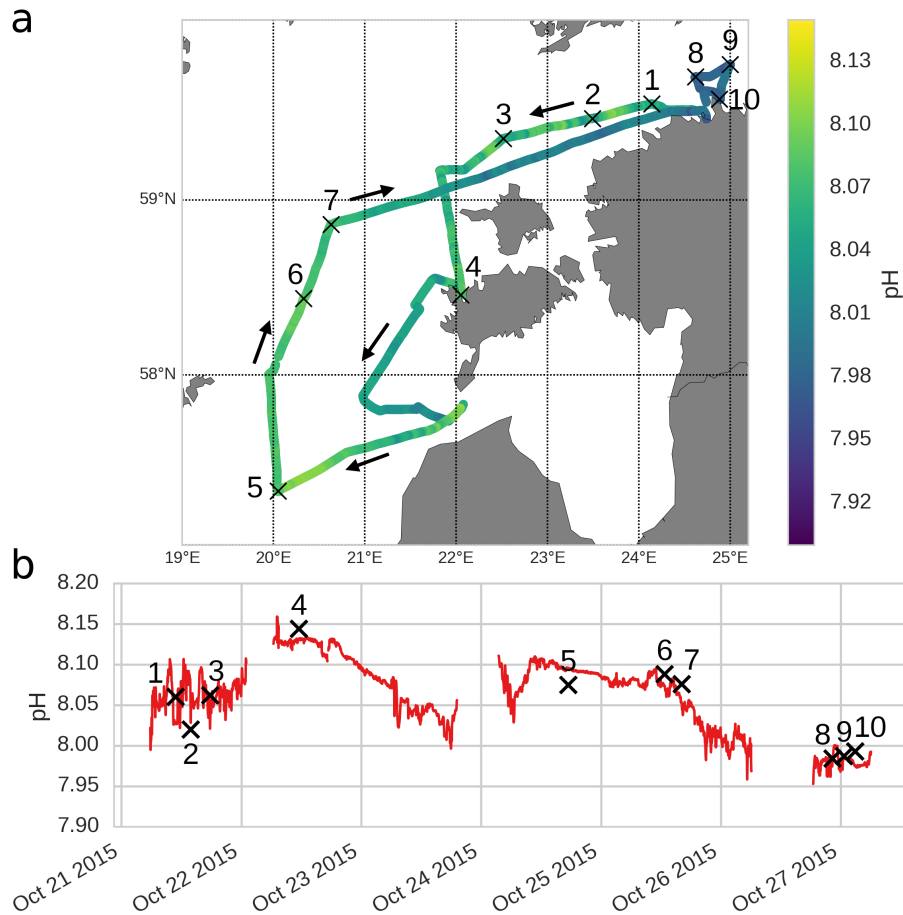


**Figure 3.6:** Continuous measurement of the surface pH during the cruise in the Baltic Sea. pH values are color coded in the upper part of the figure (a) and plotted against time in the lower part of the figure (b). Reference values (1-10) were obtained from samples of the mixed upper water layer during profiling. During stops in harbors the measurements were interrupted resulting in the breaks in the time series. The sensor was calibrated at the start of the measurement and recalibrated on the 24<sup>th</sup> of October.

correlation is visible in the daily fluctuations. Smaller fluctuations are likely to be due to the movement of water masses with the waves in the harbor [216]. Since both optodes were not positioned at the same depth, the smaller changes in concentration of DO and pH are not always identical. The average deviation from the reference values was 0.043 pH units without the outlier on September 15<sup>th</sup>. The pH optode was calibrated before and after the deployment, whereby the post calibration, which was used for the evaluation of the data, resulted in pH values which are on average 0.035 pH units higher.

This somewhat larger difference compared to the open sea measurements presented above can presumably be attributed to the higher small-scale heterogeneity of coastal seawater carbonate chemistry. The outlier on September 15<sup>th</sup> is probably due to incomplete mixing of the water layers during the sharp increase in pH. During the field survey in Kiel several other sensors developed in the SenseOcean project were deployed alongside a pontoon and the water samples were collected approximately 10 m from the optodes.

Figure 3.8 shows the results of a similar experiment in Kiel harbor in which all the three optodes (pH,  $pO_2$ , and  $pCO_2$ ) were positioned in exactly the same depth in the close proximity to each other ( $< 50$  cm). It is evident that all the optodes show good correlation over the period of 3 days. Pearson correlation coefficient of 0.945 and -0.8 are obtained between pH and DO, and pH and dissolved carbon dioxide, respectively. Moreover, the  $pO_2$  and the pH optodes, which are much faster than the  $pCO_2$  optode, resolve exceptionally well the minor changes of parameters. In fact, every fluctuation in the concentration of DO is also registered by the pH optode. Even fluctuations faster than 1 minute and smaller than 0.01 pH units and 3  $\mu$ M DO are clearly visible. This demonstrates the advantages of the new optode system which is suitable for continuous monitoring of the important parameters with time resolution better than 5 minutes and is capable of resolving even minor fluctuations of these parameters ( $< 0.005$  pH units). Some of the finer scale dynamic changes were still registered by the  $pCO_2$  optode but most of the peaks were “smoothed” due to longer response time of more than 1 hour. The long response time also complicates the calibration of the  $pCO_2$  optode and increases the error since the sensor may not reach the full equilibration during the calibration. Nevertheless, although the  $pCO_2$  optode is currently unable to compete with the  $pO_2$  and pH optodes in terms of response time, we are optimistic that significant improvements to the sensor chemistry can be made in future.

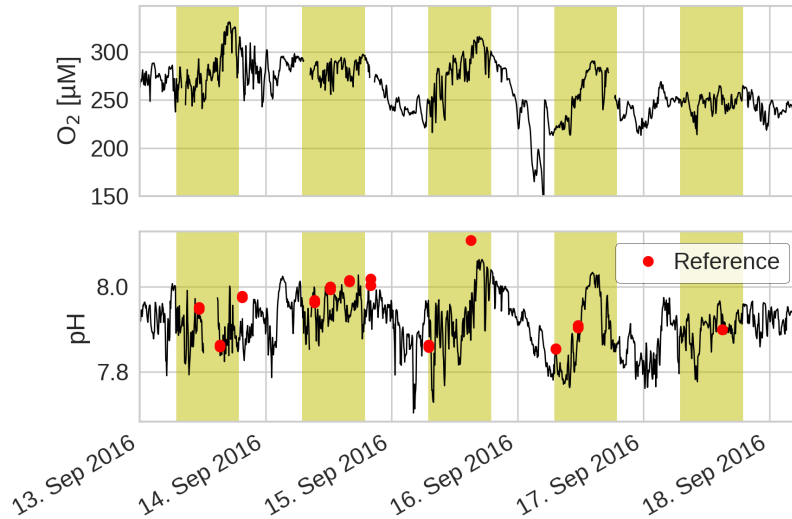


**Figure 3.7:** Simultaneous measurement of pH and  $O_2$  with two optodes in the harbour of Kiel in 2-4 m water depth (GPS: 54.330168, 10.149846). The pH reference values were recorded spectrophotometrically on discrete water samples. The yellow areas indicate the time between sunrise and sunset.

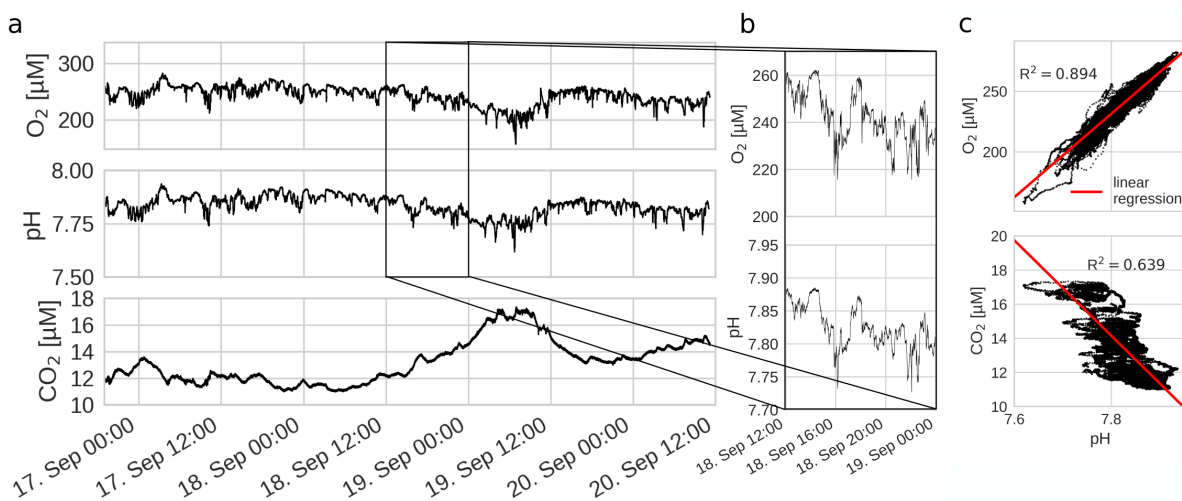


**Figure 3.8:** (a) Simultaneous measurement of pH, dissolved oxygen, and carbon dioxide with an array of three optodes in the harbor of Kiel (GPS: 54.330168, 10.149846) in approximately 2 m water depth. (b) The insert shows the fast fluctuations resolved by the pH and oxygen optodes. (c) correlation plots between pH and DO/carbon dioxide.

Simultaneous monitoring of pH, dissolved oxygen and carbon dioxide in Southampton harbor During the field-survey to Southampton, England, optodes with O<sub>2</sub>, pH, and pCO<sub>2</sub> sensing materials were used for continuous measurement within 1 week (Figure 3.9). The oxygen sensor shows periodic fluctuations of the oxygen concentration ( $\approx 5 \mu\text{M}$ ). Interestingly, a slow decrease of the oxygen saturation (287 to 280  $\mu\text{M}$ ) is visible during the field work. The pH sensors show very similar short term results. Periodic fluctuations of approximately 0.04 pH-units are visible and synchronized to the DO fluctuations. Overall, a slight increase of pH (ca. 0.05 pH units) is visible during the field trip. The pCO<sub>2</sub> sensor displays again very similar fluctuations and a slight decrease of the carbon dioxide concentration (ca. 1  $\mu\text{M}$ ) towards the end of the experiment. The temperature sensor displays values between 9.5 and 8.8 °C and most of the temperature changes are very slow. As can be seen in Figure 3.9, the data acquired for the three parameters correlate well. Pearson correlation coefficient of 0.822 and -0.901 are obtained between pH and DO, and pH and dissolved carbon dioxide on the 15<sup>th</sup> of December, respectively. This day was chosen because no artifacts influenced the measurements. In fact, every decrease in oxygen concentration is mirrored by a decrease in pH and an increase in pCO<sub>2</sub>. Even very small fluctuations are often visible on all three traces, whereby high pO<sub>2</sub> and pH and low pCO<sub>2</sub> indicate water masses with weak photosynthetic activity and vice versa.

Besides the short term fluctuations, the 5-day profiles recorded by the sensors are very interesting. All three sensors display a reduction of the amplitude of the periodic fluctuations over the course of the measurement. Furthermore, there is a weak decrease in DO ( $\approx 5 \mu\text{M}$ ) and dissolved carbon dioxide ( $\approx 2 \mu\text{M}$ ) visible with a slight increase in pH ( $\approx 0.05$  pH units). While this might be due to sensor drift, it is noted that all three sensing materials display a similar trend. Comparison of the acquired data with the tidal range over the course of the measurement (4.12 m on December 15<sup>th</sup> and 2.82 m on December 20<sup>th</sup>) suggests that the reductions in amplitude are probably due to a reduction in water exchange. This reduced exchange of Southampton water could as well influence the mean values of pO<sub>2</sub>, pH and pCO<sub>2</sub>. It is also evident, that the changes in the parameters within 1-day cycle correlate well with the periods of low and high tide. As can be seen in Figure 3.9, shortly before every low tide maxima of DO and pH and minima of carbon dioxide were visible.

Another demonstration of the sensor system was conducted in a seagrass field in Aggersund, Denmark during a 4-day deployment (Supporting Information, Figure S3.1). Pronounced day/night fluctuations of the local oxygen saturation were observed. The concentration of

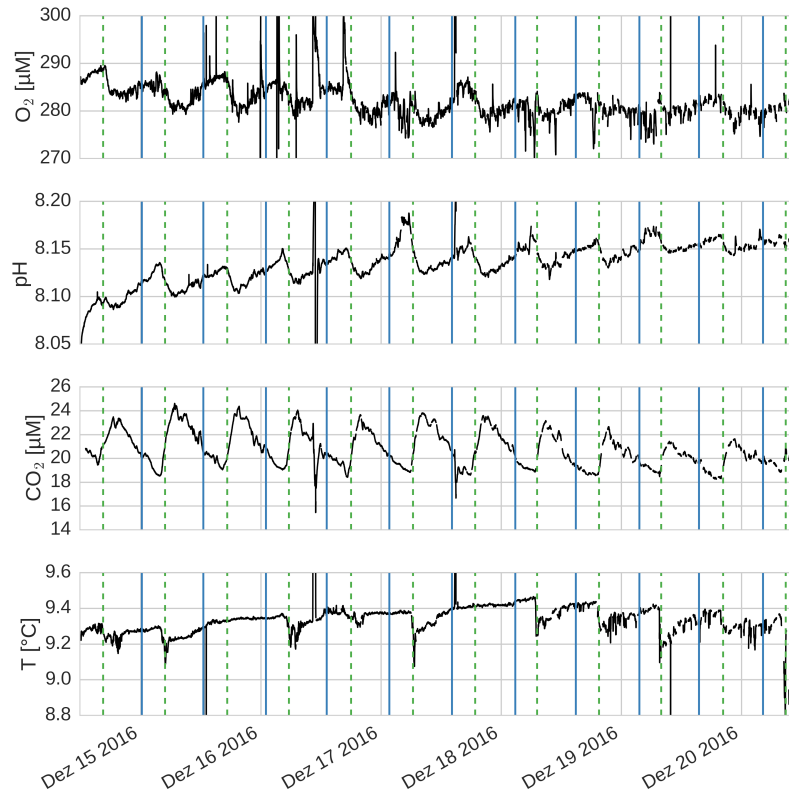


**Figure 3.9:** Simultaneous measurement of pH, dissolved oxygen and carbon dioxide with the optode system over 6 days on a pier in Southampton ( $\approx 3$  m water depth). The vertical solid blue lines and the dashed green lines indicate times of high and low tide, respectively. The artefacts on December 16<sup>th</sup> were caused by a short removal of the sensors. The displayed temperature data was recorded by the temperature sensor integrated into the oxygen optode.

dissolved oxygen reached values as high as 500  $\mu\text{M}$  which corresponds to 250 % of air saturation during the day whereas the conditions are nearly anoxic at night. More detail on this experiment can be found in the Supporting information.

### 3.6 Conclusions

In conclusion, a small and cost-effective optode system for measurement of three important oceanographic parameters is presented. The very energy efficient read-out device (1.4 million measurement points when fully charged) enables deployments over 1 year potentially without any service and the small and light design simplifies the integration of the optode in many already existing set-ups. Although the long term stability of the sensing materials for such long deployment periods has not been accessed yet, the laboratory trials (comparably high temperature of 24 °C, over 100 000 measurement points) demonstrated stable performance of the sensors for over 1 month of continuous operation. These results suggest that the sensing materials can operate reliably over significantly longer timescale, but other issues such as biofouling are likely to be more critical for long-term deployment and should be addressed in future.

Importantly, the flexible design of the optode system enables fast exchange of the analyte of interest or the dynamic range (e.g. normal range or trace oxygen sensor) via a screw-able sensor cap. This is achieved by using a shared opto-electronic unit and selecting a set of “sensing chemistries” with optical properties matching the opto-electronic components of the read-out device. This approach greatly facilitates adaption of the sensor setup on-site. The sensor system has been applied successfully in several field trips and the results show good correlation between all measured parameters and clearly demonstrate the advantages of the new optode system for continuous monitoring of pH, dissolved oxygen and carbon dioxide. Whereas the pH and oxygen optode deliver excellent time resolution with response times ( $t_{90}$ ) below 1 minute (without optical isolation) and resolve minor fluctuations of these parameters, the  $p\text{CO}_2$  optode “smoothes” the dynamics due to slower response time. While the accuracy and precision of the pH and carbon dioxide optodes is not yet good enough for ocean acidification studies without additional reference measurements, the optode system is likely to be very useful especially for measurements requiring high spatial or temporal resolution. It can greatly simplify and reduce the costs of alternating measurements of pH,  $O_2$  and carbon dioxide as only one type of device

with estimated hardware costs of around 1000 Euro is necessary. Therefore, the sensor system already now offers vast possibilities for oceanographic applications and can be extended in future for sensing of other parameters (e.g. ions) providing that the new “sensing chemistries” matching the optoelectronic set-up of the read-out device are developed.

## Acknowledgments

Financial support from is gratefully acknowledged from the European Commission Seventh Framework Programme SenseOcean (grant agreement No. 614141). JDM received funding from the EU BONUS project PINBAL through Grant No. 03F0689A.

## 3.7 Supporting Information

### 3.7.1 Preparation of the pH Sensing Films

The indicator dyes were synthesized according to literature procedures [124, 132]. The pH sensing material “pH-1” used for the field trips to the Baltic Sea was prepared by dissolving 0.25 % aza-BODIPY indicator dye in a solution of 5 % polyacryloylmorpholine-co-hydroxyethylacrylamide (99 % acryloylmorpholine, 1 % hydroxyethylacrylamide) in a mixture of 20 % dimethylsulfoxide and 80 % tetrahydrofuran (THF). This solution was transferred into a glove box under nitrogen atmosphere and 4  $\mu$ L Desmodur N75 MPA/X crosslinker and 4  $\mu$ L of a 10 % stock solution of dibutyltindilaureate in THF as catalyst were added. This “cocktail” was knife coated 3 times with a 76  $\mu$ m spacer on a 125  $\mu$ m poly(ethylene terephthalate) support and cross-linked for 2 hours at 50 °C. This resulted in a film thickness of approximately 18  $\mu$ m.

The pH sensing material “pH-2” was further improved in regard to its dynamic range by optimizing its pK<sub>a</sub> and was used for the deployments in Kiel and Southampton. It was prepared by coupling BCl<sub>3</sub>-activated acetyl-protected BF<sub>2</sub> chelate of [5-(4-hydroxyphenyl)-3-phenyl-1H-pyrrol-2-yl]-[5-(4-butoxyphenyl)-3-phenylpyrrol-2-ylidene]amine [124] to the polyacryloylmorpholine-co-hydroxyethylacrylamide polymer. 50 mg of this polymer were dissolved in 50  $\mu$ L DMSO and 400  $\mu$ L THF. Then 1.5  $\mu$ L Desmodur N75 MPA/X crosslinker and 1.5  $\mu$ L of a 10 % stock solution of dibutyltindilaureate in THF as catalyst were added. This “cocktail” was knife coated with a 76  $\mu$ m spacer on a 125  $\mu$ m poly(ethylene terephthalate) support and cross-linked for 1.5 hours at 60 °C. This corresponds to a dry film thickness of approximately 8  $\mu$ m. To facilitate measurements in direct sunlight an optical isolation was introduced by knife-coating 50 % diamond powder and 50 % carbon black in 15 % polyHEMA in ethanol/water 95/5 with a wet layer thickness of 25  $\mu$ m. This corresponds to a film thicknesses of 8  $\mu$ m for both layers and an overall film thickness of 24  $\mu$ m. The reference layers were prepared by dispersing 42 and 20 mg Egyptian blue for “pH-1” and “pH-2”, respectively in 1 mL of a 15 % solution of poly(ethylene terephthalate) in 35 v% hexafluoroisopropanol and 65 v% chloroform. These dispersions were knife coated with a 76  $\mu$ m spacer on the backside of the sensor supports.

For both sensing materials, the protecting group of the pH sensitive functionality was cleaved by submerging the sensor foils in 0.01 M sodium hydroxide solution for 30 minutes. The 5 mm circles were stamped out of the sensing film and glued with an epoxy glue onto the sensing caps with the pH-sensitive layer facing outside.

### 3.7.2 Preparation of the pCO<sub>2</sub> Sensing Films

The pCO<sub>2</sub> sensing material was prepared by dissolving 100 mg ethyl cellulose (49 % ethoxyl content), 1 mg di-hydroxy-aza-BODIPY (1 % w/w with respect to the polymer) in 1 g toluene and 670 mg ethanol. The resulting “cocktail” was flushed with carbon dioxide and 100  $\mu$ L of tetraoctylammonium hydroxide (20 % w/w TOAOH in methanol) were added. The “cocktail” was pipetted on a roughened, pre-cut (spots with 5 mm diameter) dust-free poly(ethylene naphthalate) (PEN) support. Then, 0.75  $\mu$ L of the “cocktail” were pipetted resulting in a sensing film spot of  $\approx$  2 mm diameter and  $\approx$ 14  $\mu$ m thickness. The second layer containing the secondary emitters was made of a “cocktail” consisting of 1 g of a Hyflon AD 60 solution (5 % w/w in perfluorodecalin, washed with K<sub>2</sub>CO<sub>3</sub> prior to use), 25 mg silanized Egyptian blue particles (produced analogously to the literature procedure [135] but using 1H,1H,2H,2H-perfluorooctyldimethylchlorosilane instead of trimethylchlorosilane) and 25 mg stained PS-particles (prepared according to literature [202]) homogeneously dispersed in the polymer solution. 0.75  $\mu$ L of the secondary emitter “cocktail” were pipetted on the sensing film (thickness  $\approx$ 6  $\mu$ m). Finally, the protective layer was prepared by knife-coating a 4 % w/w solution of Hyflon AD 60 in washed perfluorodecalin over the spots with a 76  $\mu$ m spacer.

### 3.7.3 Buffers for pH Sensor Characterization

For the deployment in the Baltic Sea a buffer composed of 20 mM of TRIS (tris(hydroxymethyl)aminomethane) and 20 mM of BIS-TRIS (bis(2-hydroxyethyl)amino-tris(hydroxymethyl)-methane) was used. The buffers were prepared for salinity 10 and diluted to the salinities 6.5 and 3 for measurements at lower ionic strengths. pH values between 6 and 9 in steps of 0.3 were set by automated addition of hydrochloric acid and sodium hydroxide with the same concentrations (420 mM, 167 mM and 124 mM for salinity 10, 6.5 and 3, respectively).

For all other deployments of pH sensors the sensing materials were characterized in artificial seawater at salinity 35 with 10 mM each of MES (2-(N-morpholino)ethanesulfonic acid), MOPS (3-(N-morpholino)propanesulfonic acid, TRIS and CHES (N-cyclohexyl-2-aminoethanesulfonic acid), respectively. pH values between 5 and 9.8 were set by addition of 1.4 M hydrochloric acid and 1.4 M sodium hydroxide in steps of 0.3 pH units. Temperatures between 25 and 0 °C were set in steps of 2.5 °C. Due to the negligible salinity sensitivity at high salinities no salinity

calibration was conducted. To detect potential hysteresis all calibration-curves were recorded in both directions. Importantly no hysteresis was observed for the sensing materials.

### 3.7.4 Buffers for pH Sensor Calibration

The buffers were prepared for the in-field calibration of the pH-optodes based on a recipe for artificial seawater [208]. The expected salinity in the Baltic Sea was around 3 – 10, the recipe was adapted to a salinity of 5 and the buffer capacity was reduced to 20 mM. For the deployment in Kiel the buffers were adjusted to salinity 20 with 80 mM buffer capacity. For all other deployments artificial seawater with salinity 35 and 80 mM buffer capacity was used. TRIS/TRIS\*HCl in a ratio of 1 / 3 and BIS-TRIS/BIS-TRIS\*HCl in a ratio of 3 / 1 were selected as buffer components.

The TRIS-buffer was prepared by dissolving 3.633 g sodium chloride, 0.2254 g potassium chloride, 0.1489 g magnesium chloride, 0.4515 g calcium chloride dihydrate, 1.188 sodium sulfate and 9.6912 g TRIS in 60 mL 1 M hydrochloric acid and 1940 g deionized water (Milli-Q, Millipore). The BIS-TRIS-buffer was prepared by dissolving 5.971 g sodium chloride, 0.2254 g potassium chloride, 0.1489 g magnesium chloride, 0.4515 g calcium chloride dihydrate, 1.188 sodium sulfate and 9.6912 g BIS-TRIS in a mixture of 20 mL 1 M hydrochloric acid and 1980 g deionized water (Milli-Q, Millipore).

Calibration buffers for other deployments were prepared in the same way but with 20 and 35 PSU for the deployment in Kiel and Southampton, respectively. The exact pH and temperature dependence of the calibration buffers was measured spectrophotometrically with m-cresol purple at temperatures between 3 and 15 °C. The equation from Liu et al. [95] was used for the calculation of the pH on the total scale.

### 3.7.5 Experimental Details of the Stability Experiment

A 50 L tank of artificial seawater was prepared based on a recipe from Dickson et al. [208]. The recipe was adapted by using a 50 mM TRIS concentration and addition of 100 ppm sodium azide to prevent biofouling. The components of the buffer were: 1.176 kg sodium chloride, 39.5 g potassium chloride, 260.6 g magnesium chloride, 79 g calcium chloride dihydrate 208 g sodium sulfate, 303 g TRIS, 100 mL 37 % hydrochloric acid, 5 g sodium azide and 50 kg distilled water. Throughout the experiment the buffer was mixed with a P300-i pump from Heissner ([www.heissner.de](http://www.heissner.de)) with a throughput of 300 L/h. Reference values for oxygen were obtained by

Winkler titration and for pH using spectrophotometric measurements with m-cresol purple. The pH samples were each measured spectrophotometrically three times at 23 °C and evaluated with the equation from Liu et al. [95]. The Winkler titrations were conducted three times with bottles of approximately 270 mL volume and a 0.01 M sodium thiosulfate solution which was titrated against potassium iodate.

### Sensor Calibration

The pH sensors were deployed one week after the oxygen sensors and calibrated against the first two pH reference points on day 8 of the experiment.

The oxygen sensors were calibrated with an oxygen-free solution of sodium hydrogen sulfite (2% wt. with traces of cobalt chloride as catalyst) and air saturated water. The temperature sensors of the 8 devices (5 for pH, 3 for O<sub>2</sub>) were calibrated with the thermometer GMH 3750 from GHM Messtechnik GmbH ([www.greisinger.de](http://www.greisinger.de)).

### Drift Compensation

A linear drift compensation was applied which assumes a reduction of sensor dynamics (*Top* – *Bottom*) of  $6.09 \cdot 10^{-8}$  per second. For the correction, the *Bottom* coefficient was assumed constant and the *Top* coefficient was adjusted. The *Bottom* coefficient is more stable than the *Top* coefficient because it depends only on the luminescence lifetime of the reference material while the *Top* coefficient also depends on the ratio between indicator and reference. This drift constant was determined with a separate stability experiment, using the same setup as was used for the temperature and salinity calibrations of the sensor materials. Thereby calibrations between pH 6 and 8.3 with 13 equidistant pH steps were recorded, daily. The measurement was conducted over 18 days at salinity 35 and the same buffer composition and hydrochloric acid and sodium hydroxide concentrations as in the calibration of the pH-2 sensor material was used. The obtained data was fit with Boltzmann sigmoids (equation 5) and the obtained dynamic ranges were normalized (initial *Top* – *Bottom* = 1) and fit against the total measurement time with a slope of  $6.09 \cdot 10^{-8}$  ( $R^2 = 0.9936$ ).

### Monitoring of Oxygen Dynamics in Seagrass

The optode equipped with an oxygen-sensing cap was used to monitor oxygen dynamics in a seagrass field (Aggersund, Limfjord, Denmark) during a 4-day deployment (Figure S3.1).

Pronounced day/night fluctuations of the local oxygen saturation were observed. The concentration of dissolved oxygen reached values as high as 500  $\mu\text{M}$  which corresponds to 250 % of air saturation during the day whereas the conditions are nearly anoxic at night, with minimal oxygen concentrations of 0.58 and 25  $\mu\text{M}$  for the three nights. The intensity of ambient light is one of the parameters measured by the optoelectronic unit. Despite the fact that the oxygen sensor has a black optical isolation layer, the sensing material lets some portion of the ambient light through thus converting the optode into an additional ambient light sensor. Good agreement between the recorded ambient light intensity and oxygen saturation was observed. While the sky was cloudless on June 5<sup>th</sup> and 6<sup>th</sup>, much weaker light intensity was recorded on June 7<sup>th</sup>, when clouds were present. Evidently, the oxygen dynamic concentration range recorded during this day was also much smaller than on previous days and only low supersaturation with oxygen was detected.

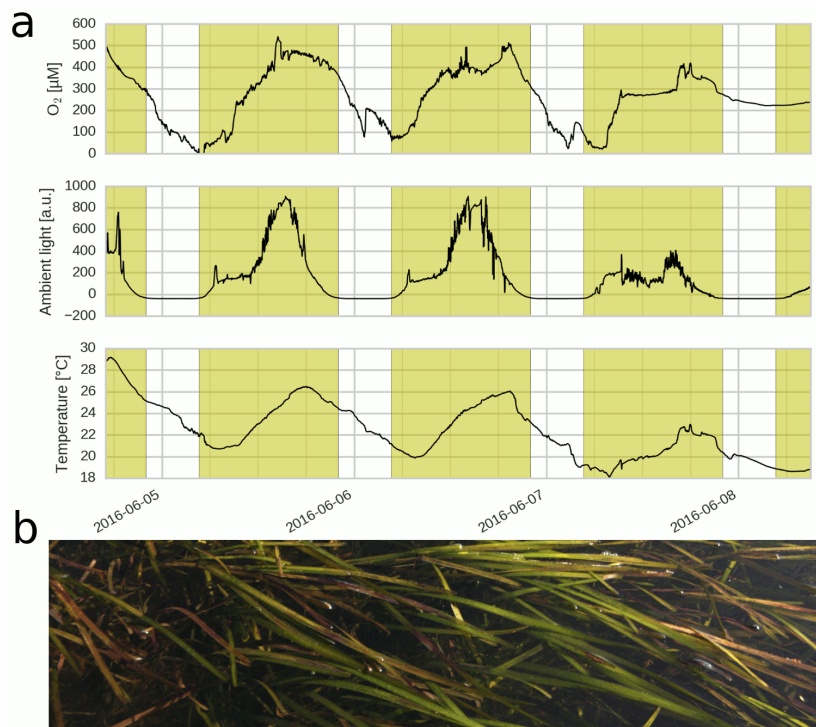


**Figure S3.1:** a: Measurement of oxygen concentration in seagrass in the Limfjord near Aggersund, Denmark (GPS: 56.975925, 9.277746) over 4 days. The optode was at a water depth of about 50 cm. The yellow areas indicate local daytime; the ambient light trace was recorded by the optode based on unmodulated background light. b: Picture of the seagrass where the optode was deployed.

---

# 4 Optical pH sensors for oceanographic applications: low cross-sensitivity to temperature and ionic strength, excellent stability and fast response

## 4.1 Preface to the Manuscript

This publication was submitted to "Sensors & Actuators: B. Chemical" and is currently under review.

Herein the development of four generations of pH sensor materials is described. The first generation utilized simple physical entrapment of the indicator dye, which resulted in insufficient response times at low temperatures. For this reason, the following sensor material generations were based on covalently coupled indicators in hydrophilic, cross-linked polymeric matrices, which resulted in fast response times even at low temperatures. For this purpose, new indicator dyes and new matrix materials were synthesized. This significantly increased the effort to obtain sensor materials and reduced the reproducibility and availability of the sensor materials. In the 3<sup>rd</sup> and 4<sup>th</sup> generations the properties and the production procedure were optimized to obtain larger amounts of sensor material with constant properties. Therefore, the simultaneous cross-linking was replaced with dedicated coupling and crosslinking steps, allowing purification between the steps and batches of stained polymer with constant indicator concentrations. An innovative coupling step was utilized for the last sensor material, which allows covalent coupling without a dedicated linker group on the aza-BODIPY indicator. This greatly improved the production procedure and led to higher amounts of available sensor material with constant properties.

An important point of this work was the characterization of the materials. All materials were characterized and optimized in regard to their long-term stability to allow deployments over long periods of time. Furthermore, their temperature and salinity cross-sensitivities were investigated and described by mathematical models to enable compensation of the effects. The materials were deployed during multiple field excursions for profiling on CTD-rosettes and on moorings.

In contrast to previously presented pH sensor materials for oceanography, the new materials offer good stability, an optimized  $pK_a$  and low sensitivity to temperature and negligible cross-sensitivity to salinity.

## **Optical pH sensors for oceanographic applications: low cross-sensitivity to temperature and ionic strength, excellent stability and fast response**

Authors: Christoph Staudinger, Martin Strobl, Johanna Breininger, Ingo Klimant, Sergey M. Borisov\*

Institute of Analytical Chemistry and Food Chemistry, Graz University of Technology, Stremayr-gasse 9, 8010, Graz, Austria

\*email: sergey.borisov@tugraz.at

Keywords: optode, aza-BODIPY, marine, seawater, fluorescence, hydrogel

### **4.2 Abstract**

The study reports preparation and detailed comparison of new pH sensor materials for seawater measurements. The composition of the sensors is optimized in several iterations to ensure optimal dynamic range, fast response time at low temperatures, low cross-sensitivity to temperature ( $\text{dpK}_a/\text{dT} \approx -0.013$  pH units/K) and negligible cross-sensitivity to ionic strength above salinity 15 PSU. Moreover, the last two generations showed no drift over 54 days at 10 °C and only a drift of 0.003 pH units/day at 25 °C. The first generation utilizes a pH indicator which is physically entrapped into a polyurethane hydrogel. This material shows satisfactory performance only at comparably high temperatures with response times being extremely long at low temperatures ( $t_{90} > 2$  h at 5 °C). The three other materials utilize cross-linked hydrophilic polymers based on poly(acryloylmorpholine) with indicator dye covalently coupled to the polymer. They feature fast response time at low temperatures ( $t_{90} < 1$  min at 5 °C). Although the stability and the sensing properties of these materials are rather similar, the synthetic effort varies considerably. The material of the fourth generation explores a novel approach of covalent coupling via B-O linkage and is characterized by low synthetic effort and the  $\text{pK}_a$  value optimal for seawater measurements (8.05 at 20 °C). Importantly, all new sensing materials are spectrally compatible

to a seawater optode system for combined pH, pO<sub>2</sub> and pCO<sub>2</sub> measurements which facilitates their application in marine environment.

### 4.3 Introduction

pH is one of the most important parameters in many different applications including chemical engineering, environmental monitoring, biotechnology [217, 218], microbiology [219, 220], and oceanography [32]. The monitoring in marine environments is especially important because the surface pH of our oceans is continuously decreasing due to absorption of anthropogenic carbon dioxide [221–223]. This acidification is estimated to reach a decrease of up to 0.8 pH units till 2300 [34]. Such drastic change of the marine environment requires intense investigation to understand and predict its consequences. Therefore, extensive and widespread monitoring with autonomous sensor systems will be important in the next decades.

Classical pH electrode belongs to one of the most widespread analytical tools, however it does not perform well in the high salinity environment due to unstable liquid junction potentials at the reference electrode [30, 53, 77]. A range of technologies have been developed to overcome the limitations of the pH electrode for seawater measurements. These include ion sensitive field effect transistors (ISFETs) [82, 83], systems based on spectrophotometric measurements [92, 93] and optodes [133, 141], ISFETs are much more mechanically robust compared to the pH electrode but similarly to it require a reference electrode. They face other challenges like light sensitivity and pressure crosstalk [39, 83, 89, 183, 184]. Spectrophotometric systems rely on ratiometric measurement of pH-sensitive absorption of an indicator dye. They are established for laboratory analysis and offer the highest precision and drift stability [93, 224]. On the other hand, autonomous devices based on this measurement principle additionally require pumps, valves and storage tanks for reagents and waste which results in bulky and expensive devices with high power consumption. Therefore, these sensors are usually limited either in sampling rate or deployment time due to the limited amount of reagents and/or battery power. Salinity and temperature cross-talks must also be compensated for accurate measurements.

Optodes represent another promising group of tools for oceanographic pH measurements. Similar to spectrophotometric systems they explore the optical properties of an indicator dye. In contrast to the former, the indicator is immobilized in a water swellable polymer matrix and is not consumed during the measurement. This material can be read-out through a transparent

window or, alternatively, be applied in a form of a fiber-optic sensor with adequate optical feedthrough connected to the inner part of a pressure housing. The power consumption of optodes is typically low [225], they are easy to miniaturize and the optode technology is already well established in oceanography (optical oxygen sensors from e.g. Aanderaa, Ocean Optics, Sea-Bird Scientific). pH optodes could achieve similar relevance in oceanography providing that several challenges are addressed. Currently, the application of optodes is limited by: (i) lack of dedicated materials with optimal dynamic range (pH between 7 and 8.5), minimized cross-talks to temperature and salinity [141] and sufficient long-term stability, and (ii) incompatibility of the pH sensing materials with compact and low cost read-out devices suitable for autonomous measurements. Furthermore, in contrast to biotechnical or in-lab applications no control of temperature or ionic strength is possible. Therefore, the materials must be well characterized in regard of their temperature and salinity sensitivity and a compensation of these influences is required. In the last years, only a few pH sensing materials for oceanographic applications were presented but they suffer from different drawbacks including high cross-sensitivity to salinity and/or of temperature, suboptimal  $pK_a$  or fast photobleaching [133, 141].

Herein we present a detailed study of several generations of pH optical sensing materials optimized for oceanographic applications. The materials were optimized in regard of dynamic range, response time and long term stability and their temperature and salinity cross-sensitivities compared. Whereas the first generation relies on an indicator physically entrapped into a commercially available hydrogel matrix, the three other materials make use of indicators covalently bound to cross-linked matrices. Among them, the material utilizing a novel strategy of covalent immobilization via B-O bond formation is particularly interesting, due to simplicity of the approach. Compatibility of the materials with a phase fluorimeter developed for oceanographic measurements with optical sensors greatly facilitates their applications.

## 4.4 Materials and Methods

### 4.4.1 Materials

4'-butoxyacetophenone, 4'-acetylbenzoic acid, 1-(3-dimethylaminopropyl)-3-ethylcarbodiimide hydrochloride, diisopropylethylamine (DIPEA), benzaldehyde, 2-amino-1,3-propanediol, hexafluoro-2-propanol, boron trichloride (1 M solution in DCM), ethyl 4-bromobutyrate, and boron trifluoride diethyl etherate were purchased from TCI Europe ([www.tcichemicals.com](http://www.tcichemicals.com)). 4'-

hydroxychalcone, and dibutyltin dilaureate were bought from ABCR ([www.abcr.de](http://www.abcr.de)). Nitromethane, ammonium acetate, dodecylamine, 1-hydroxybenzotriazole hydrate, 4-acryloylmorpholine, N-hydroxy succinimide, 3,3-dimethylbutyryl chloride, trimethylamine, potassium carbonate, N-(2-hydroxyethyl)acryl amide, meta cresol purple, acetyl chloride, trifluoroacetic acid and anhydrous sodium sulfate were purchased from Sigma Aldrich ([www.sigmaaldrich.com](http://www.sigmaaldrich.com)). Desmodur N75 MPA/X was obtained from Covestro ([www.covestro.com](http://www.covestro.com)). Deuterated chloroform ( $\text{CDCl}_3$ ) was obtained from Euriso-top ([www.eurisotop.com](http://www.eurisotop.com)). All other solvents (synthesis grade) as well as sodium chloride, potassium persulfate, and the buffer salts (tris(hydroxymethyl)aminomethane (TRIS), bis(2-hydroxyethyl)amino-tris(hydroxymethyl)methane (BIS-TRIS), 2-morpholin-4-ylethanesulfonic acid (MES),  $\text{NaH}_2\text{PO}_4$ ) were purchased from Carl Roth ([www.roth.de](http://www.roth.de)). Silica-gel (0.04-0.063 mm) and Alox was bought from Acros ([www.fishersci.com](http://www.fishersci.com)). Polyurethane hydrogel (Hydromed D4) was purchased from AdvanSource biomaterials ([www.advbiomaterials.com](http://www.advbiomaterials.com)). Carbon black was obtained from Kremer Pigmente GmbH & Co. KG ([www.kremer-pigmente.com](http://www.kremer-pigmente.com)). Diamond powder was bought from Microdiamant ([www.microdiamant.com](http://www.microdiamant.com)). N-(3-aminopropyl)methacrylamide hydrochloride was obtained from Polysciences ([www.polysciences.com](http://www.polysciences.com)). PolyHEMA was bought from Scientific Polymer Products, Inc. ([www.scientificpolymer.com](http://www.scientificpolymer.com)). Poly(ethylene glycol terephthalate) support (PET) was from Pütz ([www.puetz-folien.com](http://www.puetz-folien.com)). Egyptian blue was prepared and silanized with chlortrimethylsilan according to literature procedure [135].

#### 4.4.2 Methods

The pH of buffer solutions was adjusted with a pH meter using a glass electrode (InoLab pH/ion, WTW GmbH & Co. KG, [www.wtw.com](http://www.wtw.com)). The pH meter was calibrated at 25 °C with standard buffers of pH 7.01 and pH 4.01 (WTW GmbH & Co. KG, [www.wtw.com](http://www.wtw.com)). The NMR spectroscopic experiments were performed on a 300 MHz instrument (Bruker) in  $\text{CDCl}_3$  with TMS (tetramethylsilane) as standard. Chemical shifts ( $\delta$ ) are given in parts per million (ppm) relative to TMS and coupling constants J are stated in Hz.

MALDI-TOF mass spectra were recorded on a Micromass TofSpec 2E in reflectron mode at an accelerating voltage of +20 kV.

Absorption measurements were performed on a Cary 50 UV-VIS spectrophotometer from Varian, Palo Alto, United States ([www.varianinc.com](http://www.varianinc.com)) at medium scan rate using baseline correction and an adequate blank sample.

DLR readout of the sensor materials was conducted with the phase fluorimeter Firesting from Pyro Science GmbH at 4 kHz ([www.pyro-science.com](http://www.pyro-science.com)).

### 4.4.3 Synthesis

Only the final synthetic steps and the analytical data of the indicators and sensor materials is mentioned in this section. The synthetic steps for the precursors can be found in the supporting information.

#### Indicator 1

(4-(5,5-difluoro-7-(4-hydroxyphenyl)-1,9-diphenyl-5*H*-4 $\lambda^4$ ,5 $\lambda^4$ -dipyrrolo[1,2-*c*:2',1'-*f*][1,3,5,2]triazaborinin-3-yl)-*N*-dodecylbenzamide): Compound 1 was synthesized according to the literature procedure [124] (reaction pathway depicted in Figure S4.2).

#### Indicator 2

(4-(7-(4-((1,3-dihydroxypropan-2-yl)carbamoyl)phenyl)-5,5-difluoro-1,9-diphenyl-5*H*-5 $\lambda^4$ ,6 $\lambda^4$ -dipyrrolo[1,2-*c*:2',1'-*f*][1,3,5,2]triazaborinin-3-yl)phenyl 3,3-dimethylbutanoate): Compound 8 (25 mg, 39  $\mu$ mol, 1 eq.) was dissolved in 3 mL dry *N,N*-dimethylformamide (DMF), 3-(ethyliminomethyleneamino)-*N,N*-dimethylpropan-1-amine hydrochloride (EDC\*HCl) (15 mg, 78  $\mu$ mol, 2 eq.), *N*-hydroxysuccinimide (NHS) (9 mg, 78  $\mu$ mol, 2 eq.), *N,N*-diisopropylethylamine (DIPEA) (34  $\mu$ L, 25 mg, 195  $\mu$ mol, 5 eq.) and 2-amino-1,3-propanediol (4 mg, 1.1 eq.) were added and stirred for 3 hours at room temperature. The solvent was removed by rotary evaporation and the product purified via column chromatography with silica gel. The product was eluted with 92% dichloromethane and 8% EtOH. Yield: 17 mg (61%)

$^1\text{H}$  NMR: (300 MHz, Chloroform-*d*)  $\delta$  8.06 (m, *J* = 8.9, 5.0 Hz, 8H), 7.88 (d, *J* = 8.2 Hz, 2H), 7.53–7.34 (m, 6H), 7.23 (d, *J* = 8.1 Hz, 2H), 7.03 (d, *J* = 7.8 Hz, 2H), 4.17 (m, 1H), 4.00–3.84 (m, 4H), 2.46 (s, 2H), 1.14 (s, 9H).

MALDI-TOF *m/z* found: 728.3484, calculated: 728.2989

Reaction pathway depicted in the Figure S4.3 in the supporting information.

#### Indicator 3

(4-(4-(7-(4-acetoxyphenyl)-5,5-difluoro-1,9-diphenyl-5*H*-4 $\lambda^4$ ,5 $\lambda^4$ -dipyrrolo[1,2-*c*:2',1'-*f*][1,3,5,2]triazaborinin-3-yl)phenoxy)butanoic acid): Compound 11 (60 mg, 98.4  $\mu$ mol, 1 eq.) was dissolved

in 20 mL dry dichloromethane under inert atmosphere (nitrogen). Then DIPEA (171  $\mu\text{L}$ , 127 mg, 980  $\mu\text{mol}$ , 10 eq.) and boron trifluoride diethyletherate (187  $\mu\text{L}$ , 209 mg, 1.48 mmol, 15 eq.) were added and the reaction was stirred for 16 hours at room temperature. The solution was partitioned between dichloromethane and water in a separating funnel and the dichloromethane layer was dried over sodium sulfate. The product was purified by column chromatography on silica gel and was eluted with 95 % DCM 5 % ethyl acetate. Then it was recrystallized from dichloromethane / cyclohexane. Yield: 18 mg (28 %)

$^1\text{H}$  NMR (300 MHz, Chloroform- $d$ )  $\delta$  8.19 – 7.92 (m, 8H), 7.43 (m, 6H), 7.21 (d,  $J = 8.3$  Hz, 2H), 7.07 (s, 1H), 7.04 – 6.85 (m, 3H), 4.10 (t,  $J = 6.1$  Hz, 2H), 2.60 (t,  $J = 7.2$  Hz, 2H), 2.32 (s, 3H), 2.15 (p,  $J = 6.8$  Hz, 2H)

MALDI-TOF  $m/z$  found: 657.1675, calculated: 657.2253

Reaction pathway depicted in the Figure S4.4 in the supporting information.

#### Indicator 4

(4-(7-(4-butoxyphenyl)-5,5-difluoro-1,9-diphenyl-5*H*-5 $\lambda^4$ ,6 $\lambda^4$ -dipyrrolo[1,2-*c*:2',1'-*f*][1,3,5,2]triazaborinin-3-yl)phenyl acetate): Compound 12 (20 mg, 34.1  $\mu\text{mol}$ , 1 eq.) was dissolved in 3 mL dry dichloromethane. DIPEA (12  $\mu\text{L}$ , 8.8 mg, 68.3  $\mu\text{mol}$ , 2.0 eq.) and acetyl chloride (5  $\mu\text{L}$ , 5.5 mg, 70  $\mu\text{mol}$ , 2.1 eq.) were added and the reaction was stirred for 10 minutes at 0 °C. The reaction mixture was equilibrated 3 times between dichloromethane and water ( $\approx$ 10 mL each). The organic layer was dried over sodium sulfate and the solvent was removed under reduced pressure and purified via column chromatography on silica gel. Yield: 20 mg (93 %)

$^1\text{H}$  NMR (300 MHz, chloroform- $d$ ):  $\delta = 8.21 - 7.99$  (m, 8H), 7.46 (t,  $J = 6.0$  Hz, 6H), 7.23 (d,  $J = 8.7$  Hz, 2H), 7.12 (s, 1H), 7.07 – 6.90 (m, 3H), 4.06 (t,  $J = 6.4$  Hz, 2H), 2.34 (s, 3H), 1.90 – 1.69 (m, 2H), 1.49 (dd,  $J = 14.9, 7.5$  Hz, 2H), 1.00 (t,  $J = 7.3$  Hz, 3H).

Reaction pathway depicted in the Figure S4.5 in the supporting information.

#### 4.4.4 Polymer Synthesis

Details about the synthesis of the matrix polymers can be found in the supporting information (e.g. Figure S4.6)

#### 4.4.5 Preparation of Sensor Materials

##### pH-1 Preparation

0.2 mg indicator **1** and 100 mg Hydromed D4 were dissolved in 900 mg THF. 20 mg Egyptian blue were added and dispersed by stirring with a magnetic stirrer. This “cocktail” was then knife-coated with a 3 Mil (76  $\mu\text{m}$ ) spacer on a 125  $\mu\text{m}$  thick Mylar support, resulting in a dry film thickness of approximately 8  $\mu\text{m}$ .

##### pH-2 Preparation

0.25 mg indicator **2** were dissolved with 50 mg polymer 1 in a mixture of 200  $\mu\text{L}$  dimethylsulfoxide and 800  $\mu\text{L}$  tetrahydrofuran (THF). This solution was transferred into a glove box under nitrogen atmosphere and 4  $\mu\text{L}$  Desmodur N75 MPA/X crosslinker and 4  $\mu\text{L}$  of a 10 % stock solution of dibutyltindilaureate in THF as catalyst were added. This “cocktail” was knife coated 3 times with a 76  $\mu\text{m}$  spacer on a 125  $\mu\text{m}$  poly(ethylene terephthalate) support and cross-linked for 2 hours at 60 °C. This resulted in a film thickness of approximately 18  $\mu\text{m}$ . The protection group was cleaved by submerging the material in 0.01 M sodium hydroxide solution for 30 minutes at room temperature.

The reference layer was knife coated on the backside of the foil by dissolving 150 mg PET foil in 300  $\mu\text{L}$  hexafluoro-2-propanol and 550  $\mu\text{L}$  chloroform. The solution was filtered and 42 mg Egyptian blue were dispersed by ultrasonication. This reference “cocktail” was knife-coated with a 3 Mil spacer on the backside of the sensor foil.

##### pH-3 Preparation

##### Covalent Coupling of Indicator **3** to Polymer **2**

2.5 mg indicator **3** (3.8  $\mu\text{mol}$ ) were dissolved in 500  $\mu\text{L}$  tetrahydrofuran (THF) and 500  $\mu\text{L}$  ethanol (EtOH). 20 mg NHS (174  $\mu\text{mol}$ , 46 eq.), 10  $\mu\text{L}$  EDC (8.8 mg, 56.6  $\mu\text{mol}$ , 15 eq.) and 0.2 mL MES buffer (100 mM, pH 6) were added and stirred at room temperature for 4 hours. This mixture was added to 500 mg polymer 2 (17.7  $\mu\text{mol}$   $\text{NH}_2$ -groups, 4.7 eq) in 30 mL EtOH/water 1/1. 5 mL 100 mM phosphate buffer with pH 7.5 were added and the reaction mixture was stirred for 2 hours at room temperature.

To block remaining  $\text{NH}_2$  groups in the polymer 50  $\mu\text{L}$  acetyl chloride (55 mg, 701  $\mu\text{mol}$ ) were dissolved in 2 mL of THF and 100 mg NHS (869  $\mu\text{mol}$ , 1.25 eq.) were added and stirred at room

temperature for 10 minutes. This mixture was added to the reaction mixture and stirred for 45 minutes at room temperature.

The reaction mixture was precipitated in 200 mL ethylacetate, dissolved in 10 mL dichloromethane, centrifuged to remove insoluble salts and again precipitated in 50 mL of ethylacetate. Then the polymer was dissolved in 10 mL dichloromethane and precipitated in cyclohexane. Yield: 320 mg (64 %)

The concentration of bound indicator was determined by dissolving 7.8 mg of the polymer in 1.526 g dichloromethane with addition of 1  $\mu\text{L}$  trifluoroacetic acid to ensure complete protonation of the indicator. The absorbance of 1.22 measured in the maximum of the spectrum (1 cm cuvette) corresponds to a dye content of 0.14 w%, assuming a molar absorption coefficient of  $80\,000\text{ M}^{-1}\text{ cm}^{-1}$  for the bound dye.

### **Preparation of pH-3 Sensor Layers**

50 mg of the stained polymer were dissolved in 100  $\mu\text{L}$  dry DMSO and 400  $\mu\text{L}$  dry THF. 1.5  $\mu\text{L}$  Desmodur N75 MPA/X and 1.5  $\mu\text{L}$  of a 10 % dibutyltin dilaureat stock solution in THF were added and mixed by stirring for 2 minutes. This cocktail was knife coated with a 3 Mil (76  $\mu\text{m}$ ) spacer ( $\approx 8\ \mu\text{m}$  dry film thickness) and crosslinked by heating on a heating plate under inert atmosphere to 60 °C for 1 h.

After crosslinking the acetyl protection group was cleaved by submerging in 0.01 M NaOH for 30 minutes at room temperature.

An optical isolation was introduced by knife coating PolyHEMA with first with diamond powder and then with carbon black over the sensor film. Both solutions were prepared by dissolving 75 mg PolyHEMA in 0.5 mL EtOH/Water 95/5 and addition of either 75 mg diamond powder or carbon black. The referencing layer was coated on the backside with a 1 Mil (25  $\mu\text{m}$ ) spacer. 20 mg Egyptian blue was dispersed in a solution of 150 mg Mylar in 280 mg hexafluoro-2-propanol and 560 mg chloroform.

### **pH-4 Preparation**

#### **Covalent Coupling of Indicator 4 to Polymer 1**

10 mg indicator 4 (15.9  $\mu\text{mol}$ ) were dissolved in 3 mL dry dichloromethane in a Schlenk flask and cooled to 0 °C. 25  $\mu\text{L}$  1M  $\text{BCl}_3$  in DCM (25  $\mu\text{mol}$ , 1.57 eq.) were added and stirred for 20 minutes. This mixture was added to 1 g polymer 1 dissolved in 10 mL dry dichloromethane

and stirred for 1 hour at room temperature. The polymer was precipitated in 50 mL toluene, redissolved in 15 mL dichloromethane and again precipitated in toluene. Then the polymer was dissolved in 15 mL dichloromethane and precipitated in 50 mL cyclohexane. 781 mg (78 %) light green powder were obtained. The dye content (0.02 w %) was estimated via absorption measurement performed in the same way as for **pH-3**.

#### **Preparation of pH-4 Sensor Layers**

50 mg stained polymer were dissolved in 50  $\mu$ L DMSO and 400  $\mu$ L THF. 1.5  $\mu$ L Desmodur N75 MPA/X and 1.5  $\mu$ L of a 10 % dibutyltin dilaureate stock in THF were added and mixed by stirring for 2 minutes. This “cocktail” was knife coated with a 3 Mil (76  $\mu$ m) spacer ( $\approx$  8  $\mu$ m dry film thickness) and cross-linked by heating on a heating plate at 60 °C under inert atmosphere for 1 h. After crosslinking the acetyl protection group was cleaved by submerging in 0.01 M NaOH for 30 minutes at room temperature.

An optical isolation was introduced by knife coating PolyHEMA containing diamond powder or carbon black over the sensor film. Both solutions were prepared by dissolving 75 mg PolyHEMA in 0.5 mL EtOH/Water 95/5 (v/v) and addition of either 75 mg diamond powder or carbon black. The referencing layer was coated on the backside with a 1 Mil (25  $\mu$ m) spacer. 20 mg Egyptian blue was dispersed in a solution of 150 mg Mylar in 280 mg hexafluoro-2-propanol and 560 mg chloroform.

#### **4.4.6 Characterization of the Sensor Materials**

All presented calibration curves were recorded with an automated calibration setup. This setup consists of a temperature-controlled double walled beaker with 800 mL total volume containing a buffer with the desired composition (ionic strength, buffer capacity, buffer substances) which is continuously stirred with a magnetic stirrer. The temperature is controlled with a thermostate (F25-ME, from Julabo ([www.julabo.com](http://www.julabo.com))) with an external thermometer submerged in the buffer solution. pH changes are induced by addition of hydrochloric acid or sodium hydroxide with a syringe pump (Cavro Centris from Tecan ([www.tecan.com](http://www.tecan.com))). The pH is controlled with a pH electrode and a NaCl filled reference electrode from idronaut ([www.idronaut.it](http://www.idronaut.it)). The pH electrode is calibrated by sampling the buffer at different pH values (and temperatures) and measurement of the pH with spectrophotometric measurements with m-Cresol purple in a temperature controlled cuvette (Cary single cell Peltier accessory from

Varian (www.varianinc.com)). The spectrophotometric measurements are evaluated with the coefficients published by Liu et al. [95]. The system is capable of processing a “command list” of desired pH values and temperatures. This was used to record calibration curves by providing a list of desired (usually equally spaced) pH values. Thereby the calibration curves were always recorded in both directions (e.g. acidic to alkaline to acidic) to detect hysteresis in the calibration functions which would indicate incomplete response of the sensor materials. pH values were always held for 15 minutes if no other information is given in the more detailed description of the specific experiments. The recorded values of the last 5 minutes were then averaged for the calibration. After acquisition of a calibration curve the measurement system would either change the temperature and start the recording of the next calibration curve or wait till the next day and then start a new calibration to investigate the stability of the sensor materials. Different ionic strengths were set by exchanging the buffer and hydrochloric acid and sodium hydroxide solutions. The sensor materials were attached to the end of optical fibers and read-out with the Firesting meter from PyroScience GmbH (www.pyroscience.com).

Dynamic response was studied by switching from a pH 7.75 to a pH 8.25 phosphate buffer (adjusted with 1 M NaOH at room temperature). The ionic strength was set to 150 mM by addition of sodium chloride. Both buffers were placed in double-walled beakers equipped with a stirring bar. The temperature was adjusted with a cryostat (F12-ED from Julabo). The sensors were equilibrated for 20 h before the response was recorded. The new pH values were then held for at least 20 h. The response of the **pH-1** sensor material was normalized to its response after 20 hours. The response of the other sensor materials was normalized to their response after 1 hour.

### **Temperature Calibration pH-1 Material**

Temperature calibrations were recorded in artificial seawater based on the receipt of Dickson et al. [54] with a mixture of 20 mM of TRIS and 20 mM of BIS-TRIS at salinity 35. The pH of the buffer was changed by addition of 1.44 M hydrochloric acid or 1.44 M sodium hydroxide solution.

## 4.5 Results and Discussion

### 4.5.1 pH Optodes: General Considerations

In general, a pH optode consists of a pH sensitive indicator dye which is immobilized in a water swellable polymeric matrix, acting as a support and a solvent for the indicator. The optical properties of the indicator dye change upon protonation or deprotonation. Most pH optodes explore changes in absorption/reflectance or luminescence, the luminescent sensors being more flexible in respect to different sensor formats. Although the read-out via luminescence decay time is highly attractive due to its self-reference character, comparably few indicator dyes proved to be suitable for this scheme [118, 226]. These dyes usually suffer from moderate brightness, oxygen cross-talk and other drawbacks and it is challenging to adapt them for oceanographic applications. In contrast, numerous dye classes have been modified with pH receptors which modulate the fluorescence intensity of the chromophore in the relevant pH range.

Since intensity-based readout is too unreliable for practical measurements referencing of the pH sensors is required. Two common schemes are ratiometric 2-wavelength referencing via excitation or emission and Dual Lifetime Referencing (DLR) [103]. Whereas the former requires a more complex optical set-up (2 channels), the set-up for the DLR scheme is simple (only one excitation source, one detector, excitation and emission filters) which is particularly attractive for design of compact, low-cost and low power consuming devices. In the DLR method the excitation light is sinusoidally modulated and the ratio between pH-dependent fluorescence and pH-independent phosphorescence intensity from the reference material is determined by measuring the overall phase shift of the mixed emission of both components:

$$\cot \Phi = \cot \Phi_{ref} + \frac{1}{\sin \Phi_{ref}} \cdot \frac{A_{ind}}{A_{ref}} \quad (4.1)$$

Where  $\cot \Phi$  and  $\cot \Phi_{ref}$  are the overall phase shift and phase shift of the reference, respectively, and  $A_{ind}$  and  $A_{ref}$  are the amplitudes of the indicator and the reference, respectively.

The typical response of a DLR-referenced optical pH sensor can be described by a Boltzmann sigmoid:

$$\cot \Phi = Bottom + \frac{Top - Bottom}{1 + 10^{\frac{pH - pK_a}{slope}}} \quad (4.2)$$

Where *Bottom* and *Top* are the lower and upper limits of the calibration function, respectively,  $pK_a$  is the point of inflection of the sigmoid and *slope* describes the slope in the point of inflection.

pH sensors, as any other chemical sensors, show cross-talk to temperature. Temperature influences the protonation equilibrium of the indicator but also may affect the photophysical properties of the indicator and reference materials. In order to compensate for this cross-talk, eq. 4.3 has to be extended to enable compensate for this cross-talk by introducing additional linear temperature coefficients for the *Top* ( $Top_t$ ), *Bottom* ( $B_t$ ) and  $pK_a$  ( $pK_{a_t}$ ):

$$\cot \Phi = (B + B_t \cdot (T - 20)) + \frac{Top + Top_t \cdot (T - 20) - (B + B_t \cdot (T - 20))}{1 + 10^{\frac{pH - (pK_a + pK_{a_t} \cdot (T - 20))}{slope}}} \quad (4.3)$$

Another typical cross-sensitivity of optical pH sensors is to ionic strength (=salinity for measurements in seawater). The ionic strength affects the activity constants of the protonation equilibrium of the indicator dye and therefore the response of the sensing material. However, this effect is not linear: it is stronger at low salinities and much weaker at higher salinities. Cross-talk to salinity also depends on the charges of indicator forms involved in the equilibrium. For instance, m-cresol purple, which is the most popular indicator for spectrophotometric pH measurements, transitions between -1 and -2 and hence demonstrates a pronounced cross-sensitivity to salinity. On the other hand, dye with transition between uncharged and mono-anionic form are expected to be much less affected by variations in salinity. Equation 4.3 can be further extended with two linear ionic strength coefficients for the  $pK_a$  and Bottom parameters and can be used for measurements with high ionic strength influence over a limited range:

$$\cot \Phi = (B + B_t \cdot (T - 20) + B_s \cdot (S - 35)) + \frac{Top + Top_t \cdot (T - 20) - (B + B_t \cdot (T - 20) + B_s \cdot (S - 35))}{1 + 10^{\frac{pH - (pK_a + pK_{a_t} \cdot (T - 20) + pK_{a_s} \cdot (S - 35))}{slope}}} \quad (4.4)$$

where  $B_s$  and  $pK_{a_s}$  are the additional salinity coefficients and  $S$  is the salinity of the seawater.

#### 4.5.2 Choice of Materials

Aza-BODIPY dyes are excellent candidates for pH indicator dyes. These near-infrared dyes are very photostable, possess high molar absorption coefficients ( $\approx 80\,000\text{ M}^{-1}\text{ cm}^{-1}$ ) and good quantum yields ( $\approx 20\%$ ) [124, 132]. Furthermore, rather straightforward synthetic modifications can be done to tune their  $pK_a$  and/or to include anchor groups for either physical entrapment or covalent linkage. The simple modification is an important advantage since the most sensitive range of a pH indicator is only around  $\pm 1$  pH unit. Therefore, tuning of the  $pK_a$  value of

the indicator is necessary for it to be suitable for measurements in marine environments (pH between 7.5 and 8.5). Since the aza-BODIPY dyes bearing the hydroxyl group are uncharged in the protonated form and gain one negative charge upon deprotonation, the cross-sensitivity to ionic strength is expected to be low. Finally, the excellent photostability of the aza-BODIPY dyes enables development of sensing materials suitable for long-term monitoring with high temporal resolution ( $> 1$  Hz) which is especially interesting for profiling applications.

Egyptian blue ( $\text{CaCuSi}_4\text{O}_{10}$ ) is an ancient pigment showing bright NIR luminescence with decay time of about 100  $\mu\text{s}$  [205]. Additionally, this phosphor is excitable with red light, shows excellent chemical and photochemical stability and no cross-talk to oxygen making it an excellent reference material for the DLR method [135]. Used in form of a microcrystalline powder, this phosphor was the material of choice in this study.

Importantly, both the indicator and the reference are spectrally compatible to the optoelectronic set-up of the commercially available compact phase fluorimeters from PyroScience which are designed for read-out of oxygen sensors. This compatibility greatly facilitates application of the new pH sensors. The spectral properties of the sensor material “**pH-1**” are depicted in Figure 4.1. All other sensor materials feature very similar spectra. As can be seen, ratiometric two wavelength read-out of the sensor materials is feasible. However, DLR read-out was preferred in this work due to compatibility with the available hardware. In fact, the DLR scheme requires only one long-pass filter in front of the photodetector (RG 9 filter from Schott in our set-up), whereas for the ratiometric measurements two emission channels are necessary. Furthermore, a read-out device for oceanographic measurements presented recently [225] is also compatible to the herein presented sensor materials.

### 4.5.3 Overview of the New pH Sensing Materials

The main strategies of immobilization of the indicator dye into the matrix material are (i) simple physical entrapment of the dye and (ii) covalent coupling of the indicator dye to the matrix backbone. Covalent coupling of the indicator is desirable for multiple reasons. It prevents migration, leaching and aggregation of the indicator dye due to its reduced mobility. Thus, it generally enhances the stability of the sensor material. On the other hand, covalent coupling is usually more complex and often requires additional synthetic steps to introduce and couple linker groups on both the dye and the matrix material. Evidently, compared to the covalent immobilization, physical entrapment is more straightforward and requires less synthetic effort,

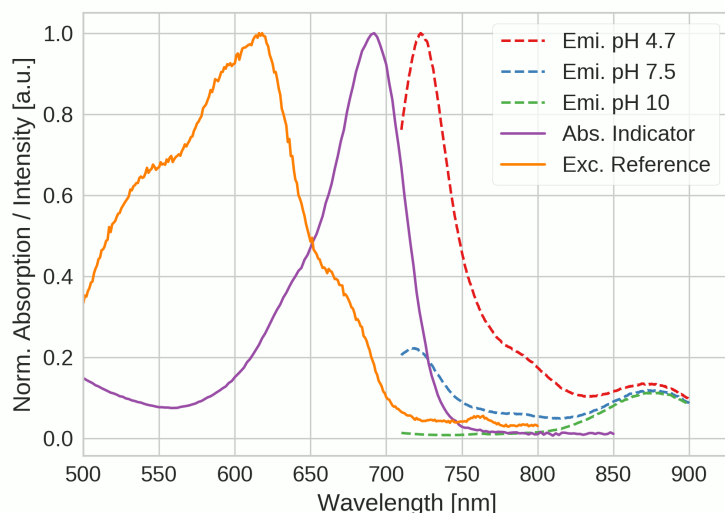


**Figure 4.1:** Spectral properties of the "pH-1" sensor material. The dashed lines indicate the emission spectra of the sensor material at different pH values. The peak at 725 nm is the emission of the fluorescent pH indicator and the emission at 870 nm is the phosphorescence of the reference material (Egyptian blue). The solid violet and orange lines are the absorption spectrum of the indicator and the excitation spectrum of the reference material ( $\lambda_{\text{em}} = 870 \text{ nm}$ ), respectively.

but in case of the pH indicators it is only feasible for fairly hydrophobic dyes (or hydrophilic dyes with a long hydrophobic chains) since highly hydrophilic dyes would leach out of the matrix very fast. Aza-BODIPY dyes, being rather hydrophobic, are suitable candidates for physical entrapment and in fact this strategy was previously shown to yield stable pH sensing materials [124, 132].

Figure 4.2 provides an overview of the developed sensor materials. Whereas the first material was prepared by physical entrapment of the indicator in polyurethane hydrogel, other materials utilize three different strategies of covalent immobilization of indicators into a cross-linked hydrophilic polymer.

### Physically Entrapped Indicator in Hydromed D4 (pH-1)

The first investigated sensing material relies on a reported azaBODIPY indicator **1** (Fig. 4.1) with a  $\text{pK}_a$  of 8.3 [124] immobilized in Hydromed D4, a polyurethane-based hydrogel matrix material. Egyptian blue was used as DLR reference phosphor. The indicator was chosen due

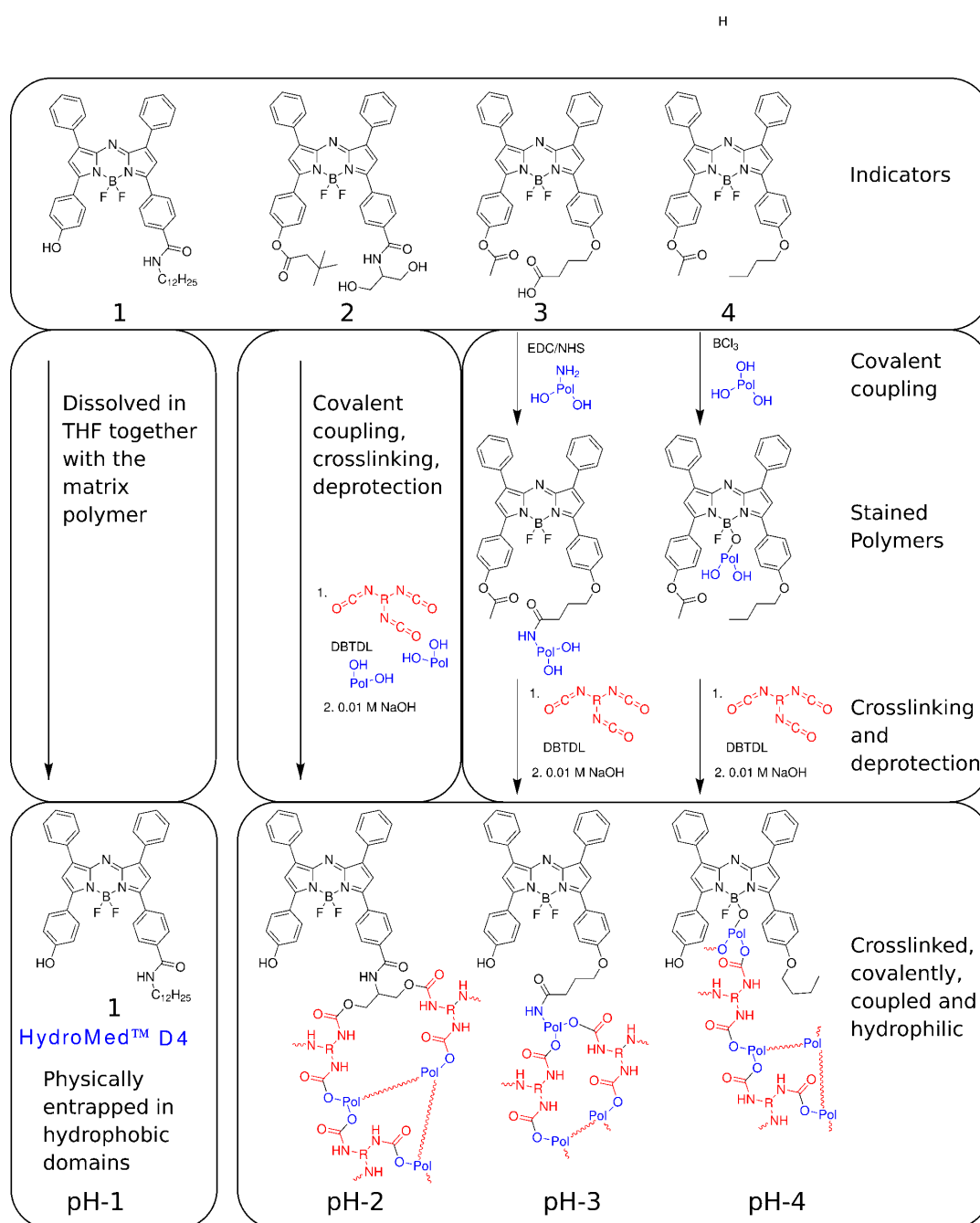


**Figure 4.2:** Overview of the sensing materials and their preparation steps. The sensing material "pH-1" is prepared by physical entrapment in the commercially available polyurethane hydrogel D4. The materials pH-2, pH-3 and pH-4 contain an indicator dye covalently coupled to a cross-linked hydrophilic polymer matrix. The commercially available Desmodur N75 MPA/X was used as multi-isocyanate cross-linker. DBTDL=dibutyltin dilaureate, Pol=Poly(acryloylmorpholine-co-hydroxyethylacrylamide), EDC=1-ethyl-3-(3-dimethylaminopropyl)carbodiimide, NHS=N-hydroxysuccinimide

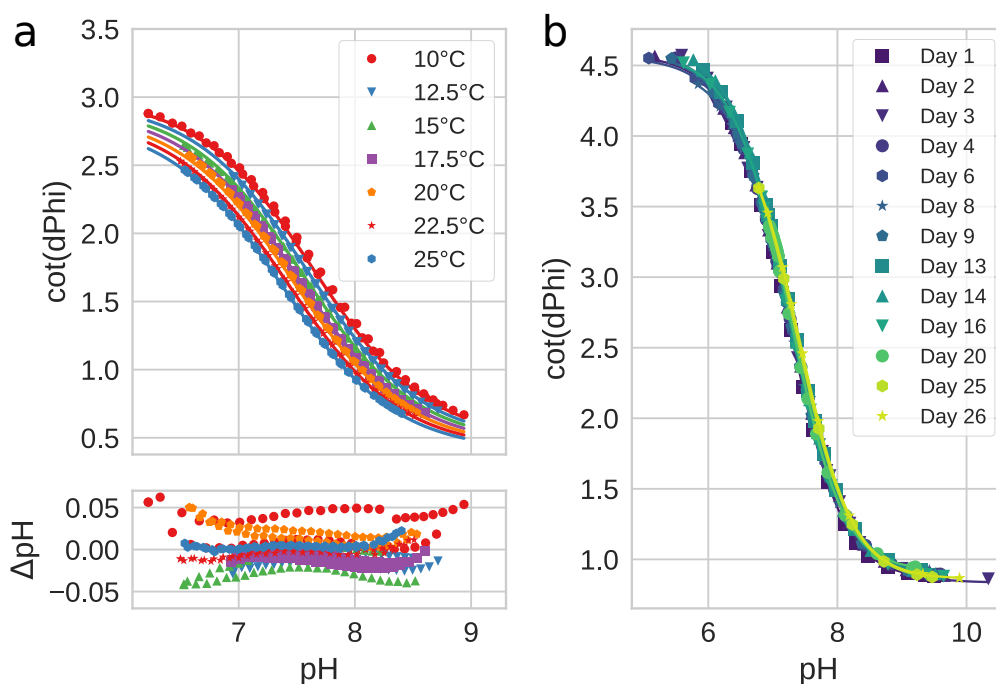
to its favorable  $pK_a$  matching well the pH of seawater and the long hydrophobic hydrocarbon chain which prevents leaching from the sensor matrix and therefore enhances the stability. The hydrogel has a water uptake of 100 % [227] and is generally assumed to contain both hydrophobic and hydrophilic domains. While the hydrophilic poly(ethyleneglycole) domains are responsible for the water uptake the hydrophobic domains solubilize the hydrophobic indicator dye. Thereby contact between indicator and aqueous phase is obtained and the indicator is well solubilized at the same time without evidence of aggregation.

Figure 4.3a shows the calibration of the material at temperatures between 10 and 25 °C. As expected, clear temperature cross-talk is observed, with the point of inflection (apparent  $pK_a$  value of the dye) of the calibration function decreasing at higher temperatures. The dependency of the inflection point on temperature is linear so that this cross-sensitivity can easily be corrected. The stability test at 25 °C over 26 days revealed that no significant change in the calibration function was observed (Fig. 4.3b).

Dynamic response times is another important characteristic of the pH sensors. As can be seen (Fig. 4.4a) the material **pH-1** shows extremely strong dependency of the response time on temperature. While the response time  $t_{95}$  is about 5 minutes at room temperature (Table 4.1) a second, very slow kinetic appears at lower temperatures. In fact, at 4 °C  $t_{95}$  is > 3 hours and the last 5 % of the signal change requires even longer time.

The strong temperature dependence of the response time is likely caused by the heterogeneous nature of the polymer matrix and changes in the polarity of the dye upon protonation/deprotonation. In the protonated form, the dye is very hydrophobic and therefore preferably located in the hydrophobic domains of Hydromed D4. On the contrary, more polar deprotonated form of the dye is located in more hydrophilic domains of the hydrogel. Thus, the change of pH and consequently in the polarity of the dye induces migration between the domains of Hydromed D4 which is manifested in the slower kinetics of the response curve. If the temperature is low this migration is increasingly slow and strongly limits the response time of the sensing material.

While the material is suitable for applications at room temperature and above it is too slow for applications at lower temperatures (Table 4.1). Moreover, the calibration of the sensors at lower temperatures is extremely time consuming. In fact, in order to record the calibration curves depicted in Fig. 4.3 the hold time per measurement point was increased from 20 min at 25 °C to 1 h at 15 °C and 2 h at 10 °C and still some hysteresis was visible at 10 °C. Furthermore, while the residuals of the calibration model are low (below 0.05 pH units between pH 7 and



**Figure 4.3:** (a) Temperature calibration of the **pH-1** sensor material. The data was fit with the eq. 4.3 and projected to the measurement temperatures for better visibility. (b) Stability test of the **pH-1** sensor material at 23 °C over 26 days.

8.5), they are not randomly distributed but show a clear grouping by temperature. This is probably caused by the strong temperature effect on this sensor material. Recording calibration curves at even lower temperatures was not sensible. Since most water masses of our oceans (except tropical waters and surface waters during summer) are characterized by even lower temperatures, it can be concluded that this sensing material is not generally applicable for seawater measurements.

### Cross-linked Hydrophilic Polymer with Covalently Coupled Indicator Dye (pH-2)

The increase of response time due to dye migration can be avoided by utilizing a homogeneous hydrophilic sensor matrix without any hydrophobic domains. However, preparation of such material is challenging. In fact, rather hydrophobic aza-BODIPY dyes show poor compatibility to hydrophilic, water swollen polymers and tend to aggregate. Although modification of the indicators with hydrophilic groups would improve this compatibility, it also strongly increases the risk of leaching of the indicator into aqueous environment and hence drift of the sensing

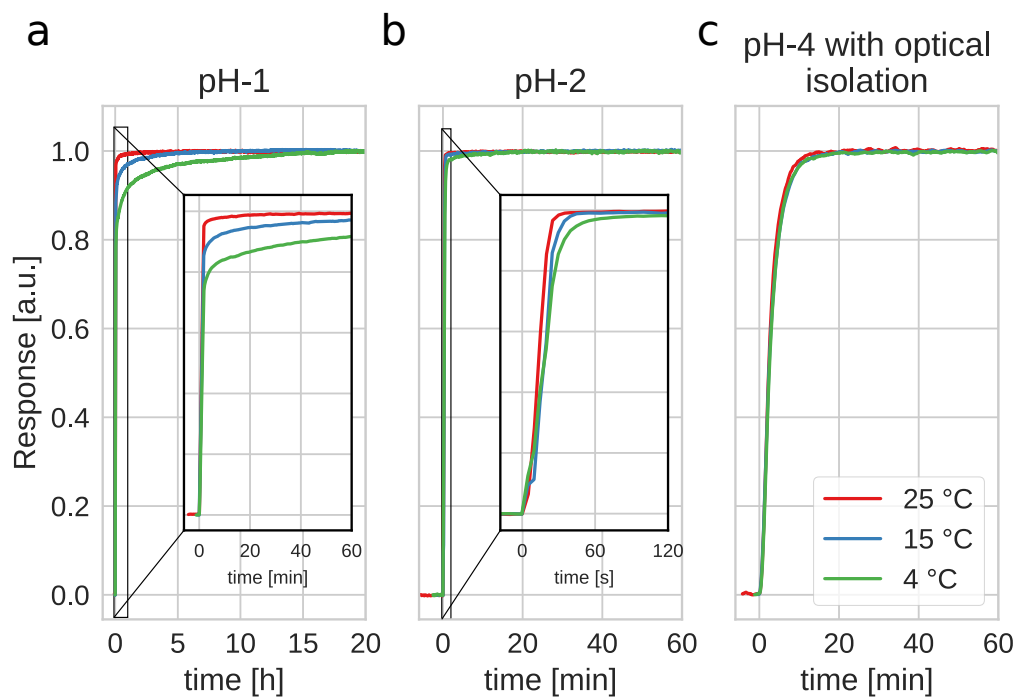


**Figure 4.4:** Temperature dependence of the response of the developed sensing materials. Responses were recorded by switching from a pH 7.75 to a pH 8.25 buffer at 4, 15 and 25 °C. The responses were normalized to 20 h for the **pH-1** sensing material (a) and 1 h for the **pH-2** (b) and **pH-4** (c) sensing materials. The inset in (a) depicts the same time scale as (b) and (c) and the inset in (b) shows the response in the first 2 minutes.

material. Evidently, covalent immobilization of the indicators into hydrophilic polymers or cross-linked networks is a promising way to address these challenges. Previously, the efficiency of this strategy was demonstrated for the hydrophobic perylene dyes [149]. Even in case of such hydrophobic indicators, the mobility of the dye is strongly reduced, due to attachment to bulky polymer chains preventing the aggregation. To ensure even better compatibility to the non-polar aza-BODIPY dyes we decided to use amphiphilic matrix polymer based on acryloylmorpholine as main component [149]. Unfortunately, this strategy of direct incorporation of the acrylamide-modified indicator dye during the polymerization and cross-linking of acryloylmorpholine failed as the dye proved to be unstable in presence of radicals. Therefore, linkage with the alcohol-isocyanate reaction resulting in formation of a hydrolytically stable urethane bond was investigated. The polymer was provided with the alcohol linker groups by addition of 1% of 2-hydroxyethylacrylamide to the acryloylmorpholine. Both monomers are rather similar which

**Table 4.1:** Response times ( $t_{63}$ ,  $t_{90}$  and  $t_{95}$ ) of the sensing materials. Dry film thicknesses of 9  $\mu\text{m}$ , 5  $\mu\text{m}$  and 25  $\mu\text{m}$  (10  $\mu\text{m}$  sensor, 15  $\mu\text{m}$  optical isolation) were measured for the **pH-1**, **pH-2** and **pH-4** sensor materials, respectively.

| T [ $^{\circ}\text{C}$ ] | <b>pH-1</b>  |              |              | <b>pH-2</b>  |              |              | <b>pH-4 with optical isolation</b> |              |              |
|--------------------------|--------------|--------------|--------------|--------------|--------------|--------------|------------------------------------|--------------|--------------|
|                          | $t_{63}$ [s] | $t_{90}$ [s] | $t_{95}$ [s] | $t_{63}$ [s] | $t_{90}$ [s] | $t_{95}$ [s] | $t_{63}$ [s]                       | $t_{90}$ [s] | $t_{95}$ [s] |
| 25                       | 29           | 150          | 330          | 9            | 13           | 15           | 125                                | 320          | 410          |
| 15                       | 53           | 430          | 1950         | 13           | 19           | 23           | 140                                | 360          | 490          |
| 4                        | 120          | 3100         | 10000        | 16           | 28           | 48           | 145                                | 360          | 490          |

ensures a homogeneous distribution of the linker groups in the polymer. Although acrylates are more readily available and cheaper, acrylamides feature higher resistance against hydrolysis which enhances the sensor stability.

The indicator was modified with linker groups by exchanging the dodecylamide-chain with 2-aminopropyl-1,3-diol (Fig. 4.1). Two linker groups per dye molecule enhance the probability and degree of coupling. Moreover, this substitution also reduces the hydrophobicity of the indicator which enhances the compatibility to the hydrophilic matrix material. Poly(acryloylmorpholine) is highly hydrophilic and water soluble so that cross-linking is necessary to obtain a stable sensing material. Commercially available multi-isocyanate (Desmodur N75 MPA/X) was selected to enable simultaneous cross-linking of the sensor matrix (via hydroxyl groups of 2-hydroxyethylacrylamide) and covalent integration of the indicator (Fig. 4.2). Although this cross-linker bases on aliphatic isocyanate groups has reduced reactivity compared to aromatic isocyanates, no colored condensation products are formed during the process. The final sensor material contains only bonds which are very resistant against hydrolysis (C-C-bonds, amide and carbamate links), is homogeneous, hydrophilic and carries no charges, which is the ideal composition of a pH sensor matrix.

In order to obtain the pH-sensing material, the “cocktail” containing the indicator dye, the polymer, the cross-linker and a catalyst (dibutyltin dilaureate) dissolved in the mixture of dimethylsulfoxide (DMSO) and tetrahydrofuran (THF) is knife-coated on a transparent support and cured for 1 hour at 60  $^{\circ}\text{C}$  under inert atmosphere to exclude oxygen and moisture. Undesirable direct crosslinking between two or more indicator dyes is avoided by an excess of OH-groups in the polymer (1:100). Importantly, it is necessary to protect the pH sensitive

OH group of the indicator dye prior to cross-linking to avoid its reaction with isocyanate. The protective acetyl group is subsequently cleaved by treatment of the sensor with 0.01 M sodium hydroxide solution. Although the covalent coupling and amphiphilic backbone of the polymer increase the compatibility between matrix and dye the solubility is still not ideal. Therefore, the indicator content was reduced to 0.05 wt% to avoid aggregation. Egyptian blue was again used as reference material. It was brought onto the backside of the sensor support to eliminate interferences and physically separate it from the indicator dye.

As can be seen, the new sensing material did not show the strongly temperature-dependent second kinetics in the dynamic response (Fig. 4.4) which confirmed the theory of migration of non-covalently coupled indicator between different domains of hydrogel D4. The material was sufficiently stable over 16 days at 30 °C with 15 recorded calibration curves. In fact, over the course of the experiment a drift of 0.09 pH units at pH 8 was observed which corresponds to 0.006 pH units/day. For longer deployments this drift can either be compensated for, or the sensor has to be recalibrated. Moreover, the drift is expected to be lower at lower temperatures typical for most envisaged deployments. The sensing material was characterized by recording calibration curves between pH 5.8 and 8.8 for the salinities 3, 6.5 and 10 and for 4, 6, 8, 10, 12.5 and 15 °C, the conditions typical for Baltic sea in spring and autumn. The obtained data was fit with eq. 4.4, a Boltzmann sigmoid with additional linear temperature coefficients for Top, Bottom and  $pK_a$ , and linear salinity coefficients for  $pK_a$  and Bottom.

Since it is not possible to depict the resulting 4 dimensional calibrations, Fig. 4.5a shows the temperature-compensated calibration functions for different salinities. The data in this plot is fit with the temperature-compensated eq. 4.3 and projected for the individual temperatures for better visibility. The same fits grouped by temperature can be found in the supporting information (Figure S4.7). The obtained residuals for the combined temperature and salinity fit (eq. 4.4) depicted in Fig. 4.5c are below 0.02 for the relevant pH range (7 to 8.5) which demonstrates that the temperature and salinity compensation works well.

All parameters except Top and Bottom were used as a "factory calibration" of the sensing material. The Top and Bottom values of the sensors are not constant and depend on the ratio between the indicator and the reference and the optics of the read-out device. Therefore, these two values were recalibrated with two buffers immediately before measurements.

While this material is definitely able to overcome the strong temperature dependence of the response time of the Hydromed D4-based material **pH-1**, it still has some drawbacks. First of

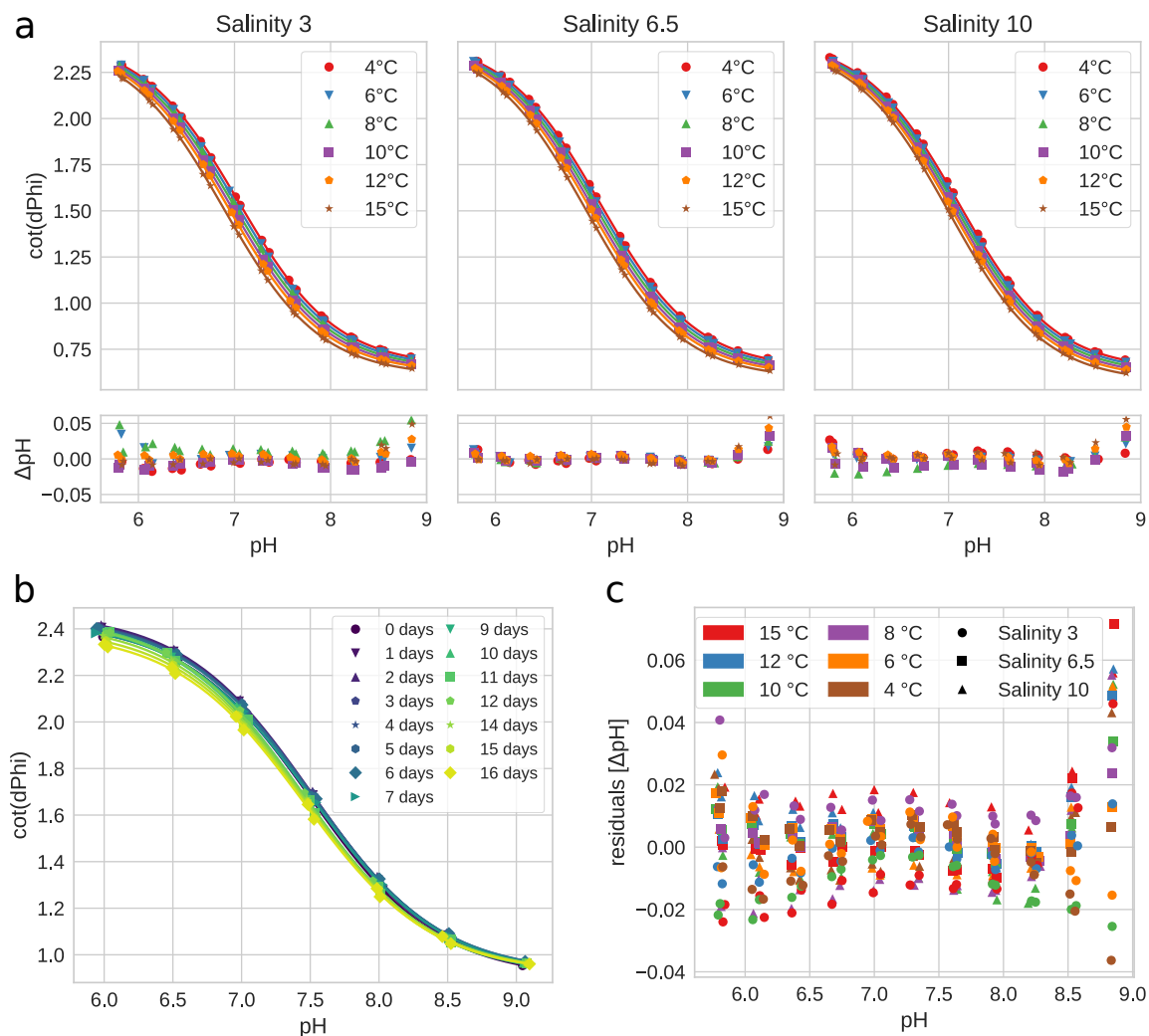


**Figure 4.5:** Calibration and stability of the **pH-2** sensing material. (a) Temperature-compensated calibration functions grouped by salinity with corresponding residuals depicted below. The data was fit with eq. 4.3. The same calibration curves grouped by temperature are shown in Fig. S4.7 of the supporting information. (b) Stability of the sensor at 30 °C over 16 days. (c) Residuals of the temperature- and salinity-compensated calibration function. The data was fit with eq. 4.4 and the obtained calibration coefficients are shown in Table S4.1 in the supporting information.

all, the point of inflection of the sensor material is not perfect for marine applications since pH in most cases can vary between 7.5 and 8.5. In fact, the apparent  $pK_a$  of the indicator in the **pH-2** is 7.23 at 20 °C which is lower than for **pH-1** relying on a very similar carboxamide indicator **1** (7.46 at 20 °C). The decrease of the  $pK_a$ ' is due to significantly more hydrophilic nature of the poly(acryloylmorpholine-co-hydroxyethylacrylamide) matrix compared to polyurethane. Secondly, some indicator molecules may remain unbound during the cross-linking step and later leach out of the membrane. Despite that this effect was evidently not observed (Fig. 4.5b), a procedure with a separate coupling step would be preferable due to possibility of purification of the polymer with the coupled indicator and removal of the unbound indicator and the side products of the reaction.

### **EDC/NHS Coupling of the Indicator to the Hydrophilic Polymer with Subsequent Cross-linking (pH-3)**

The indicators used in **pH-1** and **pH-2** sensing materials (1 and 2, respectively, Fig. 4.2) were synthesized via standard EDC/NHS coupling of amides to the carboxy-modified aza-BODIPY dyes. A similar strategy was adapted to obtain poly(acryloylmorpholine-co-hydroxyethylacrylamide) with covalently coupled pH indicator. However, a different dye precursor was utilized in order to increase the apparent  $pK_a$  value. Following the structure-property relationships established earlier [124], we substituted the electron-withdrawing carboxamide group linked to the core of the indicator with the electron-donating alkoxy group (compound 3, Fig. 4.2). The di-hydroxy-tetraphenyl-aza-dipyrromethene was alkylated with ethyl 4-bromo butyrate and converted to  $BF_2$ -chelate, following by deprotection of the COOH-group and finally protection of the phenol with an acetyl group.

In order to enable covalent coupling of the indicator to the polymer backbone, amino groups were introduced into the polymer by addition of 0.5 mol% N-(3-aminopropyl)methacrylamide to the monomer mixture. After coupling the NHS-ester of dye **3** to the polymer the remaining amino groups were converted to amide via reaction with acetic anhydride. This modification was necessary to ensure good solubility of the stained polymer. Side products and unbound indicator were removed by repeated precipitation. This stained polymer (dye content approximately 0.14 wt%) was cross-linked in the same way as **pH-2** and the indicator deprotected by treatment of the material with 0.01 M NaOH.

The stability of the sensing material at low temperatures (10 °C) common for many oceanographic applications was investigated. As can be seen (Fig. 4.6a), no noticeable drift was observed even after 54 days of continuous operation indicating suitability of the material for long-term deployment without necessity of recalibration. On the other hand, a drift of approximately 0.003 pH units per day (pH 8) was observed at 25 °C. Importantly, the drift was constant over the measurement period indicating that the drift compensation is possible. It would enable long term deployments without frequent recalibration. Evidently, for long-term deployments with significant temperature changes the temperature dependency of the drift should be taken into account.

The temperature sensitivity of the sensing material was investigated between 0 and 25 °C by recording calibration curves in 2.5 °C steps (Fig. 4.6c). A linear temperature dependence for the  $pK_a$  and Bottom coefficients was found. The Top parameter showed a distinct temperature sensitivity and required an additional linear coefficient. The salinity cross-talk of this sensing material was investigated for the salinities between 5 and 35 (Fig. 4.6e). It was found to be virtually negligible for the salinity range from 15 to 35 (Fig. 4.6f) and low on going from salinity 15 to 5. Since in most applications the salinity is very close to 35 with only minor fluctuations, no salinity compensation is required. This is a distinct advantage over spectrophotometric pH measurements which show higher salinity dependence due to the higher charge of the used indicator dye m-cresol purple (see Figure S4.8 in the supporting information).

The main advantage of this approach is its suitability for preparation of large amounts of stained polymer with constant indicator concentration. During the purification step the side products and unbound indicator can easily be removed. The stained polymer requires only a final cross-linking step and enables preparation of many pH sensors with constant properties. On the other hand, the synthetic effort required is high particularly in for the synthesis of dye **3** requiring 3 additional reaction steps. Although the synthetic effort in case of the amino-modified polymer is not higher compared to the unmodified polymer, its purification via precipitation proved to be impossible. Furthermore, despite the expectations, the  $pK_a$  of the **pH-3** sensing material was rather low and therefore not ideal for oceanographic measurements.

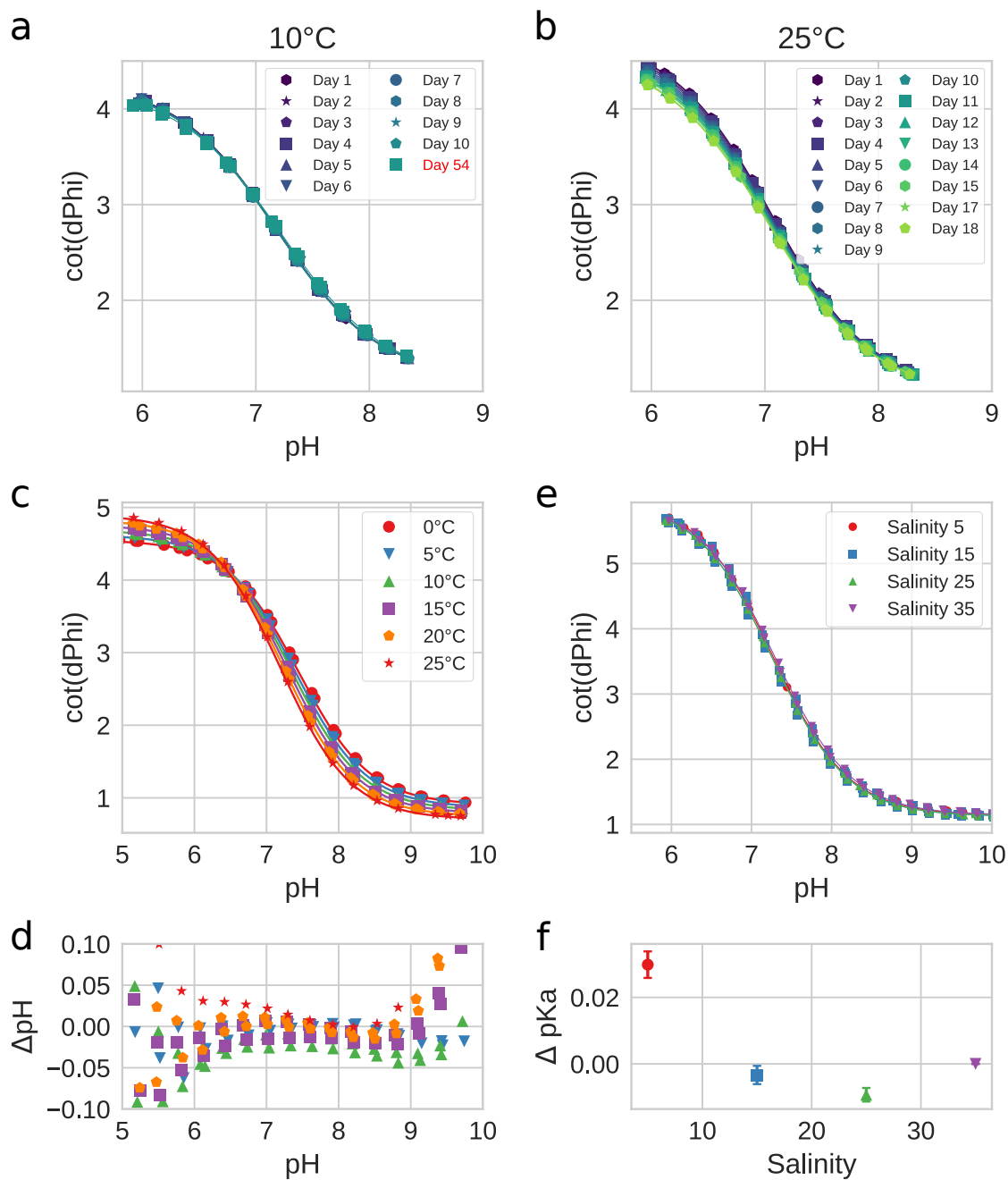


**Figure 4.6:** Calibration and stability of the **pH-3** sensing material. (a) and (b) Stability test at 10°C and 25°C, respectively. (c) Temperature cross-talk between 0 and 25°C. Additionally recorded calibration curves at 2.5, 7.5, 12.5, 17.5 and 22.5 were omitted for clarity. Lines represent the fit with eq. 4.3 projected to the measurement temperatures with the residuals shown in (d). The obtained calibration coefficients are shown in Table S4.1. (e) Salinity cross-talk at 25°C. (f) Change of  $\text{pK}_a$  compared to the  $\text{pK}_a$  value at salinity 35.

### **B-O Coupling of the Indicator to the Hydrophilic Polymer with Subsequent Cross-linking (pH-4)**

The high synthetic effort required for preparation of the material utilizing the EDC/NHS coupling reaction led us to investigate a more straightforward coupling method: direct substitution of a fluorine atom of the aza-BODIPY dye with the OH-group of the polymer. This reaction [228, 229] has only a minimal effect of the optical properties of the dyes and was demonstrated to be useful for preparation of BODIPY conjugates with sugars [230] and alcohols [231]. However, to the best of our knowledge staining of polymers with (aza)BODIPY dyes have not been reported so far. The main advantage of the method is that no dedicated linker group is required which greatly simplifies the synthesis of the dye and the polymer. The readily available hydroxy-butoxy-aza-BODIPY dye [124] was protected with an acetyl group (dye **4**, Fig. 4.1) and, after the activation with  $\text{BCl}_3$ , coupled in an one-pot reaction to the polymer backbone. This stained polymer (dye content approximately 0.02 wt%) was then cross-linked with Desmodur N75 MPA/X and the protection group cleaved with 0.01 M sodium hydroxide solution. As can be seen (Fig. 4.7), the apparent  $\text{pK}_a$  value of the sensing material is close to 8, i.e. almost ideal for measurements in seawater. Similar to **pH-3**, the new material shows no visible drift at 10 °C for almost 2 months of measurement (Fig. 4.7a). At 25 °C, a drift of 0.0021 pH units/day was observed. The temperature dependence of the material (Fig. 4.7c and 4.7d) is again predictable and can easily be compensated with linear coefficients for the  $\text{pK}_a$  and Bottom parameters. Salinity cross-talk is very similar to that observed for the **pH-3** material and requires no compensation between salinity 15 and 35 (Fig. 4.7e and 4.7f).

To avoid overload of the photodiode in direct sunlight the sensor material was equipped with additional optical insulation layers. For this purpose, 3 layers of PolyHEMA were knife coated on top of the sensor foil. The first layer was pure PolyHEMA, the second layer was PolyHEMA with titanium dioxide to enhance the signal intensity of the material due to light scattering and the third layer was PolyHEMA with carbon black. This sensor composition facilitates measurements in shallow water with direct sunlight but significantly increases the response time of the material (Fig. 4.3c). However, while the response time is increased it is not strongly temperature dependent (Table 4.1).

The coupling via the boron atom overcomes many of the challenges of the **pH-2** and **pH-3** sensing materials. It offers a method to obtain polymers with covalently coupled indicators

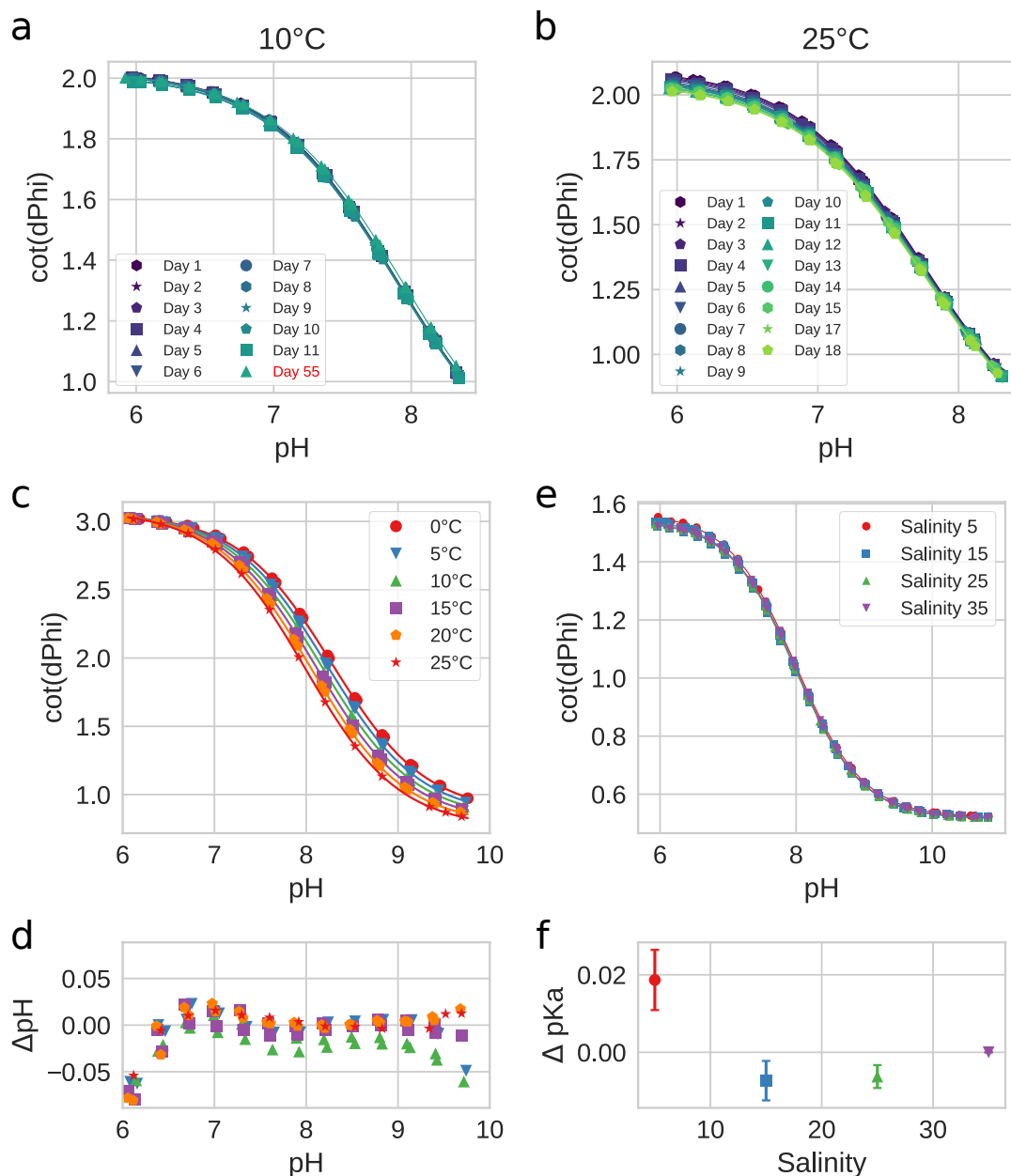


**Figure 4.7:** Calibration and stability of the **pH-4** sensing material. (a) and (b) Stability test 10°C and 25°C, respectively. (c) Temperature cross-talk between 0 and 25°C. Additionally recorded calibration curves at 2.5, 7.5, 12.5, 17.5 and 22.5 were omitted for clarity. Lines represent the fit with eq. 4.3 projected to the measurement temperatures, with the residuals shown in (d). The obtained calibration coefficients are shown in Table S4.1. (e) Salinity cross-talk at 25°C. The calibration curves were fit with eq. 4.3 (f) Change of  $\text{pK}_a$  compared to the  $\text{pK}_a$  at salinity 35.

with low synthetic effort. It requires only a simple protection step of a well-known and easily available aza-BODIPY indicator without the introduction of additional linker groups. The polymer can be synthesized and purified easily in multi-gram amounts. Finally, the linkage between the indicator dye and polymer matrix is achieved in an one pot reaction and subsequent purification of the stained polymer is possible via precipitation. Overall, the new method enables preparation of large amounts of stained polymer which requires only cross-linking to produce the sensing materials. The procedure is expected to be applicable to other indicators of the aza-BODIPY series and to other polymers bearing OH groups.

#### 4.5.4 In-situ pH Monitoring with the New Sensor Materials

The new sensing materials were validated in several field trips. The in-situ measurements were performed with a stand-alone loggers reported previously [225]. The pH profiles in the Baltic sea were acquired with the **pH-2** sensing material (Fig. 4.8a-c); the next generation of materials (**pH-3** and **pH-4**) was used for the measurements in the fjord of Kiel (Fig. 4.8d-f). As can be seen, the new sensors proved to be excellently suitable for profiling applications and continuous pH monitoring for the period of 1 week. The individual sensors demonstrated good correlation between each other and with the reference data. All depicted reference values were acquired by spectrophotometric pH measurements at 25 °C and calculated according to Müller et al. [232] and Mosley et al. [96] for the measurements in the Baltic Sea and Kiel, respectively. All acquired pH values were then converted to in-situ conditions with the CO2SYS program with the constants from Roy et al. [210].

#### 4.5.5 Comparison Between the Sensor Materials

In Table 4.2 the properties of the presented pH sensor materials are compared. **pH-1** is very straightforward to prepare but it is not suitable for typical oceanographic conditions, due to its long response time at low temperatures. The other sensor materials require higher synthetic effort but enable fast response even at low temperatures. While **pH-2** can only be prepared in small batches with potentially fluctuating properties. **pH-3** and **pH-4** offer more constant properties, due to separate coupling and cross-linking steps. Moreover, purification between these steps is possible to remove side products and impurities. All the acryloylmorpholine-based materials feature small temperature and salinity cross-talks (Table 4.2). The latter is explained by the low charge of the indicator dyes (0 protonated, -1 deprotonated) [98]. From all presented

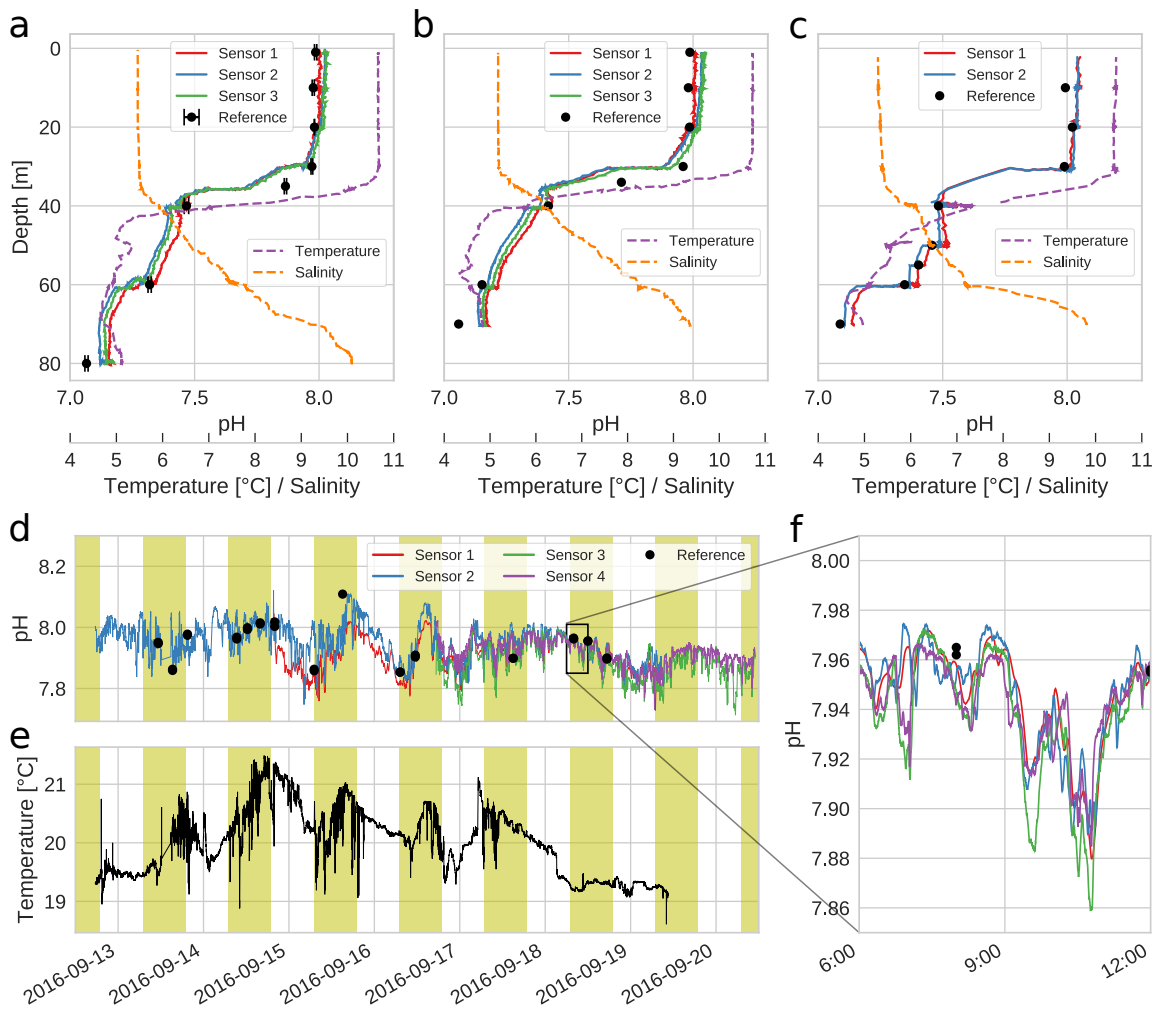


**Figure 4.8:** (a-c) Profiles recorded in the Baltic sea with the **pH-2** sensing material. Coordinates: 59.68665, 24.62128; 59.75529, 25.0009 and 59.56461, 24.88287 for (a), (b) and (c), respectively. (d) and (f) pH monitoring on a pontoon in Kiel fjord over 7 days with up to 4 pH sensors. The sensors 1, 3 and 4 were deployed elsewhere before they were added to this measurement. The sensors 1 and 2 use the **pH-4** sensing material and the sensors 3 and 4 use the **pH-3** sensing material. The sensors were 1-point recalibrated to the reference point on 2016-09-18 11:55:00 to eliminate their slight offset of around 0.06 pH units. The yellow areas indicate daytimes. (e) Temperature data recorded by sensor 2 during the deployment in Kiel Fjord.

materials **pH-4** is the most promising. It utilizes an innovative coupling reaction which requires no additional linker groups and reduces the synthetic effort considerably. Moreover, the  $pK_a$  values (8.05) at 20 °C almost ideally matches the typical seawater conditions.

#### 4.5.6 Comparison with State-of-the-art pH Optodes for Oceanographic Applications

Despite that optical pH sensors represent a promising tools for oceanographic measurements, only very few materials were developed and characterized for this application. The most thorough characterizations of the relevant pH sensor materials were conducted by Schröder et al. [133], Han et al. [175] and Clarke et al. [141] (Table 4.3). Two sensors presented by Schröder et al. [133] are based on lipophilic fluorescein derivatives showing  $pK_a$  values of 8.35 and 8.36, for the DHFA and DHFAE based materials, respectively. They feature low cross-sensitivities to salinity and temperature but showed strong drift (6 % and 8 % decrease in the signal in 24 h for DHFAE and DHFA, respectively) which is explained by leaching of impurities in the dye. However, the drift might also be due to photobleaching of the fluorescein, as the chromophore is notoriously known for its poor photostability, particularly when decorated with electron-donating alkyl substituents. Han et al. [175] presented a sensor material with an apparent  $pK_a$  value of 9.02 and strong temperature ( $\approx -0.032$  pH units/K) and salinity cross-talk, long response times of 120 s despite claims that the sensor is fast.

The sensor material tested by Clarke et al. (obtained from PreSens GmbH) featured a  $pK_a$  of 6.93 which is not ideal for seawater measurements [141]. In fact, the average surface pH of the oceans is between 7.9 and 8.2 [37], which is very well matched by the sensor material **pH-4**. The sensor investigated by Clarke et al. displayed the temperature cross-talk of -0.046 dpH/dK which is about 4-fold higher than for the new materials (Table 4.3). The salinity sensitivity of -0.01 dpH/dPSU and a drift of 0.06 pH units of 5 weeks under deployment conditions were measured. In contrast, the materials presented in this work (**pH-3** and **pH-4**) had a negligible salinity sensitivity from 15 to 35 PSU and no detectable drift at 10 °C (which is close to typical deployment conditions) after 54 days. Finally, Clarke et al. [141] utilized a rather sophisticated setup (0.2 mA, 5  $\mu$ s illumination time, detection by a photomultiplier) to minimize photobleaching of the sensor material and only 1500 measurement points were recorded per sensor spot. On the contrary, the set-up used here is compact [225] and features very low energy consumption which is particularly beneficial for long-term autonomous deployments. Moreover,

**Table 4.2:** Comparison of the properties and characteristics of the four presented sensor materials

|                              | <b>pH-1</b>  | <b>pH-2</b>               | <b>pH-3</b>               | <b>pH-4</b>               |
|------------------------------|--|---------------------------|---------------------------|---------------------------|
| Matrix                       | Hydromed D4  | Acryloyl-morpholine-based | Acryloyl-morpholine-based | Acryloyl-morpholine-based |
| Matrix Properties            | heterogeneous with hydrophilic and hydrophobic domains | homogeneous hydrophilic   | homogeneous hydrophilic   | homogeneous hydrophilic   |
| Cross-linked matrix          | no   | yes                       | yes                       | yes                       |
| Covalently coupled indicator | no   | yes                       | yes                       | yes                       |
| Synthetic effort             | low  | high                      | high                      | moderate                  |
| Scalable preparation         | yes  | no                        | yes                       | yes                       |
| pKa (20 °C)                  | 7.461  | 7.236                     | 7.240                     | 8.050                     |
| dpKa/dT                      | -0.0177  | -0.0126                   | -0.0104                   | -0.0114                   |
| dpKa/dPSU                    | n.d.   | 0.0122                    | Negligible (15-35 PSU)    | Negligible (15-35 PSU)    |
| Fast response below RT       | no   | yes                       | yes                       | yes                       |

only an additional temperature sensor is required for precise pH sensing since the salinity sensor can be omitted due to negligible salinity cross-talk of the materials. This minimizes hardware costs and greatly improves the applicability of the sensor. It should also be mentioned that excellent photostability of the aza-BODIPY indicators allows measurements with high frequency. For instance, in the simulated long term deployment with **pH-4** material [225] 120 000 single measurements points were recorded.

**Table 4.3:** Comparison with previously reported indicators

| Material                        | pK <sub>a</sub> | Temperature<br>Cross-talk        | Salinity cross-talk<br>$\Delta$ pKa between 35<br>and 15 PSU | Drift                                  | Comments  | Reference |
|---------------------------------|-----------------|----------------------------------|--|--|---|-----------|
| DHFA in<br>hydrogel<br>D4       | 8.35            | -0.0011                          | 0.10   | 8 % in 24h                             | Leaching of the<br>indicator; poor<br>photostability                      | [133]     |
| DHFAE<br>in hy-<br>drogel<br>D4 | 8.36            | -0.01                            | 0.05   | 6 % in 24h                             | Leaching of the<br>indicator; poor<br>photostability                      | [133]     |
| CPIPA                           | 9.02            | ( $\approx$ 0.032 pH<br>units/K) | n.d. (irregular)   | 30 % in 28<br>days                     | Long response<br>time of 120 s  | [175]     |
| Obtained<br>from<br>PreSens     | 6.93            | -0.046                           | 0.20   | 0.06 over 5<br>week test<br>deployment | Measurement<br>interval very<br>long to min-<br>imize photo-<br>bleaching | [141]     |
| pH-4                            | 8.050           | -0.0114                          | negligible   | Stable over<br>54 days at<br>10 °C     |   | This work |

## 4.6 Conclusions

Several new pH sensing materials were prepared and characterized with the aim to obtain a system optimal for seawater measurements according to the following requirements: (i)  $pK_a$  value close to that of the seawater; (ii) low cross-sensitivity to salinity; (iii) adequate long-term stability; (iv) fast dynamic response in the whole temperature range and (v) simplicity of material preparation. The material of the first generation, **pH-1**, utilizing a pH indicator physically entrapped into a hydrogel matrix, suffers from very slow response at low temperature. Covalent immobilization of the indicator into cross-linked hydrophilic polymer eliminates this drawback. All the materials adapting this strategy show good long-term stability and very low cross-sensitivity to salinity favorably distinguishing them from state-of-the-art pH optodes for seawater measurements and spectrophotometric assays based on m-Cresol purple indicator. On the other hand, the synthetic effort required for preparation of these sensors differs considerably. Whereas several additional synthetic steps are required for preparation of the indicators for **pH-2** and **pH-3** sensing materials, this drawback is overcome in the **pH-4** material utilizing a novel approach of polymer staining via B-O coupling. This approach makes it possible to manufacture large quantities of indicator-stained polymer from easily accessible pH indicators following an one-pot procedure. Moreover, the covalent coupling only slightly affects the  $pK_a$  value of the dye making the material **pH-4** excellently suitable for measurements in seawater. The new strategy is also expected to enable preparation of sensors for other important applications (medical, biological, biotechnological etc.) by using other indicators of the aza-BODIPY family.

## Acknowledgments

We thank Jan P. Fischer and Roland Thar from PyroScience GmbH (Aachen, Germany) for providing and developing the measurement equipment used for in-lab characterization and field trip measurements. Furthermore, we thank Prof. Eric Achterberg, Jennifer S. Clarke, Felix Geißler, André Mutzberg from GEOMAR team (Kiel, Germany) for their assistance in field measurements and recording the reference values during the measurements in Kiel harbor and Jens D. Müller from IOW (Warnemünde, Germany) for recording the reference values for the profiling measurements in the Baltic Sea. This work was supported by the European Union FP7 Project SenseOcean [grant number 614141].

## 4.7 Supporting Information

### 4.7.1 Synthesis of the Dyes

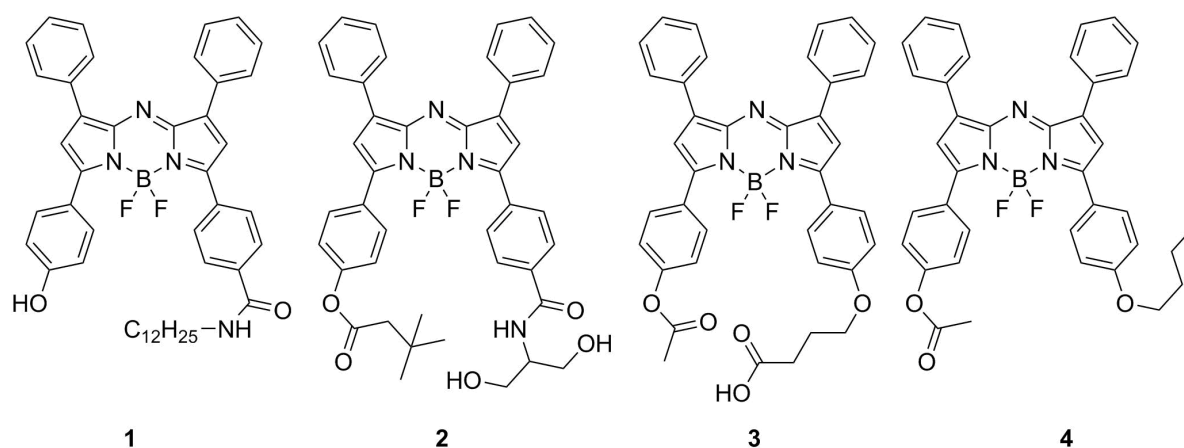


**Figure S4.1:** Overview of the used indicator dyes

**General comments:** Dye **1** was synthesized according to the literature procedure [124] (reaction pathway depicted in Figure S4.2). Synthesis of the dye **2** involves an intermediate of compound **1** synthesis. Dye **4** was obtained according to literature procedure [124, 132] with an additional protection step. The precursor for the synthesis of the compound **3** is a side-product of the reaction pathways to dyes **1**, **2** and **4**.

## Dye 1

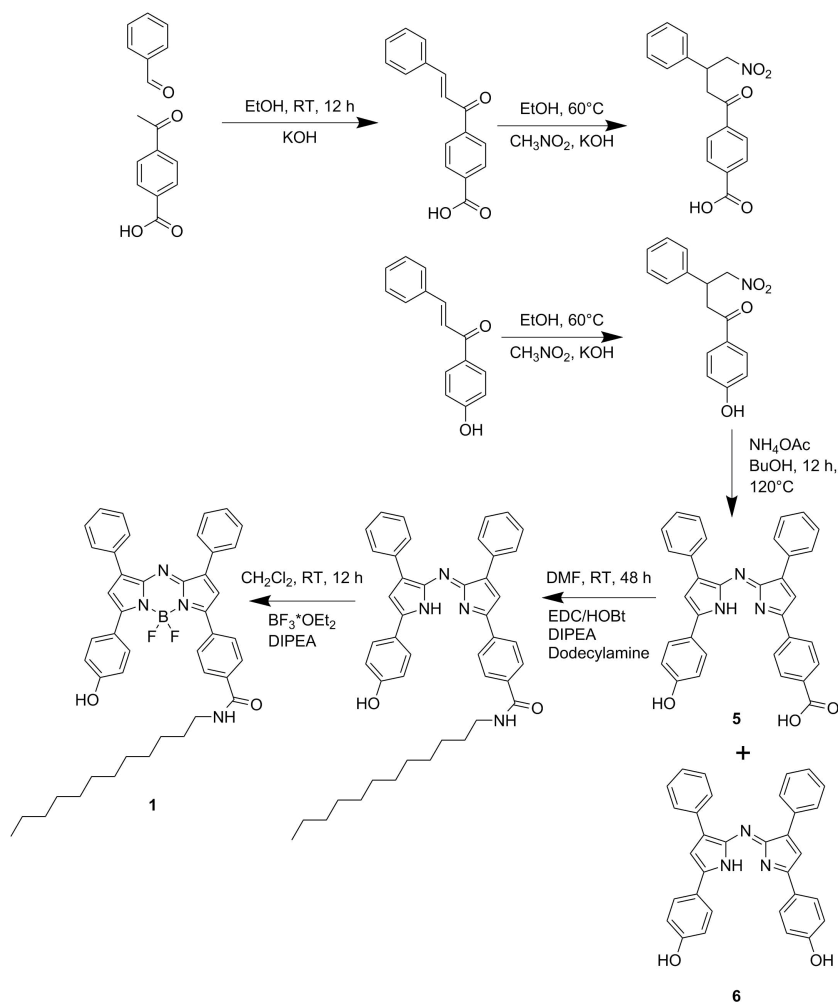
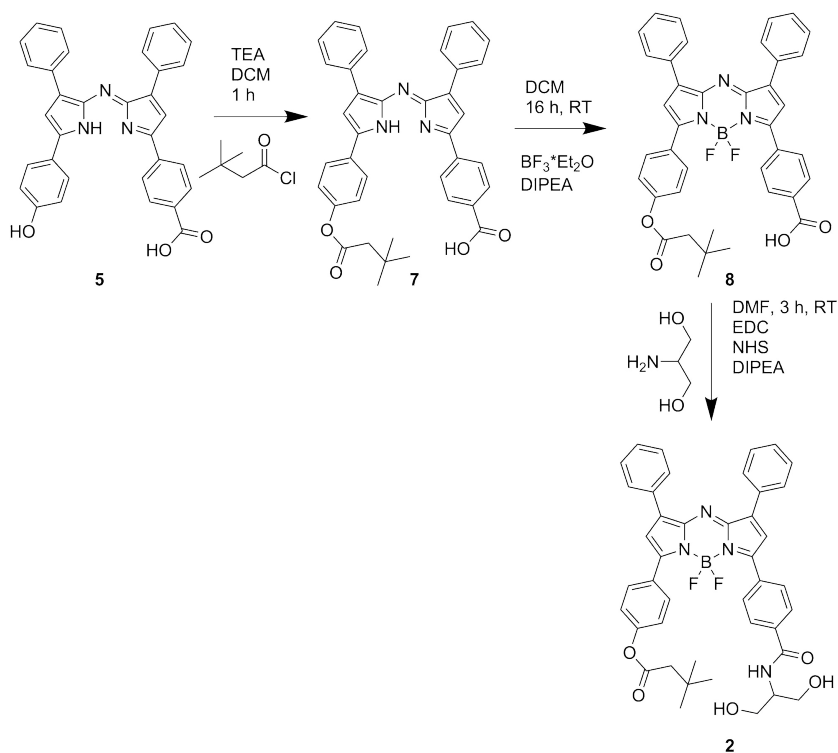


Figure S4.2: Reaction pathway to dye 1.

## Dye 2

Dye 2 was synthesized based on an intermediate (compound 5) on the reaction path to Dye 1. The intermediate was prepared as described in literature [124].



**Figure S4.3:** Reaction pathway to dye **2**.

### Compound **7**

Compound **5** (194 mg, 381  $\mu\text{mol}$ , 1 eq.) was dissolved in 10 mL dry dichloromethane. Triethylamine (117  $\mu\text{L}$ , 85 mg, 0.87 mmol, 2.2 eq.) and 3,3-dimethylbutyryl chloride (107  $\mu\text{L}$ , 105 mg, 0.87 mmol, 2.2 eq.) were added and the reaction was stirred for 1 hour at room temperature. The reaction mixture was extracted 3 times between dichloromethane and water ( $\approx 20$  mL each). The organic layer was dried over sodium sulfate and the solvent was removed by rotary evaporation. Yield: 212 mg (94 %).

### Compound **8**

Compound **7** (150 mg, 253  $\mu\text{mol}$ , 1 eq.) was dissolved in 20 mL dry dichloromethane under inert atmosphere (nitrogen). Then diisopropylethylamine (DIPEA) (440  $\mu\text{L}$ , 327 mg, 2.53 mmol, 10 eq.) and boron trifluoride diethyletherate (480  $\mu\text{L}$ , 540 mg, 3.8 mmol, 15 eq.) were added and the reaction was stirred for 16 hours at room temperature. The solution was partitioned between dichloromethane and water in a separating funnel and the dichloromethane layer was dried over sodium sulfate. Yield: 132 mg (81 %)

**Dye 3**

Dye **3** was synthesized based on a side-product (compound **6**) on the reaction paths to compound **1,2** and **4**. The side product was obtained as described in literature [124].

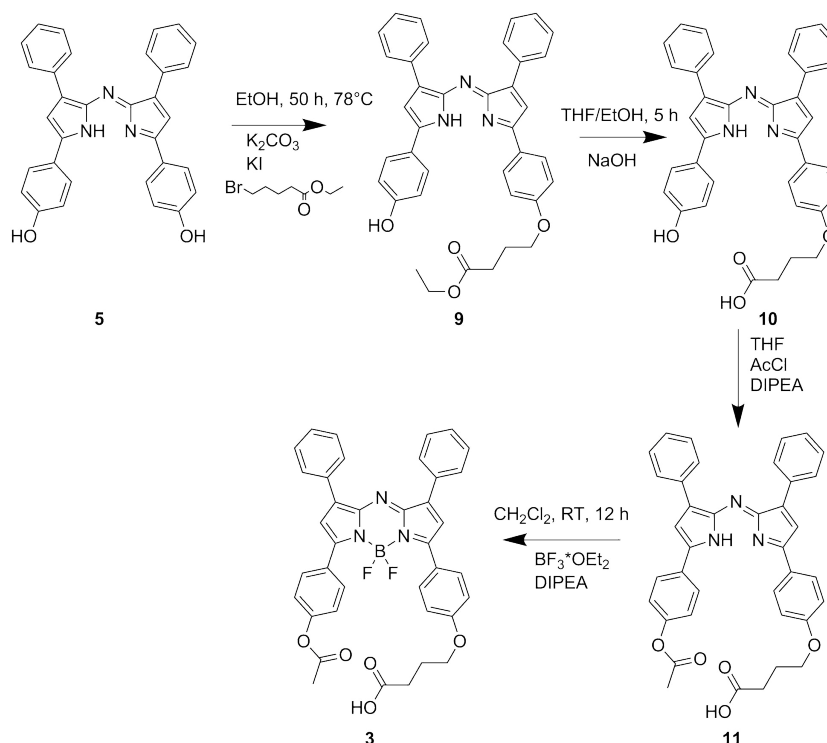


**Figure S4.4:** Reaction pathway to dye **3**.

**Compound 9**

Compound **5** (1 g, 2.1 mmol, 1 eq.) was dissolved in 10 mL DMF and ethyl 4-bromobutyrate (237  $\mu$ L, 0.323 mg, 1.66 mmol, 0.8 eq.) and potassium carbonate (290 mg, 2.1 mmol, 1 eq.) were added. The mixture was heated to 90 °C for 50 hours. After cooling the solvent was evaporated under vacuum and extracted with dichloromethane/water 3 times. The dichloromethane phase was dried with sodium sulfate and removed by rotary evaporation. The product was purified by column chromatography on silica gel and eluted with 99% DCM 1% MeOH. The crude product was used for the next reaction step without further purification. Yield of the crude product: 320 mg (26%).

**Compound 10**

Compound **9** (320 mg, 537  $\mu\text{mol}$ ) was dissolved in 10 mL EtOH and 10 mL THF. 2 mL 1 M NaOH (2 mmol) were added and stirred for 5 hours at room temperature. Then the reaction mixture was acidified with 5 % acetic acid and 2 times extracted with 100 mL water and 100 mL dichloromethane. After drying over sodium sulfate the solvent was removed by rotary evaporation. The crude product was used without further purification for the next reaction step. Yield of the crude product: 200 mg (66 %).

**Compound 11**

Compound **10** (200 mg, 0.352 mmol) was dissolved in 20 mL dry tetrahydrofuran (THF) and cooled to 0 °C. DIPEA (100  $\mu\text{L}$ , 74.2 mg, 0.574 mmol, 1.6 eq.) and acetyl chloride (40  $\mu\text{L}$ , 44 mg, 0.56 mmol, 1.6 eq.) were added and stirred for 1 h at 0 °C. The reaction was quenched by addition of 5 mL saturated sodium bicarbonate. Then the mixture was acidified by addition of 5 % acetic acid and extracted twice with 100 mL water and 100 mL dichloromethane. The dichloromethane phase was dried with sodium sulfate and the solvent was removed by rotary evaporation. The product was purified by column chromatography on silica gel, eluted with 95 % DCM 5 % ethyl acetate. The crude product was used without further purification for the next reaction step. Yield of the crude product: 60 mg (28 %).

**Dye 4**

Compound **12** was synthesized according to literature procedure [124, 132]. The reaction pathway is depicted in Figure S5.

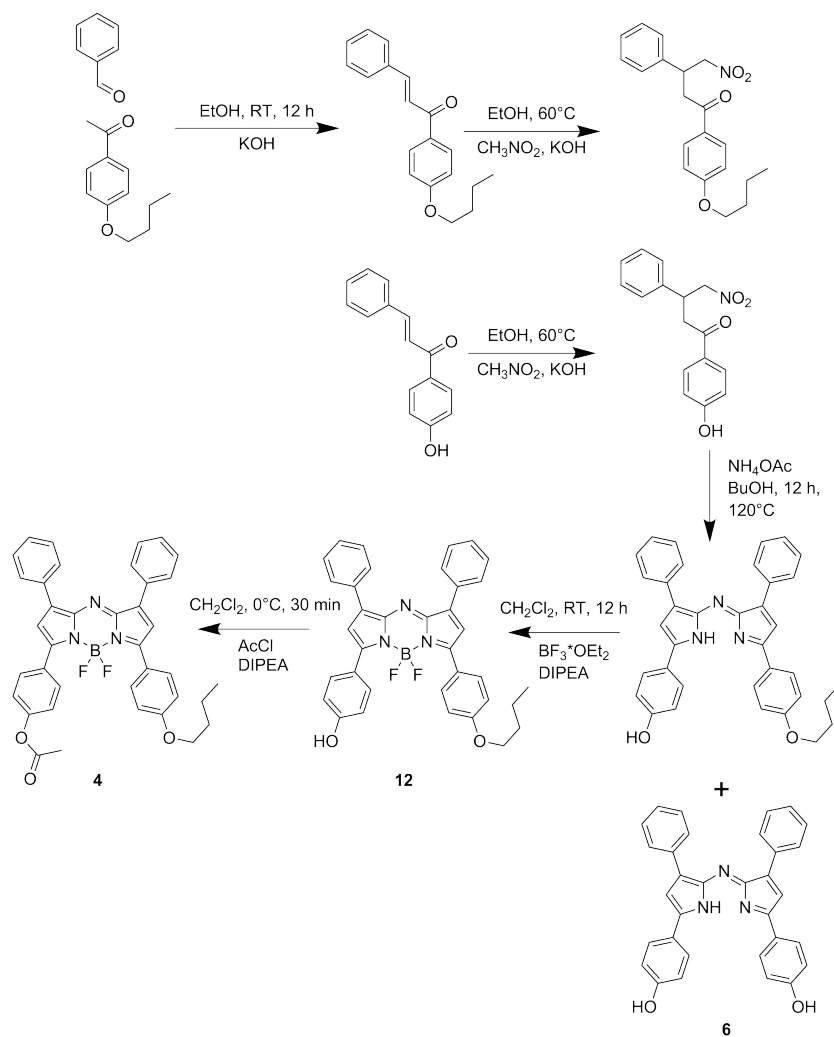


Figure S4.5: Reaction pathway to dye 4.

## 4.7.2 Synthesis of the Polymers

| Polymer 1 | 99 %   | 1 % | 0 %   |
|-----------|--------|-----|-------|
| Polymer 2 | 98.5 % | 1 % | 0.5 % |

Figure S4.6: Composition of the synthesized polymers.

**Polymer 1 (1 % OH)**

4-acryloylmorpholine (4.9 g, 34.7 mmol, 99 eq.) and N-hydroxyethyl acrylamide (37.5  $\mu\text{L}$ , 41.6 mg, 0.35 mmol, 1 eq.) were dissolved in 40 mL deionised water in a 100 mL Schlenk flask. The stabilizer in the 4-acryloylmorpholine was removed by filtration through a short ( $\approx 3$  cm) column of aluminium oxide. A small amount of potassium persulfate ( $\approx 0.5$  mg) was added. The solution was deoxygenated by bubbling argon through the mixture for 10 minutes. Then the reaction mixture was heated to 80 °C for 16 h. The obtained polymer was purified by precipitation in THF and dissolving in DCM twice. Finally, the polymer was precipitated in cyclohexane and dried. Yield: 4.3 g (86 %).

**Polymer 2 (1 %OH, 0.5 % NH<sub>2</sub>)**

4-acryloylmorpholine (1.81 mL, 2.03 g, 13.94 mmol, 98.5 eq.), N-hydroxyethyl acrylamide (15.1  $\mu\text{L}$ , 16.8 mg, 0.141 mmol, 1 eq.) and N-(3-aminopropyl)methacrylamide hydrochloride 98 % (12.9 mg, 0.071 mmol, 0.5 eq.) were dissolved in 20 mL deionised water in a 50 mL Schlenk flask. The stabilizer in the 4-acryloylmorpholine was removed by filtration through a short ( $\approx 3$  cm) column of aluminium oxide. A small amount of potassium persulfate ( $\approx 0.5$  mg) was added. The solution was deoxygenated by bubbling argon through the mixture for 10 minutes. Then the reaction mixture was heated to 80 °C for 16 h. After cooling to room temperature the reaction product was diluted with 20 mL deionized water and 20 mL ethanol, resulting in a solution with 33.3 g L<sup>-1</sup> polymer (assuming 100 % yield).

**4.7.3 Experimental Details on Deployments and Calibration****Deployment Baltic Sea**

The measurements were conducted with the sensors mounted on a CTD rosette during a research cruise on the Baltic Sea in October 2015. The details of the measurements are described elsewhere (see chapter 3).

**Deployment Kiel**

The data were recorded in September 2016 during sensor trials within EU Seventh Framework project “SenseOcean”. Multiple sensor systems were deployed simultaneously on a pontoon

and periodic reference samples were taken. The details of these measurements are described elsewhere [216].

### **Salinity Calibration by Addition of Salt**

The salinity sensitivity of the sensor material **pH-4** was tested by preparing 700 mL of a 50 mM TRIS/TRIS·HCl 1/1 buffer (4.24 g (35 mmol) TRIS + 17.5 mmol HCl) and stepwise addition of NaCl to increase the ionic strength of the buffer solution. The buffer temperature was kept constant at 37 °C throughout the experiment. The initial ionic strength was 25 mM and was increased to 50, 100, 200, 300, 500, 700, and 900 mM by addition of 1.02, 2.04, 4.09, 4.09, 8.18, 8.18, and 8.18 g NaCl. The response of the five optodes and the electrode was measured and the expected response of a spectrophotometric measurement with m-Cresol purple was calculated according to Mosley et al. [96] The pH change of the TRIS buffer was calculated according to Mosley et al. [96] and subtracted from all measurements.

## 4.7.4 Additional Information on Sensor Calibration and Cross-talk

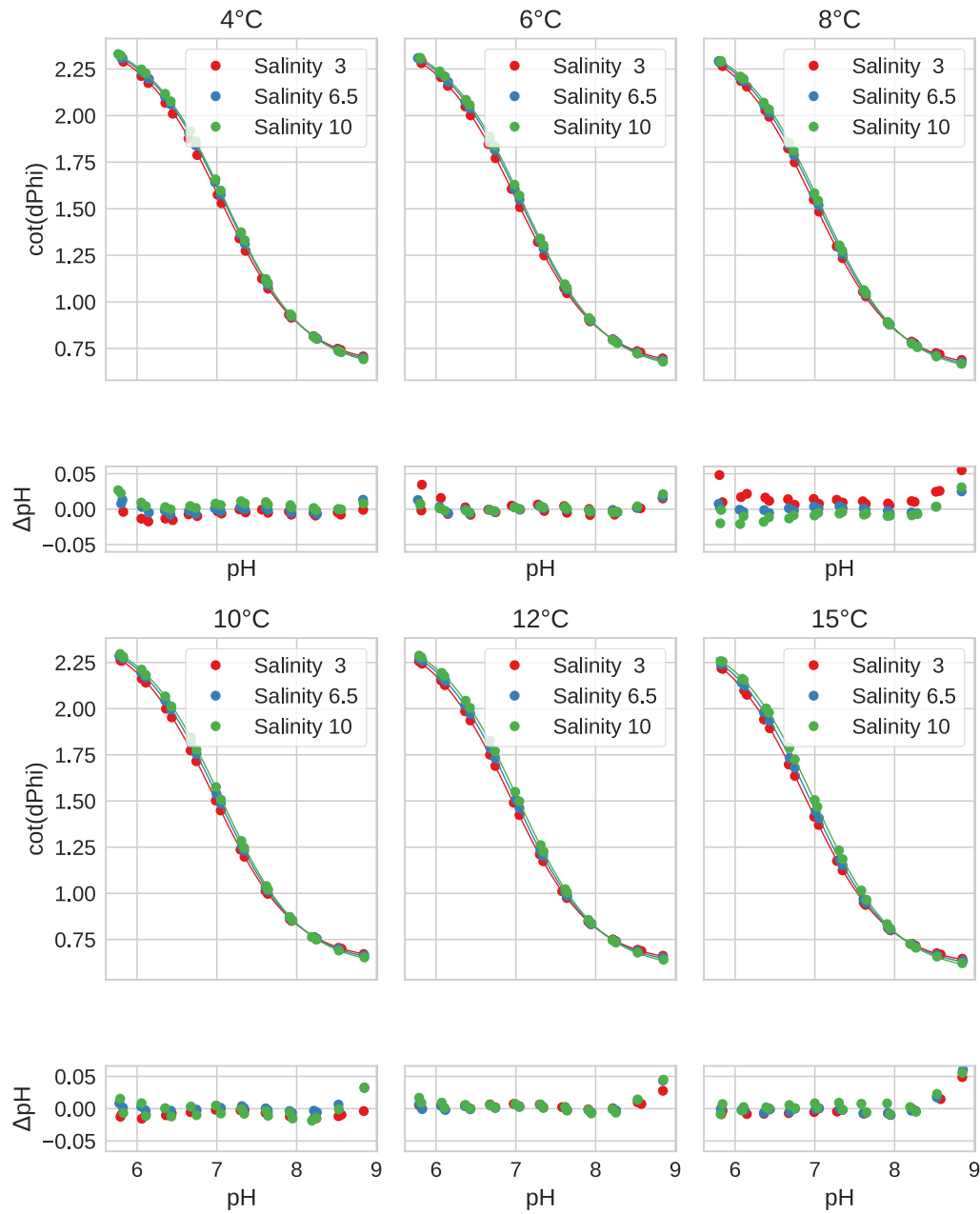


**Figure S4.7:** Calibration curve of the **pH-2** sensing material. Temperature-compensated calibration functions grouped by temperature with corresponding residuals depicted below. The data was fit with eq. 4.3.

**Table S4.1:** Calibration coefficients (eq. 4.3 (and eq. 4.4 for **pH-2**)) of the new sensor materials. Material **pH-1** was characterized at salinity 35 PSU between 10 and 25 °C. Material **pH-2** was characterized between 4 and 15 °C and salinity 3 to 10 PSU. The materials **pH-3** and **pH-4** were characterized between 0 and 25 °C at salinity 35 PSU. Material

| Material | $pK_a$ | $pK_{a_t}$ | $pK_{a_S}$ | $Top_t$  | $Bottom_T$ | $Bottom_S$ | slope |
|----------|--------|------------|------------|----------|------------|------------|-------|
| pH-1     | 7.461  | -0.0177    | -          | -0.00377 | -0.0131    | -          | 1.131 |
| pH-2     | 7.236  | -0.0126    | 0.0122     | -0.00084 | -0.0125    | -0.0045    | 1.150 |
| pH-3     | 7.240  | -0.0104    | -          | 0.00289  | -0.0109    | -          | 1.132 |
| pH-4     | 8.050  | -0.0114    | -          | 0.00033  | -0.0055    | -          | 1.173 |

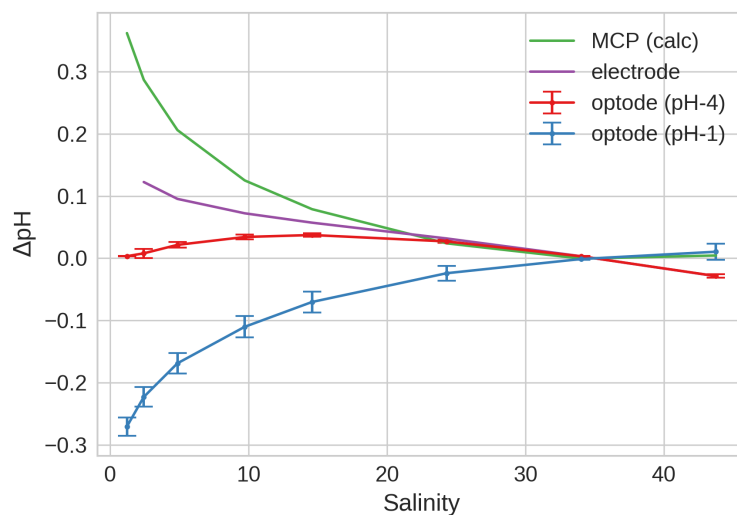


**Figure S4.8:** Salinity dependence of the **pH-4** sensor material compared to that of the pH glass electrode and spectrophotometric system based on m-cresol Purple (MCP). 5 sensors were submerged in a TRIS-buffer and sodium chloride was added in portions to increase the salinity of the solution.

## 4.7.5 NMR and MS spectra of the indicator dyes

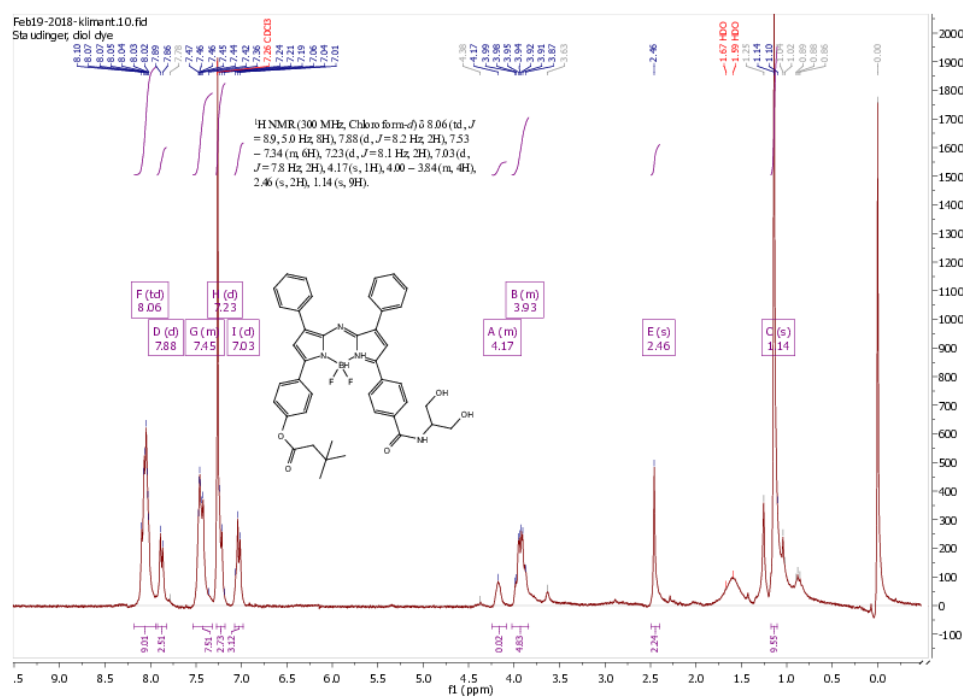


Figure S4.9:  $^1\text{H}$ -NMR spectrum (300 MHz, Chloroform-d) of indicator 2.

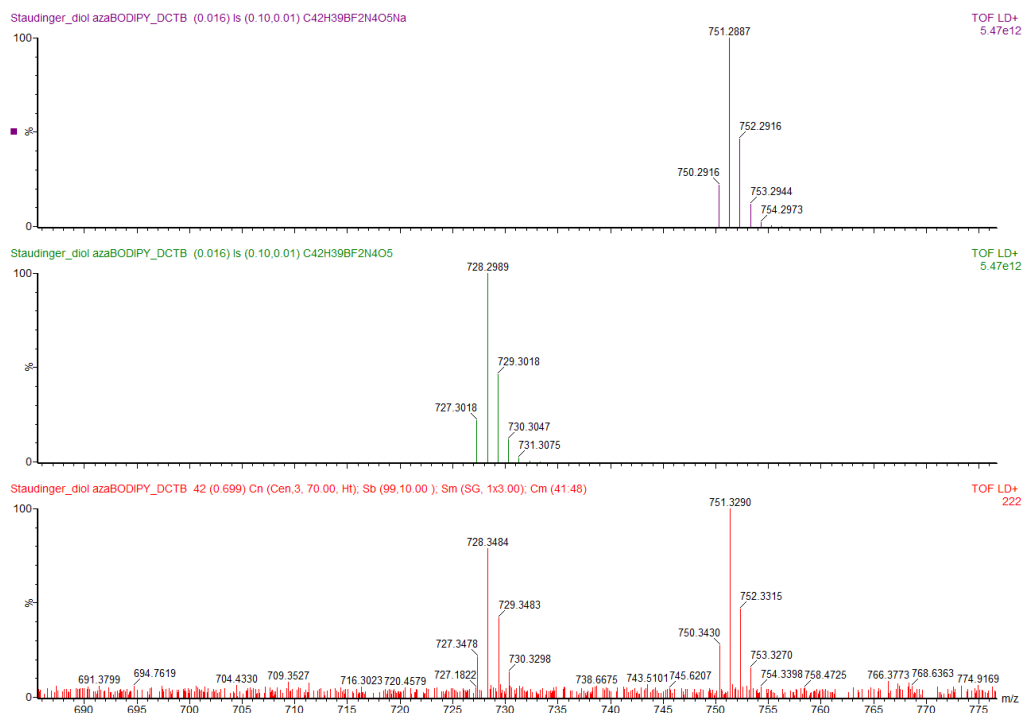


Figure S4.10: Mass spectrum (MALDI-TOF) of indicator 2.

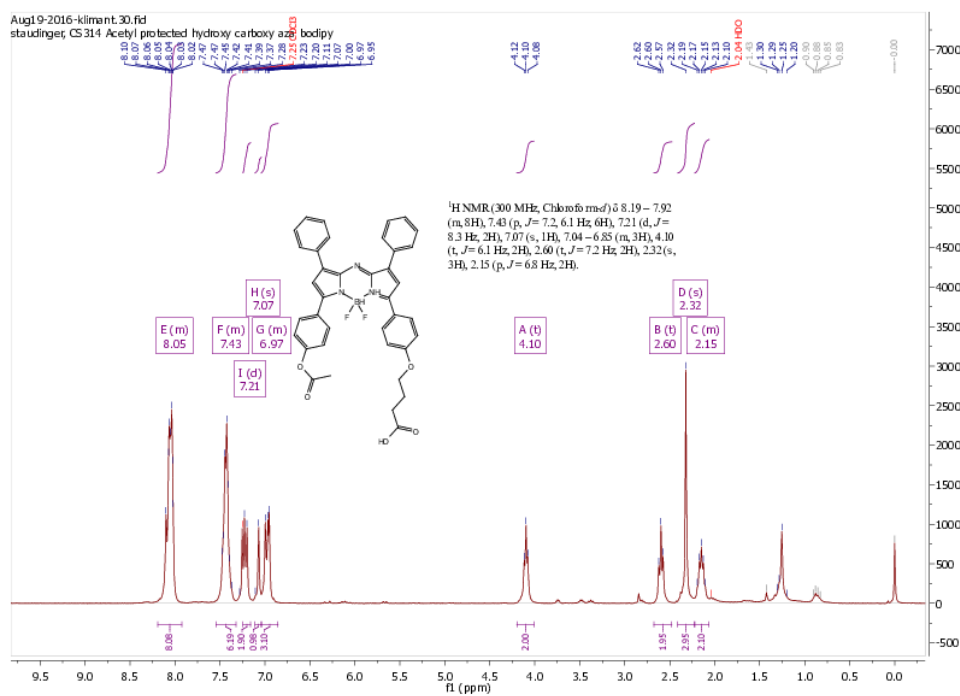
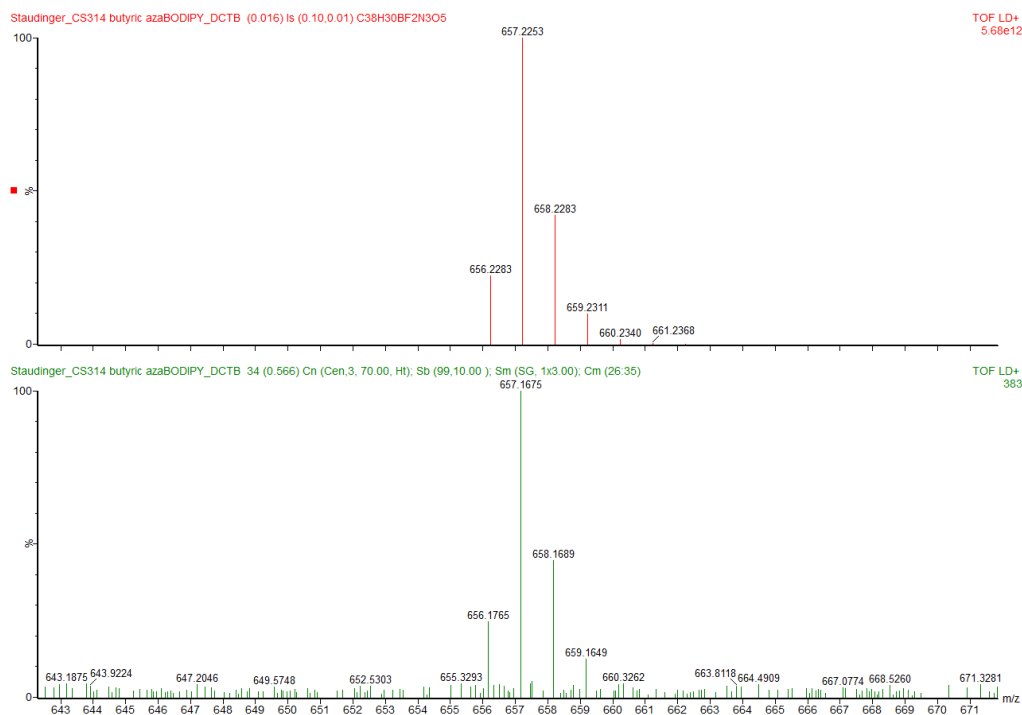
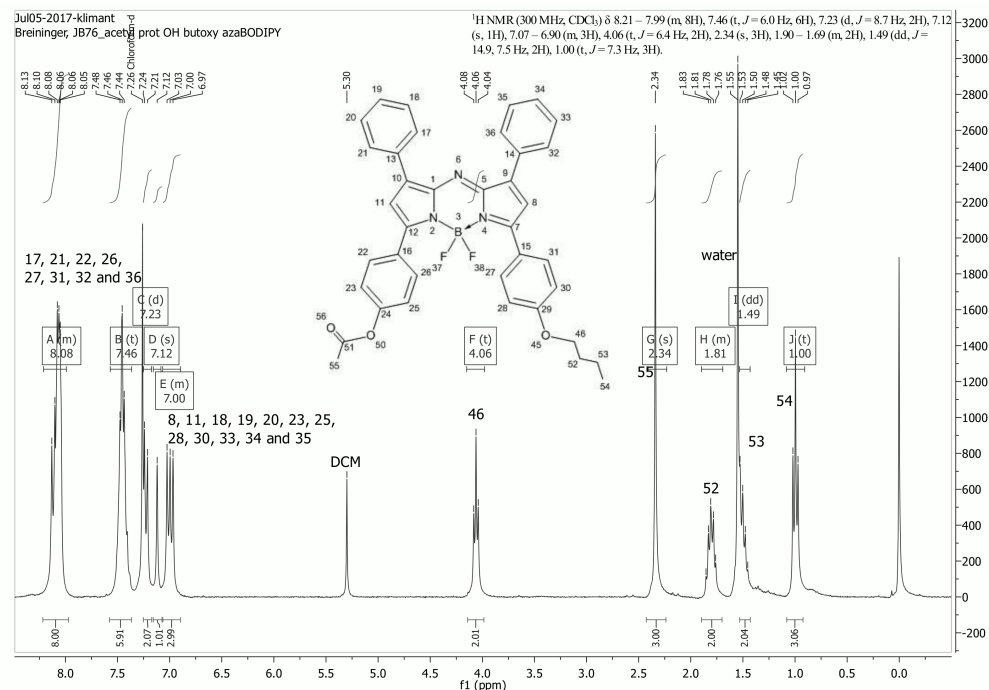


Figure S4.11:  $^1\text{H-NMR}$  spectrum (300 MHz, Chloroform- $d$ ) of indicator 3.

Figure S4.12: Mass spectrum (MALDI-TOF) of indicator **3**.Figure S4.13: <sup>1</sup>H-NMR spectrum (300 MHz, Chloroform-d) of indicator **4**.

---

# 5 Near-infrared aza-BODIPY Dyes with Fluorescence Response Solely due to Photoinduced Electron Transfer: New pH Indicators Covering the Neutral to Highly Alkaline Range

## 5.1 Preface to the Manuscript

This manuscript was prepared for submission to "Analyst" and is focused on the properties of novel aza-BODIPY pH indicators.

The motivation behind this work was the improvement of the spectral properties of existing aza-BODIPYs. While aza-BODIPYs have many favorable properties (high QY, molar absorption coefficient, red absorption, NIR emission, photostability), they have a minor drawback in their quenching behavior. Upon deprotonation the dyes are quenched by Photoinduced Electron Transfer (PET) and the absorption spectrum of the indicators shifts to higher wavelengths due to Intramolecular Charge Transfer (ICT). This shifted absorption spectrum has a large overlap with the indicator's emission and causes re-absorption of fluorescence as well as strong Förster Resonance Energy Transfer (FRET). Both effects reduce the brightness of the sensor material and induce a concentration dependence of the observed  $pK_a$ . The pH dependent absorption of the sensor material also complicates applications in multi-component systems (e.g. light harvesting, broad-range sensor materials, etc.). For these reasons, an elimination of the ICT is desirable.

aza-BODIPYs with pure PET quenching were already reported, but suffered from poor quantum yield or high synthetic effort. In this publication these challenges were overcome

by introducing the quenching hydroxy-moiety in meta-position to eliminate the conjugation. Thereby, a new set of purely PET based aza-BODIPY indicators was obtained. The non-conjugated position of the hydroxy-group also reduced the electron withdrawing effect of the core of the dye and resulted in exceptionally high  $pK_a$  values of the indicators. By introduction of two electron withdrawing chlorine groups, a dye with a  $pK_a$  value suitable for physiological conditions could be obtained.

An application of the novel indicators in a ratiometric light harvesting scheme for imaging was demonstrated. The high  $pK_a$  values and constant absorption behavior were utilized for pH imaging on concrete surfaces by Bernhard Müller and Cyrill Grengg and resulted in a manuscript, which was submitted to "Cement and Concrete Research - Journal". A second manuscript which utilized a broad-range concept for concrete measurements with enhanced dynamic range is in preparation for submission to "RILEM - Technical Letters".

# Near-infrared aza-BODIPY Dyes with Fluorescence Response Solely due to Photoinduced Electron Transfer: New pH Indicators Covering the Neutral to Highly Alkaline Range

Authors: Christoph Staudinger, Johanna Breininger, Ingo Klimant, Sergey M Borisov\*

Institute of Analytical Chemistry and Food Chemistry, Graz University of Technology, Stremayr-gasse 9, 8010, Graz, Austria

\*email: sergey.borisov@tugraz.at

Keywords: PET, light harvesting, optical sensor, optode

## 5.2 Abstract

New aza-BODIPY pH indicator dyes, whose spectral properties are modulated solely by photoinduced electron transfer (PET) are presented. This was achieved by shifting the pH sensitive hydroxyl to the meta-position of a phenyl substituent, which eliminates the conjugation to the aza-BODIPY chromophore. The new dyes show reversible "on" – "off" fluorescence response upon deprotonation of the receptor. In contrast to state-of-the-art indicators of the aza-BODIPY family, the new systems do not show changes in the absorption spectrum upon deprotonation of the receptor, eliminating potential changes in the efficiency of the inner filter effect and Förster resonance energy transfer (FRET). Introduction of electron-withdrawing or electron donating groups in the receptor results in a palette of indicators suitable for measurements from physiological (pH 7) to very alkaline (pH 13) conditions. Suitability of the new dyes as acceptors in light harvesting systems and for imaging of pH distribution is demonstrated.

## 5.3 Introduction

pH is one of the most important analytes in many applications [108] (e.g. chemical industry, biotechnology [233], marine monitoring [140]). While the pH electrode is still the most common measurement device, optical pH sensor materials are receiving increasing attention in the last

years, due to their many favorable properties. They can be deployed as inexpensive single-use sensors [233], or can be read-out remotely with optical fibers, they are not influenced by electromagnetic interferences and are available in a wide variety of formats. For instance, optical pH sensors are available as larger sensor films for pH imaging [109, 110], small spots integrated in microfluidic devices [234–238] or in microtiter plates [144], on tapered fibers with only 8-140  $\mu\text{m}$  tip diameter [114, 115] or in the form of nanoparticles [111, 113].

The sensor materials utilize indicators belonging to different chromophore classes (fluoresceins [143], rhodamines [145, 146], perylenes [148, 149], 1,4-diketopyrrolo-pyrroles [239], HPTS [139, 167], BODIPYs [150–154] and aza-BODIPYs [124, 132, 154–158]). Among them tetraaryl-aza-BODIPYs are especially interesting, due to absorption and emission in the red/NIR part of the spectrum, high molar absorption coefficients and extreme photostability [124, 132]. Moreover, their  $\text{pK}_a$  is easily tunable and different dyes suitable for measurements from pH 1.5 to 13 are available [124]. pH sensitivity is usually achieved by a hydroxyl-group in para-position of one of the aryl-substituents. Deprotonation of the phenol receptor results in fluorescence quenching, due to photoinduced electron transfer (PET). However, this is accompanied by the strong bathochromic shift of the absorption spectrum indicating an additional intramolecular charge transfer (ICT) mechanism [132]. Notably, spectral shift due to ICT is also observed for aniline-substituted pH-sensitive aza-BODIPY dyes [156]. Although such behavior is usually not critical for most applications, it definitely results in a more complex sensor behavior. First, the pH dependent change of the absorption in the sensor materials results in a change of the inner filter effect, the magnitude of this effect being dependent on dye concentration and thickness of the sensor foil. Second, in a multi-component system (consisting e.g. of a pH indicator and a reference dye) both luminescence enhancement of the second component (due to lower absorption of the indicator at the excitation wavelength) and its quenching (due to the inner-filter effect caused by the deprotonated form of the indicator) is possible. Third, since the absorption spectrum of the non-emissive deprotonated form of the indicator shows very good overlap with the emission spectrum of the protonated form and the concentration of the indicator in the sensor is fairly high (1-5 mM), quenching via Förster resonance energy transfer (FRET) is favored. Evidently, pure PET-based dyes make it possible to overcome the above limitations. Moreover, they would be attractive for application in light-harvesting systems which make it possible to overcome the limitation of the small Stokes shifts typical for fluorescent dyes. For the latter, the excitation in the maximum of the absorption band is not

possible since the excitation and emission light cannot be fully separated. In the light-harvesting system excitation in the absorption maximum of the energy donor allows utilization of the high molar absorption coefficients of the donor due to the large effective Stokes shift. This allows significant enhancement of the sensor brightness and enables thinner sensing layers and therefore fast responding sensor materials.

So far, only a few aza-BODIPY dyes with a nearly pH independent absorption spectrum have been reported. The dyes decorated with a non-conjugated spacer group between the dye and the PET-group [124] require significantly higher synthetic effort and cover only very acidic and very basic the pH values. A dye bearing a hydroxyl group in the meta-position of the conjugated aryl substituent featured about 20 nm hypsochromic shift of the absorption spectrum and a  $\approx$  2-fold decrease of the fluorescence quantum yield compared to para-substituted aza-BODIPYs [132], which are serious drawbacks.

Herein we present 5 new aza-BODIPY pH indicator dyes which are decorated with the hydroxyl group in meta-position of an aryl substituent. This receptor group is responsible for fluorescence quenching via PET effect but neither induces the pH dependency of the absorption spectra nor negatively affects the fluorescence quantum yields. Due to electronic separation of the OH group from the electron-withdrawing core, the new dyes feature significantly higher pKa values compared to the state-of-the-art aza-BODIPY indicators thus covering the pH range from  $\approx$  7 to 13. While one of the new indicators almost ideally fits the physiologically relevant conditions, the other representatives are attractive for monitoring pH in concrete [240] and studies of alkaliphilic bacteria [241].

## 5.4 Experimental

### 5.4.1 Materials

4'-butoxyacetophenone, 3-hydroxybenzaldehyde, 4'-methoxyacetophenone, diisopropylethylamine (DIPEA), benzaldehyde, 3-hydroxy-4-methoxybenzaldehyde, and boron trifluoride diethyl etherate were purchased from TCI Europe ([www.tcichemicals.com](http://www.tcichemicals.com)). 4'-hydroxychalcone and 4-methoxybenzaldehyde were bought from ABCR ([www.abcr.de](http://www.abcr.de)). 2,4-dichloro-3-hydroxybenzaldehyde and 2,6-difluoro-3-hydroxybenzaldehyde were obtained from Fluorochem ([www.fluorochem.co.uk](http://www.fluorochem.co.uk)). 2-Chloro-3-hydroxybenzaldehyde, nitromethane, ammonium acetate, potassium carbonate, trifluoroacetic acid and anhydrous sodium sulfate were purchased from

Sigma Aldrich ([www.sigmaaldrich.com](http://www.sigmaaldrich.com)). Deuterated chloroform ( $\text{CDCl}_3$ ) was obtained from Euriso-top ([www.eurisotop.com](http://www.eurisotop.com)). All other solvents (synthesis grade) as well as sodium chloride, potassium persulfate and the buffer salts (tris(hydroxymethyl)aminomethane (TRIS), bis(2-hydroxyethyl)amino-tris(hydroxymethyl)methane (BIS-TRIS), 2-morpholin-4-ylethanesulfonic acid (MES) 2-(cyclohexylamino)ethanesulfonic acid (CHES), 3-(cyclohexylamino)-1-propanesulfonic acid (CAPS) and sodium dihydrogen phosphate were purchased from Carl Roth ([www.roth.de](http://www.roth.de)). Silica-gel (0.04-0.063 mm) and aluminium oxide were bought from Acros ([www.fishersci.com](http://www.fishersci.com)). Polyurethane hydrogel (Hydromed D4) was purchased from Advan-Source biomaterials ([www.advbiomaterials.com](http://www.advbiomaterials.com)). Poly(ethylene glycol terephthalate) support (PET) was from Pütz ([www.puetz-folien.com](http://www.puetz-folien.com)). 5,5-difluoro-1,3,7,9-tetraphenyl-5*H*-4 $\lambda^4$ ,5 $\lambda^4$ -dipyrrolo[1,2-*c*:2',1'-*f*][1,3,5,2]triazaborinine (tetraphenyl aza-BODIPY), 4-(5,5-difluoro-7-(4-hydroxyphenyl)-1,9-diphenyl-5*H*-4 $\lambda^4$ ,5 $\lambda^4$ -dipyrrolo[1,2-*c*:2',1'-*f*][1,3,5,2]triazaborinin-3-yl)-*N*-dodecylbenzamide (hydroxy dodecylamide aza-BODIPY), 3,7-bis(4-butoxyphenyl)-5,5-difluoro-1,9-diphenyl-5*H*-4 $\lambda^4$ ,5 $\lambda^4$ -dipyrrolo[1,2-*c*:2',1'-*f*][1,3,5,2]triazaborinine (dibutoxy aza-BODIPY) and 1-(4-butoxyphenyl)-4-nitro-3-phenylbutan-1-one (d3) were prepared according to literature procedures [124, 132, 242].

### 5.4.2 Methods

Buffers with concentrations of 100 mM and pH values ranging from 5 to 13 were prepared with piperazine, MES, bis-TRIS, TRIS, CHES or CAPS. The pH, adjusted by adding 1 M HCl or 1 M NaOH aqueous solution, was controlled with a SevenEasy™ pH meter (Mettler Toledo, [www.mt.com](http://www.mt.com)) equipped with a glass electrode (SenTix® HW, WTW, [www.wtw.com](http://www.wtw.com)). The pH meter was calibrated using standard buffer solutions with pH of 4.01, 7.01 and 10.01 (Hanna instruments, [www.hannainstruments.at](http://www.hannainstruments.at)). The ionic strength of the buffers was set to 100 mM with NaCl as background electrolyte. The NMR spectra were acquired on a 300 MHz instrument (Bruker) in  $\text{CDCl}_3$  with tetramethylsilane (TMS) as a standard. MALDI-TOF mass spectra were recorded on a Micromass TofSpec 2E in reflectron mode at an accelerating voltage of +20 kV.

Absorption measurements were performed on a Cary 50 UV-VIS spectrophotometer from Varian, Palo Alto, United States ([www.varianinc.com](http://www.varianinc.com)). Emission and excitation spectra were recorded on a Fluorolog®3 Spectrofluorometer from Horiba Scientific ([www.horiba.com](http://www.horiba.com)) equipped with a R2658 photomultiplier tube from Hamamatsu ([www.hamamatsu.com](http://www.hamamatsu.com)) or on

a fluorescence spectrophotometer F-7000 from Hitachi ([www.hitachi-hightech.com](http://www.hitachi-hightech.com)). 100-OS precision cuvettes from Hellma Analytics with a light path of 10 mm were used ([www.hellma-analytics.com](http://www.hellma-analytics.com)). The fluorescence quantum yields were determined relative to dibutoxy aza-BODIPY dye ( $\Phi = 36\%$  in chloroform) [107].

pH sensing behavior of the dyes was investigated by diluting the THF stock solution (0.5 mg/mL) with EtOH, and subsequently mixing the resulting solution with buffer in a ratio of 1 : 1. The concentration of the dyes in the final solution was  $\approx 1.5 \cdot 10^{-6}$  M. pH calibration of the dyes physically entrapped in a hydrogel D4 was performed in glass cuvettes (1 cm path length) with the foils positioned diagonally. The cuvette was filled with buffers and washed with water after each pH buffer change.

The imaging experiments were conducted with the AD-130GE RGB + NIR camera from JAI ([www.jai.com](http://www.jai.com)). A high power yellow LED array with 12 LEDs (“12x OSRAM Oslon SSL 80 gelb Rund-Platine”) with a passive cooler and a lens array with an emission angle of  $30^\circ$  (all obtained from LED-Tech.de Optoelectronics ([www.led-tech.de](http://www.led-tech.de))) was used as excitation source. The combination of the emission filters (a foil filter (“026 bright red”) from LEE filters ([www.leefilters.com](http://www.leefilters.com)) and RG640 glass filter from Hoya ([www.hoyafilter.com](http://www.hoyafilter.com))) was mounted in front of the camera lens. The sensor material was glued to the bottom of a plastic petri dish and submerged in the buffers during the measurements. Measurement time was 2000 ms and 600 ms for the RGB and NIR channels, respectively. The images were recorded with 12 bit color depth per channel.

Calibration curves and apparent  $pK_a$  values were obtained by fitting the plot of fluorescence intensity vs. pH with the Boltzmann sigmoid:

$$I = Bottom + \frac{Top - Bottom}{1 + 10^{\frac{pH - pK_a}{slope}}} \quad (5.1)$$

where  $I$  is the fluorescence intensity,  $Bottom$  and  $Top$  are the lower and upper limits of the fluorescence intensity, respectively.  $pK_a$  is the apparent  $pK_a$  value and  $slope$  describes the slope in the point of inflection.

### Sensor foil preparation

Sensor foils were prepared via knife-coating the “cocktail” containing hydromed D4 (10 % wt. in respect to the solvent) and dye (0.2 % wt. in respect to the polymer) in THF onto the PET

support. The spacers of 1 Mil (25  $\mu\text{m}$ ) or 3 Mil (76  $\mu\text{m}$ ) were used resulting in  $\approx$  3 and 8  $\mu\text{m}$  thick sensing layer after solvent evaporation.

### 5.4.3 Synthesis

The synthetic procedures for the intermediates and NMR and MS spectra of the indicators can be found in the supporting information.

#### **3-(3,7,9-tris(4-butoxyphenyl)-5,5-difluoro-5*H*-5 $\lambda^4$ ,6 $\lambda^4$ -dipyrrolo[1,2-*c*:2',1'-*f*][1,3,5,2]triazaborinin-1-yl)phenol (Indicator 1)**

44.6 mg **e**<sub>1</sub> (65.41  $\mu\text{mol}$ , 1.00 eq) were dissolved in dry DCM under argon atmosphere in a Schlenk flask. 230  $\mu\text{L}$  N,N-diisopropylethylamine (1.32 mmol, 20.19 eq) and 160  $\mu\text{L}$  boron trifluoride diethyl etherate (1.30 mmol, 19.82 eq) were added dropwise. The solution was stirred at room temperature for 3 h during which the solution turned grey-blue. After a quantitative conversion of the ligand into the complex (monitored by TLC; DCM:CH 3:1), the solution was partitioned between DCM and aqueous NaHCO<sub>3</sub> solution (3 x 25 mL), dried over sodium sulfate and the solvent was removed under reduced pressure. The crude product was purified by column chromatography (silica-gel, DCM:CH 3:1, detection by TLC with DCM:CH 3:1 and UV/VIS spectroscopy) and recrystallization from MeOH to yield red-purple crystals.

Yield: 26.1 mg (55 %), red-purple crystals.

MS (MALDI): 729.3868 (calculated: 729.3557)

<sup>1</sup>H NMR (300 MHz, chloroform-*d*):  $\delta$  = 8.04 (t, *J* = 7.9 Hz, 6H), 7.61 (s, 1H), 7.50 (d, *J* = 7.5 Hz, 1H), 7.30 (d, *J* = 7.8 Hz, 1H), 7.06 – 6.90 (m, *J* = 8.0 Hz, 8H), 6.86 (d, *J* = 7.4 Hz, 1H), 5.06 (s, 1H), 4.13 – 3.90 (m, 6H), 1.88 – 1.70 (m, 6H), 1.51 (dd, *J* = 14.9, 7.4 Hz, 6H), 0.99 (t, *J* = 7.3 Hz, 9H).

<sup>13</sup>C APT NMR (76 MHz, chloroform-*d*):  $\delta$  = 161.83, 161.44, 160.73, 159.26, 156.72, 155.91, 145.83, 144.78, 143.58, 141.34, 134.28, 131.83, 131.54, 131.01, 129.76, 125.12, 124.23, 123.94, 121.49, 118.24, 117.44, 116.42, 116.01, 114.83, 77.16, 67.97, 31.35, 19.38, 13.98.

#### **2-chloro-3-(3,7,9-tris(4-butoxyphenyl)-5,5-difluoro-5*H*-5 $\lambda^4$ ,6 $\lambda^4$ -dipyrrolo[1,2-*c*:2',1'-*f*][1,3,5,2]triazaborinin-1-yl)phenol (Indicator 2)**

Indicator **2** was prepared analogously to indicator **1** from 62.0 mg **e**<sub>2</sub> (68.55  $\mu\text{mol}$ ).

Yield: 25.8 mg (39 %), red crystals

MS (MALDI): 763.2911 (calculated: 763.3168)

<sup>1</sup>H NMR (300 MHz, chloroform-d):  $\delta$  = 8.19 – 7.98 (m,  $J$  = 18.0, 8.9 Hz, 6H), 7.39 – 7.28 (m,  $J$  = 13.0, 6.9 Hz, 2H), 7.17 – 7.07 (m, 2H), 7.05 – 6.93 (m, 5H), 6.87 (d,  $J$  = 8.7 Hz, 2H), 5.84 (s, 1H), 4.03 (dt,  $J$  = 12.5, 6.3 Hz, 6H), 1.88 – 1.71 (m,  $J$  = 7.8, 5.7 Hz, 6H), 1.57 – 1.47 (m,  $J$  = 15.0, 7.5 Hz, 6H), 1.00 (t,  $J$  = 7.3 Hz, 9H).

<sup>13</sup>C APT NMR (76 MHz, chloroform-d):  $\delta$  = 162.06, 161.42, 160.80, 160.40, 155.51, 152.15, 146.41, 144.96, 144.00, 138.75, 132.20, 131.97, 131.60, 130.85, 127.23, 125.77, 124.80, 124.27, 123.82, 121.77, 119.60, 117.60, 116.11, 114.84, 77.16, 67.96, 31.37, 19.38, 13.97.

**2,6-dichloro-3-(5,5-difluoro-3,7,9-tris(4-methoxyphenyl)-5*H*-5 $\lambda^4$ ,6 $\lambda^4$ -dipyrrolo[1,2-*c*:2',1'-*f*][1,3,5,2]triazaborinin-1-yl)phenol (Indicator 3)**

Indicator **3** was prepared analogously to indicator **1** from 60.2 mg **e**<sub>3</sub> (96.39  $\mu$ mol).

Yield: 41.3 mg (63 %), green crystals

MS (MALDI): 671.1675 (calculated: 671.1368)

<sup>1</sup>H NMR (300 MHz, chloroform-d):  $\delta$  = 8.20 – 7.95 (m, 6H), 7.35 (d,  $J$  = 5.7 Hz, 2H), 7.15 (s, 1H), 7.08 – 6.97 (m,  $J$  = 10.8, 4.0 Hz, 5H), 6.91 (d,  $J$  = 8.4 Hz, 2H), 3.89 (d,  $J$  = 3.2 Hz, 9H).

**3-(5,5-difluoro-3,7,9-tris(4-methoxyphenyl)-5*H*-5 $\lambda^4$ ,6 $\lambda^4$ -dipyrrolo[1,2-*c*:2',1'-*f*][1,3,5,2]triazaborinin-1-yl)-2,4-difluorophenol (Indicator 4)**

Indicator **4** was prepared analogously to indicator **1** from 64.7 mg **e**<sub>4</sub> (109.4  $\mu$ mol).

Yield: 36.9 mg (53 %), purple metallic crystals

MS (MALDI): 639.1469 (calculated: 639.1959)

<sup>1</sup>H NMR (300 MHz, chloroform-d):  $\delta$  = 8.16 – 7.97 (m, 6H), 7.09 – 6.82 (m, 10H), 3.96 – 3.78 (m, 9H).

<sup>13</sup>C APT NMR (76 MHz, chloroform-d):  $\delta$  = 162.56, 161.68, 161.44, 161.30, 155.61, 152.16, 149.69, 146.58, 146.40, 144.55, 140.68, 140.43, 132.10, 131.49, 130.89, 130.10, 124.98, 124.53, 123.97, 122.12, 118.02, 117.13, 117.01, 114.48, 114.37, 114.26, 111.47, 111.15, 77.16, 55.54.

**5-(5,5-difluoro-3,7,9-tris(4-methoxyphenyl)-5*H*-5 $\lambda^4$ ,6 $\lambda^4$ -dipyrrolo[1,2-*c*:2',1'-*f*][1,3,5,2]triazaborinin-1-yl)-2-methoxyphenol (Indicator 5)**

Indicator **5** was prepared analogously to indicator **1** from 62.0 mg **e**<sub>5</sub> (103.73  $\mu$ mol, 1.00 eq).

Yield: 66.4 mg (98 %), purple metallic crystals

MS (MALDI): 645.2808 (calculated: 645.2617)

$^1\text{H}$  NMR (300 MHz, chloroform- $d$ ):  $\delta$  = 8.17 – 8.00 (m,  $J$  = 8.6, 3.5 Hz, 6H), 7.79 (d,  $J$  = 1.8 Hz, 1H), 7.64 (dd,  $J$  = 8.4, 1.7 Hz, 1H), 7.49 (t,  $J$  = 7.3 Hz, 2H), 7.42 (d,  $J$  = 7.0 Hz, 1H), 7.07 – 6.87 (m, 7H), 5.64 (s, 1H), 4.05 (t,  $J$  = 6.4 Hz, 2H), 3.97 (s, 3H), 3.89 (s, 3H), 1.86 – 1.74 (m,  $J$  = 14.5, 6.6 Hz, 2H), 1.56 (s, 2H), 0.99 (t,  $J$  = 7.3 Hz, 3H).

## 5.5 Results and Discussion

### 5.5.1 Synthesis

The synthesis of the indicators **1-5** was conducted based on the well-known route via nitro-chalkones (Fig 5.1) [242]. Here, two different nitro-chalkones ( $\mathbf{b}_x$  and  $\mathbf{d}_x$ ) are reacted to give the unsymmetrical product ( $\mathbf{e}_x$ ) along with two symmetrical derivatives bearing no and 2 pH sensing functionalities. Partly due to this reason and partly because crude nitro-chalkones were used, the yield of the aimed product in the condensation reaction is typically low (5-10%). Nevertheless, it is still acceptable since both chalkones and nitrochalkones can be prepared in large scale from inexpensive chemicals. The ligand  $\mathbf{e}_x$  is converted to the corresponding  $\text{BF}_2$  chelate (indicator  $\mathbf{x}$ ) with a good yield (40-90%). The introduction of substituents on all phenyl-rings improved the solubility of the dyes and simplified the chromatographic separation.

### 5.5.2 Photophysical Properties

The spectral properties of the new dyes are very similar to those of the reported representatives of the aza-BODIPY family (Fig. 5.2). The dyes show the absorption and emission maximum in NIR part of the spectrum. As can be seen, the spectral properties of the new dyes are very similar (Table 5.1) and the molar absorption coefficients are around  $80\,000\text{ L mol}^{-1}\text{ cm}^{-1}$ , a typical value for this dye class. The fluorescence quantum yield is about 25%, except for the indicator **5** whose  $\Phi$  is  $\approx$  2-fold lower. Fluorescence decay times show the same trend with the values of  $\approx$  2.6 ns for indicators **1-4** and only  $\approx$  1.5 ns for indicator **5**. The most important structural difference between indicators **1-4** and indicator **5** is the methoxy-group in the *o*-position to the hydroxyl group. This provides the possibility of hydrogen bonding between these two groups and might cause the reduction in quantum yield and fluorescence lifetime. In conclusion, the dyes **1-4** overcome the major limitation of the previously reported

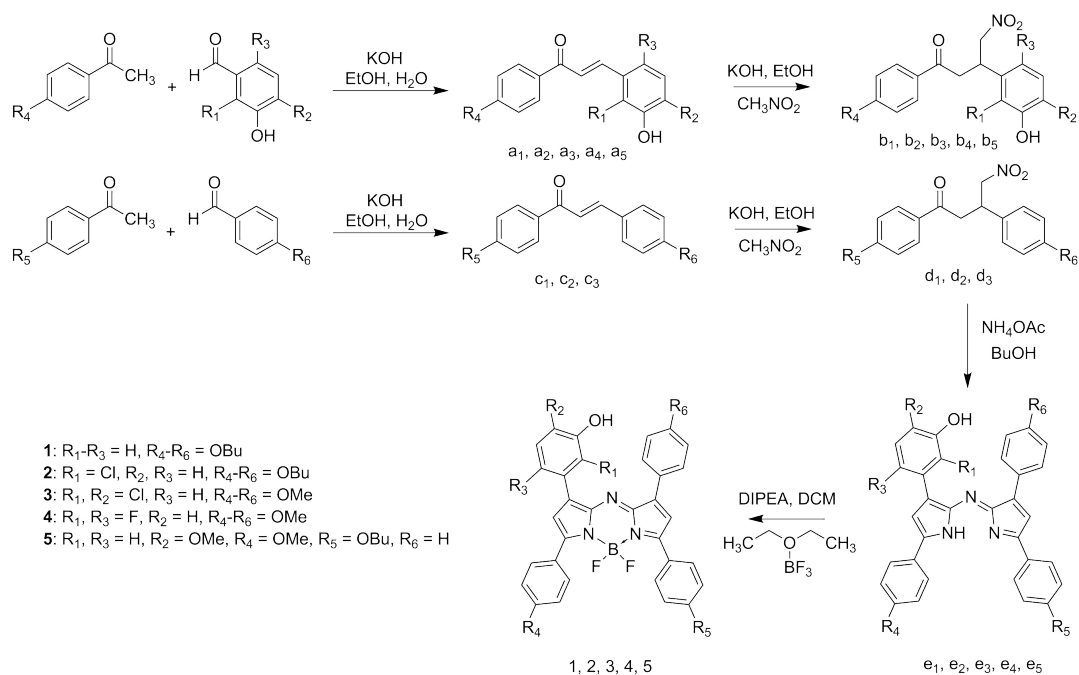


**Figure 5.1:** Synthetic route to the new aza-BODIPY dyes. Intermediates with indices belong to the respective dye.

purely PET-based aza-BODIPY dye with a meta-hydroxyl group in the “lower” phenyl ring which possessed  $\Phi$  of 10 % [132].

### 5.5.3 pH Sensing Properties

Figure 5.2a shows pH dependency of the absorption and emission spectra for indicator **3** (the spectral changes for other indicators are almost identical). It is evident that deprotonation of the hydroxyl group shows almost no effect on the absorption spectra, while it results in complete quenching of the fluorescence of the indicator. This confirms that PET is the only mechanism responsible for the spectral changes and ICT is not involved. On the contrary, a state-of-the-art aza-BODIPY indicator with a hydroxyl group in the para-position shows  $\approx 55$  nm bathochromic shift of the absorption upon deprotonation, due to enhancement of the ICT effect (Fig. 5.2c). This behavior is undesired, due to the increasing overlap between the emission of the protonated form and the absorption of the non-emissive deprotonated form of the indicator, as it promotes fluorescence quenching by FRET. Evidently, the new dyes overcome this drawback. The pH-independent absorption of the new dyes is particularly advantageous in case broad-range sensors (obtained by mixing several indicators with different pK<sub>a</sub> values)

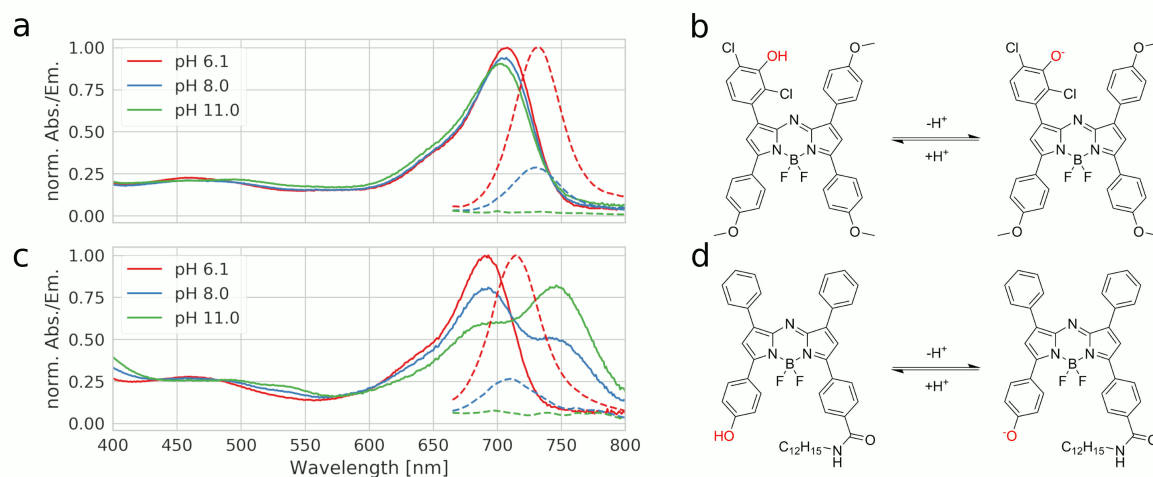


**Figure 5.2:** pH dependence of absorption (solid lines) and emission spectra (dashed lines) of the indicator **3** (a) and state-of-the-art hydroxy-aza-BODIPY pH indicator [124] (c) in Hydrogel D4; b and d show the pH equilibria for the respective dyes.

and in multi-parameter sensors (obtained by combination of probes for different species in one material) since undesired enhancement or quenching of luminescence of the components, due to modulation of the inner filter effect is avoided.

The fluorescence response of the new dyes to pH is typical for the "on"–"off" indicators (Fig. 5.3b). Generally, the  $pK_a$  values (Table 5.1) are significantly higher than for the state-of-the-art aza-BODIPY dye with conjugated phenol with the same substitution character. The relatively high  $pK_a$  values of the new dyes can be explained by the electronic decoupling of the hydroxyl group from the electron withdrawing core of the dye. Interestingly, the apparent  $pK_a$  for dye **1** is even higher than for the phenol ( $pK_a = 9.99$  [243]). This can be explained by fairly hydrophobic character of the chromophore creating a microenvironment, where the more polar anionic form is less stabilized than the uncharged form. Indicator **2**, which is decorated with a single chlorine atom in the ortho-position towards hydroxyl group, features an only slightly lower  $pK_a$  value (Table 5.1). Two fluorine atoms placed into ortho and para-positions towards the hydroxyl-group further decrease the  $pK_a$  value by about 1 unit. As can be seen, the effect of two chlorine atoms in the ortho-position towards the hydroxyl group (indicator **3**) is much stronger ( $pK_a = 7.8$ ) making this indicator promising for measurements at physiological conditions. On the other hand, the indicators **1**, **2**, **4** and **5** may be able to transfer the excellent

**Table 5.1:** Photophysical properties of the reported dyes in THF.

| Compound | $\lambda_{\text{abs}}$<br>nm | $\lambda_{\text{em}}$<br>nm | $\epsilon$<br>$\text{M}^{-1} \text{cm}^{-1}$ | QY<br>% | $\text{pK}_{\text{a}}^{\text{a}}$ | $\text{pK}_{\text{a}}^{\text{b}}$ | $\tau$<br>ns |
|----------|------------------------------|-----------------------------|--|---------|-----------------------------------|-----------------------------------|--------------|
| 1        | 696                          | 720                         | 83 200                                       | 24      | n.d. <sup>c</sup>                 | 11.7                              | 2.54         |
| 2        | 696                          | 721                         | 85 400                                       | 27      | 11.1                              | 10.8                              | 2.69         |
| 3        | 695                          | 721                         | 80 700                                       | 26      | 7.8                               | 7.5                               | 2.56         |
| 4        | 694                          | 720                         | 73 300                                       | 27      | 10.3                              | 10.3                              | 2.67         |
| 5        | 698                          | 722                         | 90 024                                       | 14      | n.d. <sup>c</sup>                 | 11.6                              | 1.57         |

<sup>a</sup>Determined in solution in EtOH/H<sub>2</sub>O 1/1.

<sup>b</sup>Determined in a Hydromed D4 sensor foil in a concentration of 0.2 w%.

<sup>c</sup>Dye solubility too poor for the titration

photophysical properties of aza-BODIPY indicators in new applications like imaging of pH on concrete surfaces [240], investigation of alkaliphilic bacteria [241] or they can be used as essential components for preparation of broad range pH sensors (usually obtained by mixing multiple pH indicators) [202]. Notably, only a few aza-BODIPY indicators have been reported with similarly high  $\text{pK}_{\text{a}}$  values and they require higher synthetic effort [124] or are no longer fluorescent and can only be used as absorption based indicators [202].

#### 5.5.4 Application of the New Dyes in Donor-Acceptor Light Harvesting Systems

Another application which benefits from the less complex behavior of the novel indicators is signal enhancement by light harvesting. In such a scheme a suitable antenna dye (donor) is used in a high concentration to absorb the excitation light and transfer the energy via FRET to the pH sensitive acceptor dye. Thereby the overall brightness of the sensor material is significantly enhanced. Such an enhancement is not possible by simply using a higher concentration of indicator as this would lead to undesired negative effects like aggregate formation, strong inner filter effect and shift of apparent  $\text{pK}_{\text{a}}$  caused by homo-FRET (energy transfer from protonated form of the indicator to its deprotonated form). By employing an antenna dye to enhance the absorption of the sensor film those problems can be avoided, as the antenna dye cannot reabsorb the emitted fluorescence or act as FRET acceptor for the pH sensitive dye. Moreover,

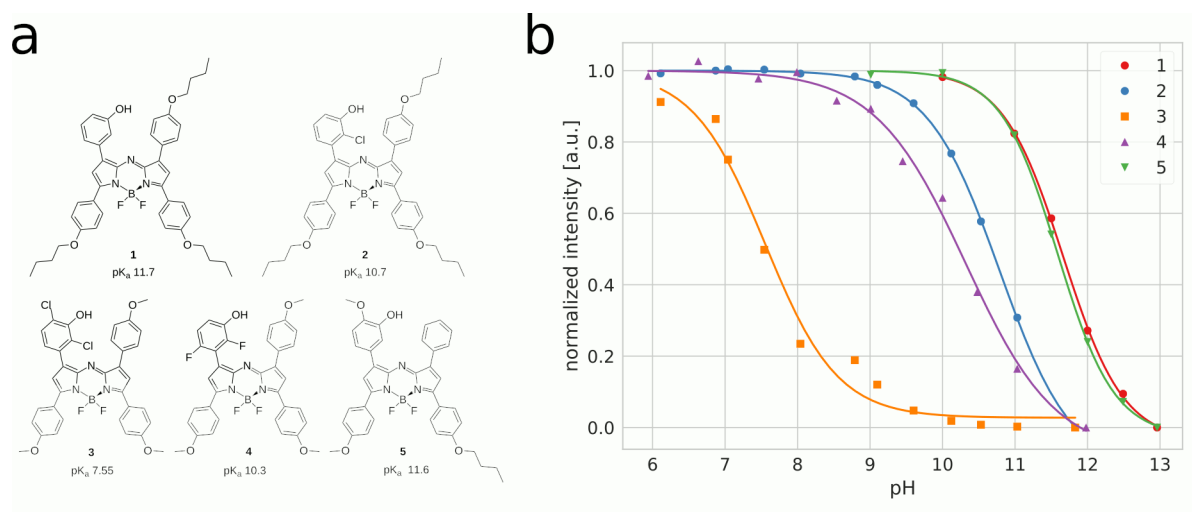


**Figure 5.3:** Structures with apparent  $pK_a$  values (a) and titration curves (b) of the new aza-BODIPY indicators.

this scheme enables an artificial increase of the Stokes shift of the sensor material, due to the hypsochromically shifted absorption of the antenna dye. A large Stokes shift is beneficial as excitation and emission light can be separated more easily and with lower losses. Moreover, potentially remaining antenna fluorescence can be used for ratiometric measurements.

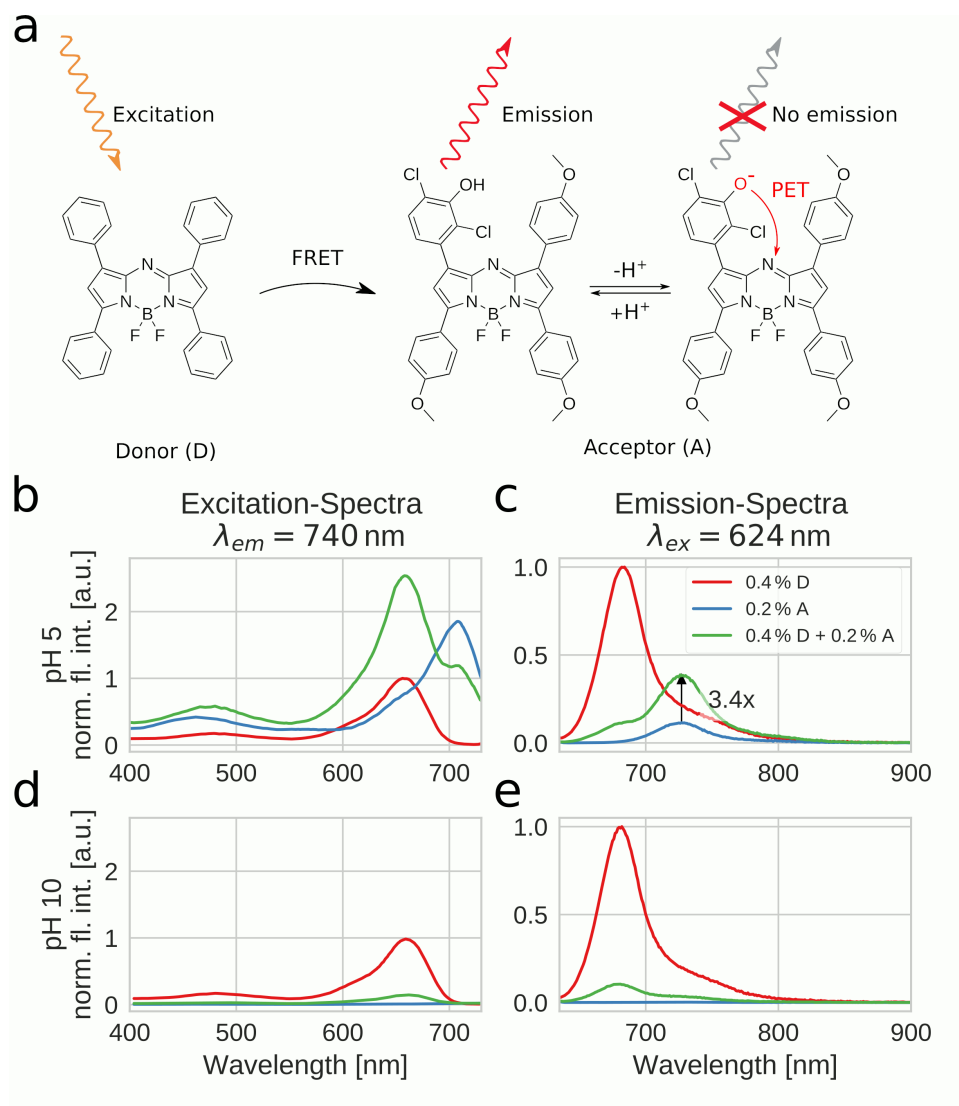
State-of-the-art para-substituted-hydroxy aza-BODIPY indicators are not ideal for this concepts as the efficiency of energy transfer depends on the overlap of the absorption and emission spectra of donor and acceptor, respectively. A strong bathochromic shift in absorption of the acceptor (see Fig. 5.2a) will lead to reduced FRET efficiency and a “turn on” effect of the donor, which reduces the dynamics of the sensor.

Figure 5.4a depicts the composition of the light harvesting system which relies on the pH-insensitive tetraphenyl aza-BODIPY as a donor and indicator **3** as an acceptor. Importantly, the absorption spectrum of **3** is bathochromically shifted by approximately 40 nm due to the electron donating ether groups (see Fig S5.1 in the supporting information) thus ensuring excellent spectral overlap between the emission of the donor and the absorption of the acceptor. The protonated indicator can indeed be efficiently excited via energy transfer from the donor (Fig. 5.4b). The corresponding emission spectra (Fig. 5.4c) of the materials clearly show that the light harvesting concept leads to a strong signal enhancement ( $\approx 3.4$  fold) of the fluorescence of the pH indicator. The energy transfer is very efficient since only a small amount of residual

donor fluorescence is visible. In basic media (Fig. 5.4d and 5.4e), fluorescence emission of the acceptor is completely quenched, while the residual fluorescence of the donor remains constant (Fig. 5.4e, peak at 690 nm). Furthermore no "turn on" of donor emission is visible upon deprotonation of the indicator. Therefore, even with a blurry cut-off by emission filters (e.g. at 700 nm) nearly all the emission light can be collected without a reduction of dynamics by increasing donor emission. The strong signal enhancement can either be used to prepare thinner and faster responding sensor films or to obtain sensors with better signal-to-noise ratios. Additionally, residual fluorescence from the donor is also very useful for referencing purposes.

### 5.5.5 Ratiometric Imaging of pH Distribution

An application of the light harvesting concept for ratiometric imaging of pH distribution is demonstrated with an inexpensive setup consisting of a yellow high power LED and a 4-channel camera (blue, green, red and NIR channels) equipped with an emission filter. Fig. 5.5 shows the spectral properties of the sensor material (0.4 wt.% antenna dye and 0.2 wt.% indicator **3**) along with the spectral sensitivity of the red and NIR camera channels. As can be seen, the emission of the indicator in the NIR channel is modulated by pH. On the other hand, the residual emission of the donor dye in the red channel is virtually pH independent thus enabling ratiometric referencing. Although this set-up may not be ideal due to the fact that only a small portion of the emission of the donor and acceptor are collected in the respective channels (Fig. 5.5), the camera is compact, affordable ( $\approx 2000$  €) and contains no moving elements. A spectral camera with custom emission filters on a rotating wheel [244] may be an interesting alternative if higher signals are desired. Nevertheless, due to strong brightness enhancement via light harvesting even the current combination is promising for imaging of the pH distribution (Fig. 5.6a). The calibration curve generated from ratiometric images (Fig. 5.6b) is very similar to that obtained for the unreferenced fluorescence intensity measurements (Fig. 5.3).



**Figure 5.4:** Enhancement of fluorescence properties of the pH sensor via light harvesting. Chemical structures of the employed donor (tetraphenyl aza-BODIPY) and acceptor (indicator 3) (a). Excitation (b, d) and emission (c, e) spectra at pH 5 (b, c) and pH 10 (d, e) for the sensor material employing light harvesting (green) and for the corresponding sensor materials containing only donor (red) and only acceptor (blue). The concentrations of the dyes are given in wt.% in respect to the polymer. The spectra were recorded with sensor foils of approximately 3  $\mu\text{m}$  film thickness in right angle mode. The emission intensities are normalized to the emission intensity of the pure donor for every plot. The absorption spectra of the sensor foil are depicted in Fig. S5.1 in the supporting information.

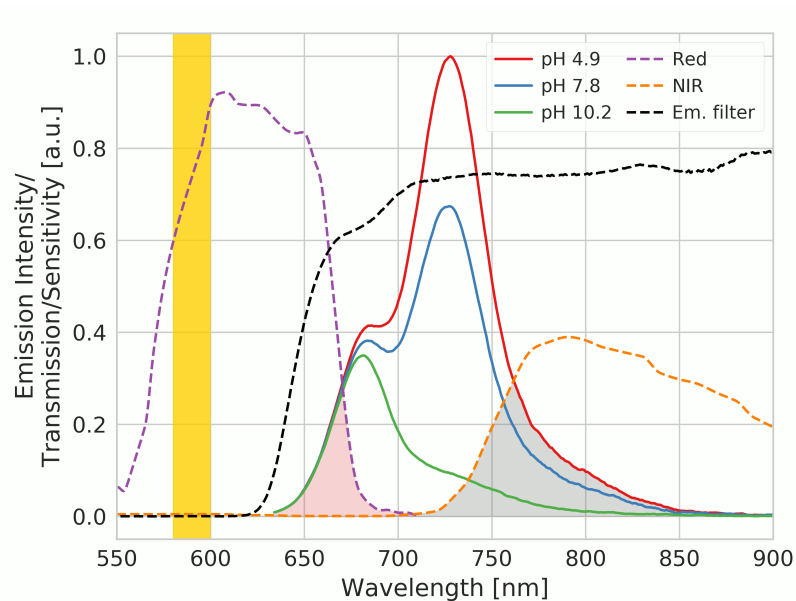


**Figure 5.5:** pH dependency of the emission spectrum of the sensor and optical properties of the imaging set-up. The orange vertical line indicates the excitation from the high power 590-nm LED; dashed purple and orange lines show the relative sensitivity of the red and NIR channels of the camera, respectively (adapted from [www.jai.com](http://www.jai.com)). The dashed black line is the transmission of the used emission filter (RG640 from Hoya combined with the “bright red” foil filter from LEE filters in front).

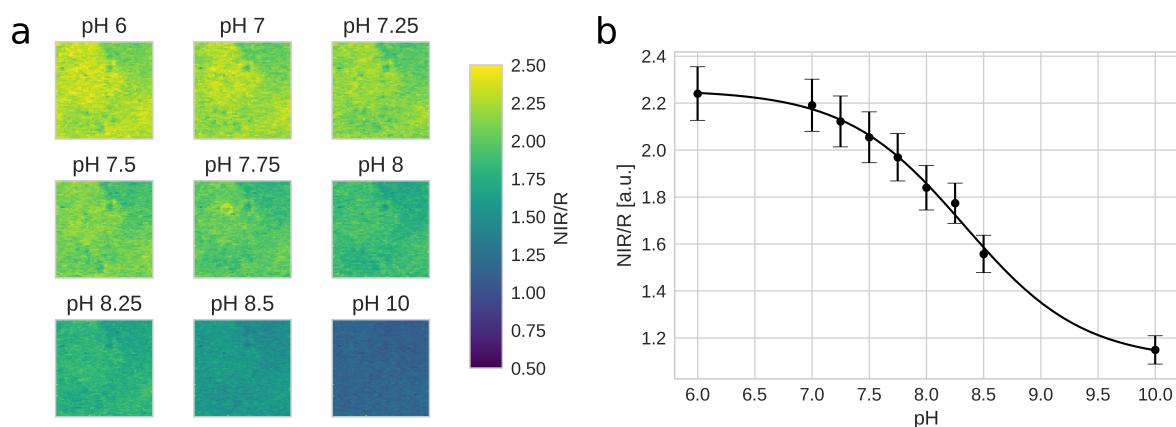


**Figure 5.6:** Imaging of pH distribution. (a) False-color images for the fluorescence ratio (NIR/red channel) for the sensor material between pH 6 and 10. (b) The corresponding calibration curve fit with Boltzmann sigmoid function.

## 5.6 Conclusions

In conclusion, 5 new pH-sensitive aza-BODIPY indicator dyes were synthesized which feature different substitution patterns compared to state-of-the-art analogs. The new indicators possess good quantum yields in the "on" state and no detectable fluorescence in the "off" state. They are purely PET-based featuring nearly pH independent absorption spectra. This simplifies the behavior of the sensor materials, due to constant inner filter effect and is promising for multi-parameter sensors and systems utilizing signal enhancement via light harvesting. The light harvesting sensor materials is demonstrated to be promising for ratiometric imaging of pH distribution with an affordable RGB-NIR camera. The apparent  $pK_a$  values between 7.5 and  $> 11.5$  enable measurements from physiological conditions to very alkaline media. Notably, most new dyes have very high  $pK_a$  values due to the decoupling from the electron withdrawing core of the dye and are therefore interesting for monitoring of pH in concrete, investigation of alkaliphiles or for the design of optical  $CO_2$  sensor materials.

## Acknowledgments

This work was supported by the European Union's Horizon2020 project STEMM-CCS (grant number 654462).

## 5.7 Supporting Information

### 5.7.1 Synthesis

#### 1-(4-butoxyphenyl)-3-(3-hydroxyphenyl)prop-2-en-1-one (**a1**)

1.00 g 4'-butoxyacetophenone (5.20 mmol, 1.00 eq) and 651.0 mg 3-hydroxybenzaldehyde (5.33 mmol, 1.02 eq) were dissolved in 5 mL EtOH in a round bottom flask. 5 mL of an aqueous potassium hydroxide solution (875.5 mg, 15.60 mmol, 3.00 eq) were added dropwise. The solution was stirred for 12 h at room temperature during which it turned orange. The reaction mixture was added dropwise to 40 mL 1 M HCl solution to precipitate a yellow solid. The product was filtered, washed with water and dried. The obtained yellow solid was used for further synthesis without purification. Crude yield: 1.34 g (87 %).

#### 1,3-bis(4-butoxyphenyl)prop-2-en-1-one (**c1**)

**c1** was obtained analogously to **a1** from 5.40 g 4'-butoxyacetophenone (28.07 mmol, 1.00 eq) and 5.00 g 4-butoxybenzaldehyde (28.08 mmol, 1.00 eq) using 20 mL and 15 mL of an aqueous KOH solution (4.77 g, 85.02 mmol, 3.03 eq). The obtained yellow solid was used for further synthesis without purification. Crude yield: 8.60 g (87 %).

#### 1-(4-butoxyphenyl)-3-(2-chloro-3-hydroxyphenyl)prop-2-en-1-one (**a2**)

**a2** was obtained analogously to **a1** from 613.9 mg 4'-butoxyacetophenone (3.20 mmol, 1.01 eq) and 498.0 mg 2-chloro-3-hydroxybenzaldehyde (3.18 mmol, 1.00 eq) using 3 mL EtOH and 3 mL of an aqueous KOH solution (539.5 mg, 9.62 mmol, 3.02 eq). The obtained yellow solid was used for further synthesis without purification. Crude yield: 907.9 mg (86 %).

#### 3-(2,4-dichloro-3-hydroxyphenyl)-1-(4-methoxyphenyl)prop-2-en-1-one (**a3**)

**a3** was obtained analogously to **a1** from 412.7 mg 4'-methoxyacetophenone (2.75 mmol, 1.12 eq) and 469.0 mg 2,4-dichloro-3-hydroxybenzaldehyde (2.46 mmol, 1.00 eq) using 5 mL EtOH and 5 mL of an aqueous KOH solution (649.00 mg, 11.57 mmol, 4.71 eq). The obtained yellow product was used for further synthesis without purification. Crude yield: 691.7 mg (87 %).

**1,3-bis(4-methoxyphenyl)prop-2-en-1-one (c2)**

**c2** was obtained analogously to **a1** from 998.6 mg 4'-methoxyacetophenone (6.65 mmol, 1.00 eq) and 810  $\mu$ L 4-methoxybenzaldehyde (6.66 mmol, 1.00 eq) using 5 mL EtOH and 5 mL of an aqueous KOH solution (1.12 g, 19.97 mmol, 3.00 eq). The obtained product (yellow powder) was used for further synthesis without purification. Crude yield: 1.60 g (90 %).

**3-(2,6-difluoro-3-hydroxyphenyl)-1-(4-methoxyphenyl)prop-2-en-1-one (a4)**

**a4** was obtained analogously to **a1** from 953.7 mg 4'-methoxyacetophenone (6.35 mmol, 1.04 eq) and 964.8 mg 2,6-difluoro-3-hydroxy-benzaldehyde (6.10 mmol, 1.00 eq) using 5 mL EtOH and 5 mL of an aqueous KOH (1.06 g, 18.89 mmol, 3.10 eq). The obtained brown product was used for further synthesis without purification. Crude yield: 1.62 g (91 %), brown powder.

**3-(3-hydroxy-4-methoxyphenyl)-1-(4-methoxyphenyl)prop-2-en-1-one (a5)**

**a5** was obtained analogously to **a1** from 998.3 mg 4'-methoxyacetophenone (6.65 mmol, 1.00 eq) and 1.02 g 3-Hydroxy-4-methoxybenzaldehyde (6.69 mmol, 1.01 eq) using 5 mL EtOH and 5 mL of an aqueous KOH solution. The obtained yellow solid was used for further synthesis without purification. Crude yield: 1.49 g (79 %), yellow powder.

**1-(4-butoxyphenyl)-3-(3-hydroxyphenyl)-4-nitrobutan-1-one (b1)**

In a round bottom flask equipped with a reflux condenser 1.34 g of **a1** (4.53 mmol, 1.00 eq) and 5.00 mL nitromethane (92.56 mmol, 20.45 eq) were mixed with 10 mL of a potassium hydroxide solution in EtOH (612.0 mg, 10.91 mmol, 2.41 eq) and stirred at 60 °C for 3 h. After cooling to room temperature the solvent was removed under reduced pressure. The brown oily residue was dissolved in 50 mL EtOAc and washed with 1 M HCl solution (3 x 50 mL). The organic phase was dried over Na<sub>2</sub>SO<sub>4</sub> and the solvent removed under reduced pressure. The crude product (brown oil) was used for further synthesis without purification. Crude yield: 2.19 g (135 %, product containing residual solvent).

**1,3-bis(4-butoxyphenyl)-4-nitrobutan-1-one (d1)**

**d1** was obtained analogously to **b1** from 1.01 g **c1** (2.87 mmol, 1.00 eq) and 3.00 mL nitromethane (55.54 mmol, 19.35 eq) using 5 mL of a KOH solution in EtOH (351.0 mg, 6.26 mmol, 2.18 eq).

The crude product (brown oil) was used for further synthesis without purification. Crude yield: 1.29 g (109 %, product containing residual solvent).

**1-(4-butoxyphenyl)-3-(2-chloro-3-hydroxyphenyl)-4-nitrobutan-1-one (b2)**

**b2** was obtained analogously to **b1** from 907.9 mg **a2** (2.74 mmol, 1.00 eq) and 3.00 mL nitromethane (55.54 mmol, 20.24 eq) using 5 mL of a KOH solution in EtOH (337.0 mg, 6.01 mmol, 2.19 eq). The crude product (brown oil) was used for further synthesis without purification. Crude yield: 1.34 g (125 %, product containing residual solvent).

**3-(2,4-dichloro-3-hydroxyphenyl)-1-(4-methoxyphenyl)-4-nitrobutan-1-one (b3)**

**b3** was obtained analogously to **b1** from 691.7 mg **a3** (2.14 mmol, 1.00 eq) and 2.5 mL nitromethane (46.28 mmol, 21.62 eq) using 3 mL of a KOH solution in EtOH (340.0 mg, 6.06 mmol, 2.83 eq). The crude product (brown oil) was used for further synthesis without purification. Crude yield: 1.08 g (131 %, product containing residual solvent).

**1,3-bis(4-methoxyphenyl)-4-nitrobutan-1-one (d2)**

**d2** was obtained analogously to **b1** from 1.60 g **c2** (5.96 mmol, 1.00 eq) and 6.5 mL nitromethane (120.33 mmol, 20.18 eq) using 10 mL of a KOH solution in EtOH (740.0 mg, 13.19 mmol, 2.21 eq) and stirring the reaction at 60 °C for 1 h. The crude product (brown oil) was used for further synthesis without purification. Crude yield: 2.41 g (123 %, product containing residual solvent).

**3-(2,6-difluoro-3-hydroxyphenyl)-1-(4-methoxyphenyl)-4-nitrobutan-1-one (b4)**

**b4** was obtained analogously to **b1** from 1.62 g **a4** (5.58 mmol, 1.00 eq) and 6.00 mL nitromethane (111.07 mmol, 19.90 eq) using 10 mL of a KOH solution in EtOH (618.00 mg, 11.02 mmol, 1.97 eq) and stirring the reaction at 60 °C for 1 h. The solution turned red-brown and a brown precipitate was formed. After cooling to room temperature the solvent was removed by rotary evaporation. The brown oily residue was dissolved in 50 mL EtOAc and washed with HCl solution (3 x 50 mL). The crude product (brown oil) was used for further synthesis without purification. Crude yield: 1.36 g (120 %, product containing residual solvent).

**3-(3-hydroxy-4-methoxyphenyl)-1-(4-methoxyphenyl)-4-nitrobutan-1-one (b5)**

**b5** was obtained analogously to **b1** 1.49 g **a5** (5.25 mmol, 1.00 eq) and 5.70 mL nitromethane (105.52 mmol, 20.11 eq) using 10 mL of a potassium hydroxide solution in EtOH (612.0 mg, 10.91 mmol, 2.08 eq) and stirring the reaction at room temperature overnight. The crude product (brown oil) was used for further synthesis without purification. Crude yield: 2.19 g (121 %, product containing residual solvent).

**(Z)-3-(2-((3,5-bis(4-butoxyphenyl)-2H-pyrrol-2-ylidene)amino)-5-(4-butoxyphenyl)-1H-pyrrol-3-yl)phenol (e1)**

474.2 mg **b1** (1.33 mmol, 1.00 eq), 507.2 mg **d1** (1.23 mmol, 0.92 eq) and 3.58 g ammonium acetate (46.66 mmol, 35.00 eq) were mixed with 25 mL BuOH in a round bottom flask equipped with a reflux condenser and stirred at 95 °C. The reaction conversion was monitored by TLC (DCM) and UV/VIS absorption spectroscopy. After 5 h the reaction mixture was cooled to room temperature and stirred over the weekend.

After removing the solvent under reduced pressure the obtained solid was dissolved in DCM and washed with water (3 x 300 mL). The organic phase was dried over Na<sub>2</sub>SO<sub>4</sub> and the solvent was removed. The crude product was purified by column chromatography (silica gel, DCM). Yield: 44.6 mg (5 %), blue solid

**(Z)-3-(2-((3,5-bis(4-butoxyphenyl)-2H-pyrrol-2-ylidene)amino)-5-(4-butoxyphenyl)-1H-pyrrol-3-yl)-2-chlorophenol (e2)**

**e2** was prepared analogously to **e1** from 522.1 mg **b2** (1.33 mmol, 1.00 eq) and 542.3 mg **d2** (1.31 mmol, 0.98 eq) using 4.09 g ammonium acetate (53.06 mmol, 39.82 eq) in 25 mL BuOH. Yield: 62.0 mg (7 %), blue metallic solid.

**(Z)-3-(2-((3,5-bis(4-methoxyphenyl)-2H-pyrrol-2-ylidene)amino)-5-(4-methoxyphenyl)-1H-pyrrol-3-yl)-2,6-dichlorophenol (e3)**

**e3** was prepared analogously to **e1** from 492.3 mg **b3** (1.28 mmol, 1.00 eq) and 441.9 mg **d2** (1.34 mmol, 1.05 eq) using 3.69 g ammonium acetate (47.35 mmol, 36.95 eq) in 25 mL BuOH. Yield: 60.2 mg (8 %), metallic blue solid

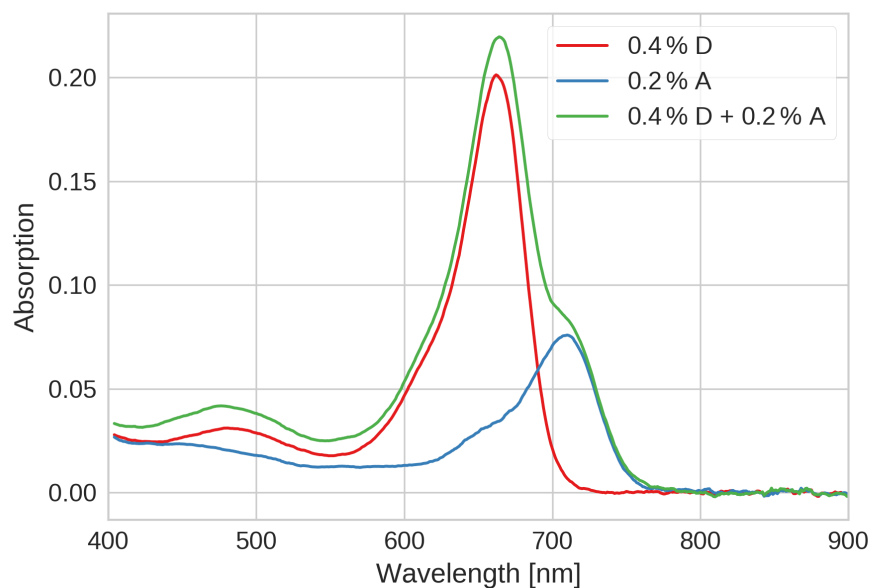


**Figure S5.1:** Absorption spectra of the light harvesting measurement foils. D...Donor (tetraphenyl aza-BODIPY), A... Acceptor (Indicator 3)

**(Z)-3-(2-((3,5-bis(4-methoxyphenyl)-2H-pyrrol-2-ylidene)amino)-5-(4-methoxyphenyl)-1H-pyrrol-3-yl)-2,4-difluorophenol (e4)**

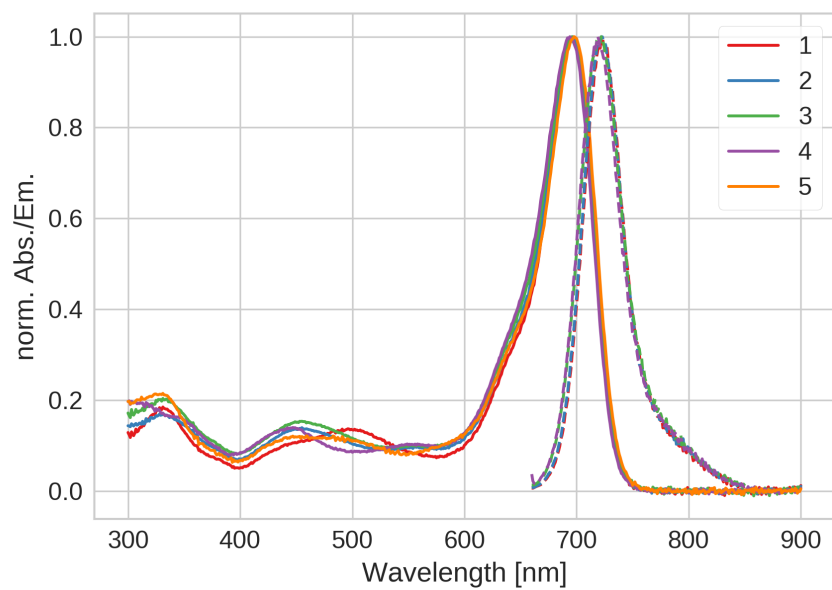
**e4** was prepared analogously to **e1** from 1.13 g **b4** (3.23 mmol, 1.00 eq) and 1.11 g **d2** (3.38 mmol, 1.05 eq) using 9.06 g ammonium acetate (117.54 mmol, 36.39 eq) in 50 mL BuOH.

Yield: 74.7 mg (4%), metallic blue solid

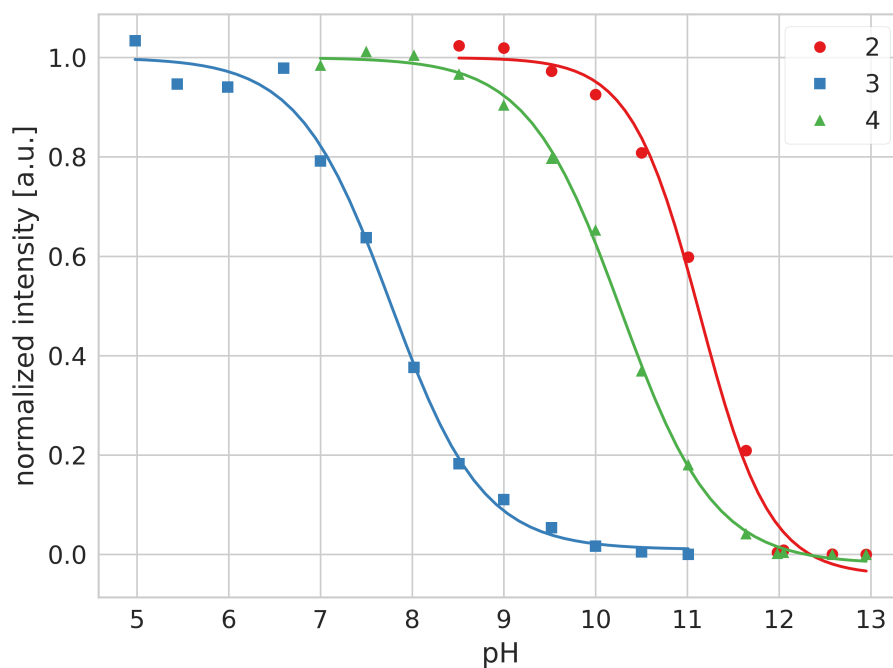
**(Z)-5-(2-((3,5-bis(4-methoxyphenyl)-2H-pyrrol-2-ylidene)amino)-5-(4-methoxyphenyl)-1H-pyrrol-3-yl)-2-methoxyphenol (e5)**

**e5** was prepared analogously to **e1** from 493.4 mg **b5** (1.43 mmol, 1.00 eq) and 493.8 mg **d3** (1.45 mmol, 1.01 eq) using 4.11 g ammonium acetate (53.32 mmol, 37.32 eq) in 25 mL BuOH.

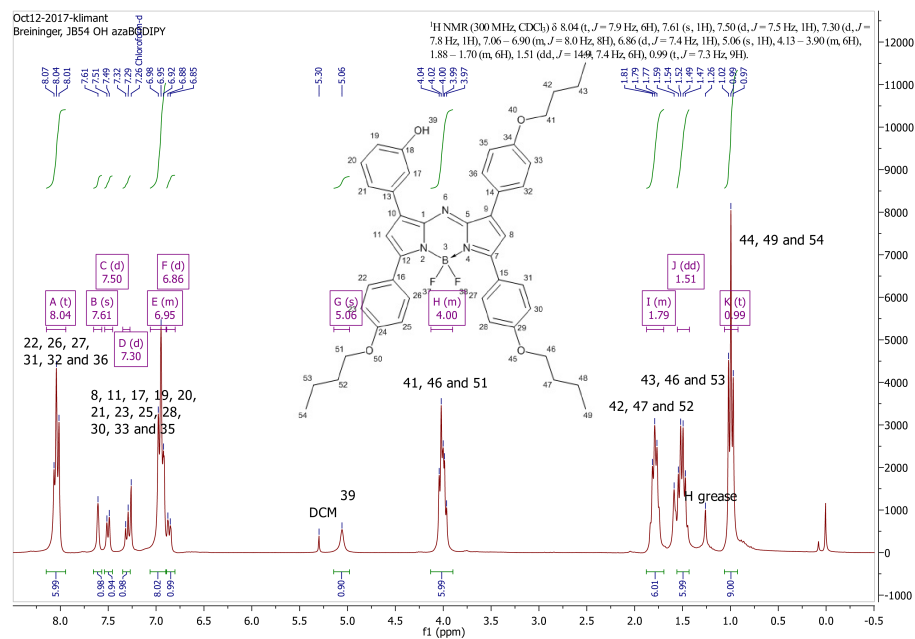
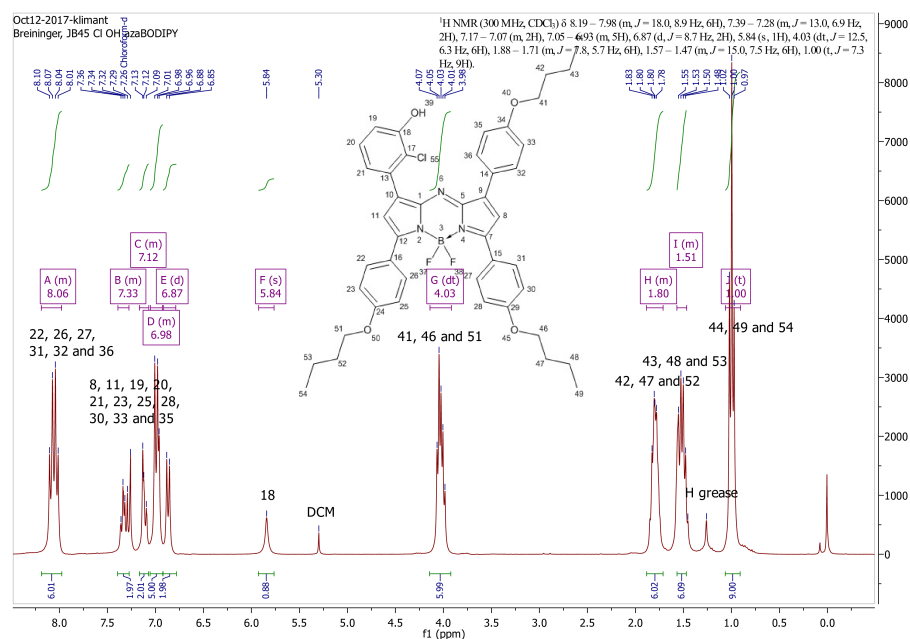
Yield: 62.0 mg (7%), dark green powder

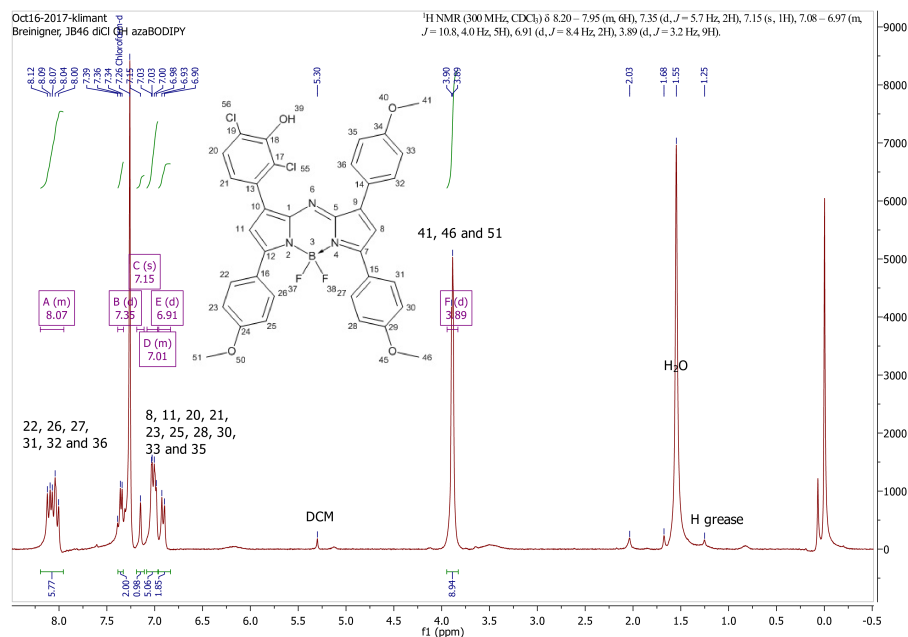
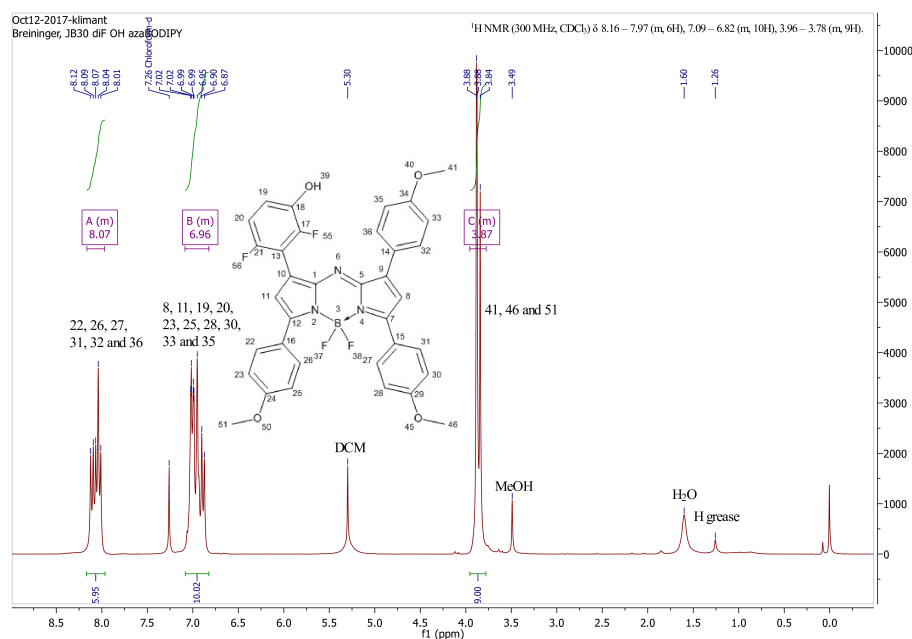


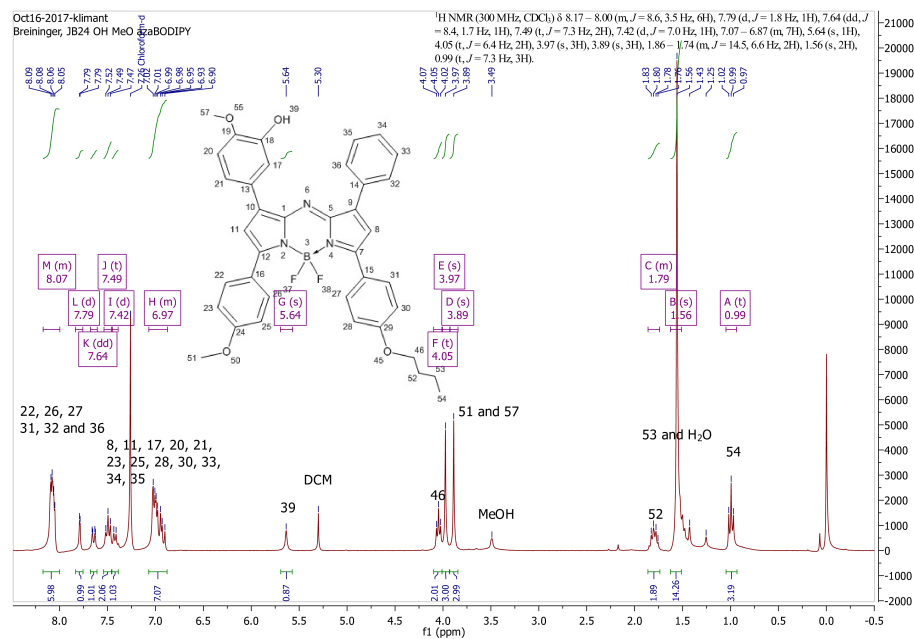
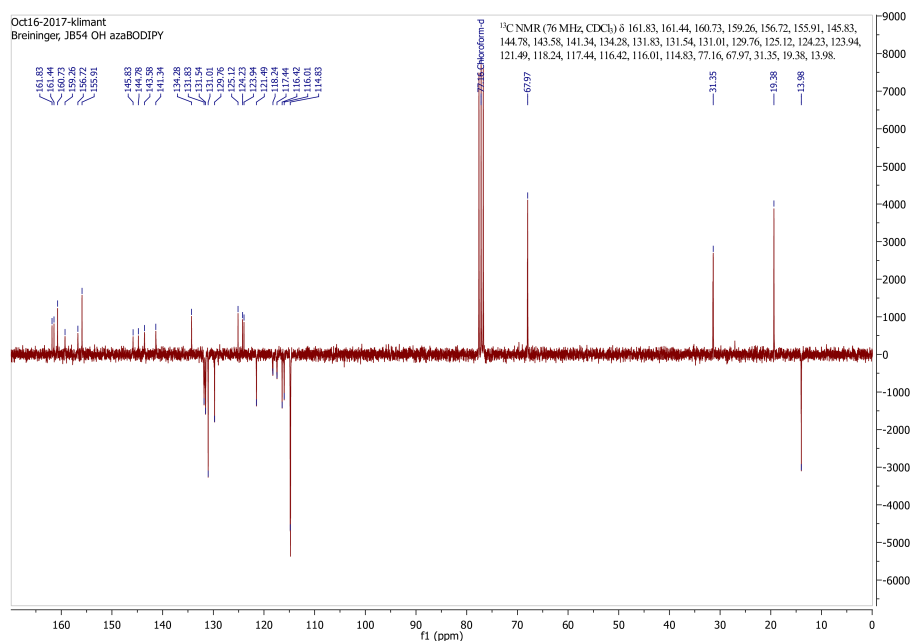
**Figure S5.2:** Normalized absorption and emission spectra (protonated) of the indicators.



**Figure S5.3:** Calibration curves of the indicators in EtOH/buffer 1:1.

Figure S5.4: <sup>1</sup>H NMR spectrum of indicator 1Figure S5.5: <sup>1</sup>H NMR spectrum of indicator 2

Figure S5.6: <sup>1</sup>H NMR spectrum of indicator 3Figure S5.7: <sup>1</sup>H NMR spectrum of indicator 4

Figure S5.8: <sup>1</sup>H NMR spectrum of indicator 5Figure S5.9: <sup>13</sup>C APT NMR spectrum of indicator 1

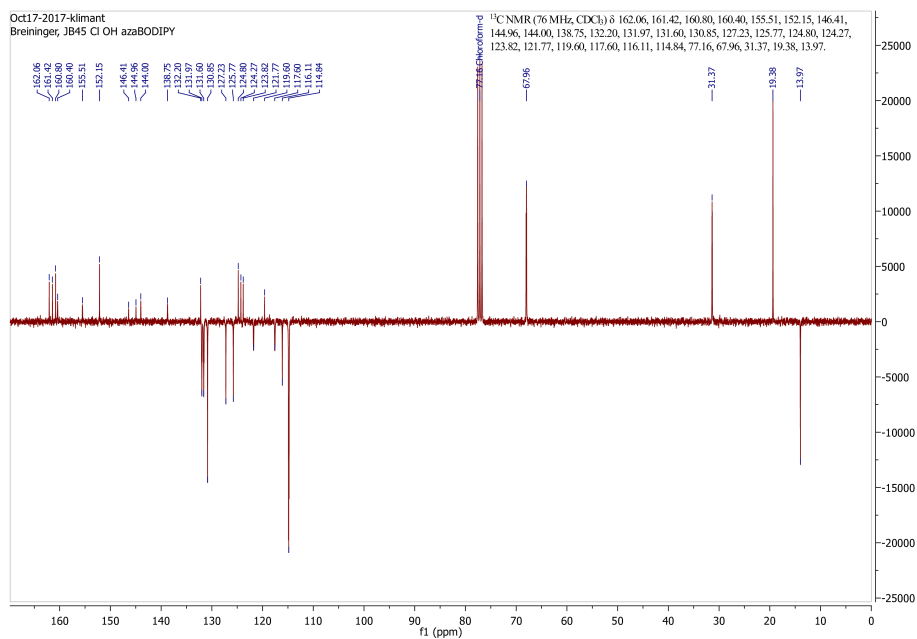


Figure S5.10:  $^{13}\text{C}$  APT NMR spectrum of indicator 2

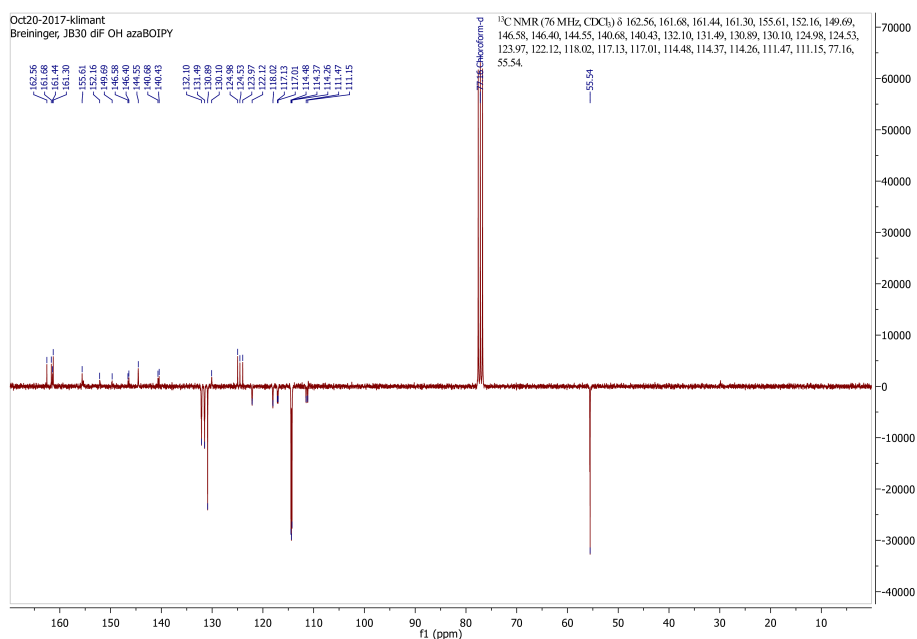


Figure S5.11:  $^{13}\text{C}$  APT NMR spectrum of indicator 4

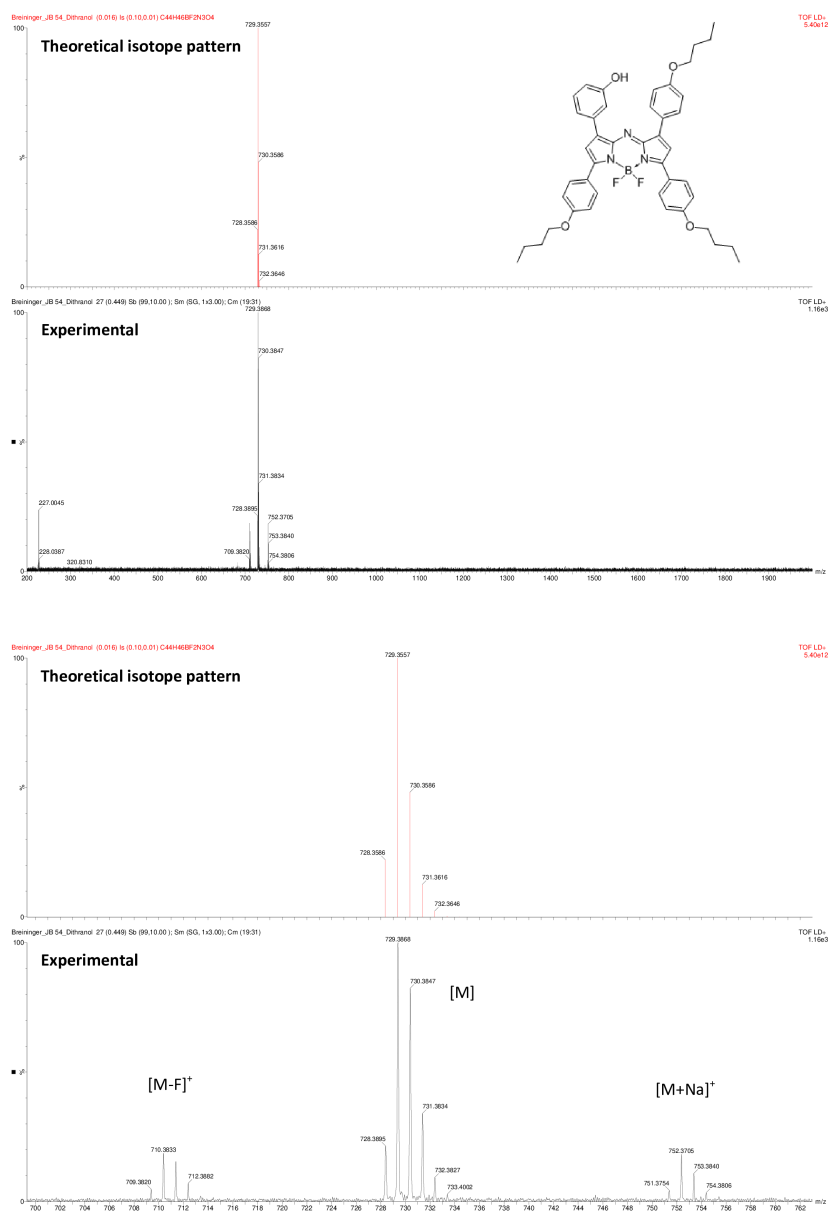


Figure S5.12: MS-spectrum of indicator 1

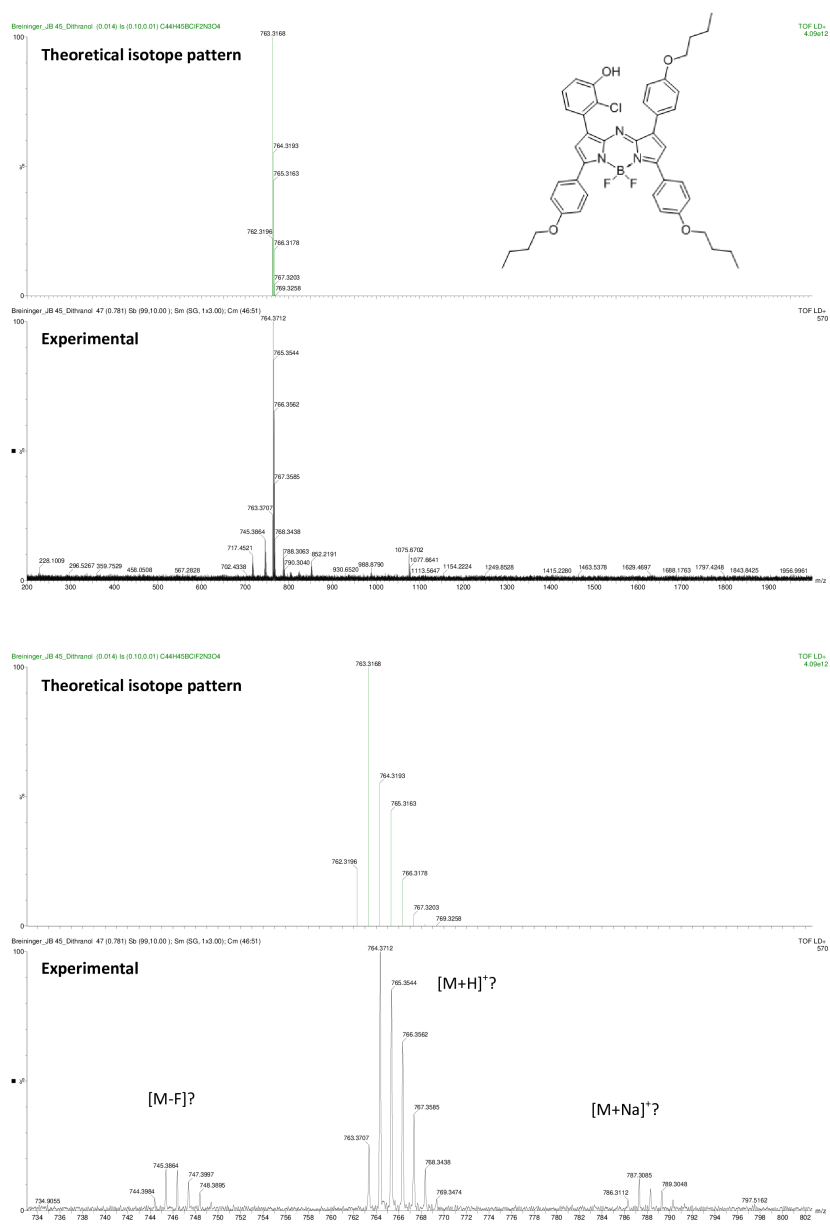


Figure S5.13: MS-spectrum of indicator 2

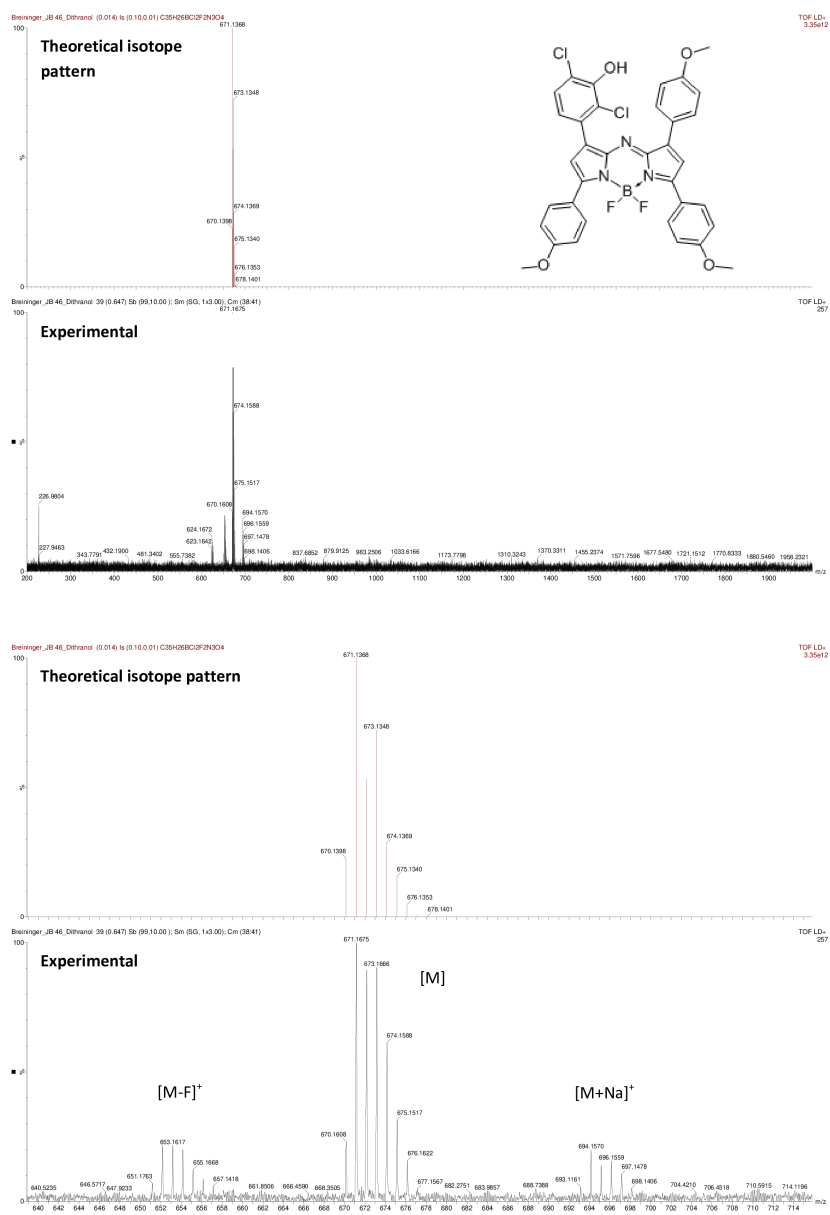
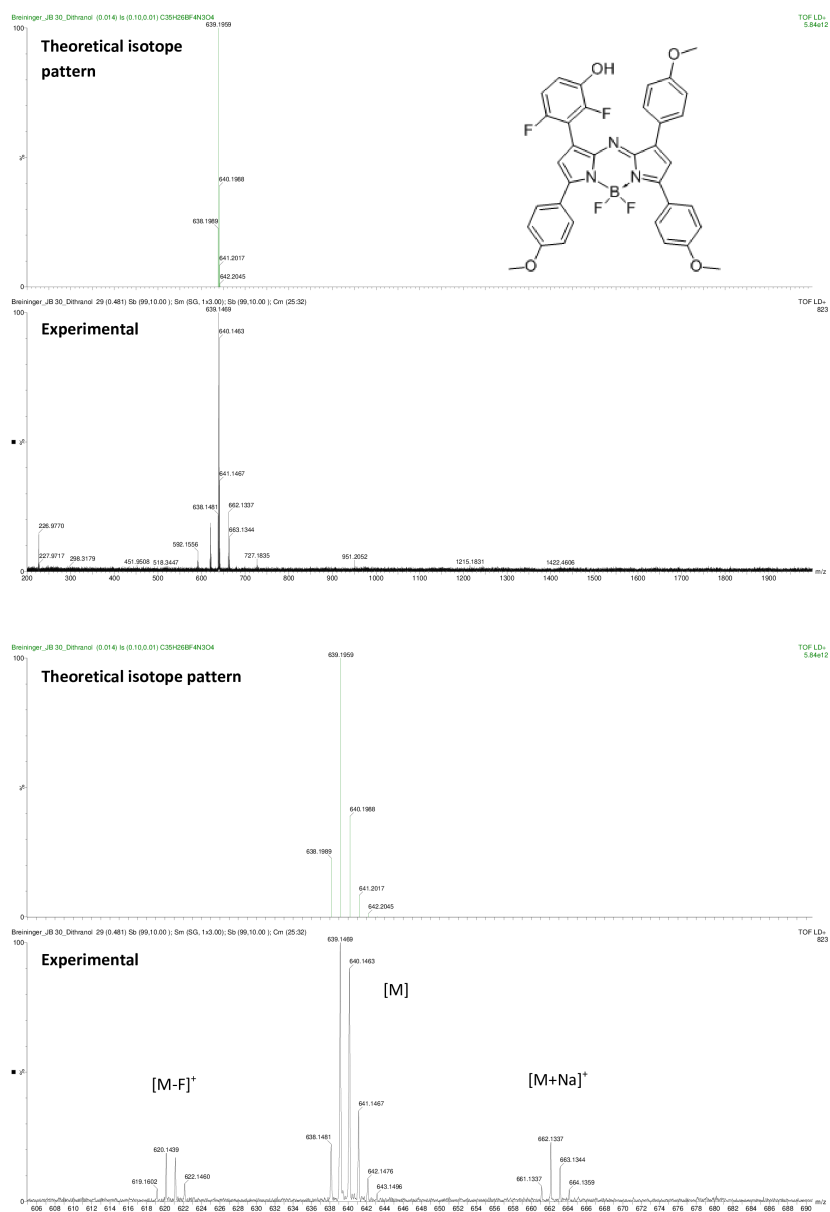


Figure S5.14: MS-spectrum of indicator 3





---

## 6 Summary and Conclusion

In conclusion a set of novel pH sensor materials for oceanographic applications was successfully developed and applied in real-life conditions. The initial response time issues were overcome by utilizing a concept with a cross-linked homogeneous and hydrophilic matrix polymer in combination with covalent coupling of the indicator dye. While this approach led to fast and stable sensor materials, it significantly complicated the sensor production. To overcome this issue, new procedures for sensor preparation were developed. An innovative boron-oxygen coupling reaction was of special interest, as it enables covalent coupling of (aza-)BODIPYs without the introduction of dedicated linker groups, and significantly simplified sensor preparation.

The novel sensor materials were thoroughly characterized in regard to their temperature and salinity cross-sensitivities, and their long-term stability. The stability proved to be excellent at the typically low temperatures of real world applications. In addition, a prospective drift compensation was established to compensate the drift at room temperature and above. The temperature cross-sensitivity was determined as  $\approx 0.012$  pH units/K and can easily be compensated. Due to the low charge of the indicator the cross-sensitivity to salinity is negligible in almost all oceanographic applications.

Oceanographic applicability was evaluated by participating in multiple international field trips. The sensors were deployed in the Baltic Sea for depth and surface profiling, for stationary measurements on a mooring in the harbor of Kiel (Germany), in a sea grass field in Limfjord (Denmark), and for stationary measurements in the harbor of Southampton (England). The utility of the sensors was demonstrated and data with high temporal resolution were obtained. In nearly all cases, the data from the three sensor types correlated well, which is interesting to draw conclusions regarding occurring (microbiological) processes. Therefore, the combination of the novel pH sensor materials with the CO<sub>2</sub> and O<sub>2</sub> materials and a combined read-out device could be a valuable tool for marine research.

Additionally, we were able to develop new aza-BODIPY indicators with enhanced optical properties due to pure quenching by photoinduced electron transfer (PET). The known issue of intramolecular charge transfer was eliminated by shifting the pH sensitive hydroxy group of the indicators to the meta position of the phenyl substituents. Thereby a set of new indicators with pH independent absorption spectrum was obtained. An application of these indicators was demonstrated by developing a light-harvesting concept for pH imaging. Moreover the indicators are currently investigated for pH imaging on concrete surfaces and could significantly improve currently employed concepts.

The developed pH sensor materials are not only applicable for oceanographic measurements, as the findings, which were received throughout the development of these materials, can also be transferred into the development of new optical pH sensors for a variety of other applications.

---

## 7 References

- (1) Sørensen, S. P. L. *Biochem. Zeitschr* **1909**, *21*, 131–304.
- (2) Haber, F.; Klemensiewicz, Z. *Zeitschrift für Physikalische Chemie* **1909**, *67U*, DOI: 10.1515/zpch-1909-6720.
- (3) Lewis, G. N.; Randall, M., *Thermodynamics and the Free Energy of Chemical Substances*; McGraw-Hill Book Company: 1923.
- (4) Sørensen, S. P. L.; Linderstrøm-Lang, K. U. *Comptes rendus des travaux du laboratoire Carlsberg* **1924**, *15*, 1–40.
- (5) Spitzer, P.; Pratt, K. W. *Journal of Solid State Electrochemistry* **2011**, *15*, 69–76.
- (6) Doede, D. R. *Yale J Biol Med* **1945**, *17*, 595–610.
- (7) James, S. C.; Janardhanam, V.; Hanson, D. T. *Journal of Phycology* **2013**, *49*, ed. by Mock, T., 608–615.
- (8) Chen, C.; Durbin, E. *Marine Ecology Progress Series* **1994**, *109*, 83–94.
- (9) Dubinsky, Z.; Rotem, J. *Oecologia* **1974**, *16*, 53–60.
- (10) Hofmann, G. E.; Barry, J. P.; Edmunds, P. J.; Gates, R. D.; Hutchins, D. A.; Klinger, T.; Sewell, M. A. *Annu. Rev. Ecol. Evol. Syst.* **2010**, *41*, 127–147.
- (11) Das, S.; Mangwani, N. *Oceanologia* **2015**, *57*, 349–361.
- (12) Kroeker, K. J.; Kordas, R. L.; Crim, R.; Hendriks, I. E.; Ramajo, L.; Singh, G. S.; Duarte, C. M.; Gattuso, J.-P. *Glob Chang Biol* **2013**, *19*, 1884–1896.
- (13) Rossi, T.; Nagelkerken, I.; Simpson, S. D.; Pistevos, J. C. A.; Watson, S.-A.; Meriliet, L.; Fraser, P.; Munday, P. L.; Connell, S. D. *Proc Biol Sci* **2015**, *282*, DOI: 10.1098/rspb.2015.1954.

- (14) Stiasny, M. H.; Mittermayer, F. H.; Swat, M.; Voss, R.; Jutfelt, F.; Chierici, M.; Puvanendran, V.; Mortensen, A.; Reusch, T. B. H.; Clemmesen, C. *PLoS One* **2016**, *11*, DOI: 10.1371/journal.pone.0155448.
- (15) Weil, R. R.; Brady, N. C.; Weil, R. R., *The nature and properties of soils*, Fifteenth edition; Pearson: Columbus, 2016; 1086 pp.
- (16) Harter, R. D. *Soil Science Society of America Journal* **1983**, *47*, 47.
- (17) Chen, M. et al. *Oncotarget* **2017**, *8*, 45759–45767.
- (18) Kellum, J. A. *Crit Care* **2000**, *4*, 6–14.
- (19) Debye, P. J. W., *The collected papers of Peter J.W. Debye*; Ox Bow Press: Woodbridge, Conn, 1988; 700 pp.
- (20) Debye, P.; Hückel, E. *Physikalische Zeitschrift* **1923**, *24*, 305.
- (21) Hamann, C. H.; Hamnett, A.; Vielstich, W., *Electrochemistry*; Wiley-VCH: Weinheim ; New York, 1998; 423 pp.
- (22) Guggenheim, E. *The London, Edinburgh, and Dublin Philosophical Magazine and Journal of Science* **1935**, *19*, 588–643.
- (23) Davies, C. W. *Journal of the Chemical Society (Resumed)* **1938**, 2093.
- (24) Guggenheim, E. A.; Turgeon, J. C. *Transactions of the Faraday Society* **1955**, *51*, 747.
- (25) *Activity coefficients in electrolyte solutions*, 2nd ed; Pitzer, K. S., Ed.; CRC Press: Boca Raton, 1991, 542 pp.
- (26) Royal Society (Great Britain), *Ocean acidification due to increasing atmospheric carbon dioxide*. OCLC: 60805277; Royal Society: London, 2005.
- (27) Azevedo, L. B.; De Schryver, A. M.; Hendriks, A. J.; Huijbregts, M. A. J. *Environmental Science & Technology* **2015**, *49*, 1495–1500.
- (28) Mora, C. et al. *PLoS Biology* **2013**, *11*, ed. by Mace, G. M., e1001682.
- (29) Orr, J. C. et al. *Nature* **2005**, *437*, 681–686.
- (30) Dickson, A. G. *Geochimica et Cosmochimica Acta* **1984**, *48*, 2299–2308.
- (31) Millero, F.; Woosley, R.; DiTrollo, B.; Waters, J. *Oceanography* **2009**, *22*, 72–85.
- (32) Doney, S. C.; Fabry, V. J.; Feely, R. A.; Kleypas, J. A. *Annual Review of Marine Science* **2009**, *1*, 169–192.

- 
- (33) Millero, F. J. *ResearchGate* **1995**, *59*, 661–677.
- (34) Caldeira, K.; Wickett, M. E. *Nature* **2003**, *425*, 365–365.
- (35) Feely, R. A.; Sabine, C. L.; Lee, K.; Berelson, W.; Kleypas, J.; Fabry, V. J.; Millero, F. J. *Science* **2004**, *305*, 362–366.
- (36) Sabine, C. L. *Science* **2004**, *305*, 367–371.
- (37) Jacobson, M. Z. *Journal of Geophysical Research* **2005**, *110*, DOI: 10.1029/2004JD005220.
- (38) *The future oceans: warming up, rising high, turning sour*; der Bundesregierung Globale Umweltveränderungen (Germany), W. B., Ed.; Special report, OCLC: ocm70857918; German Advisory Council on Global Change: Berlin, 2006, 110 pp.
- (39) Martz, T. R.; Connery, J. G.; Johnson, K. S. *Limnol. Oceanogr. Methods* **2010**, *8*, 172–184.
- (40) Logan, C. A. *BioScience* **2010**, *60*, 819–828.
- (41) Halevy, I.; Bachan, A. *Science* **2017**, *355*, 1069–1071.
- (42) Fabry, V. J.; Langdon, C.; Balch, W. M.; Dickson, A. G.; Feely, R. A.; Hales, B.; Hutchins, D. A.; Kleypas, J. A.; Sabine, C. L. *Eos, Transactions American Geophysical Union* **2008**, *89*, 143.
- (43) *textbook of clinical chemistry*, 2nd ed; Tietz, N. W., Burtis, C. A., Ashwood, E. R., Eds.; Saunders: Philadelphia, 1994, 2326 pp.
- (44) Zeebe, R. E.; Wolf-Gladrow, D. A., *CO<sub>2</sub> in seawater: equilibrium, kinetics, isotopes*; Elsevier oceanography series 65; Elsevier: Amsterdam ; New York, 2001; 346 pp.
- (45) Millero, F. J.; Feistel, R.; Wright, D. G.; McDougall, T. J. *Deep Sea Research Part I: Oceanographic Research Papers* **2008**, *55*, 50–72.
- (46) Dickson, A. G.; Goyet, C., *Handbook of Methods for the Analysis of the Various Parameters of the Carbon Dioxide System in Sea Water*, 1994.
- (47) Millero, F. J., *Chemical oceanography*, 4th ed; Taylor & Francis: Boca Raton, 2013; 571 pp.
- (48) Millero, F. *Oceanography* **2010**, *23*, 18–33.

- (49) Emeis, K.-C.; Struck, U.; Schulz, H.-M.; Rosenberg, R.; Bernasconi, S.; Erlenkeuser, H.; Sakamoto, T.; Martinez-Ruiz, F. *Palaeogeography, Palaeoclimatology, Palaeoecology* **2000**, *158*, 259–280.
- (50) Anati, D. A. *International Journal of Salt Lake Research* **1999**, *8*, 55–70.
- (51) Feistel, R.; Weinreben, S.; Wolf, H.; Seitz, S.; Spitzer, P.; Adel, B.; Nausch, G.; Schneider, B.; Wright, D. G. *Ocean Sci.* **2010**, *22*.
- (52) Leonov, A. V. *Water Resources* **2005**, *32*, 134–144.
- (53) Covington, A. K.; Whitfield, M. *Pure and Applied Chemistry* **2009**, *60*, 865–870.
- (54) Dickson, A. G. *Deep Sea Research Part I: Oceanographic Research Papers* **1993**, *40*, 107–118.
- (55) Chester, R.; Jickells, T. D., *Marine geochemistry*, 3rd ed; John Wiley & Sons: Hoboken, NJ, 2012; 411 pp.
- (56) Hansson, I. *Deep Sea Research and Oceanographic Abstracts* **1973**, *20*, 479–491.
- (57) Bates, R. G.; Hetzer, H. B. *J. Phys. Chem.* **1961**, *65*, 667–671.
- (58) Carter, B. R.; Radich, J. A.; Doyle, H. L.; Dickson, A. G. *Limnology and Oceanography: Methods* **2013**, *11*, 16–27.
- (59) López, M.; Martínez, S.; Gómez, J.; Herms, A.; Tort, L.; Bausells, J.; Errachid, A. *Procedia Chemistry* **2009**, *1*, 445–448.
- (60) Yang, B.; Patsavas, M. C.; Byrne, R. H.; Ma, J. *Marine Chemistry* **2014**, *160*, 75–81.
- (61) Okazaki, R. R.; Sutton, A. J.; Feely, R. A.; Dickson, A. G.; Alin, S. R.; Sabine, C. L.; Bunje, P. M. E.; Virmani, J. I. *Limnology and Oceanography: Methods* **2017**, *15*, 586–600.
- (62) Afmann, S.; Frank, C.; Körtzinger, A. *Ocean Sci.* **2011**, *7*, 597–607.
- (63) Rérolle, V. M. C.; Floquet, C. F. A.; Mowlem, M. C.; Connelly, D. P.; Achterberg, E. P.; Bellerby, R. R.G. J. *TrAC Trends in Analytical Chemistry* **2012**, *40*, 146–157.
- (64) Tengberg, A. et al. *Progress in Oceanography* **1995**, *35*, 253–294.

- 
- (65) Roemmich, D. H.; Davis, R. E.; Riser, S. C.; Owens, W. B.; Molinari, R. L.; Garzoli, S. L.; Johnson, G. C. *The Argo Project. Global Ocean Observations for Understanding and Prediction of Climate Variability*; Scripps Institution of Oceanography La Jolla CA, 2003.
- (66) Feder, T. *Physics Today* **2000**, *53*, 50–51.
- (67) Manley, J.; Willcox, S. In *OCEANS 2010 IEEE - Sydney*, OCEANS 2010 IEEE - Sydney, 2010, pp 1–5.
- (68) Shitashima, K *AGU Fall Meeting Abstracts* **2010**, 1–4.
- (69) Harned, H. S.; Ehlers, R. W. *Journal of the American Chemical Society* **1932**, *54*, 1350–1357.
- (70) Harned, H. S.; Robinson, R. A. *Journal of the American Chemical Society* **1928**, *50*, 3157–3178.
- (71) Baucke, F. G. *Anal Bioanal Chem* **2002**, *374*, 772–777.
- (72) Spitzer, P. *Accred Qual Assur* **2001**, *6*, 55–60.
- (73) Marczewska, B.; Marczewski, K. *Zeitschrift für Physikalische Chemie* **2010**, *224*, 795–799.
- (74) Analytics, S. pH Fibel., 2014.
- (75) *Handbook of reference electrodes*; Inzelt, G., Baucke, F. G. K., Lewenstam, A., Scholz, F., Eds., OCLC: 852634377; Springer: Berlin, 2013, 344 pp.
- (76) Degner, R., *pH-Messung*; Wiley-VCH Verlag GmbH & Co. KGaA: Weinheim, Germany, 2008.
- (77) Dickson, A. G. *Marine Chemistry* **1993**, *44*, 131–142.
- (78) Bergveld, P. *IEEE Transactions on Biomedical Engineering* **1970**, *BME-17*, 70–71.
- (79) Bergveld, P. *Sensors and Actuators B: Chemical* **2003**, *88*, 1–20.
- (80) Takeshita, Y.; Martz, T. R.; Johnson, K. S.; Dickson, A. G. *Anal. Chem.* **2014**, *86*, 11189–11195.
- (81) Hofmann, G. E. et al. *PLOS ONE* **2011**, *6*, e28983.
- (82) Martz, T. R.; Johnson, K. S.; Jannasch, H.; Coletti, L.; Barry, J.; Lovera, C. *ResearchGate* **2008**.

- (83) Bresnahan Jr., P. J.; Martz, T. R.; Takeshita, Y.; Johnson, K. S.; LaShomb, M. *Methods in Oceanography* **2014**, *9*, 44–60.
- (84) Frieder, C. A.; Nam, S. H.; Martz, T. R.; Levin, L. A. *Biogeosciences* **2012**, *9*, 3917–3930.
- (85) Cheng, Y.; Hu, C., *MOSFET modeling & BSIM3 user's guide*; Kluwer Academic Publishers: Boston, 1999; 461 pp.
- (86) Van der Schoot, B. H.; Bergveld, P.; Bos, M.; Bousse, L. J. *Sensors and Actuators* **1983**, *4*, 267–272.
- (87) Bousse, L.; De Rooij, N.; Bergveld, P. *IEEE Transactions on Electron Devices* **1983**, *30*, 1263–1270.
- (88) Neuzil, P.; Vobecky, J. In *The 8th International Conference on Solid-State Sensors and Actuators, 1995 and Eurosensors IX.. Transducers '95*, The 8th International Conference on Solid-State Sensors and Actuators, 1995 and Eurosensors IX.. Transducers '95, 1995; Vol. 2, pp 909–912.
- (89) Johnson, K. S.; Jannasch, H. W.; Coletti, L. J.; Elrod, V. A.; Martz, T. R.; Takeshita, Y.; Carlson, R. J.; Connery, J. G. *Anal. Chem.* **2016**, *88*, 3249–3256.
- (90) Bockmon, E. E.; Dickson, A. G. *Marine Chemistry* **2015**, *171*, 36–43.
- (91) DeGrandpre, M. D.; Spaulding, R. S.; Newton, J. O.; Jaqueth, E. J.; Hamblock, S. E.; Umansky, A. A.; Harris, K. E. *Limnology and Oceanography: Methods* **2014**, *12*, 830–839.
- (92) Byrne, R. H.; Breland, J. A. *Deep Sea Research Part A. Oceanographic Research Papers* **1989**, *36*, 803–810.
- (93) Clayton, T. D.; Byrne, R. H. *Deep Sea Research Part I: Oceanographic Research Papers* **1993**, *40*, 2115–2129.
- (94) Bellerby, R. *Talanta* **2002**, *56*, 61–69.
- (95) Liu, X.; Patsavas, M. C.; Byrne, R. H. *Environ Sci Technol* **2011**, *45*, 4862–4868.
- (96) Mosley, L. M.; Husheer, S. L. G.; Hunter, K. A. *Marine Chemistry* **2004**, *91*, 175–186.
- (97) Douglas, N.; Byrne, R. *Marine Chemistry* **2017**, *190*, 66–72.
- (98) Weidgans, B. M., *New fluorescent optical pH sensors with minimal effects of ionic strength*, 2004.

- 
- (99) Friis, K.; Körtzinger, A.; Wallace, D. W. *Limnology and Oceanography: Methods* **2004**, *2*, 126–136.
- (100) Rérolle, V. M. C.; Floquet, C. F. A.; Harris, A. J. K.; Mowlem, M. C.; Bellerby, R. R.G. J.; Achterberg, E. P. *Analytica Chimica Acta* **2013**, *786*, 124–131.
- (101) Perez de Vargas Sansalvador, I. M.; Fay, C. D.; Cleary, J.; Nightingale, A. M.; Mowlem, M. C.; Diamond, D. *Sensors and Actuators B: Chemical* **2016**, *225*, 369–376.
- (102) Lai, C.-Z.; DeGrandpre, M. D.; Darlington, R. C. *Front. Mar. Sci.* **2018**, *4*, DOI: 10.3389/fmars.2017.00438.
- (103) Klimant, I.; Huber, C.; Liebsch, G.; Neurauter, G.; Stangelmayer, A.; Wolfbeis, O. S. In *New Trends in Fluorescence Spectroscopy*, Valeur, P. B., Brochon, D. J.-C., Eds.; Springer Series on Fluorescence 1; Springer Berlin Heidelberg: 2001, pp 257–274.
- (104) Fritzsche, E.; Gruber, P.; Schutting, S.; Fischer, J. P.; Strobl, M.; Müller, J. D.; Borisov, S. M.; Klimant, I. *Analytical Methods* **2017**, *9*, 55–65.
- (105) Larsen, M.; Lehner, P.; Borisov, S. M.; Klimant, I.; Fischer, J. P.; Stewart, F. J.; Canfield, D. E.; Glud, R. N. *Limnol. Oceanogr. Methods* **2016**, n/a–n/a.
- (106) Hutter, L. H.; Müller, B. J.; Koren, K.; Borisov, S. M.; Klimant, I. *J. Mater. Chem. C* **2014**, *2*, 7589–7598.
- (107) Zach, P. W.; Freunberger, S. A.; Klimant, I.; Borisov, S. M. *ACS Applied Materials & Interfaces* **2017**, *9*, 38008–38023.
- (108) Wencel, D.; Abel, T.; McDonagh, C. *Analytical Chemistry* **2014**, *86*, 15–29.
- (109) Ehgartner, J.; Wiltsche, H.; Borisov, S. M.; Mayr, T. *Analyst* **2014**, *139*, 4924–4933.
- (110) Moßhammer, M.; Strobl, M.; Köhl, M.; Klimant, I.; Borisov, S. M.; Koren, K. *ACS Sensors* **2016**, *1*, 681–687.
- (111) Bishnoi, S. W.; Rozell, C. J.; Levin, C. S.; Gheith, M. K.; Johnson, B. R.; Johnson, D. H.; Halas, N. J. *Nano Letters* **2006**, *6*, 1687–1692.
- (112) Benjaminsen, R. V., *Design and application of optical nanosensors for pH imaging in cell compartments: PhD thesis*, OCLC: 823475155; DTU Nanotech, Department of Micro- and Nanotechnology: Kgs. Lyngby, 2012.

- (113) Benjaminsen, R. V.; Sun, H.; Henriksen, J. R.; Christensen, N. M.; Almdal, K.; Andresen, T. L. *ACS Nano* **2011**, *5*, 5864–5873.
- (114) Kocincova, A. S.; Borisov, S. M.; Krause, C.; Wolfbeis, O. S. *Analytical Chemistry* **2007**, *79*, 8486–8493.
- (115) Kasik, I.; Mrazek, J.; Martan, T.; Pospisilova, M.; Podrazky, O.; Matejec, V.; Hoyerova, K.; Kaminek, M. *Anal Bioanal Chem* **2010**, *398*, 1883–1889.
- (116) *Optical chemical sensors*; Baldini, F., Organization, N. A. T., Eds.; NATO science series vol. 224, OCLC: ocm68769258; Springer: Dordrecht, 2006, 535 pp.
- (117) McDonagh, C.; Burke, C. S.; MacCraith, B. D. *Chem. Rev.* **2008**, *108*, 400–422.
- (118) Clarke, Y.; Xu, W.; Demas, J. N.; DeGraff, B. A. *Analytical Chemistry* **2000**, *72*, 3468–3475.
- (119) Goncalves, H. M.; Maule, C. D.; Jorge, P. A.; Esteves da Silva, J. C. *Analytica Chimica Acta* **2008**, *626*, 62–70.
- (120) Kosch, U.; Klimant, I.; Wolfbeis, O. S. *Fresenius J Anal Chem* **1999**, *364*, 48–53.
- (121) Suhling, K. et al. *Medical Photonics* **2015**, *27*, 3–40.
- (122) Lin, H.-J.; Herman, P.; Lakowicz, J. R. *Cytometry A* **2003**, *52*, 77–89.
- (123) Orte, A.; Alvarez-Pez, J. M.; Ruedas-Rama, M. J. *ACS Nano* **2013**, *7*, 6387–6395.
- (124) Strobl, M.; Rappitsch, T.; Borisov, S. M.; Mayr, T.; Klimant, I. *Analyst* **2015**, *140*, 7150–7153.
- (125) Shen, L.; Lu, X.; Tian, H.; Zhu, W. *Macromolecules* **2011**, *44*, 5612–5618.
- (126) Niu, W.; Fan, L.; Nan, M.; Li, Z.; Lu, D.; Wong, M. S.; Shuang, S.; Dong, C. *Anal. Chem.* **2015**, *87*, 2788–2793.
- (127) Vasylevska, A. S.; Karasyov, A. A.; Borisov, S. M.; Krause, C. *Anal Bioanal Chem* **2007**, *387*, 2131–2141.
- (128) Calder, G. V.; Barton, T. J. *Journal of Chemical Education* **1971**, *48*, 338.
- (129) Reijenga, J. C.; Gagliardi, L. G.; Kenndler, E. *Journal of Chromatography A* **2007**, *1155*, 142–145.

- 
- (130) Christensen, J. J.; Hansen, L. D.; Izatt, R. M., *Handbook of proton ionization heats and related thermodynamic quantities*; Contribution from the Center for Thermochemical Studies, Brigham Young University, Provo, Utah ; no. 85; Wiley: New York, 1976; 269 pp.
- (131) Perrin, D. D, *Ionisation Constants of Inorganic Acids and Bases in Aqueous Solution*, OCLC: 1040596557; Elsevier Science: Kent, 2014.
- (132) Jokic, T.; Borisov, S. M.; Saf, R.; Nielsen, D. A.; Köhl, M.; Klimant, I. *Anal Chem* **2012**, *84*, 6723–6730.
- (133) Schröder, C. R.; Weidgans, B. M.; Klimant, I. *Analyst* **2005**, *130*, 907–916.
- (134) Gieskes, J. M. *Limnology and Oceanography* **1969**, *14*, 679–685.
- (135) Borisov, S. M.; Würth, C.; Resch-Genger, U.; Klimant, I. *Anal. Chem.* **2013**, *85*, 9371–9377.
- (136) Borisov, S. M.; Gatterer, K.; Bitschnau, B.; Klimant, I. *J Phys Chem C Nanomater Interfaces* **2010**, *114*, 9118–9124.
- (137) Hulth, S.; Aller, R. C.; Engström, P.; Selander, E. *Limnology and Oceanography* **2002**, *47*, 212–220.
- (138) Kermis, H.; Kostov, Y.; Harms, P.; Rao, G. *Biotechnology Progress* **2002**, *18*, 1047–1053.
- (139) Kermis, H. R.; Kostov, Y.; Rao, G. *Analyst* **2003**, *128*, 1181–1186.
- (140) Larsen, M.; Borisov, S. M.; Grunwald, B.; Klimant, I.; Glud, R. N. *Limnol. Oceanogr. Methods* **2011**, *9*, 348–360.
- (141) Clarke, J. S.; Achterberg, E. P.; Rérolle, V. M. C.; Abi Kaed Bey, S.; Floquet, C. F. A.; Mowlem, M. C. *Analytica Chimica Acta* **2015**, *897*, 69–80.
- (142) Zhu, Q.; Aller, R. C.; Fan, Y. *Environmental Science & Technology* **2005**, *39*, 8906–8911.
- (143) Kim, H. N.; Swamy, K. M. K.; Yoon, J. *Tetrahedron Letters* **2011**, *52*, 2340–2343.
- (144) Wu, S.; Wu, S.; Yi, Z.; Zeng, F.; Wu, W.; Qiao, Y.; Zhao, X.; Cheng, X.; Tian, Y. *Sensors* **2018**, *18*, 564.
- (145) Aigner, D.; Borisov, S. M.; Orriach Fernández, F. J.; Fernández Sánchez, J. F.; Saf, R.; Klimant, I. *Talanta* **2012**, *99*, 194–201.

- (146) Ma, Q.-J.; Li, H.-P.; Yang, F.; Zhang, J.; Wu, X.-F.; Bai, Y.; Li, X.-F. *Sensors and Actuators B: Chemical* **2012**, *166-167*, 68–74.
- (147) Daffy, L. M.; Silva, A. P. d.; Gunaratne, H. Q. N.; Huber, C.; Lynch, P. L. M.; Werner, T.; Wolfbeis, O. S. *Chemistry – A European Journal* **1998**, *4*, 1810–1815.
- (148) Pfeifer, D.; Klimant, I.; Borisov, S. M. *Chemistry - A European Journal* **2018**, DOI: 10.1002/chem.201800867.
- (149) Aigner, D.; Borisov, S. M.; Petritsch, P.; Klimant, I. *Chem. Commun.* **2013**, *49*, 2139–2141.
- (150) Werner, T.; Huber, C.; Heintl, S.; Kollmannsberger, M.; Daub, J.; Wolfbeis, O. S. *Fresenius J Anal Chem* **1997**, *359*, 150–154.
- (151) Li, Z.; Li, L.-J.; Sun, T.; Liu, L.; Xie, Z. *Dyes and Pigments* **2016**, *128*, 165–169.
- (152) Marfin, Y. S.; Shipalova, M. V.; Kurzin, V. O.; Ksenofontova, K. V.; Solomonov, A. V.; Rumyantsev, E. V. *Journal of Fluorescence* **2016**, *26*, 2105–2112.
- (153) Gotor, R.; Ashokkumar, P.; Hecht, M.; Keil, K.; Rurack, K. *Analytical Chemistry* **2017**, *89*, 8437–8444.
- (154) Loudet, A.; Burgess, K. *Chemical Reviews* **2007**, *107*, 4891–4932.
- (155) Killoran, J.; McDonnell, S. O.; Gallagher, J. F.; O’Shea, D. F. *New J. Chem.* **2008**, *32*, 483–489.
- (156) McDonnell, S. O.; O’Shea, D. F. *Organic Letters* **2006**, *8*, 3493–3496.
- (157) Murtagh, J.; Frimannsson, D. O.; O’Shea, D. F. *Organic Letters* **2009**, *11*, 5386–5389.
- (158) Kamkaew, A.; Burgess, K. *Chemical Communications* **2015**, *51*, 10664–10667.
- (159) Hinkeldey, B.; Schmitt, A.; Jung, G. *ChemPhysChem* **2008**, *9*, 2019–2027.
- (160) *Principles of Fluorescence Spectroscopy*; Lakowicz, J. R., Ed.; Springer US: Boston, MA, 2006.
- (161) Mukherjee, S.; Paul, A. K.; Krishna Rajak, K.; Stoeckli-Evans, H. *Sensors and Actuators B: Chemical* **2014**, *203*, 150–156.
- (162) Silva, A. P. d.; Vance, T. P.; West, M. E. S.; Wright, G. D. *Org. Biomol. Chem.* **2008**, *6*, 2468–2480.

- 
- (163) Aigner, D.; Freunberger, S. A.; Wilkening, M.; Saf, R.; Borisov, S. M.; Klimant, I. *Anal Chem* **2014**, *86*, 9293–9300.
- (164) Lei, J.; Wang, L.; Zhang, J. *Chem. Commun.* **2010**, *46*, 8445–8447.
- (165) Melde, B. J.; Johnson, B. J.; Charles, P. T. *Sensors (Basel)* **2008**, *8*, 5202–5228.
- (166) Chu, C. S.; Su, C. J. *Journal of Lightwave Technology* **2018**, *36*, 857–862.
- (167) Wencel, D.; MacCraith, B. D.; McDonagh, C. *Sensors and Actuators B: Chemical* **2009**, *139*, 208–213.
- (168) Alvarado mendez, E; rojas laguna, R; Andrade-Lucio, J. A.; Hernandez-Cruz, D; Lessard, R. A.; Avina-Cervantes, J. G. *Sensors and Actuators B: Chemical* **2005**, *106*, 518–522.
- (169) Peng, H.-s.; Stolwijk, J. A.; Sun, L.-N.; Wegener, J.; Wolfbeis, O. S. *Angewandte Chemie* **2009**, *122*, 4342–4345.
- (170) Boniello, C.; Mayr, T.; Bolivar, J. M.; Nidetzky, B. *BMC Biotechnology* **2012**, *12*, 11.
- (171) Begemann, J.; Spiess, A. C. *Biotechnol J* **2015**, *10*, 1822–1829.
- (172) Liebsch, G.; Klimant, I.; Krause, C.; Wolfbeis, O. S. *Anal. Chem.* **2001**, *73*, 4354–4363.
- (173) Poehler, E.; Herzog, C.; Suendermann, M.; Pfeiffer, S. A.; Nagl, S. *Engineering in Life Sciences* **2014**, *15*, 276–285.
- (174) Martínez Ferreras, F.; Wolfbeis, O. S.; Gorris, H. H. *Analytica Chimica Acta* **2012**, *729*, 62–66.
- (175) Han, C.; Yao, L.; Xu, D.; Xie, X.; Zhang, C. *Scientific Reports* **2016**, *6*, 26417.
- (176) Huber, C.; Klimant, I.; Krause, C.; Wolfbeis, O. S. *Anal. Chem.* **2001**, *73*, 2097–2103.
- (177) Kürner, J. M.; Klimant, I.; Krause, C.; Preu, H.; Kunz, W.; Wolfbeis, O. S. *Bioconjugate Chemistry* **2001**, *12*, 883–889.
- (178) Bültzingslöwen, C. v.; McEvoy, A. K.; McDonagh, C.; MacCraith, B. D.; Klimant, I.; Krause, C.; Wolfbeis, O. S. *Analyst* **2002**, *127*, 1478–1483.
- (179) Borisov, S. M.; Gatterer, K.; Klimant, I. *Analyst* **2010**, *135*, 1711–1717.
- (180) Müller, B. J.; Rappitsch, T.; Staudinger, C.; Rüschtz, C.; Borisov, S. M.; Klimant, I. *Anal. Chem.* **2017**, *89*, 7195–7202.
- (181) Strobl, M.; Walcher, A.; Mayr, T.; Klimant, I.; Borisov, S. M. *Anal. Chem.* **2017**, DOI: 10.1021/acs.analchem.6b04045.

- (182) Millero, F. J. *Chem. Rev.* **2007**, *107*, 308–341.
- (183) Le Bris, N; Birot, D *Analytica Chimica Acta* **1997**, *356*, 205–215.
- (184) Jimenez-Jorquera, C.; Orozco, J.; Baldi, A. *Sensors (Basel)* **2009**, *10*, 61–83.
- (185) Liu, X.; Wang, Z. A.; Byrne, R. H.; Kaltenbacher, E. A.; Bernstein, R. E. *Environmental Science & Technology* **2006**, *40*, 5036–5044.
- (186) Friederich, G. E.; Brewer, P. G.; Herlien, R.; Chavez, F. P. *Deep Sea Research Part I: Oceanographic Research Papers* **1995**, *42*, 1175–1186.
- (187) Fiedler, B.; Fietzek, P.; Vieira, N.; Silva, P.; Bittig, H. C.; Körtzinger, A. *J. Atmos. Oceanic Technol.* **2012**, *30*, 112–126.
- (188) Fietzek, P.; Fiedler, B.; Steinhoff, T.; Körtzinger, A. *J. Atmos. Oceanic Technol.* **2013**, *31*, 181–196.
- (189) Jiang, Z.-P. et al. *Limnol. Oceanogr. Methods* **2014**, *12*, 264–280.
- (190) Sutton, A. J. et al. *Earth System Science Data* **2014**, *6*, 353–366.
- (191) Hunt, C. W.; Snyder, L.; Salisbury, J. E.; Vandemark, D.; McDowell, W. H. *Limnol. Oceanogr. Methods* **2017**, *15*, 291–301.
- (192) Clarke, J. S.; Achterberg, E. P.; Connelly, D. P.; Schuster, U.; Mowlem, M. *TrAC Trends in Analytical Chemistry* **2017**, *88*, 53–61.
- (193) Lefèvre, N.; Ciabrini, J. P.; Michard, G.; Brient, B.; DuChaffaut, M.; Merlivat, L. *Marine Chemistry* **1993**, *42*, 189–198.
- (194) DeGrandpre, M. D.; Hammar, T. R.; Smith, S. P.; Sayles, F. L. *Limnol. Oceanogr.* **1995**, *40*, 969–975.
- (195) Lu, Z.; Dai, M.; Xu, K.; Chen, J.; Liao, Y. *Talanta* **2008**, *76*, 353–359.
- (196) DeGrandpre, M. D.; Baehr, M. M.; Hammar, T. R. *Anal. Chem.* **1999**, *71*, 1152–1159.
- (197) Severinghaus, J. W.; Bradley, A. F. *J Appl Physiol* **1958**, *13*, 515–520.
- (198) Xie, X.; Bakker, E. *Anal. Chem.* **2013**, *85*, 1332–1336.
- (199) Amao, Y.; Nakamura, N. *Sensors and Actuators B: Chemical* **2004**, *100*, 347–351.
- (200) Schutting, S.; Borisov, S. M.; Klimant, I. *Anal. Chem.* **2013**, *85*, 3271–3279.

- 
- (201) Schutting, S.; Klimant, I.; Beer, D. d.; Borisov, S. M. *Methods Appl. Fluoresc.* **2014**, *2*, 024001.
- (202) Schutting, S.; Jokic, T.; Strobl, M.; Borisov, S. M.; Beer, D. d.; Klimant, I. *J. Mater. Chem. C* **2015**, *3*, 5474–5483.
- (203) Carraway, E. R.; Demas, J. N.; DeGraff, B. A.; Bacon, J. R. *Anal. Chem.* **1991**, *63*, 337–342.
- (204) Lehner, P.; Larndorfer, C.; Garcia-Robledo, E.; Larsen, M.; Borisov, S. M.; Revsbech, N.-P.; Glud, R. N.; Canfield, D. E.; Klimant, I. *PLOS ONE* **2015**, *10*, e0128125.
- (205) Accorsi, G.; Verri, G.; Bolognesi, M.; Armaroli, N.; Clementi, C.; Miliani, C.; Romani, A. *Chem. Commun.* **2009**, 3392–3394.
- (206) Mills, A.; Chang, Q.; McMurray, N. *Anal. Chem.* **1992**, *64*, 1383–1389.
- (207) Mills, A.; Monaf, L. **1996**, *121*, 535–540.
- (208) *Guide to best practices for ocean CO<sub>2</sub> measurements*; Dickson, A. G., Sabine, C. L., Christian, J. R., Barger, C. P., North Pacific Marine Science Organization, Eds.; PICES special publication no. 3, OCLC: ocn420872251; North Pacific Marine Science Organization: Sidney, BC, 2007, 1 p.
- (209) Easley, R. A.; Byrne, R. H. *Environ Sci Technol* **2012**, *46*, 5018–5024.
- (210) Roy, R. N.; Roy, L. N.; Vogel, K. M.; Porter-Moore, C.; Pearson, T.; Good, C. E.; Millero, F. J.; Campbell, D. M. *Marine Chemistry, MAR. CHEM., MAR. CHEM., Marine chemistry* **1993**, *44*, 249–267.
- (211) Pierrot, D.; Wallace, D.; Lewis, E. *MS Excel Program Developed for CO<sub>2</sub> System Calculations*, type: dataset; Environmental Sciences Division, Oak Ridge National Laboratory, 2011.
- (212) DelValls, T.; Dickson, A. *Deep Sea Research Part I: Oceanographic Research Papers* **1998**, *45*, 1541–1554.
- (213) Garcia, H. E.; Gordon, L. I. *Limnology and Oceanography* **1992**, *37*, 1307–1312.
- (214) Mohrholz, V.; Naumann, M.; Nausch, G.; Krüger, S.; Gräwe, U. *Journal of Marine Systems* **2015**, *148*, 152–166.

- (215) Gräwe, U.; Naumann, M.; Mohrholz, V.; Burchard, H. *J. Geophys. Res. Oceans* **2015**, *120*, 7676–7697.
- (216) Geißler, F.; Achterberg, E. P.; Beaton, A. D.; Hopwood, M. J.; Clarke, J. S.; Mutzberg, A.; Mowlem, M. C.; Connelly, D. P. *Frontiers in Marine Science* **2017**, *4*, DOI: 10.3389/fmars.2017.00322.
- (217) Jeevarajan, A. S.; Vani, S.; Taylor, T. D.; Anderson, M. M. *Biotechnol. Bioeng.* **2002**, *78*, 467–472.
- (218) John, G. T.; Goelling, D.; Klimant, I.; Schneider, H.; Heinzle, E. *J. Dairy Res.* **2003**, *70*, 327–333.
- (219) Zhang, W.; Tang, B.; Liu, X.; Liu, Y.; Xu, K.; Ma, J.; Tong, L.; Yang, G. *The Analyst* **2009**, *134*, 367–371.
- (220) Tang, B.; Yu, F.; Li, P.; Tong, L.; Duan, X.; Xie, T.; Wang, X. *J. Am. Chem. Soc.* **2009**, *131*, 3016–3023.
- (221) Canadell, J. G.; Le Quere, C.; Raupach, M. R.; Field, C. B.; Buitenhuis, E. T.; Ciais, P.; Conway, T. J.; Gillett, N. P.; Houghton, R. A.; Marland, G. *Proceedings of the National Academy of Sciences* **2007**, *104*, 18866–18870.
- (222) Le Quéré, C. et al. *Nature Geoscience* **2009**, *2*, 831–836.
- (223) Byrne, R. H.; Mecking, S.; Feely, R. A.; Liu, X. *Geophysical Research Letters* **2010**, *37*, n/a–n/a.
- (224) Hammer, K.; Schneider, B.; Kuliński, K.; Schulz-Bull, D. E. *Estuarine, Coastal and Shelf Science* **2014**, *146*, 24–32.
- (225) Staudinger, C. et al. *Limnol. Oceanogr. Methods* **2018**, *16*, 459–473.
- (226) Tormo, L.; Bustamante, N.; Colmenarejo, G.; Orellana, G. *Anal. Chem.* **2010**, *82*, 5195–5204.
- (227) HydroMed Products., <http://www.advbimaterials.com/products/hydrophilic/hydromed.html> (accessed 04/18/2018).
- (228) Lundrigan, T.; Crawford, S.; Stanley Cameron, T.; Thompson, A. *Chemical Communications* **2012**, *48*, 1003–1005.
- (229) Lundrigan, T.; Thompson, A. *J. Org. Chem.* **2013**, *78*, 757–761.

- 
- (230) Liu, B.; Novikova, N.; Cather Simpson, M.; M. Timmer, M. S.; L. Stocker, B.; Söhnel, T.; C. Ware, D.; J. Brothers, P. *Organic & Biomolecular Chemistry* **2016**, *14*, 5205–5209.
- (231) Nguyen, A. L.; Bobadova-Parvanova, P.; Hopfinger, M.; Fronczek, F. R.; Smith, K. M.; Vicente, M. G. H. *Inorg. Chem.* **2015**, *54*, 3228–3236.
- (232) Müller, J. D.; Rehder, G. *Frontiers in Marine Science* **2018**, *5*, DOI: 10.3389/fmars.2018.00177.
- (233) Vachette, E.; Fenge, C.; Cappia, J.-M; Delaunay, L; Greller, G.; Barbaroux, M. **2014**, *12*.
- (234) Florea, L.; Fay, C.; Lahiff, E.; Phelan, T.; O'Connor, N. E.; Corcoran, B.; Diamond, D.; Benito-Lopez, F. *Lab on a Chip* **2013**, *13*, 1079.
- (235) Magnusson, E. B.; Halldorsson, S.; Fleming, R. M.; Leosson, K. *Biomedical Optics Express* **2013**, *4*, 1749.
- (236) Poehler, E.; Herzog, C.; Pfeiffer, S. A.; Lotter, C.; Peretzki, A. J.; Aigner, D.; Mayr, T.; Beckert, E.; Nagl, S. *Procedia Engineering* **2015**, *120*, 175–179.
- (237) Tahirbegi, I. B.; Ehgartner, J.; Sulzer, P.; Zieger, S.; Kasjanow, A.; Paradiso, M.; Strobl, M.; Bouwes, D.; Mayr, T. *Biosensors and Bioelectronics* **2017**, *88*, 188–195.
- (238) Gruber, P.; Marques, M. P.; Sulzer, P.; Wohlgemuth, R.; Mayr, T.; Baganz, F.; Szita, N. *Biotechnology Journal* **2017**, *12*, 1600475.
- (239) Aigner, D.; Ungerböck, B.; Mayr, T.; Saf, R.; Klimant, I.; Borisov, S. M. *J. Mater. Chem. C* **2013**, *1*, 5685–5693.
- (240) Liu, E.; Ghandehari, M.; Brückner, C.; Khalil, G.; Worlinsky, J.; Jin, W.; Sidelev, A.; Hyland, M. A. *Cement and Concrete Research* **2017**, *95*, 232–239.
- (241) Slonczewski, J. L.; Fujisawa, M.; Dopson, M.; Krulwich, T. A. In *Advances in Microbial Physiology*; Elsevier: 2009; Vol. 55, pp 1–317.
- (242) Gorman, A.; Killoran, J.; O'Shea, C.; Kenna, T.; Gallagher, W. M.; O'Shea, D. F. *Journal of the American Chemical Society* **2004**, *126*, 10619–10631.
- (243) *CRC handbook of tables for organic compound identification*, 3. ed., 14. print; Rappoport, Z., Ed., OCLC: 248068942; CRC Press: Boca Raton, Fla, 1985, 563 pp.

- (244) Kühl, M.; Behrendt, L.; Trampe, E.; Qvortrup, K.; Schreiber, U.; Borisov, S. M.; Klimant, I.; Larkum, A. W. D. *Frontiers in Microbiology* **2012**, *3*, DOI: 10.3389/fmicb.2012.00402.

---

## 8 Curriculum Vitae

### Christoph Staudinger

|               |   |
|---------------|---|
| Address       | Plüddemanngasse 14/11, A-8010 Graz, Austria |
| Date of Birth | 05.08.1987                                  |
| Nationality   | Austria                                     |
| E-mail        | ch.staudi@gmail.com                         |

### Education

|                   |  |
|-------------------|--|
| 04/2014 - 10/2018 | <b>PhD student</b> in Technical Chemistry at Graz University of Technology, Topic: Optical High Performance Sensor Materials for pH-Monitoring in Oceanography. Supervisor: Prof. Ingo Klimant, Co-supervision Assoc.Prof. Sergey Borisov  |
| 01/2012 - 02/2014 | <b>Master program</b> in Technical Chemistry at Graz University of Technology and Karl-Franzens University Graz (NAWI Project). Thesis: Teflon Soluble Luminophores – A Way to Outstandingly Sensitive Oxygen Sensors. Supervisor: Prof. Ingo Klimant, Co-supervision Assoc.Prof. Sergey Borisov |
| 10/2008 - 01/2012 | <b>Bachelor program</b> in Chemistry; Graz University of Technology and Karl-Franzens University Graz (NAWI Project)   |
| 09/2002 - 06/2007 | <b>A-Level</b> at HTL-Wels, Upper Austria  |

### Awards

|         |  |
|---------|--|
| 02/2015 | ASLO, Outstanding Student Presentation Award |
| 07/2015 | ASCOS 2015, First Place Student Presentation |

## Publications in Peer Reviewed Journals

**Staudinger, C.**, Breininger, J., Klimant, I., Borisov, S.M. *Near-infrared aza-BODIPY dyes with fluorescence response solely due to photoinduced electron transfer: new pH indicators covering the neutral to highly alkaline range.* prepared for submission to "Analyst"

Fritzsche, E., **Staudinger, C.**, Fischer, J.P., Thar, R., Jannasch, H.W., Plant, J.N., Blum, M., Massion, G., Thomas, H., Hoec, J., Johnson, K.S., Borisov, S.M., Klimant, I. *A validation and comparison study of new, compact, versatile optodes for oxygen, pH and carbon dioxide in marine environments.* Marine Chemistry, under review

**Staudinger, C.**, Strobl, M., Breininger, J., Klimant, I., Borisov, S.M. *Optical pH sensors for oceanographic applications: low cross-sensitivity to temperature and ionic strength, excellent stability and fast response.* Sensors & Actuators: B. Chemical, under review

Grengg, C., Müller, B., **Staudinger, C.**, Mittermayr, F., Breininger, J., Ungerböck, B., Borisov, S.M., Mayr, T., Dietzel, M. *High-resolution optical pH imaging of concrete exposed to chemically corrosive environments.* Cement and Concrete Research - Journal, under review

**Staudinger, C.**, Strobl, M., Fischer, J.P., Thar, R., Mayr, T., Aigner, D., Müller, B.J., Müller, B., Lehner, P., Mistlberger, G., Fritzsche, E., Ehgartner, J., Zach, P.W., Clarke, J.S., Geißler, F., Mutzberg, A., Müller, J.D., Achterberg, E.P., Borisov, S.M., Klimant, I. *A versatile optode system for oxygen, carbon dioxide, and pH measurements in seawater with integrated battery and logger: A versatile optode system for O<sub>2</sub>, CO<sub>2</sub>, and pH.* Limnol. Oceanogr. Methods, 16, 459-473 (2018).

Müller, B. J., Rappitsch, T., **Staudinger, C.**, Rüschtz, C., Borisov, S.M., Klimant, I. *Sodium-Selective Fluoroionophore-Based Optodes for Seawater Salinity Measurement.* Anal. Chem. 89, 7195–7202 (2017).

**Staudinger, C.** & Borisov, S. M. Long-wavelength analyte-sensitive luminescent probes and optical (bio)sensors. Methods Appl. Fluoresc. 3, (2015).

Lehner, P., **Staudinger, C.**, Borisov, S. M., Regensburger, J. & Klimant, I. Intrinsic artefacts in optical oxygen sensors—how reliable are our measurements? Chem. Weinh. Bergstr. Ger. 21, 3978–3986 (2015).

---

Lehner, P., **Staudinger, C.**, Borisov, S. M. & Klimant, I. *Ultra-sensitive optical oxygen sensors for characterization of nearly anoxic systems*. Nat Commun 5, (2014).

### Oral Presentations

**Staudinger, C.**, Strobl, M., Fischer, J.P., Müller, B.J., Lehner, P., Zach, P.W., Aigner, D., Müller, B., Ehgartner, J., Thar, R., Mistlberger, G., Mayr, T., Borisov, S.M., Klimant, I. *A pH-Optode for Seawater Monitoring*, ASLO, Granada, Spain, **2015, Outstanding Student Presentation Award**

### Poster Presentations

**Staudinger, C.**, Borisov, S.M., Lehner, P., Klimant, I. *Ultra-sensitive Optical Oxygen Sensors based on Long-decaying Phosphorescent Complexes embedded in Perfluorinated Polymers* Europtrode XII, Athens, Greece, **2014**

**Staudinger, C.**, Strobl, M., Fischer, J.P., Müller, B.J., Borisov, S.M., Klimant, I. *A stable and fast pH Optode for Seawater Measurements* Europtrode XIII, Graz, Austria, **2016**

**Staudinger, C.**, Breininger, J., Strobl, M., Fischer, J.P., Borisov, S.M., Klimant, I. *A Covalently Coupled pH Sensor Material in a Crosslinked Matrix for Oceanography* Europtrode XIV, Naples, Italy, **2018**

Ungerböck, B., Breininger, J., **Staudinger, C.**, Holtappels, M., Koopmans, D., Klimant, I., Borisov, S.M. *Fast pH Optodes for Use in pH Eddy Covariance* Europtrode XIV, Naples, Italy, **2018**

---

## 9 List of Figures

|     |  |    |
|-----|--|----|
| 2.1 | Theoretical development of the activity coefficient with increasing ionic strength for differently charged ions. Calculated with the Davies equation for the ionic charges 1, 2 and 3. . . . .   | 6  |
| 2.2 | Pt/H <sub>2</sub>   AgCl/Ag cell (Harned cell) for pH measurements, adapted from [5] . .   | 16 |
| 2.3 | Pt/H <sub>2</sub>    Pt/H <sub>2</sub> (Baucke cell) for pH measurements, adapted from [5]. . . . .  | 17 |
| 2.4 | Scheme of a glass electrode. . . . .   | 18 |
| 2.5 | Schematic representation of an ISFET (a) and a measurement circuit (b), D, G and S are drain, gate and source, respectively, V <sub>DS</sub> is the applied constant potential and I <sub>d</sub> is the current. Adapted from [79]. . . . .   | 23 |
| 2.6 | Spectra of m-cresol purple at different pH values. The peaks at approximately 430 nm and 580 nm are the absorptions of the mono-anionic di-anionic forms of the m-cresol purple, respectively. . . . .   | 24 |
| 2.7 | Dynamic range of a pH sensor material with pK <sub>a</sub> 7. In (a) the response of a pH sensor material over pH is plotted and in (b) the derivate $dSignal/dpH$ , which describes the sensitivity of the sensor is plotted. The red line marks the pK <sub>a</sub> of the sensor material, the dark gray area marks the range of highest sensitivity and the light gray are the range of sufficient sensitivity. . . . .  | 33 |
| 2.8 | Ionic strength dependence of different acid/base reactions. The solid red lines and the dashed blue lines indicate calculated data on the NBS and the "total" pH scale, respectively. These calculations were conducted on basis of the Davies equation 2.6. The dotted green lines for TRIS and m-cresol purple (mcp) were plotted based on the measurements and fits of Mosley et al. [96]. Different cases are plotted: (a) first deprotonation of an uncharged acid, (b) deprotonation of a protonated base and (c) second deprotonation of an acid. . . . . | 38 |

---

|      |  |    |
|------|--|----|
| 2.9  | Mechanism of PET quenching for pH sensing. (a) The receptor group (e.g. amine or phenol) is protonated and PET quenching is inhibited. Hence the indicator is fluorescent. (b) The receptor is deprotonated and the indicator is quenched by PET. . . . .  | 41 |
| 2.10 | Schematics of the t-DLR concept. The yellow area indicates the time when the excitation light is on. The two gray areas are the measurement windows, where the mixed emission of indicator and reference and the pure reference are measured.  | 45 |
| 2.11 | Schematics of the f-DLR concept for an indicator. In the left column the signals are depicted against time and in the right column the values are shown in polar plots. In line (a) the phase of the excitation light is shown and in the lines (b) and (c) the responses of the phosphorescent reference and the fluorescent indicators are depicted. In the polar plots the amplitude of the signals is visualized as the length of the arrows. In lines (d) and (e) the superimposed signals at low pH and high pH are shown (valid for indicators which are in the "on" state when protonated (e.g. aza-BODIPYs)). . . . . | 46 |
| 2.12 | Example of a Boltzmann sigmoid . . . . .   | 49 |
| 2.13 | Example of a temperature compensated Boltzmann sigmoid with linear coefficients for <i>Top</i> , <i>Bottom</i> and $pK_a$ : (left) 3 dimensional plot depicting the response surface; (right) Temperature projected curves for better visualization. . . . .   | 50 |
| 2.14 | Temperature and salinity projections of the 4 dimensional surface with fixed temperature and varied salinity. . . . .  | 51 |
| 3.1  | Photographic images and a sketch of the optodes. . . . .   | 58 |
| 3.2  | Cross-section, used indicators, spectral properties and response curves of the sensor materials. . . . .   | 61 |
| 3.3  | Temperature and salinity calibration of the pH sensing material pH-1. . . . .  | 67 |
| 3.4  | Stability measurement of the pH and $pO_2$ sensor materials. . . . .   | 69 |
| 3.5  | Profiles recorded at the Gotland deep monitoring station BY15. . . . .   | 72 |
| 3.6  | Continuous measurement of the surface pH during the cruise in the Baltic Sea.  | 73 |
| 3.7  | Simultaneous measurement of pH and $O_2$ with two optodes in the harbour of Kiel in 2-4 m water depth. . . . .   | 75 |

---

|       |   |     |
|-------|---|-----|
| 3.8   | Simultaneous measurement of pH, dissolved oxygen, and carbon dioxide with an array of three optodes in the harbor of Kiel and their correlation . . . . .                 | 75  |
| 3.9   | Simultaneous measurement of pH, dissolved oxygen and carbon dioxide with the optode system over 6 days on a pier in Southampton at $\approx 3$ m water depth. . . . .     | 77  |
| S3.1  | Measurement of oxygen concentration in seagrass in the Limfjord near Aggersund. . . . .   | 85  |
| 4.1   | Spectral properties of the pH-1 sensor material . . . . .   | 101 |
| 4.2   | Overview of the sensing materials and their preparation steps. . . . .  | 102 |
| 4.3   | Temperature calibration and stability data of the pH-1 sensor material. . . . .   | 104 |
| 4.4   | Temperature dependence of the response of the developed sensing materials. . . . .  | 105 |
| 4.5   | Temperature and salinity calibration and stability of the pH-2 sensing material. . . . .  | 108 |
| 4.6   | Temperature and salinity calibration and stability of the pH-3 sensing material. . . . .  | 111 |
| 4.7   | Temperature and salinity calibration and stability of the pH-4 sensing material. . . . .  | 113 |
| 4.8   | Profiling measurements in the Baltic Sea and a measurement on a mooring in Kiel fjord . . . . .   | 115 |
| S4.1  | Overview of the used indicator dyes . . . . .   | 121 |
| S4.2  | Reaction pathway to dye 1. . . . .  | 122 |
| S4.3  | Reaction pathway to dye 2. . . . .  | 123 |
| S4.4  | Reaction pathway to dye 3. . . . .  | 124 |
| S4.5  | Reaction pathway to dye 4. . . . .  | 126 |
| S4.6  | Composition of the synthesized polymers. . . . .  | 126 |
| S4.7  | Calibration curve of the pH-2 sensing material. Temperature-compensated calibration functions grouped by temperature with corresponding residuals depicted below. . . . . | 129 |
| S4.8  | Salinity dependence of the pH-4 sensor material compared to that of the pH glass electrode and spectrophotometric system. . . . .   | 130 |
| S4.9  | $^1\text{H}$ -NMR spectrum (300 MHz, Chloroform-d) of indicator <b>2</b> . . . . .  | 131 |
| S4.10 | Mass spectrum (MALDI-TOF) of indicator <b>2</b> . . . . .   | 132 |
| S4.11 | $^1\text{H}$ -NMR spectrum (300 MHz, Chloroform-d) of indicator <b>3</b> . . . . .  | 132 |
| S4.12 | Mass spectrum (MALDI-TOF) of indicator <b>3</b> . . . . .   | 133 |
| S4.13 | $^1\text{H}$ -NMR spectrum (300 MHz, Chloroform-d) of indicator <b>4</b> . . . . .  | 133 |

---

|       |  |     |
|-------|--|-----|
| 5.1   | Synthetic route to the new aza-BODIPY dyes. Intermediates with indices belong to the respective dye. . . . .   | 144 |
| 5.2   | pH dependence of absorption (solid lines) and emission spectra (dashed lines) of the indicator 3 (a) and state-of-the-art hydroxy-aza-BODIPY pH indicator. . . | 145 |
| 5.3   | Structures with apparent $pK_a$ values (a) and titration curves (b) of the new aza-BODIPY indicators. . . . .  | 147 |
| 5.4   | Enhancement of fluorescence properties of the pH sensor via light harvesting. .  | 149 |
| 5.5   | pH dependency of the emission spectrum of the sensor and optical properties of the imaging set-up. . . . .   | 150 |
| 5.6   | Imaging of pH distribution. . . . .  | 150 |
| S5.1  | Absorption spectra of the light harvesting measurement foils. D...Donor (tetraphenyl aza-BODIPY), A... Acceptor (Indicator 3) . . . . .                        | 156 |
| S5.2  | Normalized absorption and emission spectra (protonated) of the indicators. . .   | 157 |
| S5.3  | Calibration curves of the indicators in EtOH/buffer 1:1. . . . .   | 157 |
| S5.4  | $^1H$ NMR spectrum of indicator 1 . . . . .  | 158 |
| S5.5  | $^1H$ NMR spectrum of indicator 2 . . . . .  | 158 |
| S5.6  | $^1H$ NMR spectrum of indicator 3 . . . . .  | 159 |
| S5.7  | $^1H$ NMR spectrum of indicator 4 . . . . .  | 159 |
| S5.8  | $^1H$ NMR spectrum of indicator 5 . . . . .  | 160 |
| S5.9  | $^{13}C$ APT NMR spectrum of indicator 1 . . . . .   | 160 |
| S5.10 | $^{13}C$ APT NMR spectrum of indicator 2 . . . . .   | 161 |
| S5.11 | $^{13}C$ APT NMR spectrum of indicator 4 . . . . .   | 161 |
| S5.12 | MS-spectrum of indicator 1 . . . . .   | 162 |
| S5.13 | MS-spectrum of indicator 2 . . . . .   | 163 |
| S5.14 | MS-spectrum of indicator 3 . . . . .   | 164 |
| S5.15 | MS-spectrum of indicator 4 . . . . .   | 165 |
| S5.16 | MS-spectrum of indicator 5 . . . . .   | 166 |

---

## 10 List of Tables

|      |   |     |
|------|---|-----|
| 4.1  | Response times of the sensor materials at different temperatures . . . . .                        | 106 |
| 4.2  | Comparison of the properties and characteristics of the four presented sensor materials . . . . . | 117 |
| 4.3  | Comparison with previously reported indicators . . . . .  | 119 |
| S4.1 | Calibration coefficients of the new sensor materials. . . . .                                     | 130 |
| 5.1  | Photophysical properties of the reported dyes in THF. . . . .                                     | 146 |